TESIS DE LA UNIVERSIDAD
DE ZARAGOZA

2014

62

Carmelo Juez Jiménez

Development of robust, physically-based numerical models for transport processes and geomorphodynamics changes

Departamento

Ciencia y Tecnología de Materiales y Fluidos

Director/es

Murillo Castarlenas, Javier

ISSN 2254-7606

Prensas de la Universidad
Universidad Zaragoza

Tesis Doctoral

DEVELOPMENT OF ROBUST, PHYSICALLY-BASED NUMERICAL MODELS FOR TRANSPORT PROCESSES AND GEOMORPHODYNAMICS CHANGES

Autor

Carmelo Juez Jiménez

Director/es

Murillo Castarlenas, Javier

UNIVERSIDAD DE ZARAGOZA
Ciencia y Tecnología de Materiales y Fluidos

2014

Development of robust, physically-based numerical models for transport processes and geomorphodynamic changes

Carmelo Juez Jiménez

A thesis for the title of Doctor of Philosophy
Fluid Mechanics Doctoral Program

Zaragoza, March 2014

Supervisor:
Dr. Javier Murillo Castarlenas

Escuela de Ingeniería y Arquitectura Universidad de Zaragoza

Development of robust, physically-based numerical models for transport processes and geomorphodynamic changes

Abstract

Bed changes in rivers may occur under several morphodynamics and hydrodynamics conditions. The modeling of this type of phenomena can be performed coupling the Shallow Water Equations (SWE) for the hydrodynamic part and the Exner equation for the morphodynamic part. The Exner equation states that the time variation of the sediment layer is due to the sediment transport discharge through the boundaries of the volume. Considering that sediment transport discharge are computed by means of sediment capacity formulae based on 1D experimental steady flows, the assessment of these empirical relations under unsteady 1D and 2D situations must be studied. In order to ensure the reliability of the numerical experimentation, the numerical scheme must handle correctly the coupling between the 2D SWE and the Exner equation under any condition. If possible, it is convenient to express the formulation of different empirical laws under a general framework. In consequence, a finite-volume numerical scheme that includes these two main features has been chosen as a benchmark for comparing the 1D and 2D results obtained when using several well known sediment transport formulae: Meyer-Peter and Müller, Ashida and Michiue, Engelund and Fredsoe, Fernandez Luque and Van Beek, Parker, Smart, Nielsen, Wong and Camenen and Larson. In addition, a new interpretation of the Smart empirical law is presented in order to cope with bed load transport over irregular beds of changing slope. Detailed results for this new modified empirical law together with the ones obtained with Meyer-Peter and Müller (which is the sediment capacity formula more used in hydraulic engineering) are provided for every test case analyzed. Furthermore, the Root Mean Square Error (RMSE) associated to every formula at each experimental condition is calculated with the purpose of evaluating quantitatively the overall behavior of each one. The results point out that the new interpretation of the Smart formula reaches the most accurate results in all cases, but in a genuinely 2D flow, that is, a situation involving more than one flow direction, the differences among sediment transport formulae are not as noticeable as in the 1D studied situations.

Once the forecasting capacity of each sediment transport formula has been studied, another concern is the computational cost. The coupling between the SWE and the Exner equation by means of an augmented Jacobian matrix involves a high number of algebraic operations for computing the eigenvalues and the eigenvectors. Therefore, the computational cost is increased significantly, limiting the applicability of the numerical scheme to realistic situations where large domains are involved. In order to improve the computational efficiency, the coupling technique is modified, not decreasing the number of waves involved in the Riemann Problem but simplifying their definitions. The approach proposed in this thesis is a new strategy to combine concepts from hyperbolic conservation laws and conservative finite volume schemes. With the aim to control numerical stability in the most efficient form possible, a numerical eigenvalue is defined to control the discrete Exner equation in the explicit scheme. This bed wave celerity helps mainly to ensure conservation and to control automatically the numerical stability of the explicit scheme. The effects of the numerical coupling strategy proposed in this thesis are tested against exact solutions and 1D and 2D experimental data. The results emerging from this analysis show that efficiency and accuracy can be obtained when choosing an adequate sediment transport law and the stability condition is augmented by including a new celerity associated to the bed changes.

On the other hand, in environmental and civil engineering applications, geomorphological changes are not only present in rivers but also in steep areas where massive mobilizations of poorly sorted material can occur. This sliding material is usually composed by a mixture of sand and water. For simplifying the phenomenon, dry granular flows have been considered as a starting point for the understanding of the physics involved within the landslides. The hypothesis of Saint-Venant equations are considered valid for modeling these land movements. Taking advantage of this approach, in this thesis approximate augmented Riemann solvers are formulated providing appropriate numerical schemes for mathematical models of granular flow on irregular steep slopes. Fluxes and source terms are discretized to ensure steady state configurations including correct modeling of start/stop flow conditions, both in a global and a local system of coordinates. The weak solutions presented involve the effect of bed slope in pressure distribution and frictional effects by means of the adequate gravity acceleration components. The numerical solvers proposed are first tested against 1D cases with exact solution and then are compared with 2D experimental data in order to check the suitability of the mathematical models described in this thesis. Comparisons between results provided when using global and local system of coordinates are presented. Both the global and the local system of coordinates can be used to predict faithfully the overall behavior of the landslides. The performance of the numerical scheme has been studied using novel experimental situations. These laboratory works include bidimensional configurations, the inclusion of obstacles in the flow path and a variable slope in the domain. Hence, a further step in mimicking realistic situations is obtained, since the behavior of the granular flow is affected by the presence of natural elements such as boulders or trees. Three situations have been considered. The first experiment is based on a single obstacle, the second one is performed against multiple obstacles and the third one study the influence of a dike when an overtopping situation takes place. Due to the impact of the flow against the obstacles, fast moving shocks appear, and a variety of secondary waves emerge. Comparisons between computed and experimental data are presented for the three cases. The computed results show that the numerical tool previously developed is able to predict faithfully the overall behavior of this type of complex dense granular flow.

Desarrollo de esquemas numéricos robustos y basados en modelos físicos para procesos de transporte y cambios geomorfodinámicos

Resumen

Los cambios en la topografía de los ríos pueden ocurrir bajo diferentes condiciones hidrodinámicas y morfodinámicas diferentes. La modelización de este tipo de fenómenos se puede desarrollar mediante un acoplamiento entre un modelo de aguas poco profundas (SWE) para la parte hidrodinámica y la ecuación de Exner para la parte morfodinámica. La ecuación de Exner relaciona la variación temporal del nivel de fondo con los flujos de transporte de sedimento que atraviesan el volumen de control. Considerando que las fórmulas de transporte de sedimento están basadas en situaciones experimentales 1D con flujo estacionario, la validación de estas relaciones empíricas para situaciones transitorias 1D y 2D es imprescindible. Para garantizar la confianza en los resultados computacionales obtenidos, el esquema numérico empleado debe manejar correctamente el acoplamiento entre las ecuaciones 2D SWE y la ecuación de Exner bajo cualquier situación. Además, es conveniente expresar la formulación de las diferentes formulaciones de transporte general de forma general para que se puedan incorporar con facilidad al esquema numérico. En consecuencia, un esquema en volúmenes finitos que incluye ambas características ha sido utilizado para comparar los resultados 1D y 2D obtenidos con diversas fórmulas de transporte de sedimentos ampliamente conocidas: Meyer-Peter and Müller, Ashida and Michiue, Engelund and Fredsoe, Fernández Luque and Van Beek, Parker, Smart, Nielsen, Wong and Camenen and Larson. Además, una nueva interpretación de la fórmula de Smart es presentada para tener en cuenta el efecto del transporte de fondo sobre topografías irregulares con pendientes cambiante. Resultados detallados para esta nueva interpretación de la fórmula junto con los obtenidos con Meyer-Peter y Müller (que es la fórmula de sedimento más utilizada en ingeniería hidraúlica) son mostrados para cada caso analizado. Además, el error cuadrático medio asociado a cada fórmula para cada condición experimental es calculado con el propósito de evaluar cuantitativamente el comportamiento general de cada relación empírica. Los resultados demuestran que la nueva interpretación de la fórmula de Smart obtiene los resultados más precisos en todos los casos, aunque, en un caso genuinamente 2D, las diferencias entre las leyes de transporte de sedimento no son tan notables como en los casos 1D estudiados.

Una vez analizada la precisión de los resultados obtenidos con cada formulación de transporte de sedimento, se ha estudiado otro hecho importante como es el coste computacional del esquema numérico empleado. El acoplamiento entre las SWE y la ecuación de Exner a través de una matriz Jacobiana ampliada requiere un elevado número de operaciones algebraicas para calcular los valores y vectores propios. De esta manera, el coste computacional se incrementa notablemente, limitando la aplicabilidad del esquema numérico ante situaciones realistas. Para mejorar la eficiencia computacional, la técnica de acoplamiento es simplificada, pero sin reducir el número de ondas involucradas en el problema a Riemann. La aproximación considerada en esta tesis combina conceptos de las ecuaciones conservativas hiperbólicas y de los esquemas conservativos en volúmenes finitos. Con el propósito de controlar la estabilidad numérica de la forma más eficaz posible, un valor propio numérico es definido para controlar la ecuación discreta de Exner en el esquema explícito. Esta celeridad asociada al fondo ayuda principalmente a garantizar la conservación y a controlar automáticamente la estabilidad numérica del esquema explícito. Los efectos del acoplamiento numérico propuesto en este trabajo son verificados frente a soluciones exactas y casos experimentales 1D y 2D. Los resultados obtenidos muestran que eficiencia y precisión pueden obtenerse si se escoge una formulación de transporte de sedimento adecuada y además, se amplia la condición de estabilidad del esquema numérico para considerar la nueva celeridad asociada a los cambios de fondo.

Por otra parte, en la ingeniería medio ambiental y civil, los cambios geomorfológicos no están solo presentes en los ríos, sino también en áreas con fuertes pendientes donde masivas movilizaciones de terreno con escasa cohesión pueden producirse. Este material deslizante suele estar compuesto por una mezcla de arenas y agua. Para simplificar el fenómeno, los flujos granulares secos han sido considerados como un punto de partida para comprender la física involucrada en estos deslizamientos de terreno. Además, las hipótesis de las ecuaciones de Saint-Venant son válidas para modelar este tipo de movimientos térreos. Por ello, esquemas aproximados aumentados de tipo Riemann han sido formulados incorporando las características propias de flujos que evolucionan sobre pendientes elevadas. Los flujos y términos fuente son discretizados para garantizar la correcta modelización de las condiciones de parada y comienzo de movimiento tanto en coordenadas locales como en globales. Las soluciones débiles presentadas tienen en cuenta los efectos de las proyecciones de la gravedad en la distribución de presiones y en los términos de fricción. Los esquemas numéricos propuestos son primeramente testados frente a casos 1D con solución exacta y luego, son comparados con casos experimentales 2D para verificar la idoneidad de los modelos matemáticos propuestos. Los resultados obtenidos con las coordenadas locales y globales son presentados, concluyendo que ambos sistemas de coordenadas pueden ser usados para predecir adecuadamente el comportamiento de los deslizamientos de terreno.

Gracias a la herramienta numérica desarrollada para el cálculo de deslizamientos de material granular seco, una serie de situaciones experimentales nuevas han sido estudiadas. El denominador común de estos ensayos de laboratorio se basa en una configuración bidimensional, la incorporación de obstáculos al paso del flujo y una pendiente variable en el dominio de estudio. De esta manera, se intenta conseguir un mayor acercamiento a la realidad donde el comportamiento de los flujos granulares está influenciado por la presencia de elementos naturales como grandes bloques de piedra o árboles. Tres situaciones experimentales han sido consideradas. El primer experimento está basado en un único obstáculo, el segundo es realizado con varios obstáculos y el último, estudia el efecto que la presencia de un dique tiene sobre el flujo. Los resultados muestran una sucesión de rápidos choques, que evolucionan desplegando una variedad de ondas secundarias alrededor de los obstáculos. La comparativa con los datos experimentales es presentada. Los resultados computacionales muestran que el esquema numérico es capaz de predecir la evolución del flujo ante este tipo de situaciones complejas.

Dedicado a mis padres,
y a Noelia

Acknowledgements

Being this document the work of several years there are a lot of people who have helped me in different ways along the development of this thesis.

Firstly I would like to gratefully and sincerely thank Dr. Javier Murillo for his patience, well-balanced criteria, consistency decisions, and most importantly, his friendship during my PhD student period. His mentorship has been paramount for overcoming the problems that have arisen during these years. He has encouraged me to not only grow as a researcher and a engineer but also as an independent thinker. I am not going to forget the lyrics of his favorite song: *La vida es así, ...*

I would also like to thank to Prof. Dr. Pilar García-Navarro, because of her patience, guidance, understanding and combination of knowledge and experience. Also for being like the bedrock upon which the research team has been built during the past two decades. Dr. Pilar Brufau deserves too a special acknowledge since she was the person who introduced me to Javier and Pilar.

Special mention for my friends and colleagues of the Computational Hydraulics Group, Daniel Caviedes, Mario Morales and Asier Lacasta, for being a great group, always willing to help out or to start unnumbered discussions about technical and non-technical topics.

I cannot help naming also to Belén, Clara, Rosa, Héctor, et al. for all the lunch times, coffee breaks and beer times we have shared. Thanks for all the nice and funny times.

Finally, I would also thank my family for their support, for all they have taught to me and for the education they have given me. Last but not least, I sincerely thank to Noelia. For giving me all the support, encouragement, quiet patience and trust on me. Thanks also for separating me from work with her obstinacy and her smile.

Moreover, the former Science and Innovation Ministry of Spain as well as the new Research, Development and Innovation State Secretary of Spain must be acknowledged for the grant which has financially supported this work under the project CGL2011-28590.

Contents

List of Figures

List of Tables

Chapter 1

Introduction

There are an unaffordable number of physical processes over the earth surface that affect strongly to human life, most of them linked to the transport of multiple substances. A common agent is present: water. Water can participate in different ways: as a result of a high porosity in landslide events or as almost pure water in rivers. Also, many geophysical or environmental flows in earth have another relevant characteristic: the geometrical scales presented in the problem can allow us to define them mathematically as shallow type flows. This means that the vertical scales can be considered very small if compared with the horizontal ones. This aspect ratio appears in channels, rivers, oceans or even the atmosphere, but also in debris flows, landslides, tsunamis and volcanic eruptions. All these processes can be mathematically modeled and are frequently defined as flows of hyperbolic nature. The importance of all those processes makes necessary the development of predictive tools.

Predictive tools were first derived for a special type of hyperbolic flow involving gas dynamics, and the results were applied next to the shallow water equations. Shallow type flows are hyperbolic but not strictly hyperbolic, since in majority of the physical situations the governing equations include the presence of source terms. The presence of source terms constitutes a challenge since the numerical point of view, as the discretization of these terms is not an easy task.

By incorporating the presence of source terms in a specific numerical scheme, the attention has been traditionally focused on how it can be modified by a discreet balance between fluxes and source terms. In the context of the discretization of hyperbolic systems a fundamental point has been to preserve the stationary states in equilibrium with zero velocity, i.e. the well balanced property. The difficulty of constructing such schemes has been pointed out by several authors and it has driven to the development of several numerical schemes able to guarantee the well balanced property, (Alcrudo and Benkhaldoun, 2001; Chinnayya et al., 2004; LeFloch and Thanh, 2007; Bernetti et al., 2008; Rosatti and Begnudelli, 2010; LeFloch and Thanh, 2011) . On the other hand, when it comes to realistic and common problems, involving transient situations, flow characteristics impose restrictions on the time step size much larger than those given by the classical conditions which can lead to inefficient calculations and even instabilities that prevent progress in the predictive calculation. Thus, it can be argued that the presence of source terms justifies the building of new solutions in harmony with the real nature of the equations, instead of using solutions built for the simple case without source terms solutions.

The development of conservative Godunov schemes for the solution of systems of conservation laws was the starting point for the development of the best known numerical schemes. Among Godunov type methods, the HLL method Harten et al. (1983) and Roe method Roe (1986) are the most widespread. Both methods can be constructed departing from the definition of a solver of the Riemann problem (RP). In the search of approximate solvers linked to the presence of source terms, two augmented solvers named ARoe (Augmented Roe) and HLLCS (HLL with Contact wave and Source terms) were presented in Murillo and García-Navarro (2010b) and Murillo and García-Navarro (2012b) respectively. The approximate solver in Murillo and García-Navarro (2010b) was based on the upwind discretization of the source terms in Bermúdez and Vázquez-Cendón (1994) and the Roe solver defined for the homogeneous case. In Murillo and García-Navarro (2012b) the HLLCS was constructed by including the presence of source terms in the HLLC solver (Toro, 1994). Both augmented solvers were constructed by including an extra wave associated to the presence of source terms, providing a complete description of the evolution of the conserved variables in the inner estates of the RP. In consequence, the Godunov-type schemes developed were able to avoid the appearance of instabilities and negative values of the flow depth in presence of source terms.

This family of augmented schemes has been able to explain the effect of source terms in the stability, which has allow to advance to much more complex surface models generating a potential breakthrough in the development of new computational tools. In Murillo and García-Navarro (2010a) a fully coupled numerical scheme able to predict the morphodynamics changes in alluvial channels was developed. This numerical tool was established as a robust benchmark for performing a numerical assessment of different formulae in Juez et al. (2013b). Another success in the employment of augmented solvers is found in Murillo and García-Navarro (2012a), where it is stated how the introduction of bed and friction source terms can be handled even in situations which involve complex rheology forces of different nature: turbulent, dispersive, Coulomb, viscous or Yield. These results have driven to formulate numerical schemes appropriate for mathematical models of granular flow under steep and irregular slopes in Juez et al. (2013a).

These advances in simulation techniques through the description of augmented solvers constitute the basis of this thesis. Hence, the main purpose is the development of robust, physically-based numerical schemes on the basis of Roe augmented solvers, which can simulate accurately hydrodynamic, transport processes and geomorphodynamic changes.

1.1 Goal

The physic of the problems described above needs to be described in order to define suitable mathematical models. A theoretical framework is established for the two phenomena studied in this work: the sediment transport in alluvial channels and the geomorphodynamic flow over steep areas. The relevant formulation of these 2D phenomena derives from the depth-averaged equation of bulk mass conservation, mixture momentum conservation and conservation of the mass of the different sediments. The main goal of this thesis is the development of numerical models able to handle with the mathematical model studied. The milestones overcame in this work for achieving this goal are detailed below

- Numerical assessment of several closure equations for bed-load transport

  Usual formulations for morphodynamic bed load transport are given by empirical sediment transport laws. The different sediment transport capacity formulae, used worldwide to control the erosion and deposition rates that deform the bed in transient cases, are based on equilibrium closure equations obtained from experimental observation in 1D steady cases. Their general applicability to 2D unsteady problems requires a careful analysis to assess whether they are able to predict sediment transport in complex transient flows. This point is of paramount importance and requires a well tested and robust numerical method. For this reason, the numerical scheme proposed in Murillo and García-Navarro (2010a) and based on a Jacobian-coupled model has been chosen as a numerical benchmark for analyzing the relative performance of several well-known formulations under different morphodynamic conditions in 1D and 2D configurations.

- Development of a efficient and robust weakly-coupled numerical technique for the shallow water equations and the Exner equation

  Recent advances in free surface flows over mobile bed have shown that accurate and stable results in realistic problems can be provided if an appropriate coupling between the shallow water equations (SWE) and the Exner equation is performed. This coupling can be done if using a suitable Jacobian matrix, as the one employed in the previous milestone. However, when considering this coupling option despite that the SWE are enhanced by only considering one extra conservation law, i.e, the sediment mass conservation, the computational cost may become unaffordable in situations where the initial SWE for rigid bed can be used involving large time and space scales without giving up to the adequate level of mesh refinement. In order to restore the computational efficiency, the coupling technique has been studied and simplified, not decreasing the number of waves involved in the Riemann Problem but simplifying their definitions. The effects of the approximations made have been tested against experimental data which include transient problems over erodible bed. The simplified model has been formulated under a general framework able to insert any desirable discharge solid load formula.

- Development of a 2D dry granular flow solver

  Landslides, rockfalls and debris avalanches take place when a mixture of mud, sand and rocks slide down a slope together. As suggested by Denlinger and Iverson (2004) the study of granular flows constitutes an starting point for the understanding of the more complex mass movement phenomena mentioned before. For this reason a numerical scheme following Murillo and García-Navarro (2010b) is developed, taking into account the particularities which arises in this type of flows and ensuring quiescent equilibrium stages. Taking advantage on the reliability of the numerical scheme developed, a series of novel experimental cases which represent small-scale up-to-date environmental problems have been studied for delving into the physics of this type of phenomena.

1.2 Outline

The outline of the present document is structured in two parts. Part I is devoted to the sediment motion involving the presence of water. Part II addresses the mass motion over steep areas, i.e. landslides.

Within Part I the milestones 1.1,1.1 are developed. In Chapter 2 a brief introduction of the science of sediments dealing with water bodies is provided. In Chapter 3 different mathematical models are described in order to clarify the assumptions made in these type of flow, leading to as suitable description of the problem by means of a reduced set of partial differential equations. In Chapter 4 the bed load formulations employed in this work are described, and are written using a differentiable expression. The study of the numerical assessment of several closure equations for bed-load transport, milestone 1.1, is developed within Chapter 5 and Chapter 7. The development of a efficient and robust weakly-coupled numerical technique for the shallow water equations and the Exner equation, milestone 1.1, is performed from Chapter 8 to Chapter 10. For the achievement of each milestone, several 1D and 2D experimental test cases presenting transient states, complex geometries and wet/dry boundaries have been been compared with the computational results. The particular conclusions and future research line are also included.

Part II brings together all the features regarding the mass motion over steep areas. Therefore the milestone 1.1 is addressed here. Chapter 11 provides an introduction of the nature of landslides and the previously laboratory work developed for its study. Chapters 12 and 13 describe the numerical schemes particularized for this phenomena when using both local and global coordinate systems. Chapter 14 presents the verification of the numerical models and Chapter 15 is devoted to the conclusions and further research. Once the reliability of the numerical scheme has been proven, a series of small-scale environmental problem are studied in Chapter 16. Chapter 17 shows the results obtained. Finally, Chapter 18 summarizes the conclusions of these small-scale environmental problem and future research lines.

Part I

Sediment motion in alluvial channels

Chapter 2

Sediment transport

The science of sediment transport deals with the interrelationship between flowing water and sediment particles. Despite having been studied since the 1950s and being widely employed in real-life engineering (Nielsen, 1992; Julien, 1998), the develop in the improvement of sediment management remains at present one of the most active topics in the field of hydraulic research

The hydraulic and sediment systems are not static even under nature conditions, the cyclic flooding events cause an imbalance on the sediment processes leading to changes in river and coastal morphology. These differences on the sediment transport behavior can be largely augmented by human activities such as river regulation, agriculture, forestry, dredging, coastal and port construction and soil degradation. For this reason there is a a general agreement about the significance of sediment management in rivers, estuaries and coastal areas.

Additionally, sediment not only affects to the morphodynamic changes. Sediment is also a key part of the ecosystem and directly concerns the biodiversity: it is the responsible of the habitat formation and of the adequate ecological and chemical quality of the water volumes.

In order to develop a sustainable use of river, coastal and marine environments several practical solutions have been proposed. However, some of this sediment management actions have been only focused on the initial domains of concern, leading to local positive effects, but causing unforeseen negative consequences in other places.

For all these reasons, the inclusion of sediment management into river, coastal management programs has became a reality and allows to get closer to the holistic idea which represents the understanding of the water bodies, where the same level of importance should be paid to the whole, the local river, coastal and marine environment, and to the interdependence of each part, i.e. the hydrology, the hydraulic, the sediment, the biology and the pollutant issues.

In response to the necessity of the integration of sediment in the water bodies management a computational tool is required for the analysis and prediction of these complex systems. The forecasting capacities of the numerical technology allow to obtain proactive solutions and provides not only a local but also, a global feed-back on how a man-made action or a natural event may alter a particular domain. In this fashion this thesis pushes the development of numerical morphodynamic models for increasing accuracy and efficiency. Since the sediment environmentals (river, coastal and marine) are wide an each one has its own particularities, this document is focused on the river ones.

2.1 State of the art

It is generally accepted that two of the fundamental concerns in modern sediment hydraulic engineering practice is the need for accurate and, in the same level of importance, efficient schemes for computing the shallow water equations together with the movement of sediment particles. The numerical strategy proposed must mimic the principal phenomenae observed in the flow field and in the movable bed.

In the search for capturing this physically significant processes Hudson and Sweby (2002, 2005) studied the influence of steady and unsteady approaches in the mathematical model when computing free surface flows considering a bed-load transport. It was commanded to consider the unsteady system contrary to what was assumed in earlier works (De Vriend et al., 1993; Abderrezzak and Paquier, 2011). Ignoring unsteady hydrodynamical effects means that the time scales of the morphodynamics changes are smaller in comparison with the morphodynamic ones and only nearly steady process where the bed changes are generated in a slow way could be computed.

Focusing on the numerical techniques employed for obtaining the solution, a classification between asynchronous and synchronous strategies can be established (Aricò and Tucciarelli, 2008). Asynchronous procedures imply that the changes in the bed level are not of enough importance for affecting the hydrodynamic equations during a computational time step. This way, the continuity and momentum equations for the fluid phase are decoupled of the sediment continuity equation. They are also known as uncoupled models. On the other hand, numerical methods which solve at the same time step the hydrodynamic and morphodynamic equations are called synchronous and also, coupled. De Vriend et al. (1993) justified that asynchronous/uncoupled techniques were only valid for a limited range of hydrodynamic regimes governed by low Froude numbers and weak interactions between the flow and bed dynamics. For this reason, other authors, Holly and Rahuel (1990); Cao et al. (2002); Wu and Wang (2004); Xia et al. (2010); Cordier et al. (2011), have studied synchronous/coupled procedures, able to handle a wider range of hydrodynamic and morphodynamic situations. In some of those previous works, despite considering an extra equation for computing the sediment dynamics no additional conditions to the classical Courant-Friedrichs-Lewy (CFL) were provided for controlling the numerical stability. In particular, the lack of knowledge of an automatic numerical stability condition in Wu et al. (2012) has driven to calibrate, by trial and error a CFL condition for obtaining a stable solution to each particular case.

In order to overcome the challenge when building a self-stable numerical scheme, several strategies have been proposed: ones are based on the development of the exact form of the eigenvalues through the mathematical model (Kassem and Chaudry, 1998; Tassi et al., 2008; Lyn and Altinakar, 2002; Cao et al., 2006; Goutière et al., 2008) and other in the numerical treatment of the whole set of equations (Hudson and Sweby, 2002, 2005). This work is focused on this last idea. In Hudson and Sweby (2002, 2005) thanks to the Riemann theory and using a Roe's approximate Jacobian matrix of the whole system of equations was developed. Hence, the hydrodynamic and morphodynamic equations were not only solved at the same time step but also the wave celerities, which participate in the stability condition, incorporated information from both phases: water and sediment. The term coupled-Jacobian will be used for that model from now on. The main drawback of this Jacobian matrix was a strong dependence on the bed reference level. Additionally, this Jacobian matrix included the definition of the sediment transport formula through the Grass law, Grass (1981). This formula is based in a power law of the velocity, which is nicely differentiable, and in a global calibration parameter, which is unique for all the computational domain and must be tuned in each particular problem.

Following with the Jacobian-coupled strategy, other schemes have been proposed and extended to 2D triangular meshes more recently. In Castro Diaz et al. (2009) the identification of the approximate Jacobian matrix was achieved by means of the distribution theory (Dal Maso et al., 1995). However, this numerical technique needs to select families of paths that cannot be generalized. In Soares-Frazao and Zech (2010) a first order HLLC scheme was proposed and a novel wave-speed estimator was provided for the Exner equation. The results were affected by numerical diffusion and a fine mesh was required by obtaining accurate results. The work in Rosatti et al. (2008a) described a Roe solver for a two-phase problem where the attention was devoted to the non-linear relations between primitive and conserved variables. Only the 1D approach of the problem was studied. In Canestrelli et al. (2010); Siviglia et al. (2013) high order numerical techniques were explained over fixed and mobile beds. However, no clear evidence of the behavior of the numerical scheme under a real and experimental case is provided, since only a laboratory test case is studied in the second word. Additionally, the high computational cost of such schemes is not addressed.

In Murillo and García-Navarro (2010a) a novel coupled-Jacobian model was proposed and the Jacobian matrix was built with independence of the bed level reference. Regarding the calibration coefficient of Grass law, the uniqueness of this parameter in all the problem was avoided, (Murillo and García-Navarro, 2010a), by writing the law in terms of several bed-load sediment transport formulae. Numerical solutions obtained probed to be robust and accurate. Nevertheless, the applicability of this numerical scheme to a real situation, where the domain contains kilometers of river and several types of sediment, is in somehow limited by the computational cost, which is prohibitively expensive. The computational time is highly penalized by the number of algebraic operations need for computing the eigenvectors and eigenvalues of the augmented Jacobian matrix. In order to overcome this huge numerical effort in Serrano et al. (2012) a partially coupled model was proposed, although the quality of the results were compromised by the poor sediment transport law employed. Furthermore, no clear evidence of the effect of the bed wave speed in the time step restriction was provided.

2.2 Outline

Following the previous effort made by the authors mentioned above, the concern of this part of the work is twofold: accuracy and efficiency. The first one is related with the sediment transport law employed. Several well known capacity formulae based on 1D experimental steady flows have been analyzed under unsteady 1D and 2D situations. Moreover, a new interpretation of the Smart (1984) empirical law is presented in order to cope with bed load transport over irregular beds of changing slope. Detailed results for this new modified empirical law together with the ones obtained with Meyer-Peter and Müller (1948) (which is the sediment capacity formula more used in hydraulic engineering) are provided for every test case analyzed. Furthermore the Root Mean Square Error (RMSE) associated to every formula at each experimental condition is calculated with the purpose of evaluating quantitatively the overall behavior of each one. In order to ensure the reliability of the numerical experimentation the coupled-Jacobian model previously developed and tested in Murillo and García-Navarro (2010a) has been used.

The second objective, the efficiency, has been addressed studying a novel weakly-coupled numerical strategy for coupling the hydrodynamic and the morphodynamic models. The sediment transport law employed in the simulations have been the most accurate one chosen from the previous analysis. Some of the experimental test cases employed when studying the accuracy among the sediment discharge formulae are also employed in this part of the work. Results of the computational cost between the coupled-Jacobian scheme and the weakly-coupled scheme are provided. Furthermore, a clear evidence of how a non-carefully treatment of the stability condition can ruined the numerical results is provided.

The outline of this part is as follows: in Chapter 3 different mathematical models are described in order to clarify the assumptions made in these type of flow, leading to a suitable description of the problem by means of a reduced set of partial differential equations. In Chapter 4 the bed load formulations employed in this work are described, and are written using a differentiable expression. Chapter 5 presents the coupled-Jacobian numerical scheme used to study the differences among the bed-load discharge formulae and a novel numerical discretization of the Smart one is provided. Chapter 6 displays the numerical results obtained with the coupled-Jacobian model in 1D and 2D test cases when using several sediment discharge formulae. Chapter 7 is devoted to the conclusions about the bed-load formulae studied and further research. The novel weakly-coupled numerical scheme proposed in this thesis is showed in Chapter 8. Results obtained with this numerical strategy are depicted in Chapter 9 and conclusions and future research lines are written in Chapter 10.

Chapter 3

Mathematical model

3.1 Mathematical modeling of sediment motion

In this chapter the mathematical model which governs the dynamics of the sediment transport problem will be described. The equations express the depth averaging of the mass and momentum conservation laws, under the hypothesis of hydrostatic pressure and negligible vertical accelerations (SWE) and are extended to include the morphodynamic evolution of the bed.

Along this chapter, the physics of the problem is analyzed departing from a general and complex two fluid layer model, where the set of equations is reduced ending up in a one fluid layer model coupled with the bed evolution Exner equation. First, for the sake of clarity, the formulation is presented considering only the vertical plane and 1D flow. Then, the extension to 2D situations is indicated.

3.2 Two layer model

The model involves the following assumptions:

i) Based on experimental observations Fraccarollo and Capart (2002), and as a first assumption, the flow is considered stratified and composed by two fluid layers (hence the name of the model) and one solid layer, as shown in Figure 3.1. The upper liquid-solid layer is called the suspended layer of thickness h_1: the heterogeneous liquid-granular flow behaves as an effective medium with little slip between water and transport layer, sediment transport is produced by suspension. The medium layer, of thickness h_2, will be referred to as transport layer: the sediment phase is mostly transported as bed load, supported by frictional and collisional grain-grain interactions. The lower layer, defined by the position of the bed level, z, is commonly defined as the morphodynamic layer: the bed boundary is viewed as a transition between two mediums with different behaviors, the solid phase and the fluid phase.

ii) Both upper layers transport granular material, with variable size and density. The amount of granular material transported is defined by means of the depth averaged volumetric concentration, ϕ.

3.2.1 1D Conservation equations

The domain is divided in three layers, Figure 3.1, limited by interfaces. Interface Γ_w is the air-water/suspended load boundary at the flow free surface. Interface Γ_s defines the upper limit of the transport layer, separating the low concentration layer above from the high concentration liquid-granular mixture below. The third interface, Γ_b, acts as a boundary between the fluid and the solid behavior.

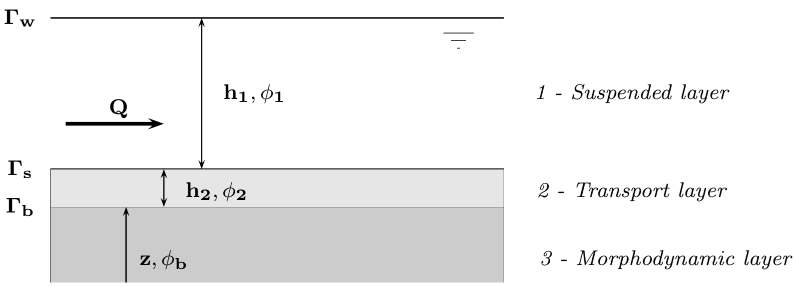

Figure 3.1: Interfaces in the domain

Every layer between the interfaces has its own depth (h_1, h_2, z), depth averaged velocity (u_1, u_2) and depth averaged concentration (ϕ_1, ϕ_2, ϕ_b).

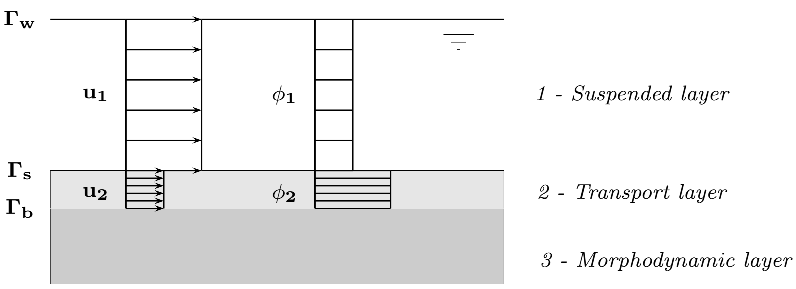

Figure 3.2: Depth averaged quantities within the layers

Through these interfaces solid material exchanges take place.

Mass conservation

The balance of mass applied in an arbitrary control volume, Ω, using the Reynolds transport theorem, yields the general integral equation

$$\frac{\partial}{\partial t}\int_{\Omega}\rho(x,t)d\Omega = 0 \Leftrightarrow \frac{\partial}{\partial t}\int_{\Omega}\rho d\Omega + \int_{\Gamma}\rho u_r n d\Gamma = 0 \tag{3.1}$$

where Γ are the sections across fluxes interact (mobile boundaries and fixed boundaries), ρ is the mass density, u_r is the relative velocity between the flow velocity and the speed of boundary Γ ($u_r = u$ - v) and n is the outward unit vector normal to Γ. For a better comprehension Figure 3.3 is plotted below.

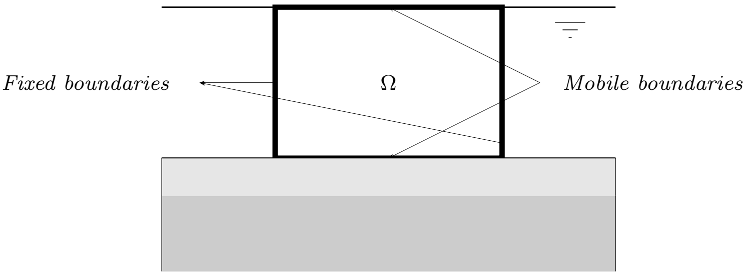

Figure 3.3: Reynolds theorem applied in an arbitrary volume

Applying (3.1) to the spatial control volume of layer 1, the following integral formula is obtained

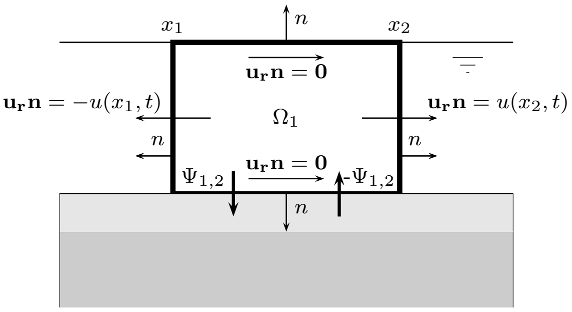

Figure 3.4: Mass conservation in layer 1

$$\underbrace{\frac{d}{dt}\int_{x_1}^{x_2}\int_{A_1(x,t)}\rho_1 dA dx}_{\textit{Local variation}} + \underbrace{\int_{A_1(x_1,t)} -\rho_1 u dS}_{\textit{Flow boundary fixed 1}} + \underbrace{\int_{A_1(x_2,t)} \rho_1 u dS}_{\textit{Flow boundary fixed 2}} + \\ + \underbrace{\int_{x_1}^{x_2} \{-(B\rho_1\Psi_{2,1}) + (B\rho_1\Psi_{1,2})\}\, dx}_{\textit{Flow bottom}} = 0 \tag{3.2}$$

where $A_1(x,t)$, $A_2(x,t)$ are the crossed areas, located at coordinates x_1 and x_2, respectively, and B is the width.

The convective inertia term has been split in two contributions, the first one belongs to the fixed boundaries (horizontal flows) and the second one to the mobile boundaries (vertical flows). In the horizontal exchange the relative velocity u_r is equal to u, the flow velocity, because the speed of boundary is equal to zero, due to is fixed. In the vertical exchange u_r is the difference between the two velocities. The term of u_r is rewritten as a flow per unit length, $\Psi_{i,j} = \frac{Q}{A}$, where Q is the flow, A is the transversal section equal to Bdx, being B the width. Hence, the product $\rho\Psi_{i,j}$ is just a material flux per unit area.

After time integrating, applying Leibnitz rule, the width B is eliminated and the integral form of mass conservation in layer 1 is rewritten as

$$\int_{t_1}^{t_2}\int_{x_1}^{x_2}\frac{\partial}{\partial t}(\rho_1 h_1)dxdt + \int_{t_1}^{t_2}\int_{x_1}^{x_2}\frac{\partial}{\partial x}(\rho_1 h_1 u_1)dxdt - \\ - \int_{t_1}^{t_2}\int_{x_1}^{x_2}\rho_1\Psi_{2,1}^{net}dxdt = 0 \tag{3.3}$$

In differential form is expressed as

$$\frac{\partial(\rho_1 h_1)}{\partial t} + \frac{\partial(\rho_1 h_1 u_1)}{\partial x} - \rho_1\Psi_{2,1}^{net} = 0 \tag{3.4}$$

Splitting the above formulation in its two components, the differential equations are expressed as one part of sediment material (3.5) and another part of water (3.6)

$$\frac{\partial(\rho_1 h_1 \phi_1)}{\partial t} + \frac{\partial(\rho_1 h_1 \phi_1 u_1)}{\partial x} - \rho_1\Psi_{s_{2,1}}^{net} = 0 \tag{3.5}$$

$$\frac{\partial(\rho_1 h_1 (1-\phi_1))}{\partial t} + \frac{\partial(\rho_1 h_1 (1-\phi_1) u_1)}{\partial x} - \rho_1\Psi_{w_{2,1}}^{net} = 0 \tag{3.6}$$

Following the same procedure the mass conservation for layer 2, Figure 3.5, leads to

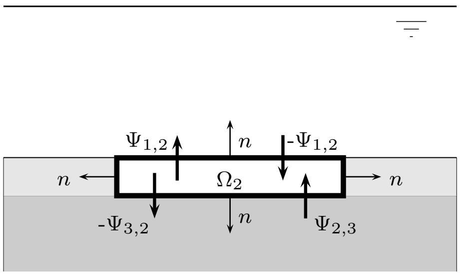

Figure 3.5: Mass conservation in layer 2

$$\frac{\partial(\rho_2 h_2)}{\partial t} + \frac{\partial(\rho_2 h_2 u_2)}{\partial x} - \rho_2 \Psi_{3,2}^{net} + \rho_2 \Psi_{2,1}^{net} = 0 \tag{3.7}$$

and finally for layer 3

$$\frac{\partial(\rho_b z \phi_b)}{\partial t} + \rho_b \Psi_{3,2}^{net} = 0 \tag{3.8}$$

Momentum conservation

The balance of linear momentum, (3.9), applied in an arbitrary control volume, Ω, using the Reynolds transport theorem, yields the general integral equation

$$\frac{d}{dt}(P) = \frac{d}{dt}\int_{\Omega} \rho u d\Omega \tag{3.9}$$

$$\frac{\partial}{\partial t}\int_{\Omega} \rho u d\Omega + \int_{\Gamma} (\rho u (u_r n)) d\Gamma = \int_{\Gamma} (\mathbf{f}_s) d\Gamma + \int_{\Omega} (\rho \mathbf{f_v}) d\Omega \tag{3.10}$$

being f_s the stresses and f_v the volumetric forces.

The application of momentum conservation is only available in layer 1 and layer 2 where there exists velocity. The momentum equation applied to layer 1, Figure 3.6, using Gauss theorem, leads to

$$\underbrace{\frac{d}{dt}\int_{\Omega_1} \rho_1 u_1 d\Omega}_{\textit{Local inertia}} + \underbrace{\int_{\Gamma_1} \rho_1 u_1 u_r n d\Gamma}_{\textit{Convective inertia}} = \underbrace{\int_{\Omega_1} g \rho_1 d\Omega}_{\textit{Gravity force}} + \underbrace{\int_{\Gamma_1} (-pn) d\Gamma}_{\textit{Pressure forces}} + \underbrace{\int_{\Gamma_1} (\tau n) d\Gamma}_{\textit{Tangential forces}} \tag{3.11}$$

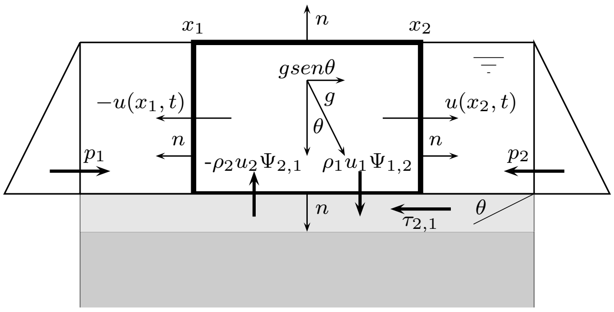

Figure 3.6: Momentum balance in layer 1

where g is the acceleration gravity, p is the pressure (normal stress) and τ is the shear stress.

Expressing (3.11) in differential form:

$$\frac{\partial(h_1\rho_1u_1)}{\partial t}+\frac{\partial(h_1\rho_1u_1^2)}{\partial x}+g\frac{\partial\left(\frac{1}{2}\rho_1h_1^2\right)}{\partial x}+g\frac{\partial(z\rho_1h_1)}{\partial x}= \\ =(\rho_2u_2\Psi_{2,1}-\rho_1u_1\Psi_{2,1})-\tau_{2,1} \tag{3.12}$$

Following the same procedure for layer 2 the corresponding differential form is obtained:

$$\frac{\partial(h_2\rho_2u_2)}{\partial t}+\frac{\partial(h_2\rho_2u_2^2)}{\partial x}+g\frac{\partial}{\partial x}\left(\frac{1}{2}\rho_2h_2^2+\rho_1h_1h_2\right)+g\frac{\partial(z\rho_2h_2)}{\partial x}= \\ =-(\rho_2u_2\Psi_{2,1}-\rho_1u_1\Psi_{2,1}+\rho_2u_2\Psi_{3,2})+(\tau_{2,1}-\tau_{2,3}) \tag{3.13}$$

Summary of conservation equations of layers and bed

A summary of the conservation equations obtained from a 1D flow over a mobile bed with a two layer fluid model is provided below

Total mass, layer 1

$$\frac{\partial(\rho_1h_1)}{\partial t}+\frac{\partial(\rho_1h_1u_1)}{\partial x}+\rho_1\Psi_{2,1}^{net}=0 \tag{3.14}$$

Total mass, layer 2

$$\frac{\partial\rho_2h_2}{\partial t}+\frac{\partial(\rho_2h_2u_2)}{\partial x}-\rho_2\Psi_{3,2}^{net}+\rho_2\Psi_{2,1}^{net}=0 \tag{3.15}$$

Sediment mass, bed

$$\frac{\partial(\rho_bz\phi_b)}{\partial t}+\rho_b\Psi_{s3,2}^{net}=0 \tag{3.16}$$

Sediment mass, layer 1

$$\frac{\partial(\rho_1 h_1 \phi_1)}{\partial t} + \frac{\partial(\rho_1 h_1 u_1 \phi_1)}{\partial x} - \rho_1 \Psi^{net}_{s2,1} = 0 \tag{3.17}$$

Sediment mass, layer 2

$$\frac{\partial(\rho_2 h_2 \phi_2)}{\partial t} + \frac{\partial(\rho_2 h_2 u_2 \phi_2)}{\partial x} - \rho_b \Psi^{net}_{s3,2} + \rho_1 \Psi^{net}_{s2,1} = 0 \tag{3.18}$$

Momentum of the mixture, layer 1

$$\begin{aligned} \frac{\partial(h_1 \rho_1 u_1)}{\partial t} + \frac{\partial(h_1 \rho_1 u_1^2)}{\partial x} + g\frac{\partial}{\partial x}\left(\frac{1}{2}\rho_1 h_1^2\right) + g\frac{\partial(z\rho_1 h_1)}{\partial x} &= \\ = (\rho_2 u_2 \Psi_{2,1} - \rho_1 u_1 \Psi_{2,1}) - \tau_{2,1} \end{aligned} \tag{3.19}$$

Momentum of the mixture, layer 2

$$\begin{aligned} \frac{\partial(h_2 \rho_2 u_2)}{\partial t} + \frac{\partial(h_2 \rho_2 u_2^2)}{\partial x} + g\frac{\partial}{\partial x}\left(\frac{1}{2}\rho_2 h_2^2 + \rho_1 h_1 h_2\right) + g\frac{\partial(z\rho_2 h_2)}{\partial x} &= \\ = -(\rho_2 u_2 \Psi_{2,1} - \rho_1 u_1 \Psi_{2,1} + \rho_2 u_2 \Psi_{3,2}) + (\tau_{2,1} - \tau_{2,3}) \end{aligned} \tag{3.20}$$

In case that the granular material is not homogeneous in size or density, the subscript p should be employed to distinguish among cases with non uniform size and specific weight distributions, inside each liquid-granular layer. Thus the formulation becomes:

Total mass, fraction p, layer 1

$$\frac{\partial(\rho_{1p} h_1)}{\partial t} + \frac{\partial(\rho_{1p} h_{1p} u_1)}{\partial x} + \rho_{1p} \Psi^{net}_{2,1} = 0 \tag{3.21}$$

Total mass, fraction p, layer 2

$$\frac{\partial \rho_{2p} h_{2p}}{\partial t} + \frac{\partial(\rho_{2p} h_{2p} u_2)}{\partial x} - \rho_{2p} \Psi^{net}_{3,2} + \rho_{2p} \Psi^{net}_{2,1} = 0 \tag{3.22}$$

Sediment mass, bed

$$\frac{\partial(\rho_b z \phi_b)}{\partial t} + \rho_b \Psi^{net}_{s3,2} = 0 \tag{3.23}$$

Sediment mass, fraction p, layer 1

$$\frac{\partial(\rho_{1p} h_{1p} \phi_{1p})}{\partial t} + \frac{\partial(\rho_{1p} h_{1p} u_1 \phi_{1p})}{\partial x} - \rho_{1p} \Psi^{net}_{s2,1} = 0 \tag{3.24}$$

Sediment mass, fraction p, layer 2

$$\frac{\partial(\rho_{2p} h_{2p} \phi_{2p})}{\partial t} + \frac{\partial(\rho_{2p} h_{2p} u_s \phi_{2p})}{\partial x} - \rho_b \Psi^{net}_{s3,2} + \rho_{1p} \Psi^{net}_{s2,1} = 0 \tag{3.25}$$

Momentum of the mixture, layer 1

$$\frac{\partial(h_{1p}\rho_{1p}u_1)}{\partial t}+\frac{\partial(h_{1p}\rho_{1p}u_1^2)}{\partial x}+g\frac{\partial}{\partial x}\left(\frac{1}{2}\rho_{1p}h_{1p}^2\right)+g\frac{\partial(z\rho_{1p}h_{1p})}{\partial x}= \\ =(\rho_{2p}u_2\Psi_{2,1}-\rho_{1p}u_1\Psi_{2,1})-\tau_{2,1} \tag{3.26}$$

Momentum of the mixture, layer 2

$$\frac{\partial(h_{2p}\rho_{2p}u_2)}{\partial t}+\frac{\partial(h_{2p}\rho_{2p}u_2^2)}{\partial x}+g\frac{\partial}{\partial x}\left(\frac{1}{2}\rho_{2p}h_{2p}^2+\rho_{1p}h_{1p}h_{2p}\right)+g\frac{\partial(z\rho_{2p}h_{2p})}{\partial x}= \\ =-(\rho_{2p}u_2\Psi_{2,1}-\rho_{1p}u_1\Psi_{2,1}+\rho_{2p}u_2\Psi_{3,2})+(\tau_{2,1}-\tau_{2,3}) \tag{3.27}$$

There are $(5+2)N_p$ equations, being N_p the number of size fractions p which had the bed material, and $(5+2)N_p$ independent variables: the flow depth for each layer, h_{1p}, h_{2p}; the depth averaged velocity in layer 1, u_1 and in layer 2, u_2; the bottom elevation, z and finally the sediment concentration in layer 1 of fraction p, ϕ_{1p} and in layer 2, ϕ_{2p}.

Several closure equations are required to express the shear stress between layers, $\tau_{2,1}$ and $\tau_{2,3}$ and the sediment fluxes, $\Psi_{2,1}$ and $\Psi_{3,2}$ in terms of the independent variables. This represents such a complex task that it justifies further simplification of the model. Next section is devoted to discuss this.

3.3 One layer model

The one layer model, Figure (3.7), is built upon a set of assumptions in relation to the two layer model: (i) a unique layer of depth h is considered, which includes previous layer 1 and 2, (ii) continuity approach, assuming the same velocity for the liquid and for the solid phase, u, which leads to continuity of momentum and consequently to a continuity of shear stresses, avoiding the necessity of calculating τ_{ij} between interfaces.

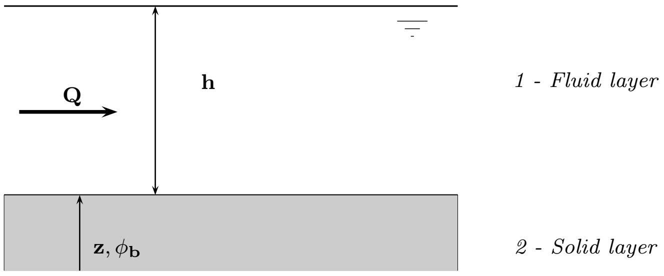

Figure 3.7: Interfaces in the domain

3.3.1 Conservation equations

The relevant formulation of the model derives from the depth-averaged equation of bulk mass conservation, mixture momentum conservation and conservation of the mass of the different constituents.

The term ϕ_p represents the scalar depth-averaged volumetric concentration of component p, with $p = 1, ..., N_p$ and N_p the number of different components transported. The mixture density is given by $\rho_m = \rho_w r$ where ρ_w is the density of the water and r means the relative density of the bulk mixture with respect the clean water

$$r = 1 + \sum_{p=1}^{N_p} \Delta_p \phi_p \tag{3.28}$$

where $\Delta_p = (\rho_p - \rho_w)/\rho_w$ is the relative density of the solid phase p. It is assumed that dissolved species with low concentration do not change bulk density $\Delta_p = 0$. In case of having an unique specie the relative density of the bulk mixture becomes $r = 1 + \Delta\phi$.

Mass conservation

Considering a generic control volume for a horizontal flow over a mobile bed where the velocity is depth averaged, defined in Figure 3.7, the Reynolds transport for mass conservation at the liquid layer leads to:

$$\int_{x_1}^{x_2} \frac{\partial}{\partial t}(\rho_m h)dx + \int_{x_1}^{x_2} \frac{\partial}{\partial x}(\rho_m hu)dx + \int_{x_1}^{x_2} \rho_m \Psi_s^{net} dx = 0 \tag{3.29}$$

and to the sediment balance mass

$$\int_{x_1}^{x_2} \frac{\partial}{\partial t}(h \sum_{p=1}^{N_p} \rho_p \phi_p)dx + \int_{x_1}^{x_2} \frac{\partial}{\partial x}(hu \sum_{p=1}^{N_p} \rho_p \phi_p)dx + \int_{x_1}^{x_2} \sum_{p=1}^{N_p} \rho_p \Psi_p^{net} dx = 0 \tag{3.30}$$

Following the same procedure for mass sediment balance at the bottom and considering, $\phi_{b_p} = (1 - p_p)$, being p_p the porosity of each sediment, drives to

$$\int_{x_1}^{x_2} \frac{\partial}{\partial t}(z \sum_{p=1}^{N_p} \rho_p (1 - p_p))dx - \int_{x_1}^{x_2} \sum_{p=1}^{N_p} \rho_p \Psi_p^{net} dx = 0 \tag{3.31}$$

The term Ψ_s^{net}, which appears in the above set of equations, includes the vertical sediment flux, suspension transport, and the horizontal sediment flux, bed load transport.

$$\Psi_s^{net} = \Psi_{load} + \Psi_{susp} \tag{3.32}$$

Momentum equation

For the x direction, and considering Figure 3.7, the momentum conservation equation for the mixing layer, which is the unique zone where there exists velocity, and with the x component of the gravity mass force equal to 0, $(\mathbf{f_v})_x = 0$, leads to

$$\int_{x_1}^{x_2} \frac{\partial}{\partial t}(\rho_m hu)dx + \int_{x_1}^{x_2} \frac{\partial}{\partial x}(\rho_m hu^2)dx = \int_{x_1}^{x_2} p_b dx - \int_{x_1}^{x_2} \tau_b dx \tag{3.33}$$

The term of superficial forces, $(\mathbf{f_s})_x$, has been split in its two components, the hydrostatic pressure, p_b, and the friction term exerted over the bed, τ_b.

$$\mathbf{f_s} = p_b - \tau_b \tag{3.34}$$

Summary of conservation equations

The set of developed differential equations is newly written below in terms of the relative density r.

Total mass

$$\frac{\partial(hr)}{\partial t} + \frac{\partial(hur)}{\partial x} = \sum_{p=1}^{N_p} \Delta\Psi_p^{net} \tag{3.35}$$

Sediment mass, bed

$$\frac{\partial(z)}{\partial t} + \sum_{p=1}^{N_p} \frac{\Psi_p^{net}}{(1-p_p)} = 0 \tag{3.36}$$

Sediment mass of the mixing layer for specie p

$$\frac{\partial(h\phi_p)}{\partial t} + \frac{\partial(hu\phi_p)}{\partial x} = \Psi_p^{net} \tag{3.37}$$

Momentum of the mixing layer

$$\frac{\partial(hur)}{\partial t} + \frac{\partial[hu^2r + (1/2)gh^2r]}{\partial x} = \frac{p_b}{\rho_w} - \frac{\tau_b}{\rho_w} \tag{3.38}$$

There are $3+N_p$ equations and $3+N_p$ variables, being N_p the number of species: the flow depth, h, the mean flow velocity, u, the bed level, z, and the depth averaged sediment concentration, ϕ_p. Furthermore two closure equations are still needed, one for the bed shear stress, τ_b, and another one for the formulation of the sediment flux between flow and bed, Ψ_p^{net}. In the search for the simplest model involving the minimum number of closure relations, the above formulation can be transformed into Exner equation, next presented.

3.3.2 Exner equation

The above set of equations may be manipulated leading to a simpler model. Inserting Ψ_p from (3.36) in (3.37) leads to the following sediment mass conservation,

$$\frac{\partial z}{\partial t} + \frac{1}{(1-p_p)} \frac{\partial (hu\phi_p)}{\partial x} = -\frac{1}{(1-p_p)} \frac{\partial (h\phi_p)}{\partial t} \tag{3.39}$$

The second term on the left hand side of (3.39) is the derivative of transported sediment flow $q_{s,x} = hu\phi_p$ along the x coordinate, whereas the term on the right side contains information about the temporal evolution of the bed level due to vertical fluxes of material in cases of suspended material. They become the Exner equation (Kalinske, 1947), expressed as follows

$$\frac{\partial z}{\partial t} + \xi \frac{\partial q_{s,x}}{\partial x} = \xi \omega_s \left(E_s - c_b \right) \tag{3.40}$$

with $\xi = \frac{1}{1-p_p}$, ω_s the settling velocity of the sediment particles, E_s a dimensionless factor accounting for the sediment material entering the volume by suspension and ϕ_b is the suspended material concentration. Both terms of $q_{s,x}$ and $\xi \omega_s \left(E_s - \phi_b \right)$ can be estimated if using empirical closure formulae, that depend on the flow conditions.

Regarding the bulk density, it can be evaluated assuming that the volumetric concentration is given by the closure formulae themselves (Rosatti et al., 2007). In many environmental problems, the bulk density remains almost constant and furthermore low concentrations of transported material are present. This means that further simplications over liquid phase mass and momentum conservation equations are admissible, allowing the elimination of the dependence with the relative density of the mixture, r. Alternatively, assuming that the sediment material presents low concentration and does not change the bulk density, the relative density of the mixture, r can be made constant and equal to 1.

Gathering the depth averaged set of equations which governed the 1D flow and the sediment dynamics leads to

Mass

$$\frac{\partial(h)}{\partial t} + \frac{\partial(hu)}{\partial x} = 0 \tag{3.41}$$

Momentum

$$\frac{\partial(hu)}{\partial t} + \frac{\partial[hu^2 + (1/2)gh^2]}{\partial x} = \frac{p_b}{\rho_w} - \frac{\tau_b}{\rho_w} \tag{3.42}$$

Sediment mass, bed

$$\frac{\partial z}{\partial t} + \xi \frac{\partial q_{s,x}}{\partial x} = \xi \omega_s \left(E_s - c_b\right) \tag{3.43}$$

The extension of the formulation of the shallow water equations to unsteady 2D flow over mobile bed using the Exner equation approach is:

Mass

$$\frac{\partial(h)}{\partial t} + \frac{\partial(hu)}{\partial x} + \frac{\partial(hv)}{\partial y} = 0 \tag{3.44}$$

Momentum in x direction

$$\frac{\partial(hu)}{\partial t} + \frac{\partial[hu^2 + (1/2)gh^2]}{\partial x} + \frac{\partial(huv)}{\partial y} = \frac{p_{bx}}{\rho_w} - \frac{\tau_{bx}}{\rho_w} \tag{3.45}$$

Momentum in y direction

$$\frac{\partial(hu)}{\partial t} + \frac{\partial(huv)}{\partial x} + \frac{\partial[hv^2 + (1/2)gh^2]}{\partial y} = \frac{p_{by}}{\rho_w} - \frac{\tau_{by}}{\rho_w} \tag{3.46}$$

Sediment mass, bed

$$\frac{\partial z}{\partial t} + \xi \frac{\partial q_{s,x}}{\partial x} + \xi \frac{\partial q_{s,y}}{\partial y} = \xi \omega_s \left(E_s - c_b\right) \tag{3.47}$$

with (u, v) the depth averaged components of the velocity vector along the (x, y) coordinates.

Considering that the present work is focused on the numerical simulation of bed load transport since the influence of the suspended load is assumed negligible, the Exner equation turns into a reduced form:

$$\frac{\partial z}{\partial t} + \xi \frac{\partial q_{s,x}}{\partial x} + \xi \frac{\partial q_{s,y}}{\partial y} = 0 \tag{3.48}$$

Chapter 4

Bed load transport

4.1 Introduction

Sediment transport includes suspended and bed-load sediment transport. Suspended sediment is present when the flux is intense enough for allowing the sediment grains to move away from the bed. Bed-load transport is the kind of sediment motion where the grains roll, slide or even jump over the bed, Figure 4.1. In this work it is faced the study of bed-load sediment transport and the suspended transport is neglected.

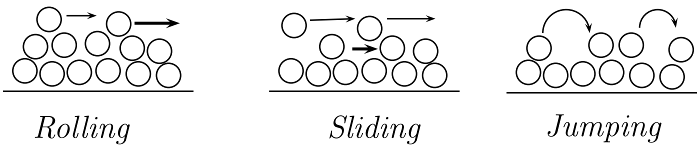

Figure 4.1: Types of sediment transport

As it has been depicted in the previous chapter, when using the Exner equation, horizontal solid fluxes can be evaluated using capacity formulae. In this chapter, different formulations empirically proposed for the modeling of non-cohesive granular material flows are presented and written following a unified expression. In this work mass exchange fluxes associated to suspended load will be considered negligible in comparison with bed load transport, and therefore will not be included in the mathematical model.

4.2 Description of bed load formulation

Considering a bidimensional flow where the solid transport is focused on the bed load, the Exner equation can be written as

$$\frac{\partial z}{\partial t} + \xi \frac{\partial q_{s,x}}{\partial x} + \xi \frac{\partial q_{s,y}}{\partial y} = 0 \tag{4.1}$$

The formulation of the bed load discharge q_s can be based on deterministic laws (Meyer-Peter and Müller, 1948), (Camenen and Larson, 2005), (Smart, 1984) or in probabilistic methods (Kalinske, 1947), (Einstein, 1950), always supported by experimentation. Grass (Grass, 1981) discussed one of the most basic sediment transport laws that in 2D can be written as (Hudson, 2001)

$$q_{s,x} = A_g u \left(u^2 + v^2\right) \qquad q_{s,y} = A_g v \left(u^2 + v^2\right) \tag{4.2}$$

This deterministic formulation is well suited for the modeling of non-cohesive granular material and, as a basic feature, this model does not involve any sediment movement threshold but assumes that the flow is always able to mobilize the bed. The model requires a dimensional calibration constant A_g, accounting for the effects associated to the grain size and the kinematic viscosity. Ranging typically from 0 to 1, it represents a stronger interaction between flow and sediment as it approaches 1.

Following the idea presented in (Murillo and García-Navarro, 2010a), A_g can be determined by using the empirical deterministic formulae avoiding the necessity of expressing this quantity as a calibration constant in each particular problem. To do this, several empirical formulations for sediment transport will be analyzed assuming that it is possible to write them all as

$$A_g = A_g(h, q_{s,x}, q_{s,y}) \tag{4.3}$$

The bed load transport is often represented by the following dimensionless parameter,

$$\Phi = \frac{|\mathbf{q}_s|}{\sqrt{g(s-1)d_m^3}} \tag{4.4}$$

where $s = \rho_p/\rho_w$ is the ratio between solid material (ρ_p) and water densities, and d_m is the median diameter.

The dimensionless bottom shear stress or Shields parameter, can be expressed as:

$$\theta = \frac{|\mathbf{T}_b|}{g(\rho_s - \rho_w)d_m} \tag{4.5}$$

where $\mathbf{T}_b = (\tau_{b,x}, \tau_{b,y})$ is the shear stress at the bottom due to the steady flow, that written in terms of the Manning-Strickler's coefficient (16.2) can be expressed as

Formula	Φ
Meyer-Peter and Müller (1948)	$8\ (\theta-\theta_c)^{3/2}$
Ashida and Michiue (1972)	$17\ (\theta-\theta_c)(\sqrt{\theta}-\sqrt{\theta_c})$
Engelund and Fredsoe (1976)	$18.74\ (\theta-\theta_c)(\sqrt{\theta}-0.7\sqrt{\theta_c})$
Luque and van Beek (1976)	$5.7\ (\theta-\theta_c)^{3/2}$
Parker (1979) fit to Einstein (1950)	$11.2\ \theta^{3/2}\,(1-\theta/\theta_c)^{9/2}$
Smart (1984)	$4\ \ (d_{90}/d_{30})^{0.2}\ \ S_o^{0.6}\ C\theta^{1/2}(\theta-\theta_c^S)$
Nielsen (1992)	$12\ \theta^{1/2}(\theta-\theta_c)$
Wong (2003)	$4.93\ (\theta-\theta_c)^{1.6}$
Wong (2003)	$3.97\ (\theta-\theta_c)^{3/2}$
Camenen and Larson (2005)	$12\ \theta^{3/2}\exp\left(-\theta/\theta_c\right)$

Table 4.1: Summary of sediment formulae

$$\begin{array}{ll} \frac{\tau_{b,x}}{\rho_w} = ghS_{f,x} & S_{f,x} = \frac{n^2u\sqrt{u^2+v^2}}{h^{4/3}} \\ \frac{\tau_{b,y}}{\rho_w} = ghS_{f,y} & S_{f,y} = \frac{n^2v\sqrt{u^2+v^2}}{h^{4/3}} \end{array} \tag{4.6}$$

This allows to express $|\mathbf{T}_b|$ as

$$|\mathbf{T}_b| = \sqrt{\tau_{b,x}^2+\tau_{b,y}^2} = \sqrt{(\rho_w ghS_{f,x})^2+(\rho_w ghS_{f,y})^2} \tag{4.7}$$

leading to the following expression for the Shields parameter:

$$\theta = \frac{n^2}{(s-1)d_m h^{1/3}}(u^2+v^2) = \frac{n^2}{(s-1)d_m h^{1/3}}|\mathbf{u}|^2 \tag{4.8}$$

Different commonly applied empirical deterministic formulae are written in terms of Φ and θ. The formulae tested in this work are gathered in Table 4.1, where d_{90} and d_{30} are the grain diameter for which 90% and 30% of the weight of a nonuniform sample is finer respectively, C is the flow resistance factor $C = u/(ghS_f)^{0.5}$, S_o is the bed slope, θ_c is the critical Shields parameter, Table 4.2, expressing the sediment movement threshold, and

$$\theta_c^S = \theta_c \cos\phi\left(1-\frac{\tan\phi}{\tan\psi}\right) \tag{4.9}$$

with ϕ the angle of the bed slope and ψ the angle of repose of saturated bed material. Using (4.8) and (4.4) the transport formulae in (4.1) can be expressed as

$$|\mathbf{q}_s| = K_0\ K_1\ (u^2+v^2)^{3/2} = A_g|\mathbf{u}|^3 \tag{4.10}$$

Formula	θ_c
Meyer-Peter and Müller (1948)	0.0470
Ashida and Michiue (1972)	0.0500
Engelund and Fredsoe (1976)	0.0500
Fernández Luque and Van Beek (1976)	0.037–0.0455
Parker (1979) fit to Einstein (1950)	0.030
Smart(1984)	0.0470
Nielsen (1992)	0.0470
Wong (2003)	0.0470
Wong (2003)	0.0495
Camenen and Larson(2005)	0.0400

Table 4.2: Summary of threshold of non dimensional shear stress

with $A_g = K_0\ K_1$, $K_0 = \frac{g^{1/2} n^3}{(s-1) h^{1/2}}$ and K_1 varying in each case as displayed in Table 4.3.

Formula	K_1
Meyer-Peter and Müller (1948)	$8\,(1-\theta_c/\theta)^{3/2}$
Ashida and Michiue (1972)	$17\ (1-\theta_c/\theta)(1-\sqrt{\theta_c/\theta})$
Engelund and Fredsoe (1976)	$18.74\ (1-\theta_c/\theta)(1-0.7\sqrt{\theta_c/\theta})$
Fernández Luque and Van Beek (1976)	$5.7\ (1-\theta_c/\theta)^{3/2}$
Parker (1979) fit to Einstein (1950)	$11.2\ \ (1-\theta/\theta_c)^{9/2}$
Smart(1984)	$4\ \ (d_{90}/d_{30})^{0.2}\ \ S_o^{0.6}\ C\,(1-\theta_c/\theta)$
Nielsen (1992)	$12\ (1-\theta_c/\theta)$
Wong (2003)	$4.93\,(1-\theta_c/\theta)^{3/2}\,(\theta-\theta_c)^{0.1}$
Wong (2003)	$3.97\,(1-\theta_c/\theta)^{3/2}$
Camenen and Larson(2005)	$12\ \exp\,(-\theta/\theta_c)$

Table 4.3: Summary of Grass coefficients written for sediment formulae

These more complex definitions provided for A_g, (4.10), allows to standardize sediment transport formulae and perform a study about their relative behavior under different hydrodynamic and morphodynamic conditions.

Chapter 5

CJ numerical scheme

5.1 Introduction

The numerical scheme proposed in Murillo and García-Navarro (2010a) and based on a coupled-Jacobian (CJ) strategy has been chosen as a numerical benchmark for analyzing the relative performance of the bed load formulae described in the previous section. The development of the numerical scheme departs from the previous system of equations presented in the one layer model for the shallow water (3.41) and for the Exner model (8.8) which are written in a 2D coupled form as follows:

$$\frac{\partial \mathbf{U}}{\partial t} + \frac{\partial \mathbf{F}(\mathbf{U})}{\partial x} + \frac{\partial \mathbf{G}(\mathbf{U})}{\partial y} = \mathbf{S}(\mathbf{U}, x, y) \tag{5.1}$$

where

$$\mathbf{U} = (h,\ q_x,\ q_y,\ z)^T \tag{5.2}$$

with

$$\begin{aligned} \mathbf{F} &= \left(q_x,\ \tfrac{q_x^2}{h} + \tfrac{1}{2}gh^2,\ \tfrac{q_xq_y}{h},\ A_g\tfrac{q_x(q_x^2+q_y^2)}{h^3}\right)^T \\ \mathbf{G} &= \left(q_y,\ \tfrac{q_xq_y}{h},\ \tfrac{q_y^2}{h} + \tfrac{1}{2}gh^2,\ A_g\tfrac{q_y(q_x^2+q_y^2)}{h^3}\right)^T \end{aligned} \tag{5.3}$$

and the source term $\mathbf{S}$

$$\mathbf{S} = \left(0,\ \frac{p_{b,x}}{\rho_w} - \frac{\tau_{b,x}}{\rho_w},\ \frac{p_{b,y}}{\rho_w} - \frac{\tau_{b,y}}{\rho_w},\ 0\right)^T \tag{5.4}$$

In the next section, the finite volume scheme is described.

5.2 Description of the finite volume scheme

To introduce the finite volume scheme, (5.1) is integrated in a constant size volume or grid cell Ω using Gauss theorem:

$$\frac{\partial}{\partial t}\int_{\Omega}\mathbf{U}d\Omega+\oint_{\partial\Omega}\mathbf{E_n}dl=\int_{\Omega}\mathbf{S}d\Omega \tag{5.5}$$

where $\mathbf{E_n}=\mathbf{F}n_x+\mathbf{G}n_y$ and $\mathbf{n}=(n_x,n_y)$ is the outward unit normal vector to the volume Ω. In order to obtain a numerical solution of system (5.1) we divide the domain in computational cells, Ω_i, using a mesh fixed in time, and (12.9) is applied to each cell

$$\frac{\partial}{\partial t}\int_{\Omega_i}\mathbf{U}d\Omega+\sum_{k=1}^{NE}\int(\mathbf{E_n})_k^{\downarrow}dl_k=\int_{\Omega_i}\mathbf{S}d\Omega \tag{5.6}$$

Here $(\mathbf{E_n})_k^{\downarrow}$ is the value of the interface flux function through the edge k to be defined, $\mathbf{n}_k=(n_x,n_y)$ is the outward unit normal vector to the cell edge k, and NE is the number of edges in cell i. Assuming a piecewise representation per cell of the conserved variables,

$$\mathbf{U}_i^n=\frac{1}{A_i}\int_{\Omega_i}\mathbf{U}(x,y,t^n)d\Omega \tag{5.7}$$

(12.15) is written as

$$\frac{\partial}{\partial t}\int_{\Omega_i}\mathbf{U}d\Omega+\sum_{k=1}^{NE}(\mathbf{E_n})_k^{\downarrow}l_k=\sum_{k=1}^{NE}\mathbf{T}_{\mathbf{n},b}l_k+\sum_{k=1}^{NE}\mathbf{T}_{\mathbf{n},s}l_k \tag{5.8}$$

where l_k is the corresponding edge length and $\mathbf{T}_b\mathbf{n}$ and $\mathbf{T}_s\mathbf{n}$ are suitable integrals of the bed slope and friction source terms (Murillo et al., 2009):

$$(\mathbf{T}_{\mathbf{n},b})_k=\left(\frac{p_b}{\rho_w}\right)_k\begin{pmatrix}0,n_x,n_y\end{pmatrix}_k^T \quad (\mathbf{T}_{\mathbf{n},s})_k=g(\widetilde{h}S_f)_k d_{\mathbf{n}}\begin{pmatrix}0,n_x,n_y\end{pmatrix}_k^T \tag{5.9}$$

with $\widetilde{h}=1/2(h_i+h_j)$, i and j the cells sharing edge k, $S_{f,k}$ the friction slope and $d_{\mathbf{n}}$ the normal distance between neighboring cell centers.

The numerical scheme is constructed by defining an approximate Jacobian matrix $\widetilde{\mathbf{J}}$ at each k edge each cell combining the normal flux $\mathbf{E_n}$ with the bed slope source term $\mathbf{T}_{\mathbf{n},b}$ at each cell edge

$$(\delta\mathbf{E}-\mathbf{T_b})_{k\mathbf{n}_k}=\widetilde{\mathbf{J}}_{\mathbf{n},k}\delta\mathbf{U}_k \tag{5.10}$$

with $\delta(\mathbf{E_n})_k = (\mathbf{E}_j - \mathbf{E}_i)_{\mathbf{n}_k}$, $\delta\mathbf{U}_k = \mathbf{U}_j - \mathbf{U}_i$, and $\mathbf{U}_i$ and $\mathbf{U}_j$ the initial values at cells i and j sharing edge k. The approximate Jacobian matrix $\widetilde{\mathbf{J}}$ is

$$\widetilde{\mathbf{J}}_{\mathbf{n},k} = \begin{pmatrix} 0 & n_x & n_y & 0 \\ (\widetilde{c}^2 - \widetilde{u}^2)n_x - \widetilde{u}\widetilde{v}n_y & 2\widetilde{u}n_x + \widetilde{v}n_y & \widetilde{u}n_y & p_{bz}n_x \\ -\widetilde{u}\widetilde{v}n_x + (\widetilde{c}^2 - \widetilde{v}^2)n_y & \widetilde{v}n_x & \widetilde{u}n_x + 2\widetilde{v}n_y & p_{bz}n_y \\ \widetilde{A} & \widetilde{B} & \widetilde{C} & 0 \end{pmatrix} \tag{5.11}$$

being $\widetilde{u}$, $\widetilde{v}$ and $\widetilde{c}$ the Roe averaged variables (Roe, 1986)

$$\widetilde{u} = \frac{u_i\sqrt{h_i} + u_j\sqrt{h_j}}{\sqrt{h_i} + \sqrt{h_j}}, \qquad \widetilde{v} = \frac{v_i\sqrt{h_i} + v_j\sqrt{h_j}}{\sqrt{h_i} + \sqrt{h_j}}, \qquad \widetilde{c} = \sqrt{g\frac{h_i + h_j}{2}} \tag{5.12}$$

and the coefficients $\widetilde{A}$, $\widetilde{B}$ and $\widetilde{C}$ equal to

$$\begin{aligned} \widetilde{A} &= -(C_1n_x + C_2n_y)\widetilde{u} - (C_2n_x + C_3n_y)\widetilde{v} \\ \widetilde{B} &= (C_1n_x + C_2n_y) \\ \widetilde{C} &= (C_2n_x + C_3n_y) \end{aligned} \tag{5.13}$$

where

$$\begin{aligned} C_1 &= A_{g,k}\,\xi\frac{(u_i^2 + u_iu_j + u_j^2)}{\sqrt{h_ih_j}} + A_{g,k}\,\xi\frac{v_iv_j}{\sqrt{h_ih_j}} \\ C_2 &= A_{g,k}\,\xi\frac{(u_iv_i + u_jv_j)}{\sqrt{h_ih_j}} \\ C_3 &= A_{g,k}\,\xi\frac{(v_i^2 + v_iv_j + v_j^2)}{\sqrt{h_ih_j}} + A_{g,k}\,\xi\frac{u_iu_j}{\sqrt{h_ih_j}} \end{aligned} \tag{5.14}$$

As the coefficient A_g is not a constant but varies from cell to cell, at every edge k a local $A_{g,k}$ value is defined as an arithmetic mean between cells

$$A_{g,k} = \frac{A_{g,i} + A_{g,j}}{2} \tag{5.15}$$

where the $A_{g,i}$ coefficients are obtained through the relations presented in the bed load formulation chapter. Other average possibilities have been tested leading to negligible differences.

From the approximate Jacobian matrix in (5.11) a set of four real eigenvalues $\widetilde{\lambda}_k^m$ and eigenvectors $\widetilde{\mathbf{e}}_k^m$ are obtained (see Appendix A for their detailed expression). Vector $\mathbf{U}$ is then split through the matrix eigenvectors basis, $\widetilde{\mathbf{P}}$, as

$$\delta\mathbf{U}_k = \widetilde{\mathbf{P}}_k\mathbf{A}_k \tag{5.16}$$

with

$$\widetilde{\mathbf{P}_k} = (\widetilde{\mathbf{e}}^1, \widetilde{\mathbf{e}}^2, \widetilde{\mathbf{e}}^3, \widetilde{\mathbf{e}}^4) \qquad \mathbf{A}_k = \begin{pmatrix} \alpha^1 & \alpha^2 & \alpha^3 & \alpha^4 \end{pmatrix}_k^T \tag{5.17}$$

The friction source terms are also projected onto the matrix eigenvectors basis, $\widetilde{\mathbf{P}}$, in 5.18, to guarantee the exact equilibrium between fluxes and source terms

$$(\mathbf{T}_{\mathbf{n},s})_k = \widetilde{\mathbf{P}}_k \mathbf{B}_k \tag{5.18}$$

with

$$\mathbf{B}_k = \begin{pmatrix} \beta^1 & \beta^2 & \beta^3 & \beta^4 \end{pmatrix}_k^T \tag{5.19}$$

The complete details of the coefficients can be found in Murillo and García-Navarro (2010a). Gathering all the previous information the volume integral in the cell at time t^{n+1} is expressed as

$$\mathbf{U}_i^{n+1} = \mathbf{U}_i^n - \sum_{k=1}^{NE} \sum_{m=1}^{4} (\widetilde{\lambda}^- \alpha - \beta^-)_k^m \widetilde{\mathbf{e}}_{JI,k}^m l_k \frac{\Delta t}{A_i} - \sum_{k=1}^{NE} \delta \mathbf{E}_{Ii,k} \mathbf{n}_k l_k \frac{\Delta t}{A_i} \tag{5.20}$$

being l_k the length of the edge normal to the n_k vector and

$$\widetilde{\beta}_k^{\pm,m} = \frac{1}{2}(1 \pm sign(\widetilde{\lambda}))_k^m \beta_k^m \qquad \widetilde{\lambda}_k^{\pm,m} = \frac{1}{2}(\widetilde{\lambda} \pm |\widetilde{\lambda}|)_k^m \tag{5.21}$$

in (5.20) the second term of the right side evaluates the flux in the cell edge and the third term completes the updating formula to consider the spacial variation of A_g, see Appendix B for further details.

The updated value $\mathbf{U}_i^{n+1}$ in (5.20) can be interpreted as a cell average of the contributions of the local RPs, and in consequence the time step Δt is taken small enough so that there is no interaction of waves from the k neighboring Riemann problems. In the 2D framework, considering unstructured meshes, the relevant distance, that will be referred to as χ_i in each cell i must consider the volume of the cell and the length of the shared k edges,

$$\chi_i = \frac{A_i}{\max_{k=1,NE} l_k} \tag{5.22}$$

Considering that each k RP is used to deliver information to a pair of neighboring cells of different size, the distance $\min(A_i, A_j)/l_k$ is relevant, so in case that the water depth is greater than zero in all the regions of the RP solution the time step is limited by

$$\Delta t \leq CFL\ \Delta t^{\widetilde{\lambda}} \qquad \Delta t^{\widetilde{\lambda}} = \frac{\min(\chi_i, \chi_j)}{\max|\widetilde{\lambda}^m|} \tag{5.23}$$

with CFL=1/2 in the case of rectangular or structured triangular cells and, according to computational experience, CFL close to 1 for triangular unstructured grids as the construction of finite volume schemes from direct application of one-dimensional fluxes leads to reduced stability ranges (Toro, 2001).

5.3 Numerical discretization of the bed slope in the generalized Grass coefficient for the Smart formulation

Empirical formulations for bed load transport presented in the previous chapter are written as a function of the bed friction slope, except in the case of the Smart formulation, that considers an additional term based on an estimation of the bed slope along the preferential flow direction.

$$\Phi = 4\ (d_{90}/d_{30})^{0.2}\ S_o^{0.6}\ C\theta^{1/2}(\theta - \theta_c^S) \tag{5.24}$$

where Φ is the dimensionless sediment transport, θ is the dimensionless shear stress, d_{90} and d_{30} are the grain diameters for which 90% and 30% of the weight of a non-uniform sample is finer respectively, S_o stands for the bed slope along the preferential flow direction, θ_c is the critical Shields parameter, and C is the flow resistance factor $C = u/(ghS_f)^{0.5}$, being u the unique velocity in the 1D experimental tests carried out by Smart and S_f the friction slope along that direction, calculated as 16.2.

In a 2D model both the bed slope and friction slope are defined along the two horizontal coordinate directions. This subsection is devoted to the discussion of their correct evaluation in that case. As the Smart formula was derived from 1D experimental cases involving the bed slope in the flow direction, in 2D simulation it is necessary to evaluate the bed slope in the local flow direction, $|S_{o,\mathbf{u}}|$. The bed slope in the flow direction is given by:

$$|S_{o,\mathbf{u}}|_i = |\mathbf{S}_{o,i}\mathbf{n}_{\mathbf{u},i}| \tag{5.25}$$

where $\mathbf{n}_{\mathbf{u},i}$ is the unit vector associated to the local velocity $\mathbf{u}, i$ at each cell i. As in 2D the bed level surface is defined by a plane, the following technique, able to handle both rectangular and triangular meshes, is used to evaluate the bed slope $\mathbf{S}_{o,i} = (S_{o,x}, S_{o,y})$ in each cell (Murillo et al., 2009),

$$S_{o,x} = \left(\sum_{k=1}^{NE}\left(\frac{\delta z\, n_x}{d_{\mathbf{n}}}\right)\right)\left(\sum_{k=1}^{NE}|n_x|\right)^{-1} \quad S_{o,y} = \left(\sum_{k=1}^{NE}\left(\frac{\delta z\, n_y}{d_{\mathbf{n}}}\right)\right)\left(\sum_{k=1}^{NE}|n_y|\right)^{-1} \tag{5.26}$$

where δz is the difference of bottom heights, d_n is the normal distance between the centers of cells and n_x, n_y are the components of the normal vector along the axis.

Furthermore, in cases where the flow finds a nil or an adverse slope $\mathbf{S}_{o,i}\mathbf{u}_i \leq 0$ the bed slope in (5.25) is replaced by the friction slope computed in cell i, $\mathbf{S}_{f,i}$, with the components as defined in (16.2) . This option will be referred to as Smart CFBS (Combined Friction and Bed Slope). In case of using under any morphodynamic condition the friction slope, the option will be called Smart.

5.4 Geomorphological collapse

Together with the morphodynamic changes associated to the bed, when managing transient geomorphological flows in realistic cases, the geotechnical equilibrium bank characteristics can be ruined, leading to dramatic channel metamorphosis. This effect needs to be modeled to reproduce correctly bed geometry evolution in combination with flow action. In this work the effect of the geomorphological collapse is introduced in the simulation by a simple mass conservative mechanism of slope sliding failure, assuming that the angle of repose of submerged material of the bed can be approximated by the friction angle. The failure mechanism is applied by comparison between the bed slope in each cell edge k, computed as $\frac{\delta z_k}{d_{n_k}}$, and the angle of repose of saturated bed material.

Chapter 6

CJ scheme: numerical results

6.1 Introduction

This Chapter gathers 1D and 2D cases with experimental data in order to study the relative behavior of the numerical results predicted when using different sediment transport formulae. These closure laws were derived from 1D experimental steady flows and are going to be tested in order to verify their capacity of prediction in unsteady situations. In addition, a novel numerical discretization of the classical Smart formula is also tested.

Firstly 1D results are presented. A series of sudden dam break test cases are presented, with a combination of morphodynamic and hydrodynamic situations. In the next test case, dam erosion in time due to flow overtopping is considered. In all these numerical experiments the flow finds different regions under subcritical or supercritical regime. The last experiment considers a case of fully subcritical flow, with an important discontinuity at the bottom.

The second section of this chapter is devoted to 2D hydro-morphodynamic changes. The dam failure is the first test case studied. Then, two test cases of dam break over a channel with a a/symmetric enlargement are analyzed.

6.2 One dimensional cases

6.2.1 Dam break test cases

These experiments were performed in a flume designed at the UCL Civil Engineering Department (Spinewine and Zech, 2007). The flume had a length of 6 m, 3 m on both sides of a central gate simulating an idealized dam. The channel width was set constant and equal to 25 cm. The bed material was uniform coarse sand with the

Test	h_L	h_R	z_L	z_R
A	0.35	0.00	0.00	0.00
B	0.40	0.00	-0.05	0.00
D	0.25	0.00	0.10	0.00
F	0.25	0.10	0.10	0.00

Table 6.1: Summary of dam break test cases

following properties: particle sizes ranging from 1.2 to 2.4 mm, with $d_{50} = 1.82$ mm, density $\rho_s = 2683$ kg m^{-3}, a friction angle $\varphi = 30^o$, negligible cohesion, porosity $p = 0.47$ and was characterized by a Manning roughness factor $n = 0.0165$ sm$^{-1/3}$.

Table 6.1 summarizes the set of experiments selected in this work. The regions upstream and downstream the gate were filled with sediments and different water depths. The three first test cases, A, B, and D, have been chosen to guarantee the correct performance of the numerical scheme in combination with a discharge formulation, in cases where morphological changes are produced in presence of dry bed and null, adverse or in favorable slope. Case F allows checking if the numerical scheme in combination with a discharge formulation is able to handle with the different type of waves that may arise in a dam break case over wet bed. Numerical simulations have been performed using $\Delta x = 0.01$ m and CFL = 1.0. In all the simulations the bed domain is considered deformable and no boundary condition is imposed at the downstream section.

6.2.2 Test A

Test A is a dam break over dry bed with an initially plain bed level. The flow evolves in time leading to a left moving rarefaction wave upstream the gate ending in a flooding front dominated by friction. The experimental results are close to those ones obtained for dam break cases over dry and fixed bed (Dressler, 1954). In Figure 6.1 numerical results and experimental data have been plotted for test case A, for times ranging from 0 to 1.5 seconds. The front wave is numerically well reproduced in space and time when using Smart CFBS.

Figure 6.2 shows the numerical results and experimental data for the dam break test case A using MPM (left) and Smart CFBS (right). In this case little scour is produced and both formulations provide indistinguishable results. The Smart CFBS formulation provides a correct tracking of the advance velocity, bed level and water level surface in time, as shown in Figure 6.1. Considering that the numerical scheme is conservative, differences among measured and computational data are expected to be produced by the lack of an infiltration parameter in the numerical model.

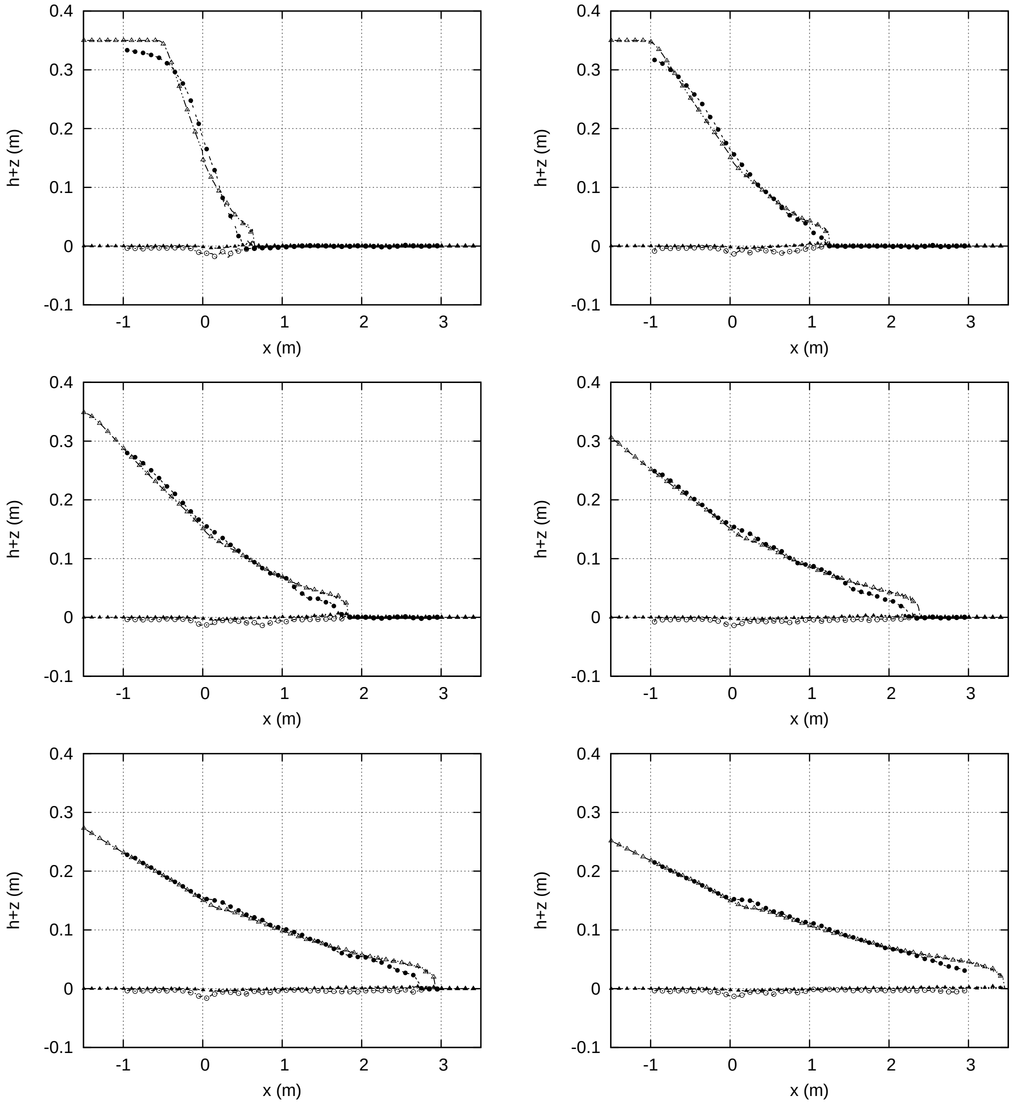

Figure 6.1: Numerical results and experimental data for the dam break test case A at times t = 0.025, 0.050, 0.075, 0.100, 0.125 and 1.5 s, using a variable value of A_g computed using Smart CFBS: measured water level surface (− ● −), measured bed level surface (− ○ −), computed water level surface (−△−), computed bed level surface (−▲−)

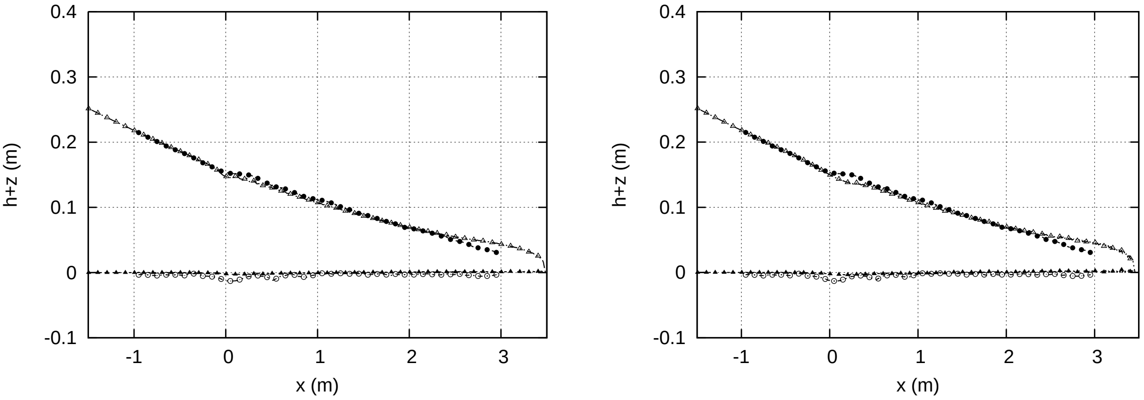

Figure 6.2: Numerical results and experimental data for the dam break test case A at $t = 1.5$ s, using a variable value of A_g computed using MPM (left) and Smart CFBS (right): measured water level surface ($- \bullet -$), measured bed level surface ($- \circ -$), computed water level surface ($-\triangle-$), computed bed level surface ($-\blacktriangle-$)

The similarity among computational results for the different discharge formulations is clear when observing Figure 6.3, that displays the modulus of the water level surface error (left) and bed level (right) error in x for the different formulations at $t = 1.5$ s. The RMSE (Root median square error) for the different formulations plotted at Figure 6.4, confirms that in plain bed, accurate results are given by all formulas.

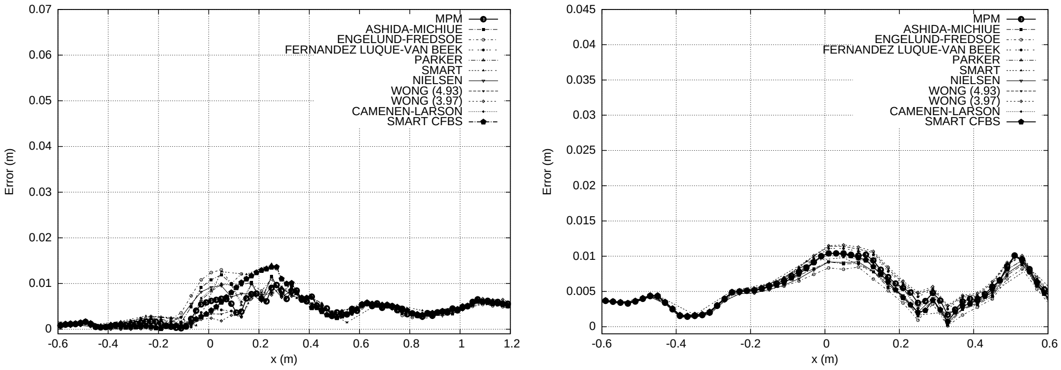

Figure 6.3: Modulus of the water level surface error (left) and bed level error (right) in x for the different formulations at $t = 1.5$ s in test A

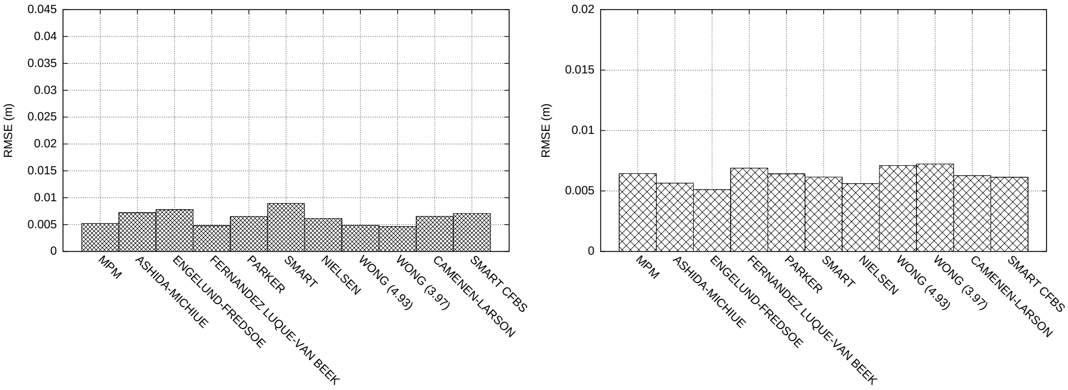

Figure 6.4: RMSE for water level surface (left) and bed level surface (right) with different formulas at $t = 1.5$ s in test A

6.2.3 Test B

Test B is a case of advance front over dry bed and adverse discontinuity. The flow evolves leading to a left moving rarefaction wave ending in front wave dominated by friction. Figure 6.5 shows how front wave celerity is well reproduced in time when using the Smart CFBS formula. Figure 6.6 shows the numerical results and experimental data for the dam break test case B when using MPM (left) and Smart CFBS (right). In both cases, the most relevant difference with measured data is observed over the step, due to the lack of erosion with respect to experimental data. Upstream and downstream the step both numerical simulations provide identical results, being able to reproduce accurately the free surface level in space.

The lack of precision over the upward step is observed for all discharge formulations if observing Figure 6.7, that provides level errors in space. The rest of the domain presents an acceptable error. The RMSE for water level surface (left) and bed level surface (right) at $t = 1.5$ s plotted at Figure 6.8 shows that in this test case there is not clearly a more advantageous formula.

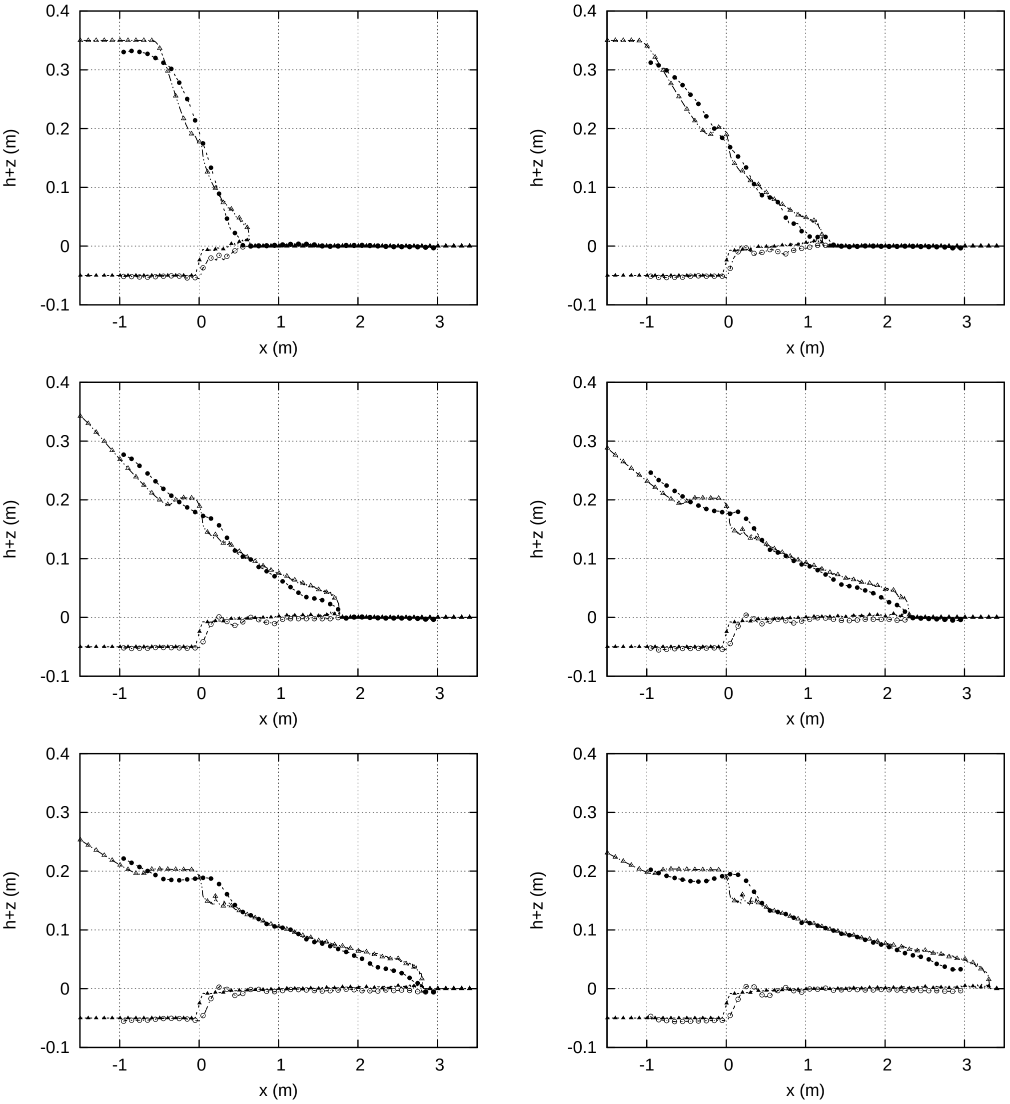

Figure 6.5: Numerical results and experimental data for the dam break test case B at times $t = 0.025$, 0.050, 0.075, 0.100, 0.125 and 1.5 s, using a variable value of A_g computed using Smart CFBS: measured water level surface (− ● −), measured bed level surface (− ○ −), computed water level surface (−△−), computed bed level surface (−▲−)

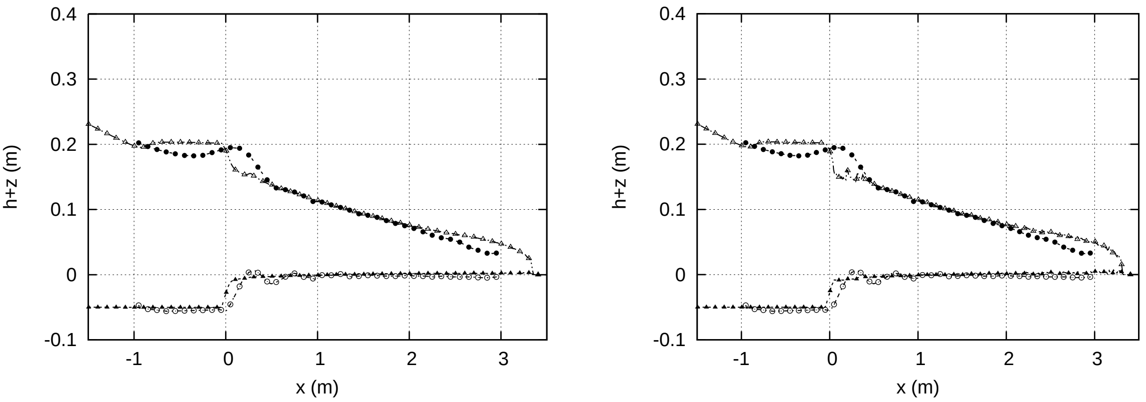

Figure 6.6: Numerical results and experimental data for the dam break test B at $t = 1.5$ s, using a variable value of A_g computed using MPM (left) and Smart CFBS (right): measured water level surface (− ● −), measured bed level surface (− ○ −), computed water level surface (−△−), computed bed level surface (−▲−)

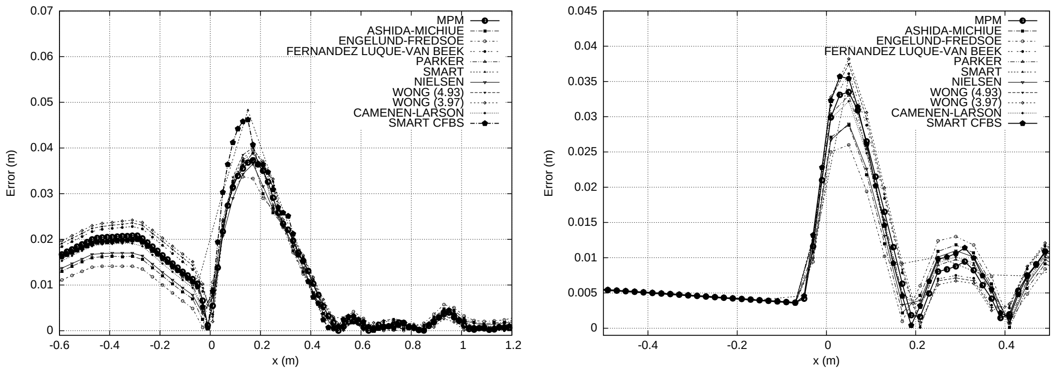

Figure 6.7: Modulus of the water level surface error (left) and bed level error (right) in x for the different formulations at $t = 1.5$ s in test B

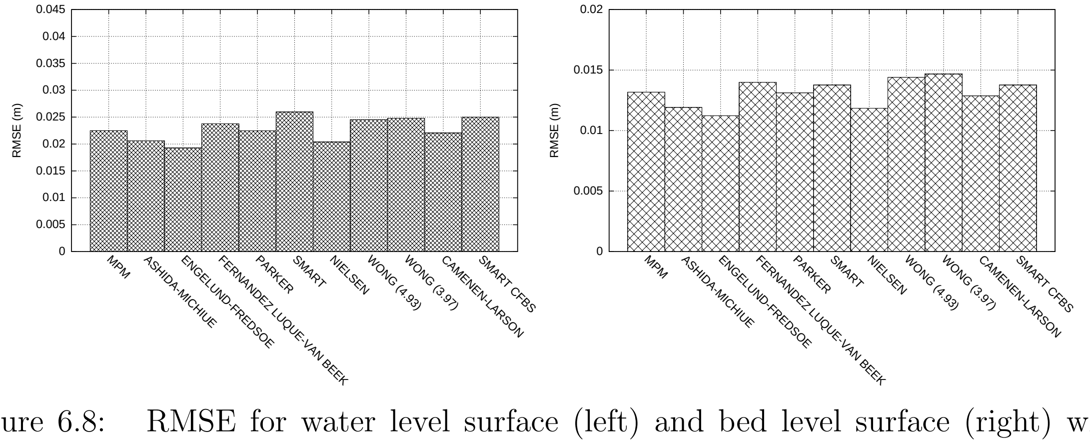

Figure 6.8: RMSE for water level surface (left) and bed level surface (right) with different formulas at $t = 1.5$ s in test B

6.2.4 Test D

Test D represents a reservoir partially filled with sediments and includes a downward step. In this case, once flow passes through the gate location accelerates and decelerates in the friction dominated front. Figure 6.9 shows numerical results and experimental data for the dam break using MPM (left) and Smart CFBS (right). Smart CFBS formulation is able to handle perfectly with this kind of bed discontinuity, tracking the water level surface and redrawing correctly the bed level. Different time instants captured in Figure 6.10 allow appreciating the accuracy and the grade of detail of the computational results in time. Free surface and bed levels are correctly captured for both rarefaction wave and advance front wave, as well as, the bed level at the discontinuity point.

Figure 6.11 shows how Smart CFBS formulation provides the lowest level for bed level (right) and free surface (left) error in space at $t = 1.5$ s if compared with the rest of formulations. Also, the RMSE for water level surface (left) and bed level surface (right) displayed in Figure 6.12 confirms that Smart CFBS formulation gives the better results. Compared with test cases A and B, error is drastically reduced with the proposed formulation.

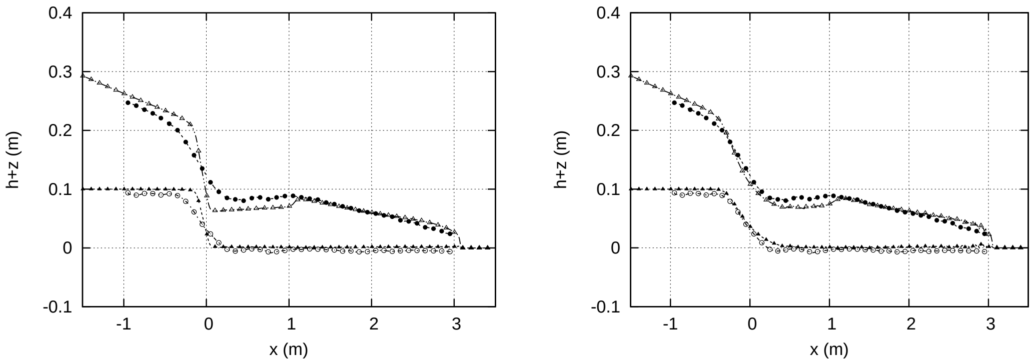

Figure 6.9: Numerical results and experimental data for the dam break test case D at $t = 1.5$ s, using a variable value of A_g computed using MPM (left) and Smart CFBS (right): measured water level surface (− ● −), measured bed level surface (− ○ −), computed water level surface (−△−), computed bed level surface (−▲−)

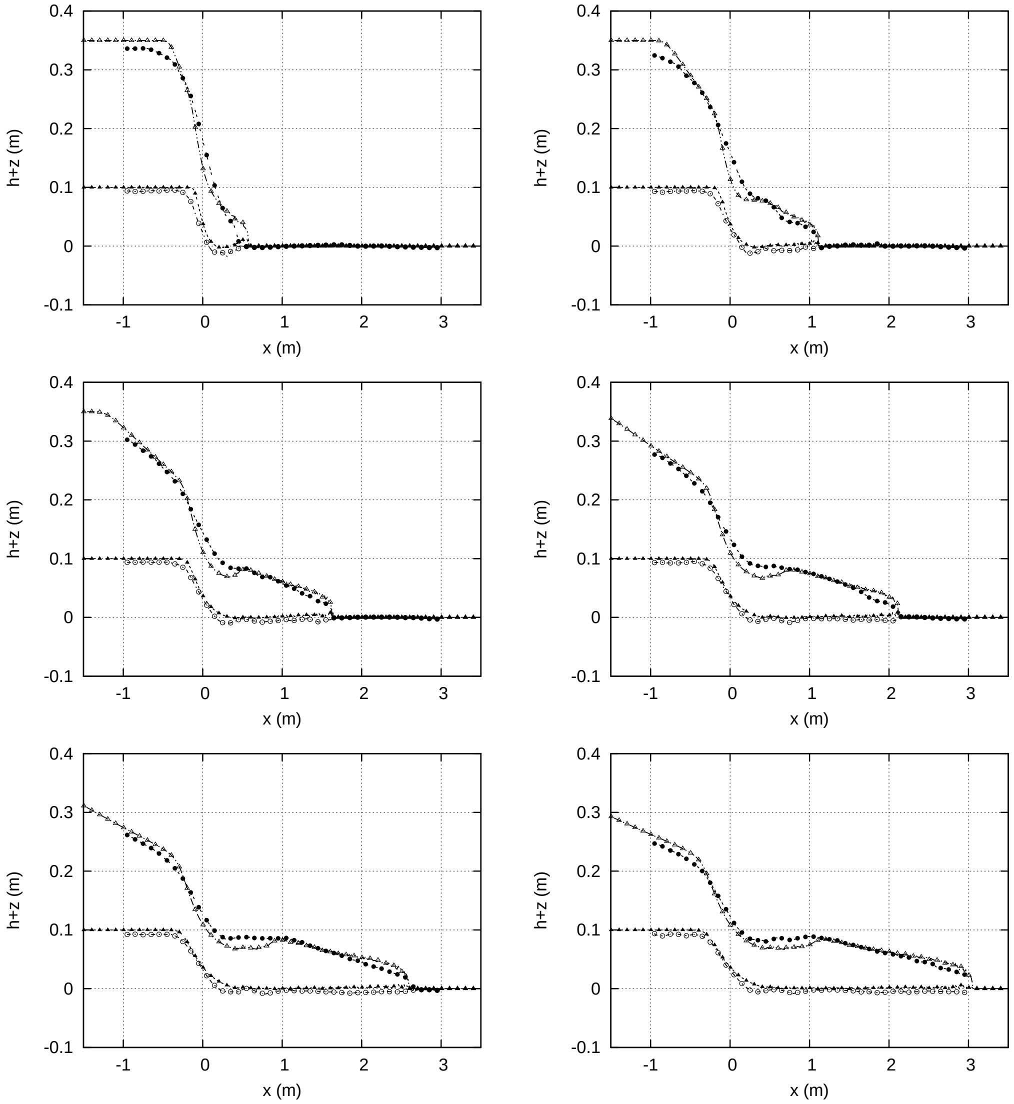

Figure 6.10: Numerical results and experimental data for the dam break test case D at times t = 0.025, 0.050, 0.075, 0.100, 0.125 and 1.5 s, using a variable value of A_g computed using Smart CFBS: measured water level surface (− ● −), measured bed level surface (− ○ −), computed water level surface (−△−), computed bed level surface (−▲−)

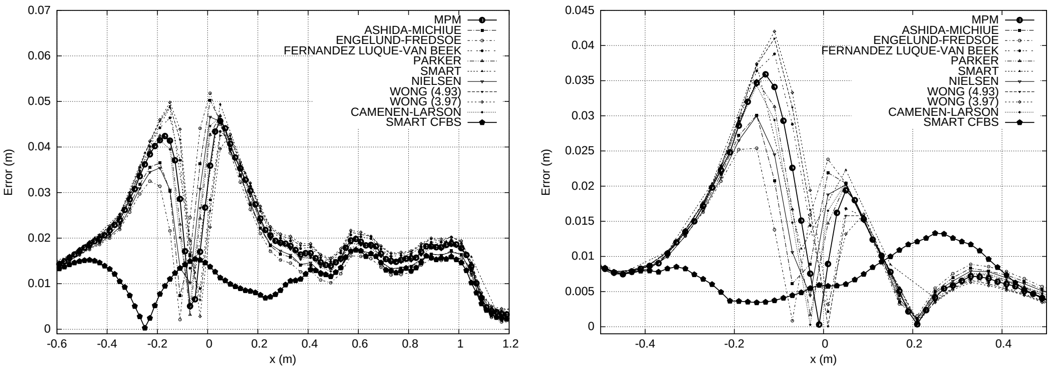

Figure 6.11: Modulus of the water level surface error (left) and bed level error (right) in x for the different formulations at $t = 1.5$ s in test D

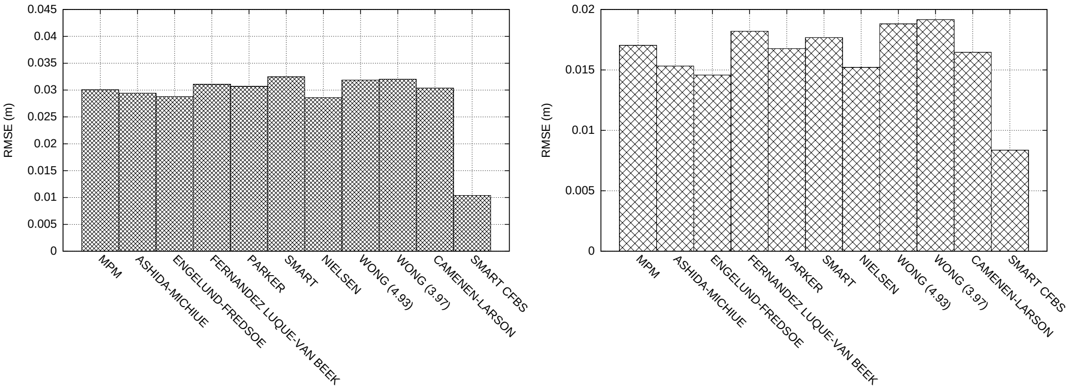

Figure 6.12: RMSE for water level surface (left) and bed level surface (right) with different formulas at $t = 1.5$ s in test D

6.2.5 Test F

Test F is the last dam break studied in this paper. It is the case of a downward bed step combined with an initial layer of clear water in the downstream reach. The flows evolves in time leading to a left moving rarefaction wave upstream the gate, followed by an steady hydraulic jump downstream the gate and ending up in a right moving shock. Figure 6.13 gathers numerical results and experimental data for the dam break test case F using MPM (left) and Smart CFBS (right). The results of Smart CFBS show that the experimental data is well depicted by numerical predictions in the rarefaction, the hydraulic jump and in the moving shock.

Figure 6.14 plots free surface and bed level at different times, where it can be observed how the shock celerity is perfectly captured by the numerical scheme in combination with Smart CFBS formulation. Small differences produced in the shock wave are attributable to fast transient energy variations associated to the existence of a hydraulic jump.

Smart CFBS leads to the smallest error in comparison with the other discharge formulas, as it is appreciated in Figure 6.15, where modulus of the water level surface error (left) and bed level error (right) in x are plotted. Figure 6.16 displays RMSE for water level surface (left) and bed level surface (right) with different formulas at $t = 1.5$ s leading to the same conclusion.

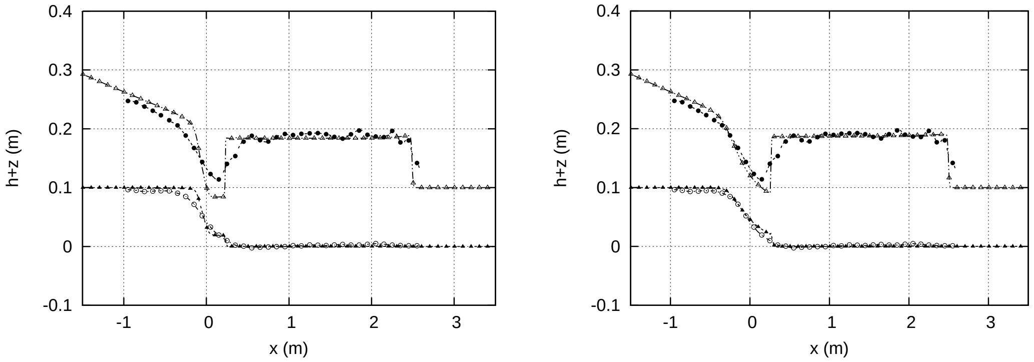

Figure 6.13: Numerical results and experimental data for the dam break test F at $t = 1.5$ s, using a variable value of A_g computed using MPM (left) and Smart CFBS (right): measured water level surface (− ● −), measured bed level surface (− ○ −), computed water level surface (−△−), computed bed level surface (−▲−)

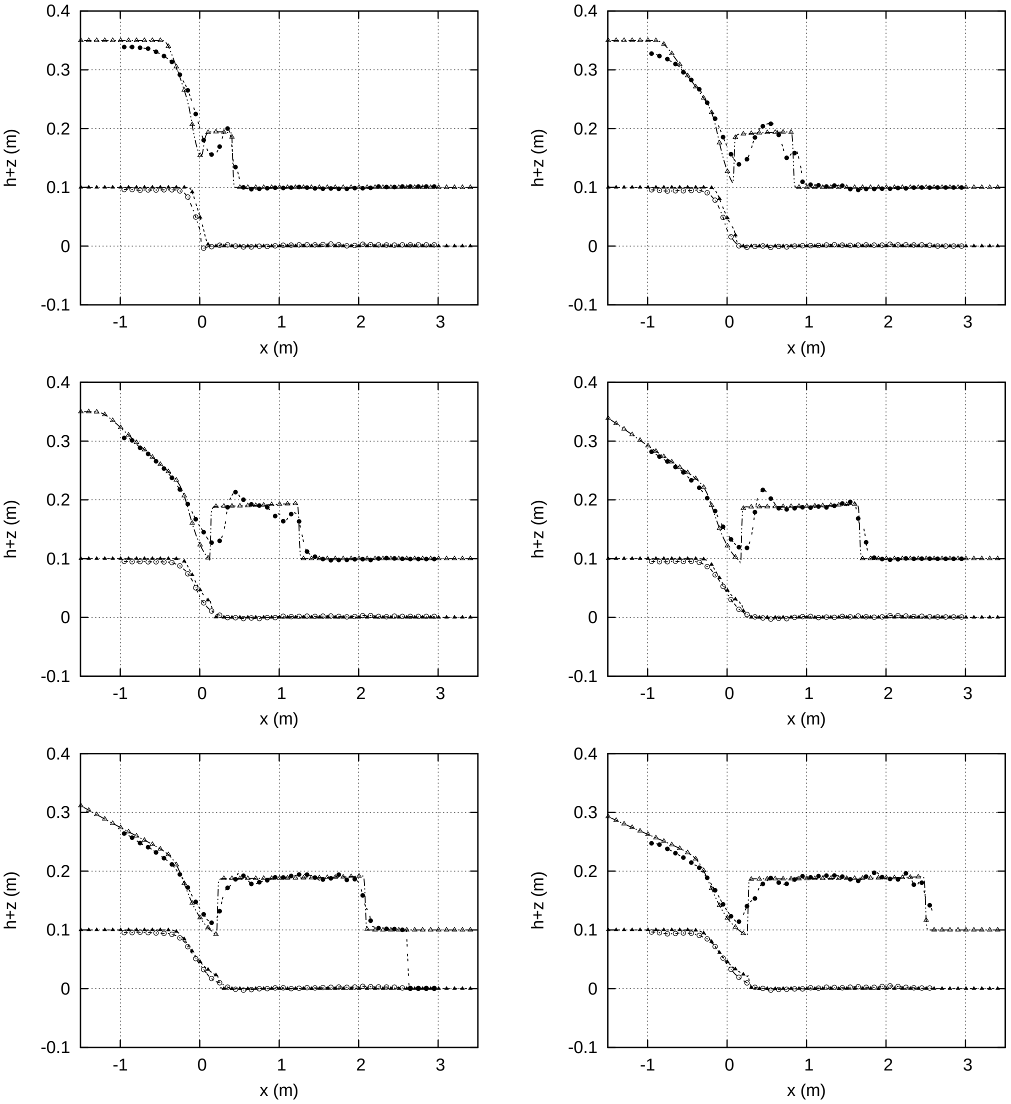

Figure 6.14: Numerical results and experimental data for the dam break test case F at times $t = 0.025$, 0.050, 0.075, 0.100, 0.125 and 1.5 s, using a variable value of A_g computed using Smart CFBS: measured water level surface (– ● –), measured bed level surface (– ○ –), computed water level surface (–△–), computed bed level surface (–▲–)

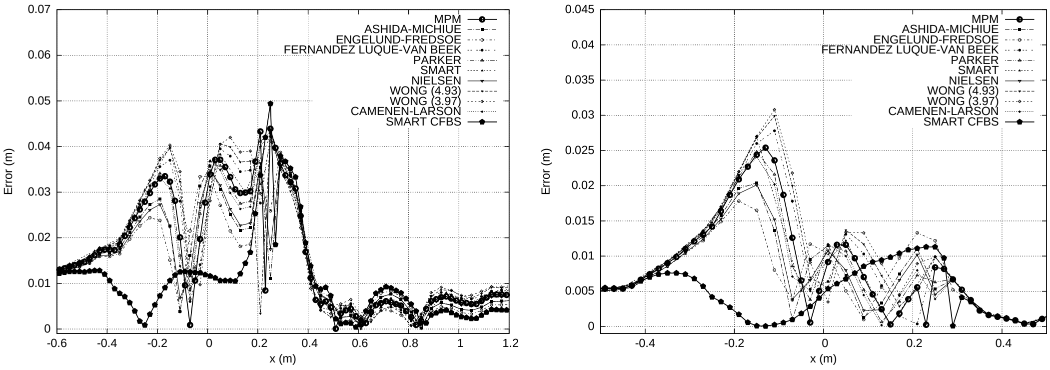

Figure 6.15: Modulus of the water level surface error (left) and bed level error (right) in x for the different formulations at $t = 1.5$ s in test F

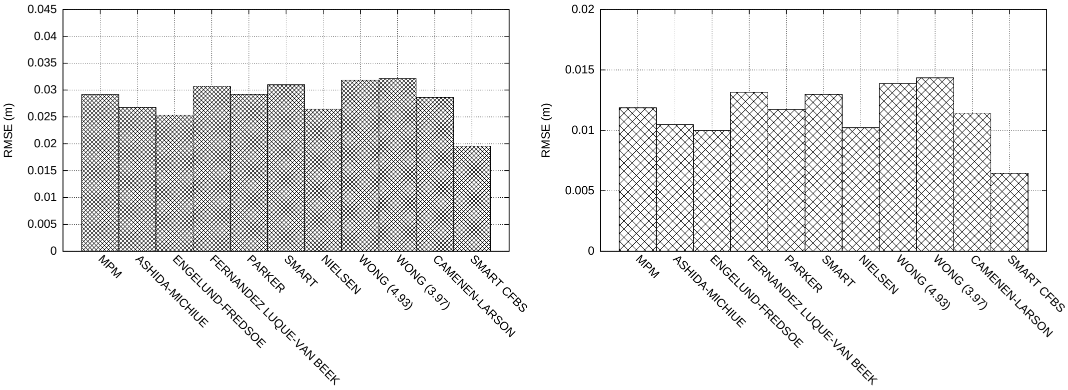

Figure 6.16: RMSE for water level surface (left) and bed level surface (right) with different formulas at $t = 1.5$ s in test F

6.2.6 1D Numerical modeling of dam failure

Dam surface erosion and slope sliding failure in time due to flow overtopping was studied in Tingsanchali and Chinnarasri (2001). Figure (6.17) shows a sketch of the experimental setup. Experiments were carried out in a rectangular flume 35 m long, 1.0 m deep, and 1.0 m wide. The height and crest width of the dam were fixed at 0.80 m and 0.30 m. The upstream slope was fixed at 1V:3H, while the downstream slopes set to 1:5. The dam was made of sand with the following characteristics: $\rho_p = 2650 kgm^{-3}$, $d_{30} = 0.52mm$, $d_{50} = 0.86mm$, $d_{90} = 3.80mm$ and $d_m = 1.13mm$. A friction angle of $\varphi = 30^o$ was suggested, and the porosity was estimated by using the formula described in Wu and Wang (2007):

$$p = 0.013 + \frac{0.21}{(d_{50}1000 + 0.002)^{0.21}} \tag{6.1}$$

and the Manning roughness coefficient by the Strickler formula:

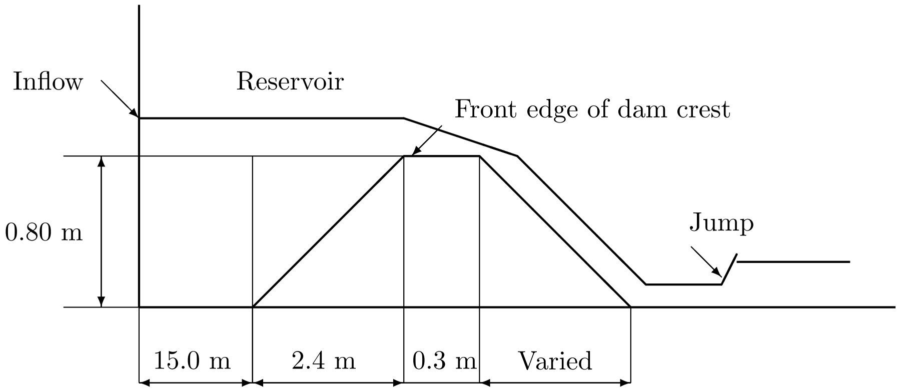

Figure 6.17: Sketch of the dam failure experimental setup

$$n = \frac{1}{26} d_{90}^{1/6} \tag{6.2}$$

To have a uniform overflowing across the flume width, in the experiment reproduced in this work a vertical plate was held at the dam crest across the flume width until the upstream water level was 3 cm higher than the dam crest. The vertical plate was lifted up suddenly to allow the overflow to start.

In the dam breaching experiment three zones can be distinguished. The first is a subcritical region in the reservoir area, characterized by a very low velocity. The second zone is a supercritical region of highly unsteady flow over a steep bed slope in the downhill slope of the dam, starting at the front edge of the dam crest. The third zone, downstream of the dam is characterized by the presence of a hydraulic jump. The dam erosion model was computed in all cases using cells $\Delta x = 0.05$ m and CFL = 1.

During the development of this experiment bed level was recorded in time at three stations: SA, SB and SC, located respectively 15, 65 and 115 cm downstream from the edge of the original dam crest. The overtopping discharge was also caught along time, as well as, the reservoir level, just upstream the breach. The results presented below compare these experimental data with the computed ones, in order to validate the accuracy of the numerical method.

In Figure 6.18 (a) and (b) the numerical results for water level and bed level using MPM and Smart CFBS, respectively, are plotted. Figure 6.18 (c) and (d) show measured and computed bed level surface in time evolution at stations SA, SB and SC using MPM and Smart CFBS respectively. While MPM clearly underestimates the erosion rate, Smart CFBS provides results in good agreement with experimental data. Experimental and computed values of reservoir free surface level are displayed in Figure 6.19 (a) and

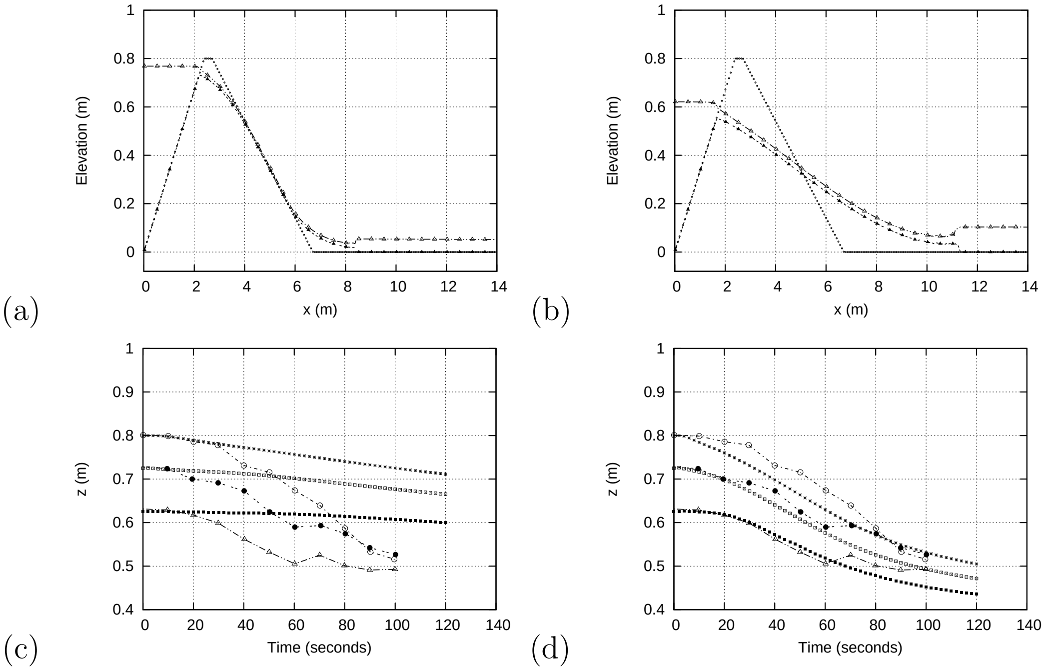

Figure 6.18: Initial bed level (- - -), computed water level surface (−△−) and bed level surface (−▲−) at $t = 120$ s using (a) MPM and (b) Smart CFBS. Bed level surface evolution in time measured at stations SA (− ○ −) (−□−),SB (− ● −), and SC (−△−) and computed at stations SA (− ⋆ −),SB (−□−), and SC (−■−) using (c) MPM and (d) Smart CFBS

(b) using MPM and Smart CFBS respectively. Better accuracy is reached when using the new proposed formulation.

Figure 6.20 (a) and (b) depicts the evolution in time of overtopping discharge using MPM and Smart CFBS respectively. It is observed that the maximum experimental overtopping discharge is reached by Smart CFBS while MPM predictions are quite far away from experimental data. Figure 6.20 shows the maximum overtopping discharge which is achieved with different formulas. The continuous line at the top of the image represents the maximum experimental overtopping discharge which is only well calculated with Smart CFBS formula.

Modulus of bed level error in time at stations SA, SB and SC with different formulas are shown in Figure 6.21 (a), (b) and (c), respectively. Smart CFBS formulation is the one which introduces less error in computed values. RMSE for bed level with different formulas in time appears plotted in Figure 6.21 (d). Newly, Smart CFBS presents the best agreement with experimental data in the three stations.

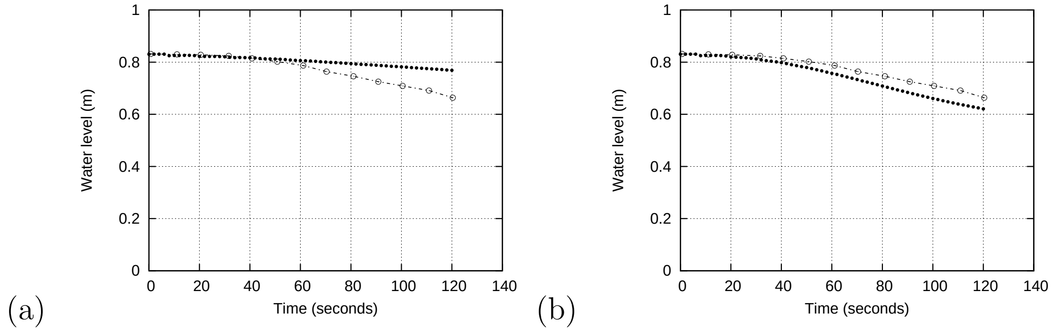

(a) (b)

Figure 6.19: Evolution in time of the measured water reservoir level (— ○ —) and computed water reservoir level (— ● —) using (e) MPM and (f) Smart CFBS

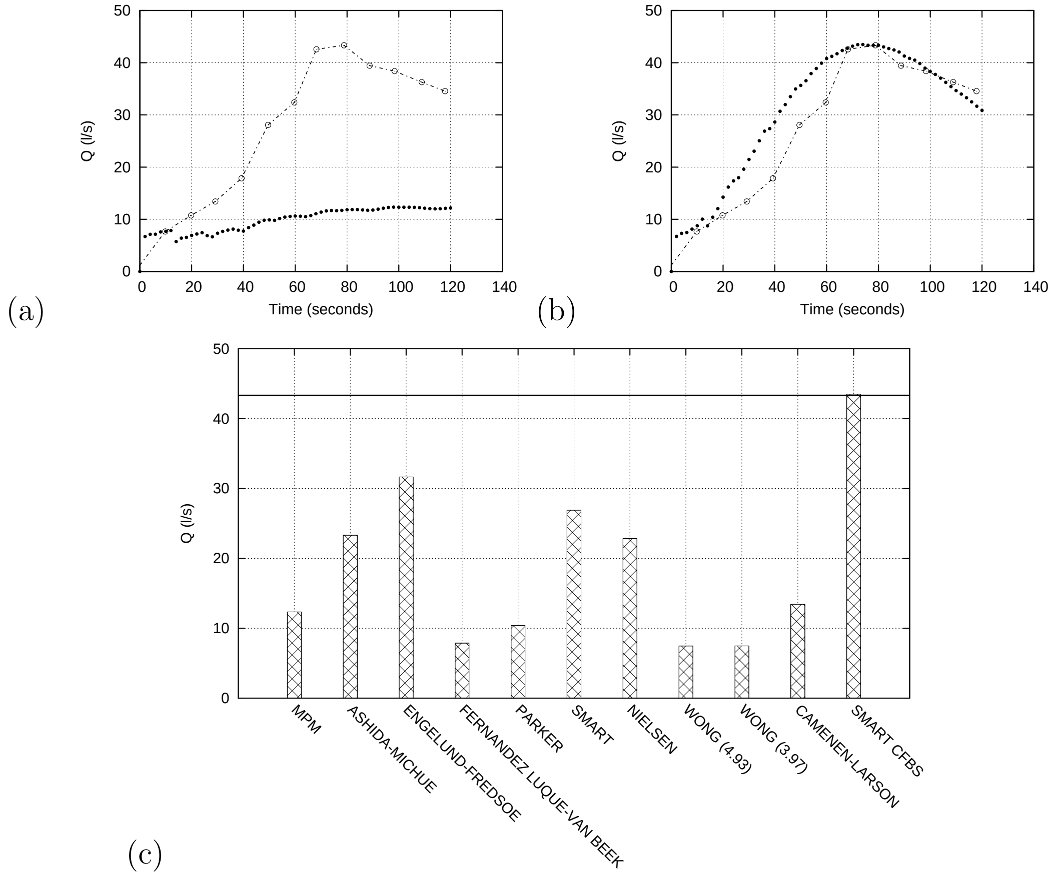

(a) (b) (c)

Figure 6.20: Evolution in time of the measured (— ○ —) and computed (— ● —) overtopping discharge using (a) MPM and (b) Smart CFBS. Maximum overtopping discharge with different formulas (c)

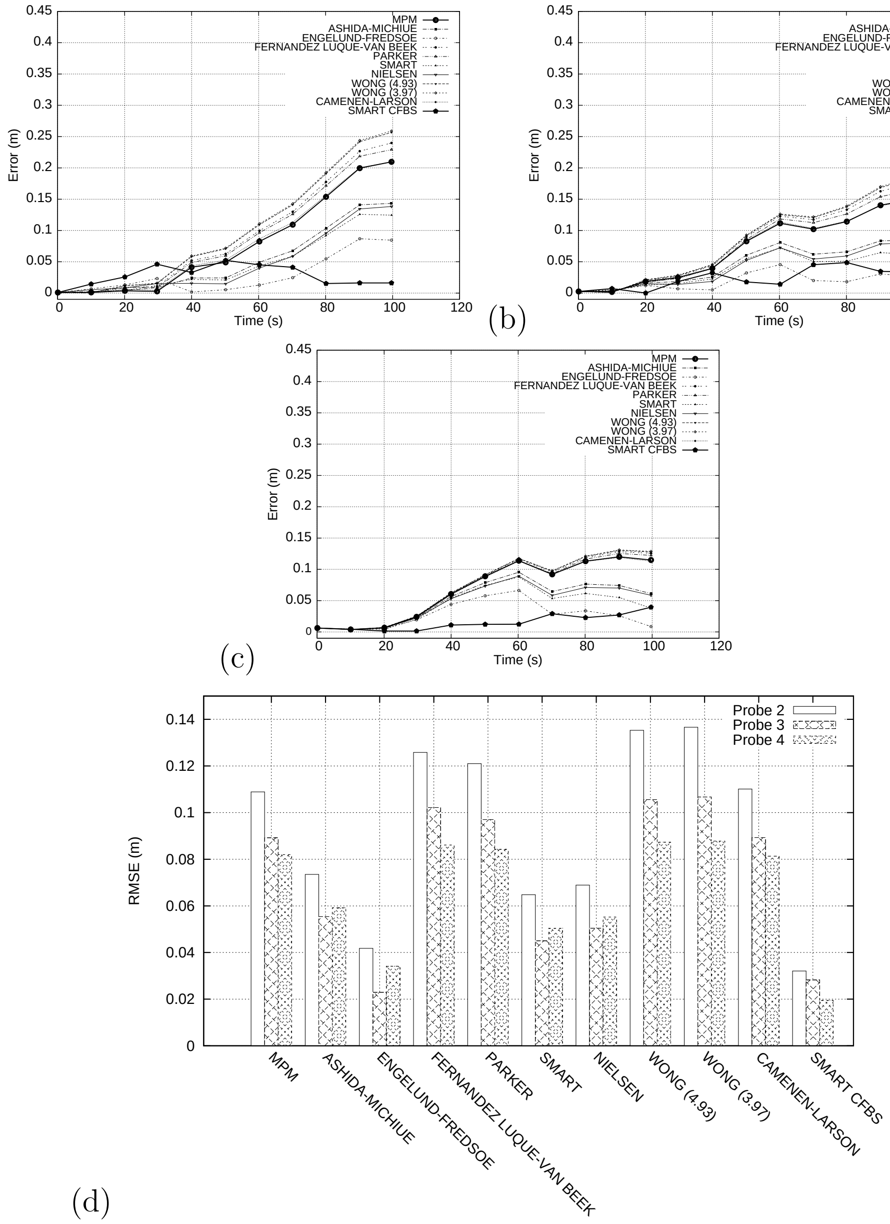

(a) (b) (c) (d)

Figure 6.21: Modulus of bed level error in time at (a) station SA, (b) station SB and (c) station SC with different formulas. RMSE for bed level z with different formulas in time (d)

6.2.7 Sand cube

The last experiment studied in this paper is a test where the flow has a subcritical regime in opposition to previous tests. The experiment was made in a 15 m long channel, with a cross section of 0.5 x 0.5 m^2, at the Hydraulics Laboratory of the Civil Engineering School of the University of A Coruña (Spain) (Peña et al., 2008).

The bottom of the flume was characterized by uniform slope, 0.00052, and a sediment layer 4.5 cm height, was placed in the central part, between 4.5 and 9 m from its upstream end. A sketch can be appreciated in Figure 6.22. The sand employed had the following properties: $\rho_s = 2680 kgm^{-3}$, $d_{50} = 1mm$ (uniform size), $\varphi = 30^o$, negligible cohesion, porosity $p = 0.5$ and was characterized by a Manning roughness factor $n = 0.015$ sm$^{-1/3}$.

Initial conditions used were a water surface level downstream set to 0.115 m and a flow value enforced to be 21.8 l/s. Numerical simulations were performed using cells $\Delta x = 0.05$ m and CFL = 1.

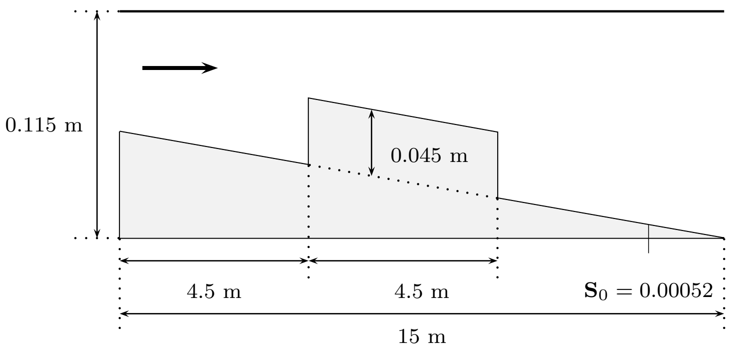

Figure 6.22: Sand cube sketch

Figure 6.23 shows experimental data and numerical results calculated using MPM (left) and Smart CFBS (right) at different times. The bed evolution in time is well described with Smart CFBS. In the first part of the simulation there is an important mobilization of material up to time $t = 40$ min, when the sediment bed tends to stabilize. Most relevant differences between numerical and experimental data appear downstream the cube. This difference is more noticeable at time $t = 120$ min and is attributable to the fact that in the sediment transport model suspended load is not considered. A careful data analysis of the measured bed level reveals that at this time, the initial mass associated to the cube is not conserved, may be due to suspension effects. On the other hand, the numerical scheme used in this work is exactly mass conservative, so differences between numerical and experimental data downstream the cube are expectable. The results provided by MPM formula are unable to gather information correctly, leading to a poor bed level prediction as time increases.

Correct performance of Smart CFBS in comparison with the rest of sediment discharge formulae is well appreciated in Figure 6.24, where the modulus of bed level error in x

(left) and RMSE for bed level surface at time t = 120 min (right) are plotted. Smart CFBS presents the more accurate results.

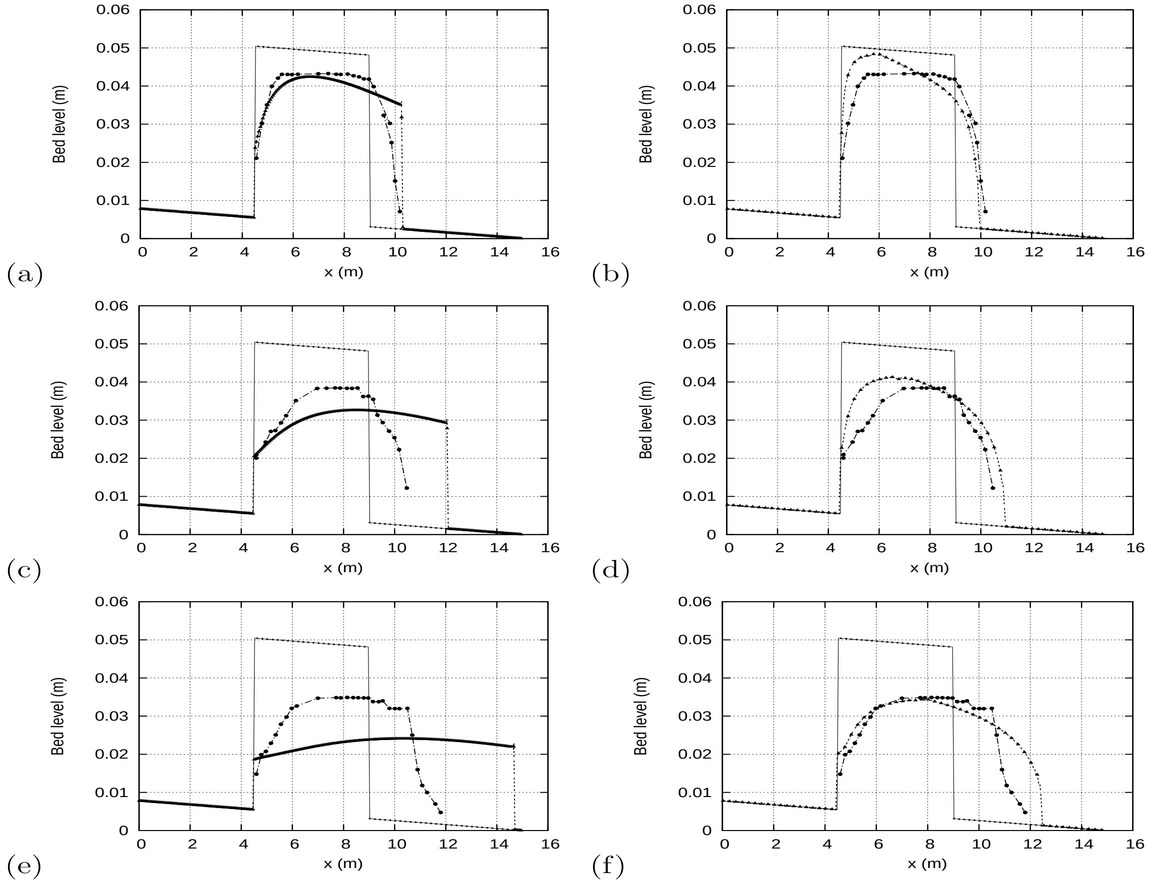

(a) (b) (c) (d) (e) (f)

Figure 6.23: Results for the sand cube test case. Initial bed level $(\cdots)$, measured bed and water level $(- \bullet -)$ and computed $(-\triangle-)$ using MPM at times (a) t = 10 min, (c) t = 40 min, (e) t = 120 min, and using Smart CFBS at times (b) t = 10 min,(d) t = 40 min, (f) t = 120 min

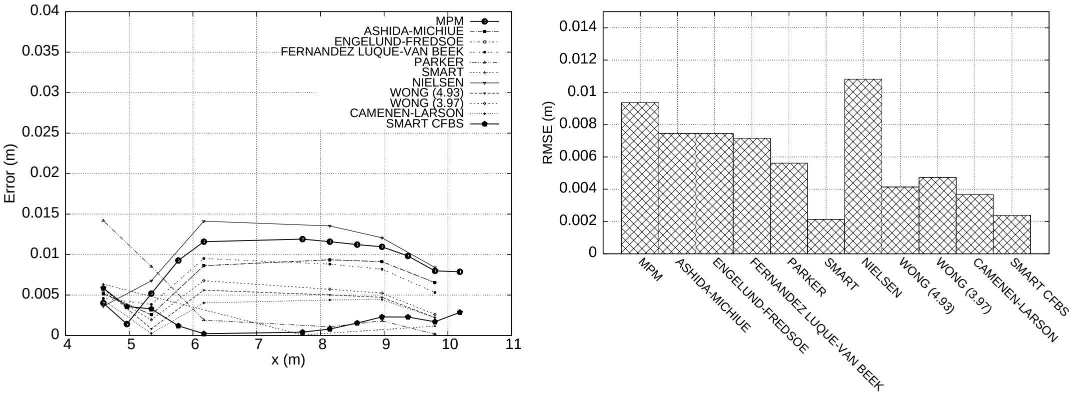

Figure 6.24: Results for the sand cube test case. Modulus of the bed level error in x for the different formulations after 120 min (left) and RMSE for bed level surface with different formulae at 120 min (right)

6.3 Two dimensional cases

6.3.1 2D Numerical modeling of dam failure

The test case studied above, in section 6.2.6, is reproduced in a 2D mesh. Being the flow mostly onedimensional in this case, it is important to check the performance of the numerical discretization of the empirical formulations in a 2D mesh to ensure that numerical results are not influenced by the grid definition. This case is of great interest, as it allows a direct comparison between 1D and 2D simulations in a wide variety of flow conditions.

2D numerical simulations have been performed using a coarse unstructured triangular mesh, with a maximum cell size of 0.01m^2, Figure 6.25. The CFL is retained equal to 0.5. Figure 6.26 displays the numerical results obtained using Smart CFBS formulation for both the water level and the bed level. During the first seconds the erosion rate reduces drastically the height of the crest and downstream the dam a hydraulic jump appears. At the final stage of the simulation, a large wedge has been developed. Also, the presence of incipient antidunes is observed.

Figures 6.27 (a) and (b) show the water and bed level surface computed after 120s using MPM and Smart CFBS formulations respectively. The bed level evolution recorded in time at the three stations SA, SB and SC, located downstream from the edge of the original dam crest, are plotted in Figures 6.27 (c) and (d). The evolution of the measured and computed water reservoir level is depicted in Figures 6.27 (e) and (f). In all cases the Smart CFBS formulation presents accurate results, while the MPM formulation shows noticeable discrepancies with respect to the experimental data.

Figures 6.28 (a) and (b) display the measured and computed overtopping discharge just upstream the breach using MPM and Smart CFBS formulations respectively. It

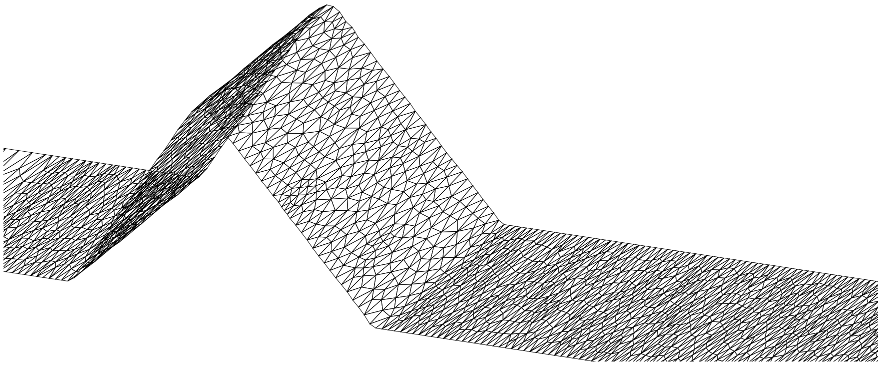

Figure 6.25: Detail of the triangular mesh

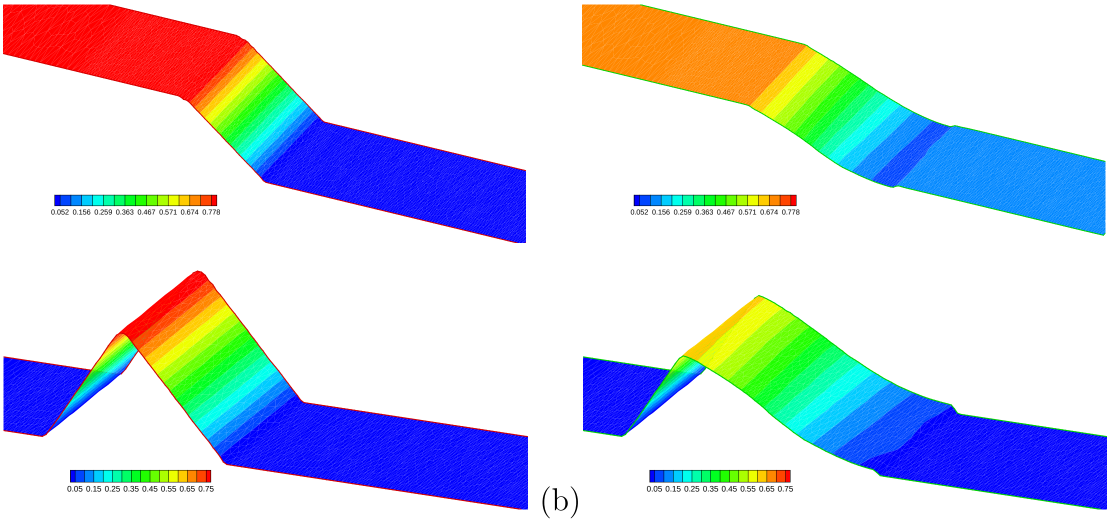

(a) (b)

Figure 6.26: Numerical results of water level (top image) and bed level (bottom level) in the dike at 0s (a) and 120s (b) using Smart CFBS formulation.

is observed that the experimental overtopping discharge is better tracked with Smart CFBS while MPM predictions are quite far from experimental data.

The relative performance of the different formulations in terms of RMSE is plotted in Figure 6.29 at the three stations SA, SB and SC, showing important differences among numerical results depending of the experimental law selected. The Engelund and Fredsoe sediment transport relation was derived for a wide range of slopes, and Figure 6.29 shows how this formulation leads to low values of RMSE. The Smart formula was derived for a set of experimental cases with steep slopes, therefore it can be expected that in this case any numerical discretization would provide accurate predictions. Contrarily, numerical simulation shows that the Smart FS discretization leads to less accurate results if compared with those given by the Smart CFBS discretization. The rest of formulations, derived from experiments ranging from low to medium slopes provide higher RMSE.

When comparing the numerical results of the 2D simulation with those obtained of a

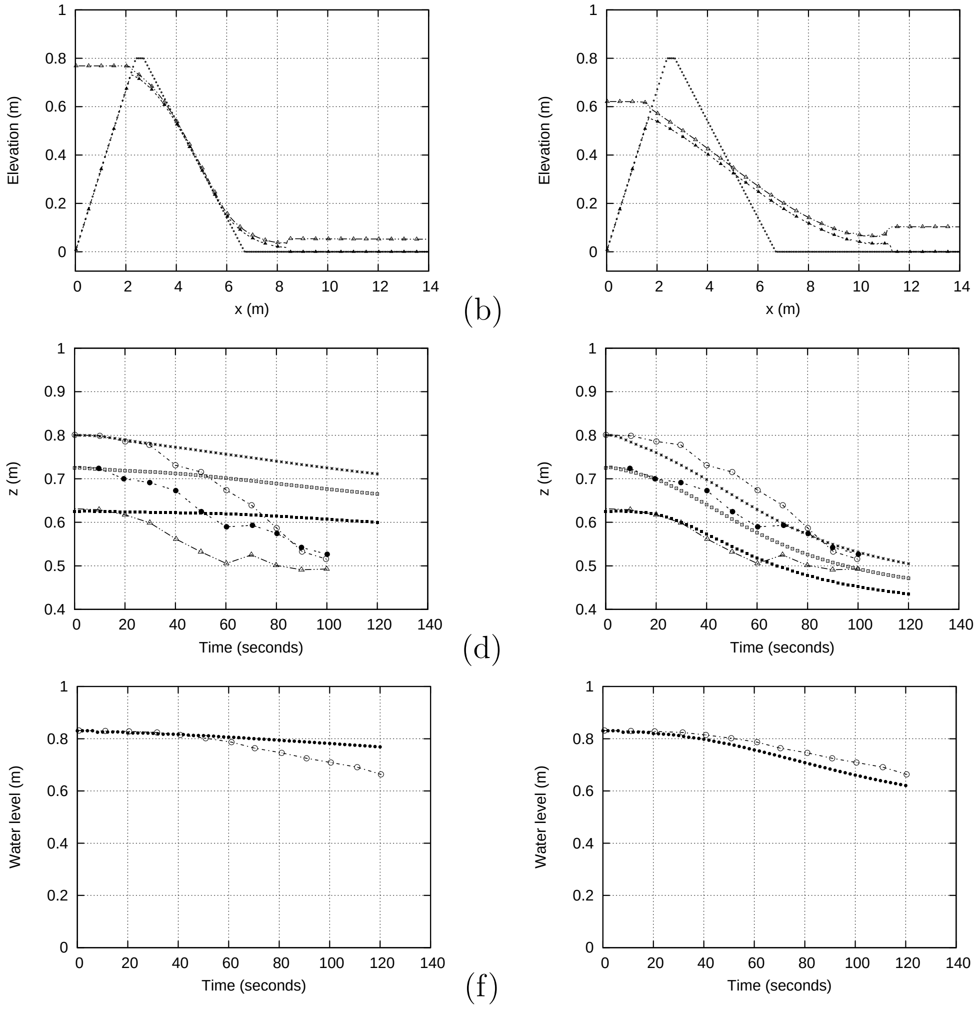

(a) (b) (c) (d) (e) (f)

Figure 6.27: Initial bed level (- - -), computed water level surface (−△−) and bed level surface (−▲−) at $t = 120$ s using (a) MPM and (b) Smart CFBS. Bed level surface evolution in time measured at stations SA (− ○ −) (−□−),SB (− ● −), and SC (−△−) and computed at stations SA (− ⋆ −),SB (−□−), and SC (−■−) using (c) MPM and (d) Smart CFBS. Evolution in time of the measured water reservoir level (− ○ −) and computed water reservoir level (− ● −) using (e) MPM and (f) Smart CFBS.

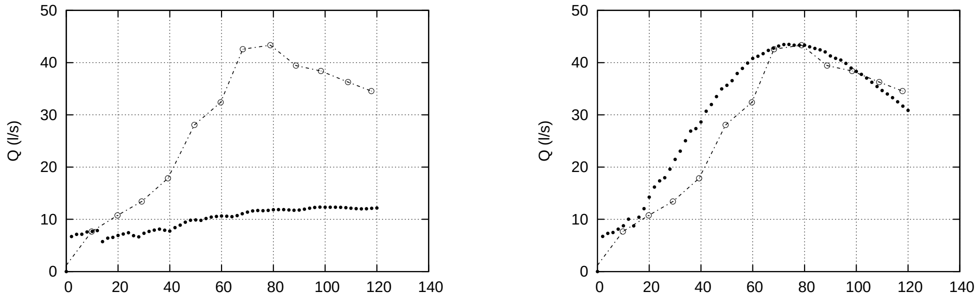

(a) (b)

Figure 6.28: Evolution in time of the measured (−○−) and computed (●−) overtopping discharge using (a) MPM and (b) Smart CFBS.

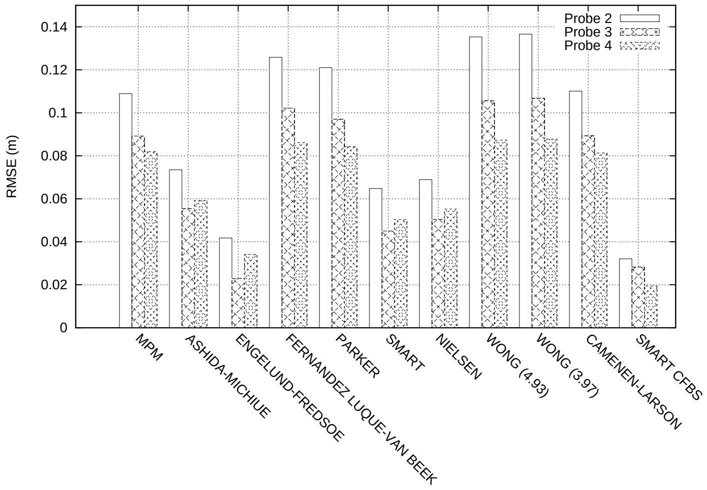

Figure 6.29: RMSE for bed level z at stations SA, SB and SC $(-\triangle-)$ with different formulas in time.

1D discretization, section 6.2.6, it can be observed that the RMSE is slightly bigger in the 2D cases and that 2D results follow closely the tendencies given by the 1D formulation.

6.3.2 Symmetric configuration for 2D dam break flow over erodible bed

This experiment was designed at the laboratory of UCL (Soares-Frazao et al., 2012) consisting of a dam break over a 3.6 m wide and about 36 m long flume. The gate was connected to an upstream reservoir and was 1 m wide. The sand was extended over 9 m downstream the gate and 1 m upstream the gate, having a thickness of 0.085 m. A complete sketch of the set up of the experiment is shown in Figure 6.30. The properties of the sand were ρ_s = 2630 kg m^{-3}, d_{50} = 1.61 mm, $\varphi = 30^o$, negligible cohesion, porosity $p = 0.40$ and was characterized by a Manning roughness factor n= 0.019 sm$^{-1/3}$. Initial conditions used were: upstream, the water level was imposed to 0.047 m, and downstream, a control section at the end of the flume with the same height as the sand layer, 0.085 m. The measurements carried out during the experiments consisted of recording the water level evolution for the first 20 s at different probes, Figure 6.31, and the longitudinal bed profiles measured from $x = 0.5$ m to $x = 8$ m at two y coordinates, Table 6.2, and at $t = 100$ s.

The domain was discretized on a non-uniform triangular mesh, with a higher density downstream the widening, being the total number of cells equal to 12500. The CFL used was imposed to 0.5.

Figures in 6.32 show a sequence of plant views of the computed bed evolution in time predicted by the Smart CFBS discretization, characterized by fast morphodynamic changes. Figure 6.32 (a) at $t = 10$ s shows how the flow generates a wavefront which

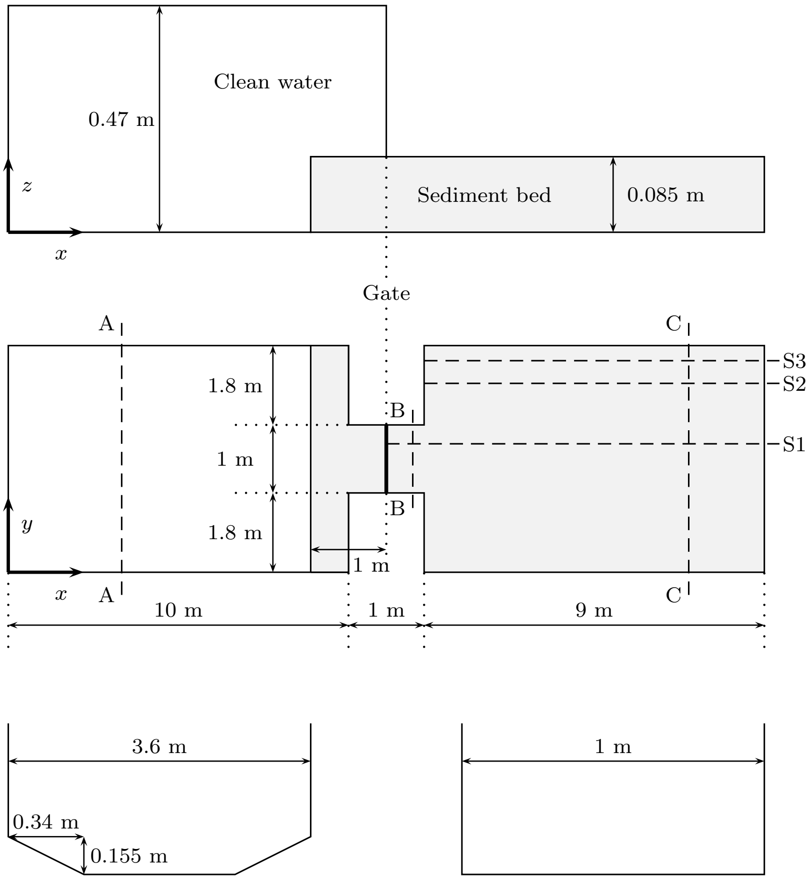

Figure 6.30: Experimental set up: transversal sketch, 2D sketch and cross sections (AA-CC and BB)

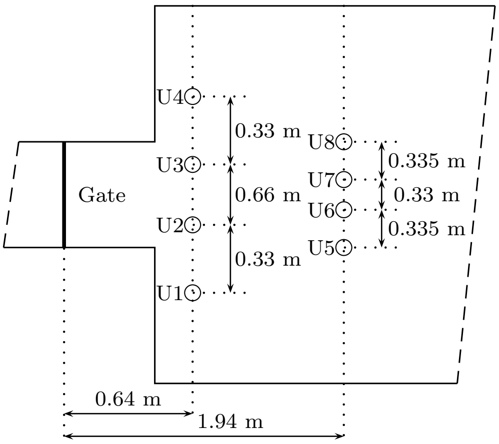

Figure 6.31: Position of probes in the experiment

Section	*Y coordinate (m)*
S1	0.20
S2	0.70

Table 6.2: Position of the sections

causes an important erosion process in the enlargement zone of the channel. While the flooding wave advances the sand particles grabbed in this process are carried out to the wavefront and to the wall, where they tend to sediment, as shown in Figure 6.32 (b) at $t = 20$s respectively. Symmetric elongated sedimentary bodies appear on the right and left banks of the channel, that grow in time to merge generating a diamond-shaped erosion region at $t = 40$s, shown in Figure 6.32 (c). At $t = 60$ s most of the morphodynamic changes have taken place, and the drainage of the water contained in the upstream reservoir smooths the bed surface, attenuating the bed forms previously generated. For longer times, no more important morphodynamic changes happen. At $t = 100$ s, Figure 6.32 (f) shows how only the diamond-shaped erosion region in the enlargement zone, generated by the sudden change in flow direction after the opening of the gate, remains in time. The rest of the bed surface becomes almost planar.

Figure 6.33 displays the final bed surface at $t = 100$ s obtained with the experimental data (left) and with the numerical results using Smart CFBS formula (right). Numerical results follow correctly the tendency of the final bed morphology although they tend to underestimate the length of the diamond-shaped body and the thickness of the eroded layer, resulting in smaller heights for the deposition forms. In the experimental data the length of the bed-form zones is bigger than the one provided by the numerical simulation. This may be explained, if considering that, due to the underestimation of erosion rates along the numerical simulation, the magnitude of the bed forms is smaller, and consequently, they are more easily eroded. Also, differences between numerical and experimental bed surfaces can be justified by two important points: i) the 2D SW model neglects the vertical accelerations and decreases the erosion/deposition rate and ii) errors associated to the reconstruction of the experimental bed surface, which was generated through the interpolation of measured bed profiles.

The results shown in, Figures 6.34, 6.35, display the experimental bed level against the computed one using the MPM and the Smart CFBS formulae at the two control sections. The first one, section S1, which is placed to study the effect of the flow over the bottom in the enlargement zone presents differences between both load discharge formulae. The Smart CFBS formula obtains a better tracking of the sedimentary process, getting more accurate results for the maximum erosion position, $x = 1.4$ m, and in the maximum deposition position, $x = 2.6$ m.

At the second control section, section S2, differences are also noticeable between both sediment transport formulae, being the Smart CFBS the formula which achieves a better averaged bed level. The computed results obtained with MPM show a zone at

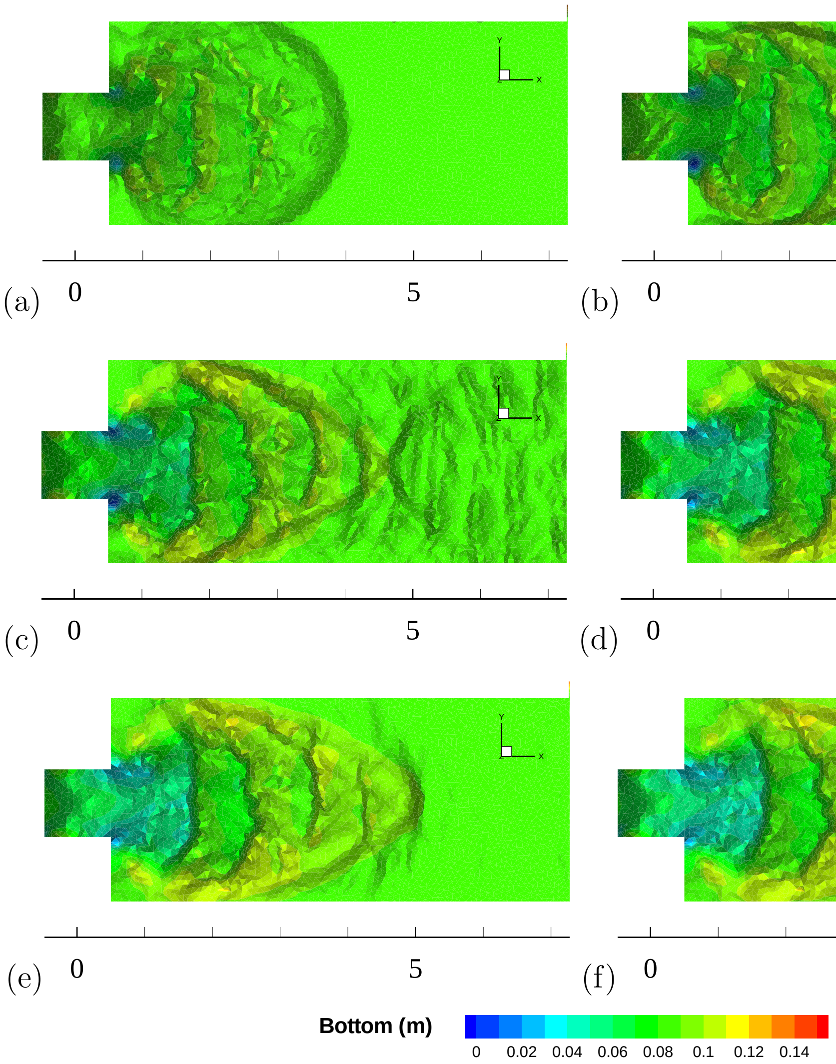

Figure 6.32: Numerical results of bed level in the enlargement zone at 10s (a), 20s (b), 40s (c), 60s (d), 80s (e) and 100s (f) using Smart CFBS formula

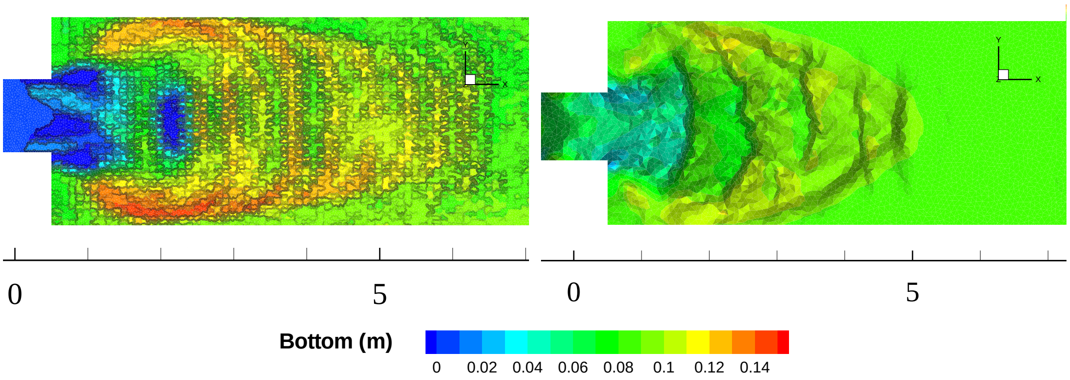

Figure 6.33: Experimental results (left) and numerical results using Smart CFBS formula (right) of bed level in the enlargement zone at 100s

$x = 1.2$ m where erosion is clearly overestimated.

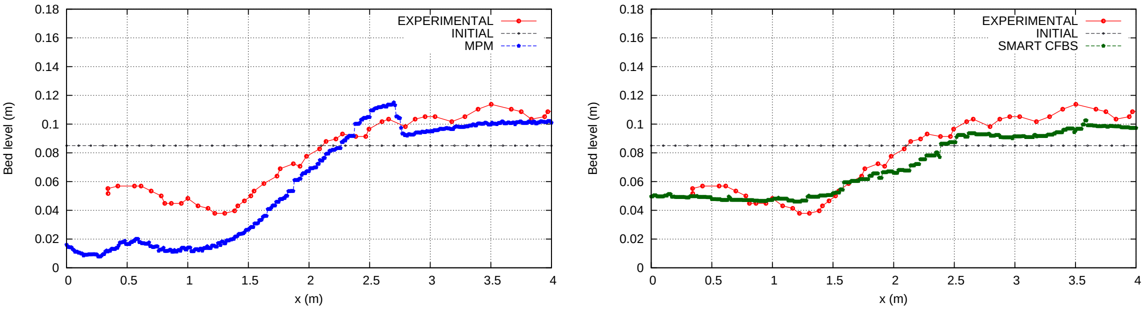

Figure 6.34: Numerical results of bed level with MPM (left) and Smart CFBS (right) against experimental data at section S1 ($y = 0.2$ m) and at $t = 100$ s

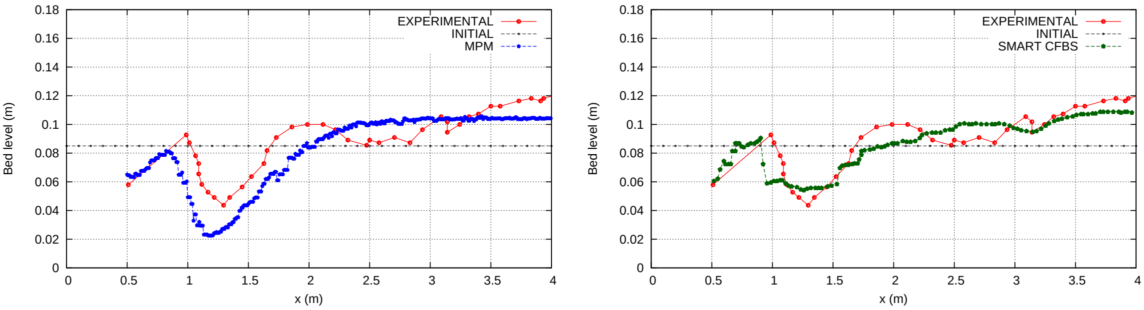

Figure 6.35: Numerical results of bed level with MPM (left) and Smart CFBS (right) against experimental data at section S2 ($y = 0.7$ m) and at $t = 100$ s

The RMSE of every section and every bed load discharge are shown in Figure 6.36. The results obtained with Smart CFBS are always among the ones which provide less error.

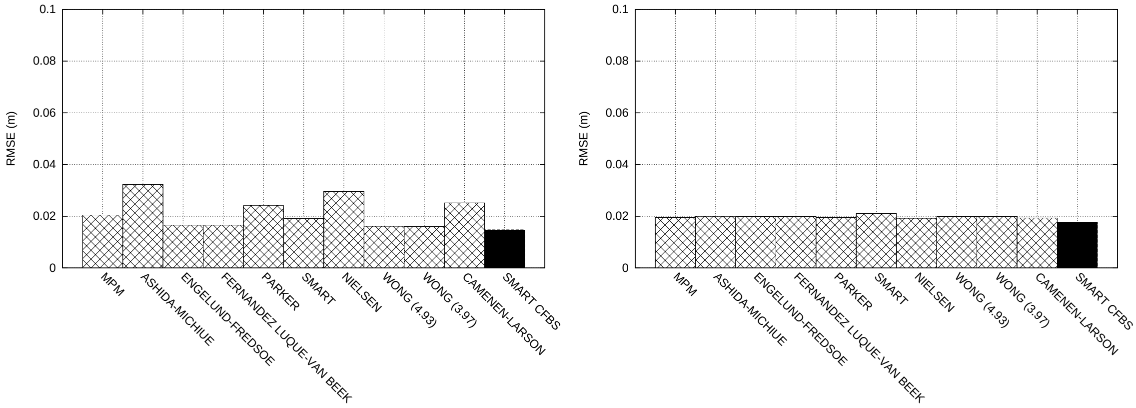

Figure 6.36: RMSE values corresponding to the two control sections, S1 (left) and S2 (right), and obtained with every sediment transport formula

In the case of the probes, the results are presented in Figures 6.37 and 6.38. The water level measured is compared with the results obtained using the MPM and Smart CFBS formulae. Both formulations provide similar values, except at probes U2 and U3 where the Smart CFBS formula shows a better tracking of the water level evolution in time. Probes which are further from the widening location obtain more accurate predictions and this is justified by the reduced influence of the erosion/deposition rates in those zones.

The RMSE value associated to every probe and to every bed load transport formula is displayed in Figures 6.39 and 6.40. The RMSE provided by probes which are close to the enlargement zone, U1, U2, U3 and U4, presents a bigger error, as it is has been argued previously. Smart CFBS formula is always between formulations with less associated error.

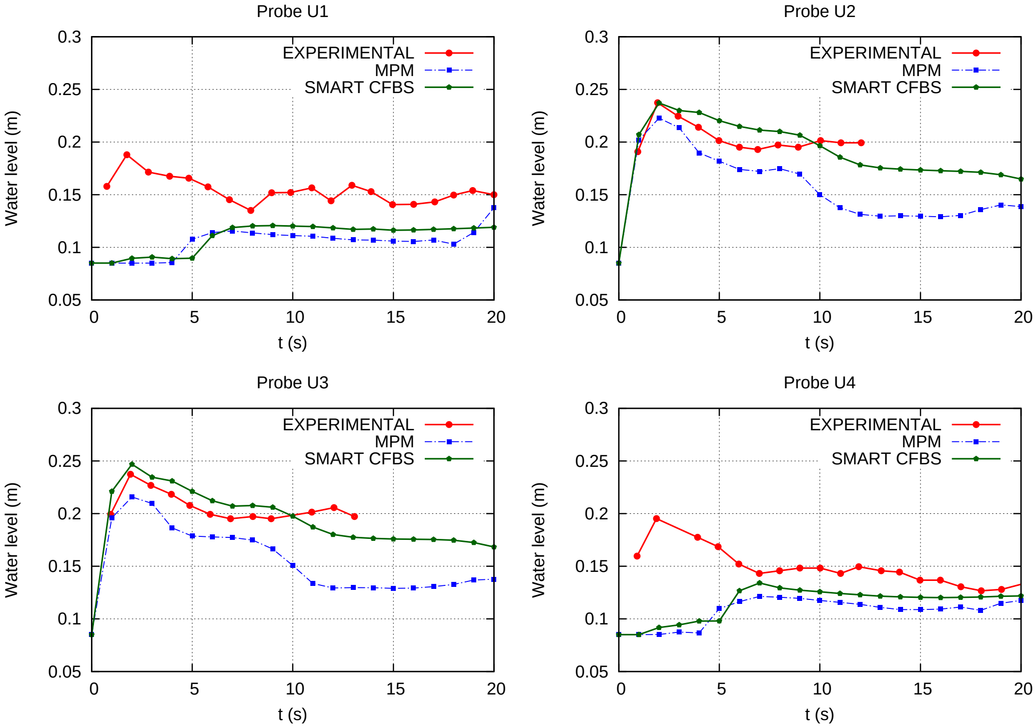

Figure 6.37: Probe U1 (x = 0.64 m, y = -0.99 m). Probe U2 (x = 0.64 m, y = -0.33 m). Probe U3 (x = 0.64 m, y = 0.33 m). Probe U4 (x = 0.64 m, y = 0.99 m). Comparison between experimental values and MPM and Smart CFBS water level at t = 20 s

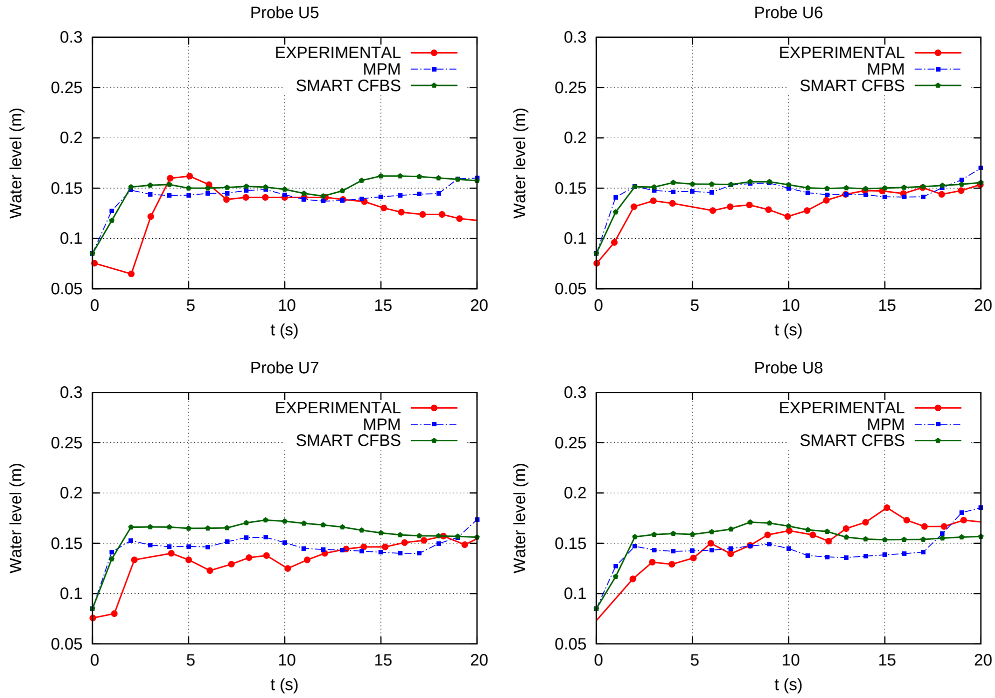

Figure 6.38: Probe U5 (x = 1.94 m, y = -0.5 m). Probe U6 (x = 1.94 m, y = -0.165 m). Probe U7 (x = 1.94 m, y = 0.165 m). Probe U8 (x = 1.94 m, y = 0.5 m). Comparison between experimental values and MPM and Smart CFBS water level at t = 20 s

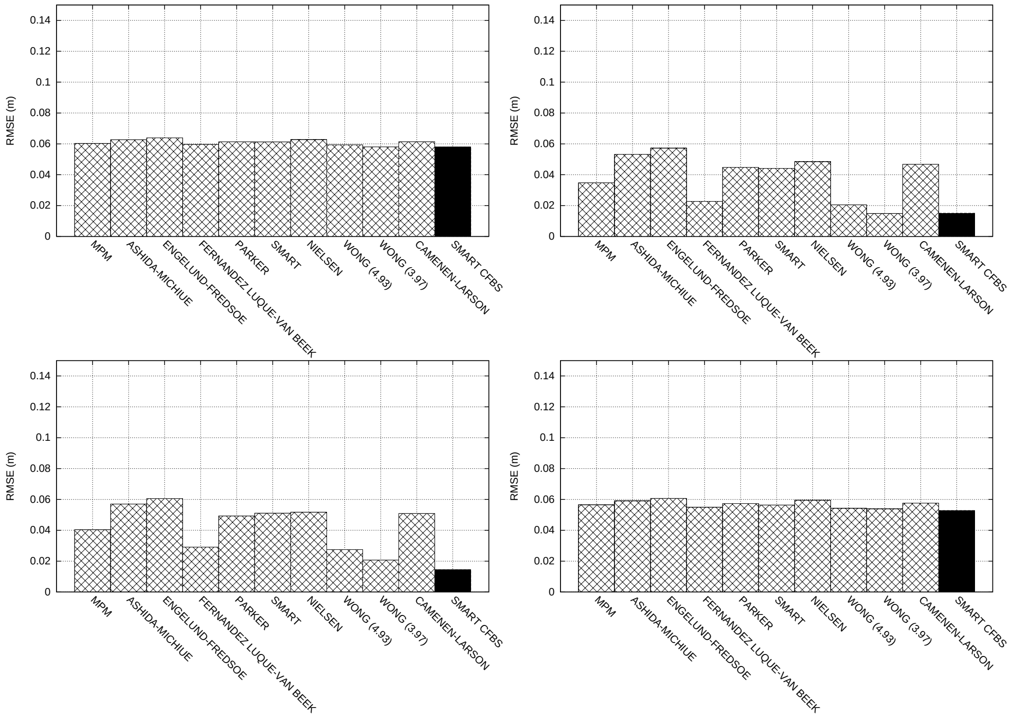

Figure 6.39: RMSE values corresponding to four probes (U1, U2, U3, U4, from left to right and from top to the bottom) and computed for every sediment transport formula

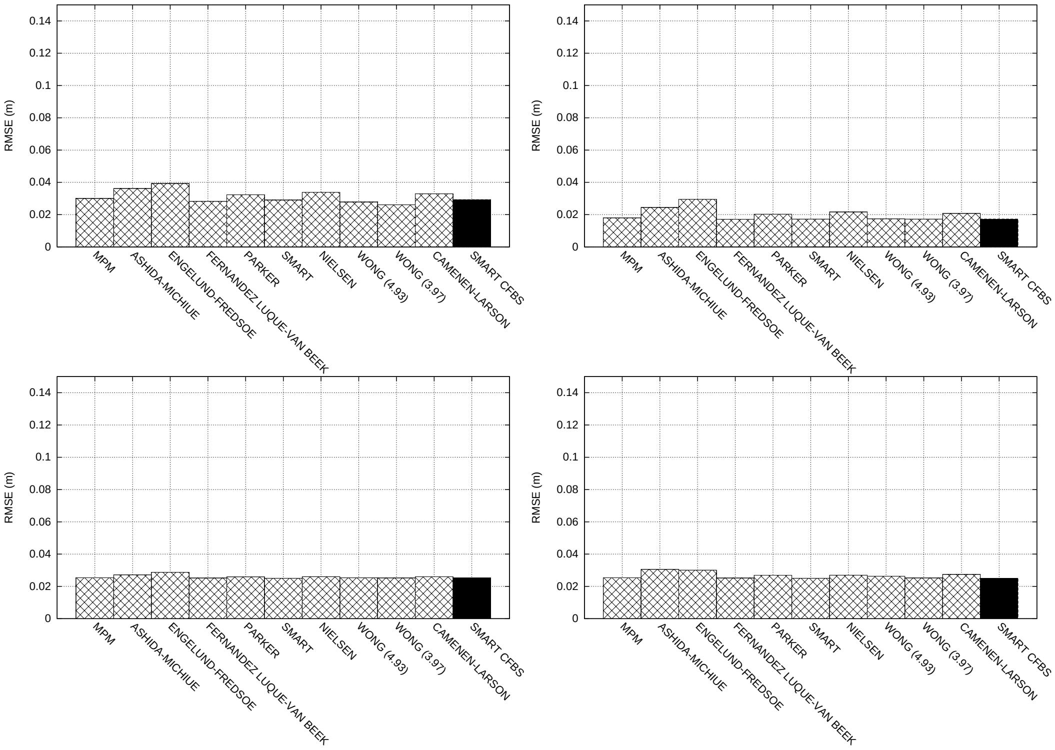

Figure 6.40: RMSE values corresponding to four probes (U5, U6, U7, U8, from left to right and from top to the bottom) and computed for every sediment transport formula

6.3.3 2D Dam break with a sudden enlargement

A dam break over a dry and erodible bed experiment was performed at the laboratory of the Civil and Environmental Engineering Department of the UCL (Palumbo et al., 2008; Goutière et al., 2011) and is numerically reproduced here. This experiment allows to test the ability of the different empirical formulations and discretizations in a 2D flow configuration proposed in this work.

The upstream reservoir was 3 m long and the total channel length was 6 m. The initial water depth upstream was set to 0.25 m whilst the sediment layer was 0.1 m deep over the flume. A change in width was imposed 1 m downstream of the end of the reservoir, ranging from 0.25 m to 0.5 m. A schematic sketch of the experimental set up is shown in Figure 6.41. The bed material was uniform sand with the following properties: median diameter $d_{50} = 1.65$ mm, density $\rho_s = 2630$ kg m^{-3}, friction angle $\varphi = 15^o$, negligible cohesion, porosity $p = 0.42$ and was characterized by a Manning roughness factor $n = 0.0185$. The water level evolution was measured at different points, whose location is indicated in Table 6.3. The bed level was also recorded at specific sections at the end of the experiment, displayed in Table 6.4. Once the gate is opened the flow remains 1D until it arrives to the enlargement zone, where the flow suffers a sudden change in its direction. The abrupt expansion generates a recirculating region and a strong erosion at that point. The sand is transported and deposited on the left side of the channel.

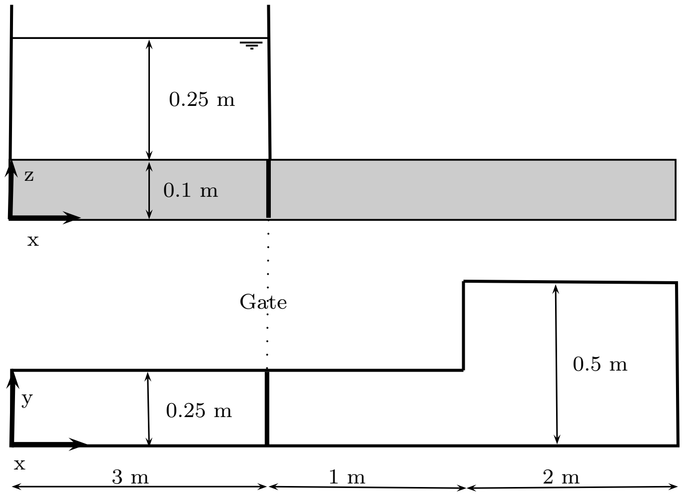

Figure 6.41: Sketch of the experimental flume

The domain is discretized using a non uniform triangular mesh of 4300 triangles, locally refined downstream the gate, as shown in Figure 6.42. The smallest cell area is approximately 0.001 m^2. The bed domain is considered deformable and a free flow boundary condition is imposed at domain exit.

Probe	*X coordinate (m)*	*Y coordinate (m)*
U1	3.75	0.125
U3	4.20	0.375
U6	4.95	0.125
U7	4.95	0.375

Table 6.3: Position of the probes

Probe	*X coordinate (m)*
S1	4.10
S3	4.20
S5	4.30
S7	4.40
S9	4.50

Table 6.4: Position of the sections

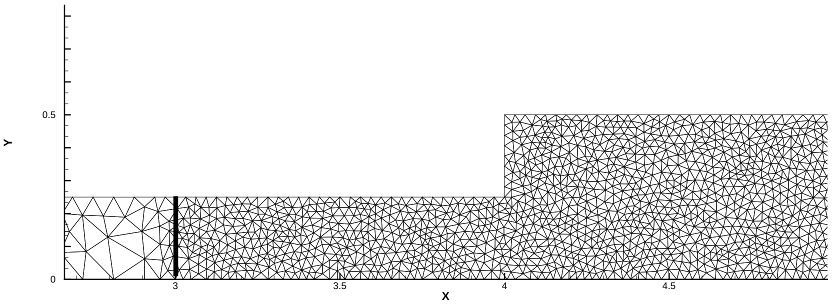

Figure 6.42: Part of the triangular mesh. The gate is remarked with a thick line at x = 3 m

Figure 6.43 displays several computed results at times 2s (a), 3s (b), 5s (c) and 20s (d) showing the bed level surface. Most of the morphodynamic change takes place during the first five seconds of the dam break, Figures 6.43 (a), (b) and (c). The erosion rate is of utmost importance at the corner of the enlargement zone, and is caused by the sudden change in flow velocity direction after the abrupt widening. A peak of material is formed at the left side of the channel. The sediment particles grabbed in this process are settled next to the right wall where the flow reduces its velocity. As a result of the bed deformation an elongated sedimentary body appears on the right bank. At time t = 20s, (d), the initial strong erosion in the corner zone has been partially filled with sediment particles transported from the upstream zone. The rest of the bed level surface does not change noticeably.

The experimental data and computational results for the water level surface obtained with every sediment transport formula for each probe are displayed in Figure 6.44.

Computed results at probe U1, which is placed within the channel, where the flow is mostly one dimensional, provided accurate results with respect the experimental data. Numerical simulations at probe U3, located closer to the enlargement zone, where erosion is of maximum importance, reproduce less accurately the measured water surface level if compared with the rest of probes. Numerical results for probes U6 and U7 located downstream the widening zone lead to accurate predictions of water level surface. Numerical predictions using MPM, Smart, Wong (3.97), Fernandez Luque and Van Beek and Smart CFBS obtain closer results to the experimental data. Smart formula provides less accurate results than the Smart CFBS one, although it achieves in tracking the general trend of temporal evolution.

The measured bed level after the dam break event and the numerical predictions at cross sections S1, S3, S5 and S7, S9 are plotted in Figures 6.45 (left) and 6.46 (left). The RMSE obtained with every sediment transport discharge formula at cross sections S1, S3, S5 and S7, S9 are plotted in Figures 6.45 (right) and 6.46 (right) respectively.

All sediment transport formulations are able to describe the deposition of material on the left bank and the erosion on the right bank. More noticeable differences appear among them for the predicted bed level at the right bank, where deposition processes take place.

On the left bank (y=0, looking upstream) of section S1, located close to the widening zone, all sediment transport formulations predict a bed profile that follows closely the pattern given by the experimental data. Smart CFBS, Wong (4.93) and Wong (3.97) formulae provide the most accurate bed elevations levels. Regarding the right bank (y=0.5), all formulations generate a less sharp slope than the one given by the experiments and Wong (4.93) and Wong (3.97) also obtained the most accurate results. Sections S3 and S5 show that the numerical results track correctly the bed level surface for both left and right banks, giving similar results and RMSE values. The Smart CFBS formula provides the least error. Section S7 shows that on the left bank the level of erosion is well captured with independence of the formulae. Noticeable differences among sediment discharge formulae appear in the stagnation flow region, located at the right wall, where Smart CFBS obtained a better prediction for the bed slope shape.

At Section S9, Figure 6.46, which is the cross section placed farthest from the enlargement location, numerical results present the lowest values of RMSE. The bed level on the left bank is newly well tracked by all the formulations but the key zone close to the right bank is only well predicted by Smart CFBS and Wong (4.93) and Wong (3.97).

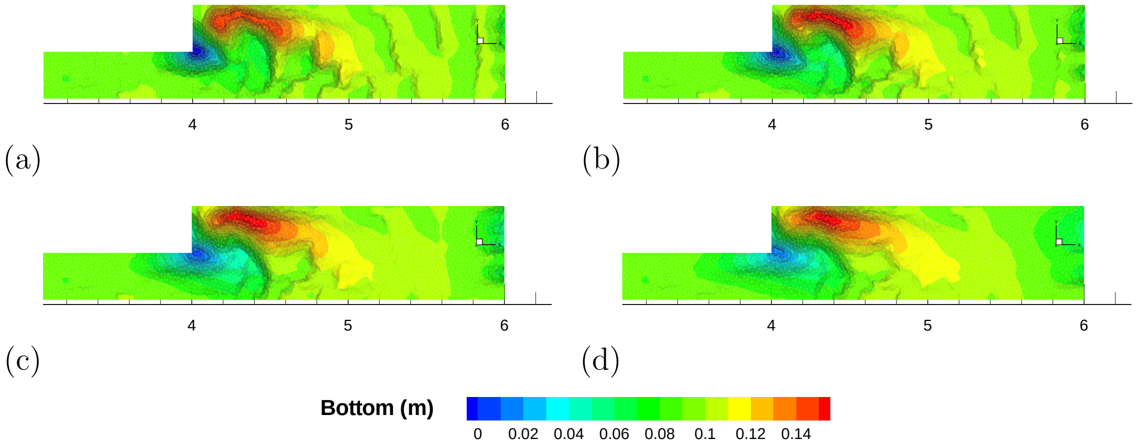

Figure 6.43: Numerical results of water level (top image) and bed level (bottom level) in the enlargement zone at 2s (a), 3s (b), 5s (c) and 20s (d)

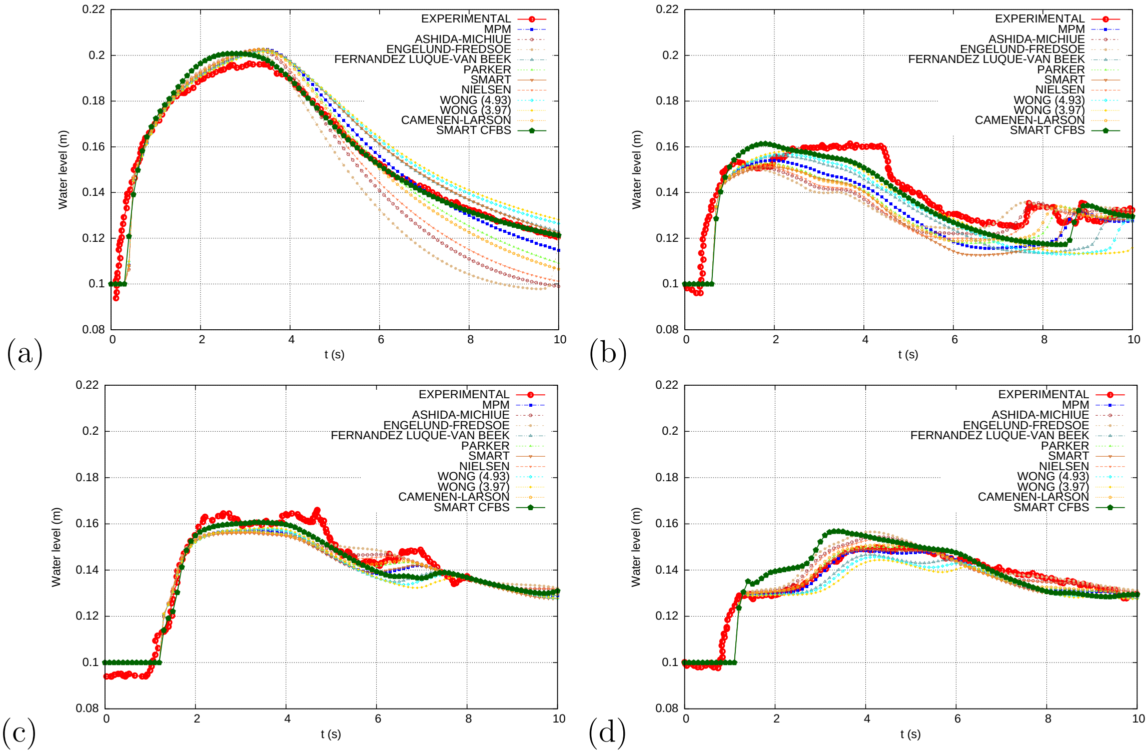

Figure 6.44: Numerical results and experimental data of water level for probes U1 (a), U3 (b), U6 (c), U7 (d)

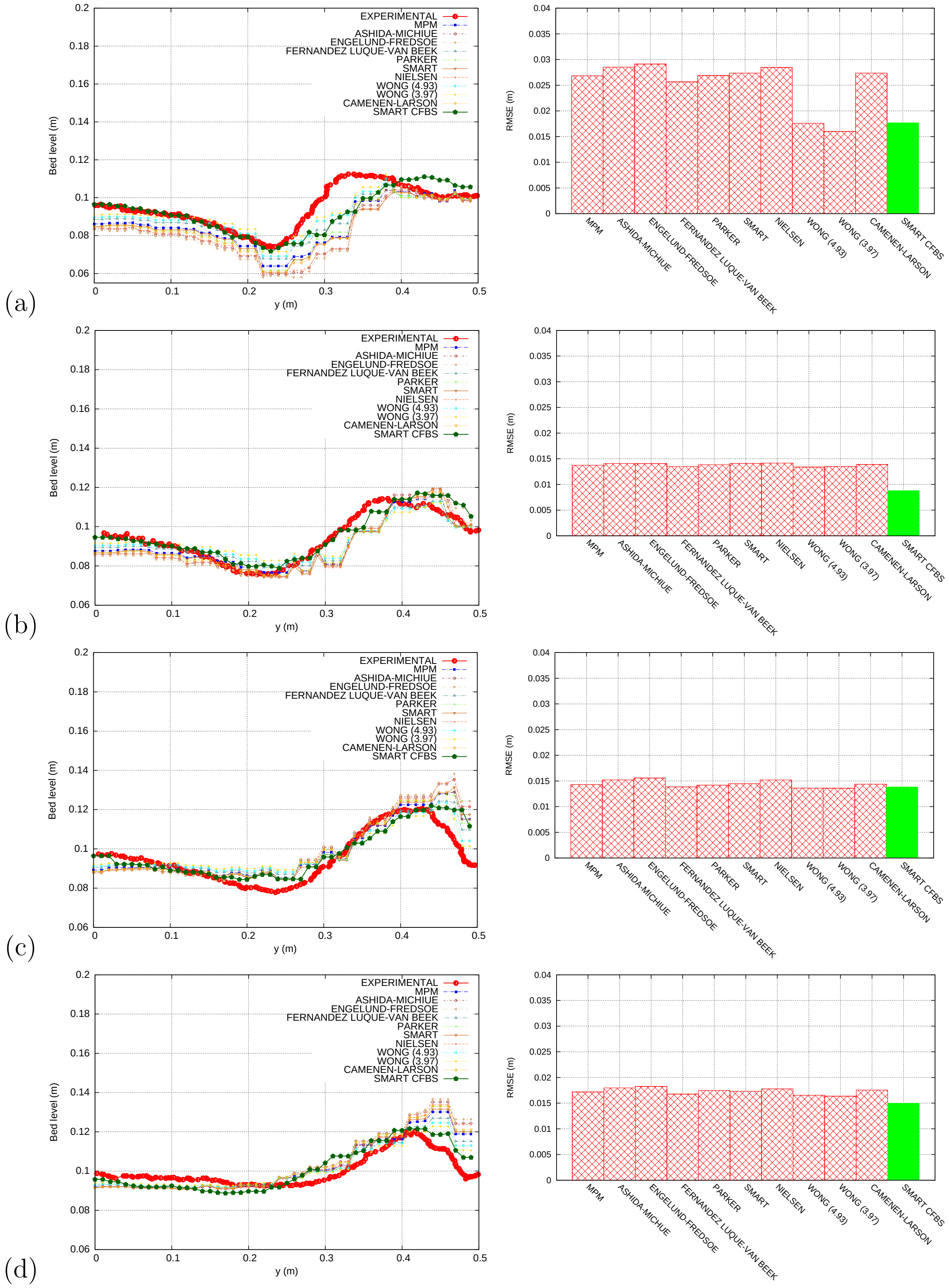

Figure 6.45: Numerical results and experimental data of bed level for sections S1 (a), S3 (b), S5 (c), S7 (d), and its corresponding RMSE obtained with every sediment transport formula

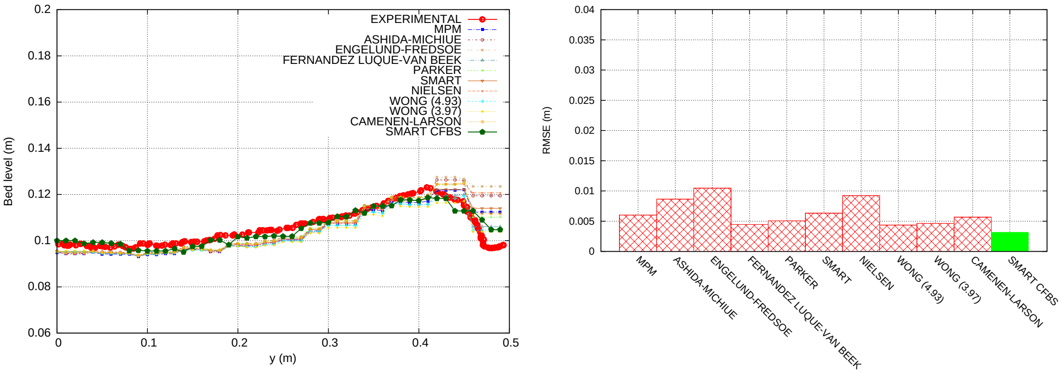

Figure 6.46: Numerical results and experimental data of bed level for section S9, and its corresponding RMSE obtained with every sediment transport formula

.

Chapter 7

CJ scheme: conclusions

Several well-known sediment discharge formulae have been studied and included in a general form in a coupled-Jacobian model for the shallow water equations and the Exner equation. Additionally, the Smart formula, that includes the bed slope, has been formulated in both in 1D, 2D configurations and extended to distinguish among different situations. In special, the possibility to evaluate situations where the flow encounters an adverse slope, and consequently has a less erosion capacity as well as other situations where the flow reaches a favorable slope and has a bigger erosion rate has been included. This discretization has been called Smart CFBS (Combined Friction and Bed Slope).

1D test cases

In the first set of test cases, the bed load formulae have been applied to solve dam break flows over dry/wet initial conditions. Whilst advance front celerity has been well captured in the dam break cases over dry bed with independence of the type of capacity formula used, noticeable differences appear in the bed level predictions, except in the dam break test case A with initially flat bed level and in the case B with adverse slope. In experiment D, over favorable slope and dry bed, erosion produces a meaningful variation of the initial bed step, leading to a rate of erosion and deposition only well captured in time and space if using Smart CFBS formula. In test case F, where both sides are initially filled with water, and a favorable slope is present, only Smart CFBS formula leads to a correct erosion evolution in time, that becomes negligible in the final stage of the experiment. From this set of test cases it can be concluded that Smart CFBS formula can be recommended for dam break test cases with null, adverse and favorable slopes, and wet/dry problems.

When numerically modeling dam erosion and failure it has been found that Smart CFBS formula is applicable in all cases analyzed in this study. Also, Engelund and Fredsoe capacity formula provides correct results in bed level predictions, although Smart CFBS formula estimates much better the maximum discharge values reached in all experiments. It is also worth mentioning that, for downstream steep slopes, the computational time associated to the peak discharge value is calculated earlier.

The computed sand cube test showed that the best agreement between experimental and numerical data are obtained with Smart (computing slope as friction slope) and Smart CFBS. This can be explained considering that, in this case, unsteady hydrodynamic effects are a quasi-steady process of slowly varying bed-load, and friction slope is adapted to bed slope.

2D test cases

For the first experiment, the dike failure by overtopping, characterized by a one-dimensional flow, it was clearly stated that the Smart CFBS formulation provides the most accurate results in time and in space.

In the second experiment, a symmetric dam break over a mobile bed in a channel with an enlargement zone was numerically reproduced. In this case a two-dimensional flow is generated and differences among different sediment formulations are less noticeable. Numerical results follow the tendency of the final bed morphology, underestimating the length of the diamond-shaped body and the thickness of the eroded layer. In the third experiment, where an erodible channel with a sudden enlargement produces a two-dimensional flow, the computational results provided good agreement with experimental values for the different sediment formulae.

Comparing with previous results from other authors (Spinewine and Zech, 2004; Abderrezzak and Paquier, 2011; Wu and Wang, 2007, 2008) it can be stated that the numerical scheme used in this work allows to clarify the differences among different formulations which were derived by 1D stationary laboratory experiments.

The Smart CFBS discretization reaches the more accurate results in all cases, although in a genuinely 2D flow, that is, a situation involving more than one flow direction, the differences between sediment transport formulae are not as noticeable as in the 1D situations. The results and conclusions of this part of the document have been published in Juez et al. (2013b).

7.1 Further research

Numerical experimentation is necessary to include non-equilibrium state formulation in the mathematical model. Hence, it is necessary to develop the one layer model derived of mass conservation equations, section 3, including a non uniform density along the longitudinal profile. Several authors have suggested to include the difference between the actual transported material and the equilibrium sediment transport capacity by means of the definition of an adaptation length.

The inclusion of the suspended transport coupled with the bed load model developed here is other natural follow-up of this work. For this phenomenon, both mathematical and numerical model are still to be studied. Another important feature that should be addressed is the numerical assessment of the the bed load sediment transport discharge formulae under a bed composed of a non-uniform sand particles. The interaction between grains of different diameter requires an additional effort.

The study of the mathematical and numerical properties of more complex friction laws for the definition of the shear stress at the bottom is also necessary. This feature is oriented to the definition of a hyperconcentrated model, where the rheology of the flow presents a pseudo plastic behavior due to high values of depth averaged concentrations.

Chapter 8

Weakly-coupled numerical scheme

8.1 Introduction

The development of the novel numerical strategy proposed for coupling the hydrodynamic and the morphodynamic models is described in this Chapter. The weakly-coupled numerical scheme will be noted as WC from now on. The numerical scheme departs from the previous system of equations presented in the one layer model for the shallow water (3.41) and for the Exner model (8.8) which are written separately as follows:

Hydrodynamic model

Neglecting diffusion of momentum due to viscosity and turbulence, wind effects and the Coriolis term, the two-dimensional shallow water equations are formulated as,

$$\frac{\partial \mathbf{U}}{\partial t} + \frac{\partial \mathbf{F}(\mathbf{U})}{\partial x} + \frac{\partial \mathbf{G}(\mathbf{U})}{\partial y} = \mathbf{S}\left(\mathbf{U}, x, y\right) \tag{8.1}$$

where

$$\mathbf{U} = \left(h,\ q_x,\ q_y\right)^T \tag{8.2}$$

are the conserved variables with h representing the water depth, $q_x = hu$ and $q_y = hv$, with (u, v) the depth averaged components of the velocity vector $\mathbf{u}$ along the (x, y) coordinates respectively. The fluxes of these variables are given by:

$$\mathbf{F} = \left(q_x,\ \frac{q_y^2}{h} + \frac{1}{2}gh^2,\ \frac{q_x q_y}{h}\right)^T, \qquad \mathbf{G} = \left(q_y,\ \frac{q_x q_y}{h},\ \frac{q_y^2}{h} + \frac{1}{2}gh^2\right)^T \tag{8.3}$$

where g is the acceleration of the gravity. The source terms of the system are

$$\mathbf{S} = \left(0,\ \frac{p_{b,x}}{\rho_w} - \frac{\tau_{b,x}}{\rho_w},\ \frac{p_{b,y}}{\rho_w} - \frac{\tau_{b,y}}{\rho_w}\right)^T \tag{8.4}$$

which express the x-component and y-component of: i) the pressure force along the bottom line, $p_{b,x}$ and $p_{b,y}$, being ρ_w the water density, that in differential form are expressed as a function of the bed slope, $\mathbf{S_o}$

$$\begin{array}{ll} \frac{p_{bx}}{\rho_w} = ghS_{o,x} & S_{o,x} = -\frac{\partial z}{\partial x} \\ \frac{p_{by}}{\rho_w} = ghS_{o,y} & S_{o,y} = -\frac{\partial z}{\partial y} \end{array} \tag{8.5}$$

and ii) the bed shear-stress, $\tau_{b,x}$ and $\tau_{b,y}$.

System (8.1) is time dependent, non-linear, and is non-homogeneous due to the presence of source-terms. The pure shallow water model is hyperbolic since the eigenvalues of its Jacobian matrices are always real. The presence of the source-terms leads to a non-strictly hyperbolic system. However, it is assumed that under the hypothesis of dominant advection it can be classified and numerically dealt with as belonging to the family of hyperbolic systems. Hence, the mathematical properties of (8.1) include the existence of a Jacobian matrix, $\mathbf{J_n}$, of the flux normal to a direction given by the unit vector, $\mathbf{n}$, $\mathbf{E_n} = \mathbf{F}n_x + \mathbf{G}n_y$, defined as

$$\mathbf{J_n} = \frac{\partial \mathbf{E_n}}{\partial \mathbf{U}} = \frac{\partial \mathbf{F}}{\partial \mathbf{U}} n_x + \frac{\partial \mathbf{G}}{\partial \mathbf{U}} n_y \tag{8.6}$$

whose components are

$$\mathbf{J}_n = \begin{pmatrix} 0 & n_x & n_y \\ (g_z h - u^2)n_x - uvn_y & vn_y + 2un_x & un_y \\ (g_z h - v^2)n_y - uvn_x & vn_x & un_x + 2vn_y \end{pmatrix} \tag{8.7}$$

The eigenvalues of this Jacobian matrix ($\lambda_1 = \mathbf{un} - c$, $\lambda_2 = \mathbf{un}$ and $\lambda_3 = \mathbf{un} + c$, with $c = \sqrt{gh}$) constitute the wave speeds in the linearized problem and provide information about directions in which the information travels.

Morphodynamic model

Sediment dynamics are assumed to be well modeled through the bed-load Exner equation,

$$\frac{\partial z}{\partial t} + \xi \frac{\partial q_{s,x}}{\partial x} + \xi \frac{\partial q_{s,y}}{\partial y} = 0 \tag{8.8}$$

where z is the bed elevation, $\xi = \frac{1}{1-p}$, p is the material porosity, $q_{s,x}$ and $q_{s,y}$ denote the solid transport discharge along the (x, y) coordinates respectively, influenced by the water depth h and the depth averaged velocities u and v.

The formulation of the bed load discharge, q_s, assumes an instantaneous adaptation of the flow transport capacity to the hydrodynamic conditions, and is based on Grass law as explained in Chapter 4. The constant A_g has been written by means of several empirical formulae as explained in Chapter 4.

Despite of the fact that the Exner equation is not actually hyperbolic, it is possible to write a wave speed estimation associated to the sediment flux as follows

$$\lambda_b = \xi \frac{\partial \mathbf{q_{sn}}}{\partial z} \tag{8.9}$$

The computation of this bed wave speed is not directly extracted from the characteristics theory. However, it constitutes the basis of the upwind strategy that is explained in the following sections. Its definition and participation in the stability of the method is of utmost importance as it was stated in a previous work, (Cordier et al., 2011).

8.2 Finite Volume Model

To introduce the finite volume scheme, system (8.1) and equation (8.8) are integrated in a grid cell Ω_i

$$\frac{\partial}{\partial t} \int_{\Omega} \mathbf{U} d\Omega + \int_{\Omega} (\overrightarrow{\nabla} \mathbf{E}) d\Omega = \int_{\Omega} \mathbf{S} d\Omega \tag{8.10}$$

$$\frac{\partial}{\partial t} \int_{\Omega} z d\Omega + \int_{\Omega} \xi (\overrightarrow{\nabla} \mathbf{q_s}) d\Omega = 0 \tag{8.11}$$

Using Gauss theorem (8.10) and (8.11) are written as

$$\frac{\partial}{\partial t} \int_{\Omega_i} \mathbf{U} d\Omega + \oint_{\partial\Omega_i} \mathbf{E_n} dl = \int_{\Omega_i} \mathbf{S} d\Omega \tag{8.12}$$

$$\frac{\partial}{\partial t} \int_{\Omega_i} z d\Omega + \oint_{\partial\Omega_i} \xi \mathbf{q_{sn}} dl = 0 \tag{8.13}$$

where vector $\mathbf{n}$ is outward to the cell Ω_i, as displayed in Figure 12.2. The second integral in (12.9) and (8.13) can be explicitly expressed as a sum over the cell edges,

$$\frac{\partial}{\partial t} \int_{\Omega_i} \mathbf{U} d\Omega + \sum_{k=1}^{NE} \int \mathbf{E_{n}}_k dl_k = \int_{\Omega} \mathbf{S} d\Omega_i \tag{8.14}$$

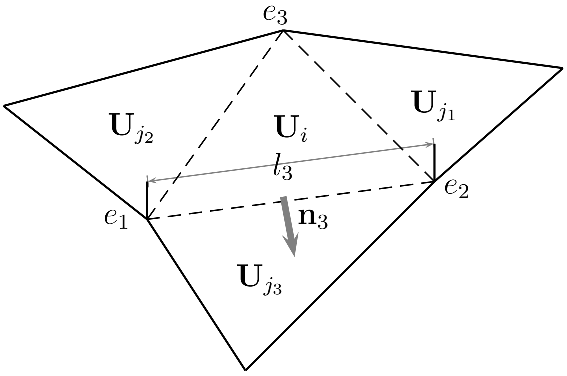

Figure 8.1: Cell parameters

$$\frac{\partial}{\partial t}\int_{\Omega_i} z d\Omega + \sum_{k=1}^{NE} \xi \int \mathbf{q}_{\mathbf{sn}k} dl_k = 0 \tag{8.15}$$

with $\mathbf{n}_k = (n_x, n_y)$ the outward unit normal vector to the cell edge k, dl_k is aligned in the direction of the edge and NE is the number of edges in cell i, as shown in Figure 12.2.

Assuming a first order in space approach, (12.10) and (8.15) become

$$\frac{\partial}{\partial t}\int_{\Omega_i} \mathbf{U} d\Omega + \sum_{k=1}^{NE} \mathbf{E}_{\mathbf{n}k} l_k = \int_{\Omega} \mathbf{S} d\Omega_i \tag{8.16}$$

$$\frac{\partial}{\partial t}\int_{\Omega_i} z d\Omega + \sum_{k=1}^{NE} \xi \mathbf{q}_{\mathbf{sn}k} l_k = 0 \tag{8.17}$$

Also, the volume integrals of the source terms are expressed in terms of appropriate contour integrals by projecting the source terms onto the normal direction $\mathbf{n}_k$ to each cell edge as follows

$$\int_{\Omega_i} \mathbf{S} d\Omega_i \approx \sum_{k=1}^{NE} \int_{x'} \left[\mathbf{S}_k dx'_k\right] l_k \tag{8.18}$$

being x' the coordinate normal to cell edge k, as shown in Figure B.1. Then, the initial system of equations in (8.1) is transformed in

$$\frac{\partial}{\partial t}\int_{\Omega_i} \mathbf{U} d\Omega + \sum_{k=1}^{NE} \left(\mathbf{E}_{\mathbf{n}} - \int_{x'} \mathbf{S}_k dx'\right)_k l_k = 0 \tag{8.19}$$

System (12.15) and equation (8.17) will be solved using approximate linear solutions of initial value problems according to the Godunov method, where $\mathbf{U}_i^n$ is the cell-average value of the solution $\mathbf{U}(x, y, t)$ for the ith cell at time t^n

$$\mathbf{U}_i^n = \frac{1}{A_i} \int_{\Omega_i} \mathbf{U}(x, y, t^n) d\Omega \tag{8.20}$$

being A_i the cell area. Assuming a piecewise representation of the variables within the cell drives to define an uniform value for each variable.

The development of the numerical scheme in the Godunov method can be completed by the definition of an approximate solver of the Riemann problem, hereafter RP, governed by the fluxes at each side of each edge, $\mathbf{E}_j$ and $\mathbf{E}_i$ for the hydrodynamic model and $\mathbf{q_s}_j$,$\mathbf{q_s}_i$ for the morphodynamic model. For the Roe's approximate solver this solution is given by an approximate Jacobian matrix constructed through the flux difference $(\delta\mathbf{E})_k = \mathbf{E}_j - \mathbf{E}_i$ and $(\delta\mathbf{q_s})_k = \mathbf{q_s}_j - \mathbf{q_s}_i$ (Roe, 1986).

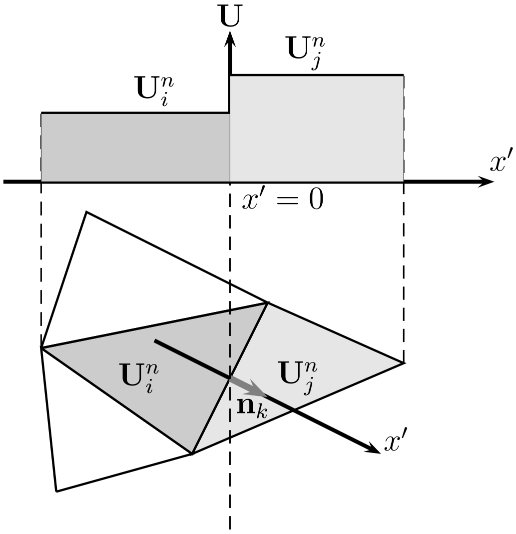

Figure 8.2: Riemann problem in 2D along the normal direction to a cell side

8.3 Approximate Riemann Solution for the Hydrodynamic model

The next step consists of defining a local 1D RP at each k edge, as shown in Figure B.1. This is done projecting the fluxes onto the normal direction $\mathbf{n}_k$ to each cell edge. Therefore in a k edge the following local RP, including bed slope and friction terms, along the x' direction (i.e. the coordinate normal to the cell edge) is defined

$$\frac{\partial \mathbf{U}}{\partial t}+\frac{\partial (\mathbf{E_n})}{\partial x'}-\mathbf{S}=0 \tag{8.21}$$

with the following initial conditions

$$\mathbf{U}(x',0)=\left\{\begin{array}{lll}\mathbf{U}_i & if & x'<0\\ \mathbf{U}_j & if & x'>0\end{array}\right. \tag{8.22}$$

The exact solution of the local RP provides the variation of $\mathbf{U}$ in time and space, $\mathbf{U}\left(x^{'},t\right)$, and additionally the exact value of the normal flux crossing the edge, $(\mathbf{E_n})_k$. Variation of $\mathbf{U}(x',t)$ can be obtained by integrating (8.21) over a suitable control volume such as the one shown in Figure 8.3. It is showed a local RP with initial values $\mathbf{U}_i$, $\mathbf{U}_j$, over the time interval $[0,\Delta t]$ and the space interval $[-\Delta x',\Delta x']$, where

$$-\Delta x'\leq \lambda_{min}\Delta t, \quad \Delta x'\geq \lambda_{max}\Delta t \tag{8.23}$$

Integrating (8.21) over the control volume $[0,\Delta t]\times[-\Delta x',\Delta x']$

$$\int_{x'=-\Delta x'}^{x'=\Delta x'}\int_{t=0}^{t=\Delta t}\left(\frac{\partial \mathbf{U}}{\partial t}+\frac{\partial \mathbf{E_n}}{\partial x'}-\mathbf{S}\right)\,dx'dt=0 \tag{8.24}$$

and reordering the following expression of integral volume for $\mathbf{U}(x',t)$ is obtained

$$\int_{-x'}^{+x'}\mathbf{U}(x',t=\Delta t)\;dx'=\Delta x'\left(\mathbf{U}_j+\mathbf{U}_i\right)-\delta(\mathbf{E_n})_k\Delta t+\int_{-x'}^{x'}\int_{0}^{\Delta t}\mathbf{S}\;dx'dt \tag{8.25}$$

The source term involved in the Riemann solver is linearized driving to consider a discontinuity at point $x'=0$, Figure 8.3. Assuming that source terms are not necessarily constant in time, the following time linearization of the nonconservative term is applied (Vázquez-Cendón, 1999; Murillo and García-Navarro, 2010b)

$$\int_{-\Delta x'}^{\Delta x'}\int_{0}^{\Delta t}\mathbf{S}\;dx'dt\approx\Delta t\int_{-\Delta x'}^{\Delta x'}\mathbf{S}(x',0)\;dx'=\Delta t\bar{\mathbf{S}}_k^n \tag{8.26}$$

where $\bar{\mathbf{S}}$ is a suitable numerical source vector (Murillo and García-Navarro, 2011, 2010b). Once all the terms of the volume integral in (8.25) are defined, the variation of the conserved variables is assumed to be given by

$$\int_{-\Delta x'}^{+\Delta x'}\mathbf{U}(x',t=\Delta t)\;dx'=\Delta x'\left(\mathbf{U}_i+\mathbf{U}_j\right)-\delta\mathbf{M}_k\Delta t \tag{8.27}$$

with

$$\delta \mathbf{M} = \delta \mathbf{E_n} - \bar{\mathbf{S}}_\mathbf{n} \tag{8.28}$$

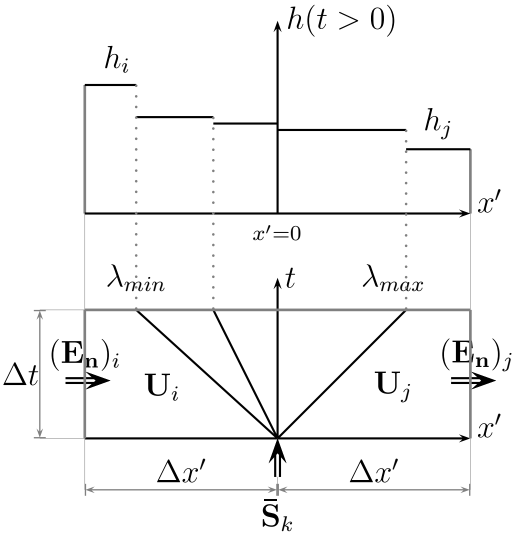

Figure 8.3: Integration control volume defined by a time interval $[0, \Delta t]$ and a space interval $[-\Delta x', \Delta x']$

Consistency condition for the Hydrodynamic Model

The exact solution of the local RP in (8.21) $\mathbf{U}(x', t)$ is not easily derivable and additionally, its computational cost is high enough for not using a exact solver. Therefore, a strategy for handling it can be based in a approximation through a constant coefficient linear problem,

$$\frac{\partial \hat{\mathbf{U}}}{\partial t} + \mathbf{L}_{\mathbf{n},k} \frac{\partial \hat{\mathbf{U}}}{\partial x'} = 0 \tag{8.29}$$

with the same initial conditions as the ones proposed in (8.22)

$$\hat{\mathbf{U}}(x', 0) = \begin{cases} \mathbf{U}_i & if \quad x' < 0 \\ \mathbf{U}_j & if \quad x' > 0 \end{cases} \tag{8.30}$$

This approximation will provide a set of linearized or weak solutions, that will be referred to as $\hat{\mathbf{U}}(x', t)$. In this case, the term $\hat{\mathbf{U}}(x', t)$ include the presence of a source term, as it appears in the original RP (8.21).

Thanks to the Consistency Condition (Toro, 2009) it must satisfied that the integral of the approximate solution $\hat{\mathbf{U}}(x',t)$ of the linearized RP over control volume $[0,\Delta t]\times[-\Delta x',\Delta x']$ must be equal to the integral of the exact solution $\mathbf{U}(x',t)$ given in (8.29)

$$\int_{-\Delta x'}^{\Delta x'} \hat{\mathbf{U}}(x',t=\Delta t)\;dx' = \int_{-\Delta x'}^{\Delta x'} \mathbf{U}(x',t=\Delta t)\;dx' \tag{8.31}$$

This fashion, making use of relationship from (12.27), it is possible to equalize the following terms

$$\int_{-\Delta x'}^{\Delta x'} \hat{\mathbf{U}}(x',t=\Delta t)\;dx' = \Delta x'\left(\mathbf{U}_i+\mathbf{U}_j\right) - \delta\mathbf{M}_k\Delta t \tag{8.32}$$

Bearing in mind (12.44), (8.29) is integrated over the control volume pictured in Figure 8.3

$$\int_{x'=-\Delta x'}^{x'=\Delta x'}\int_{t=0}^{t=\Delta t}\left(\frac{\partial\hat{\mathbf{U}}}{\partial t}+\mathbf{L}_{\mathbf{n},k}\frac{\partial\hat{\mathbf{U}}}{\partial x'}\right)\;dx'dt = 0 \tag{8.33}$$

and reordering, the following expression is obtained at each k edge

$$\int_{-\Delta x'}^{\Delta x'} \hat{\mathbf{U}}(x',t=\Delta t)\;dx' = \Delta x'\left(\mathbf{U}_i+\mathbf{U}_j\right) - \mathbf{L}_{\mathbf{n},k}\delta\mathbf{U}_k\Delta t \tag{8.34}$$

and since we want to satisfy (12.44), the constraint that follows is

$$\delta\mathbf{M}_k = \mathbf{L}_{\mathbf{n},k}\delta\mathbf{U}_k \tag{8.35}$$

The construction of the constant linear matrix $\mathbf{L}_{\mathbf{n},k}$ is based on the definition of an approximated Jacobian matrix of the non-linear flux $\mathbf{E}_{\mathbf{n}}$, $\widetilde{\mathbf{J}}_{\mathbf{n},k}$ (Roe, 1986)

$$\delta(\mathbf{E}_{\mathbf{n}})_k = \widetilde{\mathbf{J}}_{\mathbf{n},k}\delta\mathbf{U}_k \tag{8.36}$$

This approach provides a set of 3 real eigenvalues $\widetilde{\lambda}_k^m$ and 3 eigenvectors $\widetilde{\mathbf{e}}_k^m$. With them, it is possible to define matrix $\widetilde{\mathbf{P}}=(\widetilde{\mathbf{e}}^1,\widetilde{\mathbf{e}}^2,\widetilde{\mathbf{e}}^3)$ making use of the Roe's averages, Roe (1986). The approximate matrices $\widetilde{\mathbf{P}}$, and $\widetilde{\mathbf{P}}^{-1}$ diagonalize $\widetilde{\mathbf{J}}_k$

$$\widetilde{\mathbf{P}}_k^{-1}\widetilde{\mathbf{J}}_{\mathbf{n},k}\widetilde{\mathbf{P}}_k = \widetilde{\mathbf{\Lambda}}_k \tag{8.37}$$

with $\widetilde{\mathbf{\Lambda}}_k$ a diagonal matrix with eigenvalues $\widetilde{\lambda}_k^m$ in the main diagonal

$$\widetilde{\mathbf{\Lambda}}_k = \begin{pmatrix} \widetilde{\lambda}^1 & 0 & 0 \\ 0 & \widetilde{\lambda}^2 & 0 \\ 0 & 0 & \widetilde{\lambda}^3 \end{pmatrix}_k \tag{8.38}$$

Difference in vector $\mathbf{U}$ across the grid edge is projected onto the matrix eigenvectors basis

$$\delta\mathbf{U}_k = \widetilde{\mathbf{P}}_k\mathbf{A}_k \tag{8.39}$$

where $\mathbf{A}_k = (\begin{array}{ccc} \alpha^1 & \alpha^2 & \alpha^3 \end{array})_k^T$ contains the set of wave strengths.

Furthermore, for linking the source terms to the set of eigenvalues they are also projected onto the matrix eigenvectors basis

$$(\bar{\mathbf{S}}_\mathbf{n})_k = (\widetilde{\mathbf{P}}\mathbf{B})_k \tag{8.40}$$

with $\mathbf{B}_k = (\beta^1, \beta^2, \beta^3)_k^T$. Using (12.28), (12.48) and (12.56) matrix $\delta\mathbf{M}_k$ can be expressed as

$$\delta\mathbf{M}_k = \widetilde{\mathbf{J}}_{\mathbf{n},k}\delta\mathbf{U}_k - \widetilde{\mathbf{P}}_k(\mathbf{B})_k = \sum_{m=1}^{3}\left(\widetilde{\lambda}\,\theta\alpha\widetilde{\mathbf{e}}\right)_k^m \tag{8.41}$$

with

$$\theta_k^m = \left(1 - \frac{\beta}{\widetilde{\lambda}\alpha}\right)_k^m \tag{8.42}$$

or in matrix form

$$\delta\mathbf{M}_k = (\widetilde{\mathbf{P}}\widetilde{\mathbf{\Lambda}}\mathbf{\Theta}\widetilde{\mathbf{P}}^{-1})_k\delta\mathbf{U}_k \tag{8.43}$$

Therefore the value for the desired matrix $\mathbf{L}_{\mathbf{n},k}$ in (12.47) is

$$\mathbf{L}_{\mathbf{n},k} = (\widetilde{\mathbf{P}}\widetilde{\mathbf{\Lambda}}\mathbf{\Theta}\widetilde{\mathbf{P}}^{-1})_k \tag{8.44}$$

where $\mathbf{\Theta}$ is a diagonal matrix

$$\mathbf{\Theta}_k = \begin{pmatrix} \theta^1 & 0 & 0 \\ 0 & \theta^2 & 0 \\ 0 & 0 & \theta^3 \end{pmatrix}_k \tag{8.45}$$

that relates fluxes and source terms and that becomes equal to the identity matrix in absence of source terms.

2D first order finite volume for the Hydrodynamic Model

Definition of matrix $\mathbf{L}_{\mathbf{n},k}$ allows to define directly right-going and left-going wave propagations. This way the flux $\delta\mathbf{M}_k$ is written in splitting way as follows

$$\delta\mathbf{M}_k = \delta\mathbf{M}^-_{i,k} + \delta\mathbf{M}^+_{j,k} \tag{8.46}$$

with

$$\delta\mathbf{M}^-_{i,k} = (\widetilde{\mathbf{P}}\widetilde{\mathbf{\Lambda}}^-\mathbf{\Theta}\widetilde{\mathbf{P}}^{-1})_k\delta\mathbf{U}_k \qquad \delta\mathbf{M}^+_{j,k} = (\widetilde{\mathbf{P}}\widetilde{\mathbf{\Lambda}}^+\mathbf{\Theta}\widetilde{\mathbf{P}}^{-1})_k\delta\mathbf{U}_k \tag{8.47}$$

the flux splitting version of the Godunov first order method is

$$\mathbf{U}_i^{n+1} = \mathbf{U}_i^n - \sum_{k=1}^{NE}\delta\mathbf{M}^-_{i,k}\frac{\Delta t\ l_k}{A_i} \tag{8.48}$$

Superindex $^-$ becomes necessary to distinguish from outcoming fluxes to cell i at edge k, that will be referred to as $\delta\mathbf{M}^+_{j,k}$, as they update the adjacent j cell sharing the k edge.

8.4 Approximate Riemann Solution for the Morphodynamic model

Coming back to the equation which governs the sediment dynamics (8.8), the same steps followed with system (8.1) can be applied. A local 1D RP is obtained projecting the sediment fluxes onto the normal direction $\mathbf{n}_k$ of each k edge of each cell

$$\frac{\partial z}{\partial t} + \xi\frac{\partial(\mathbf{q}_{\mathbf{sn}})}{\partial x'} = 0 \tag{8.49}$$

Using the integral form of (8.49) the weak solutions of the RP can be found. For this purpose a suitable control volume, Figure 8.4, is integrated over the following time interval $[0, \Delta t]$ and the space interval $[-\Delta x', \Delta x']$, with x' sufficiently large,

$$\int_{-\Delta x'}^{+\Delta x'} z(x', t = \Delta t)\ dx' = \Delta x'\,(z_i + z_j) - \xi\delta\mathbf{q}_{\mathbf{sn}}\Delta t \tag{8.50}$$

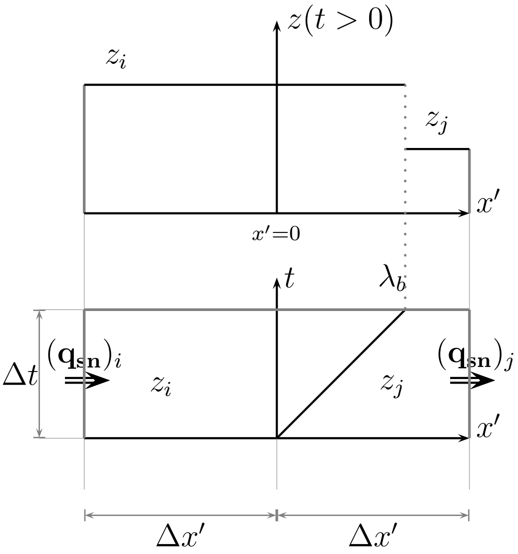

Figure 8.4: Integration control volume defined by a time interval $[0, \Delta t]$ and a space interval $[-\Delta x', \Delta x']$

Again, the piecewise representation of the variables is hypothesized and the first order Godunov method is used for updating the averaged quantities.

Consistency condition for the Morphodynamic Model

Following the philosophy employed for the hydrodynamic model a Roe approach is going to be used, i.e., the solution of each RP is obtained from the exact solution of a locally linearized problem defined by an approximate solution $\hat{z}(x,t)$. This constant linear problem is based on the definition of an approximate wave speed of the non-linear sediment flux, $\mathbf{q_{sn}}$. This following equivalent equation is written

$$\frac{\partial \hat{z}}{\partial t} + \widetilde{\lambda}_{\mathbf{bn},k} \frac{\partial \hat{z}}{\partial x'} = 0 \tag{8.51}$$

with the following initial conditions

$$\hat{z}(x',0) = \left\{ \begin{array}{lll} z_i & if & x' < 0 \\ z_j & if & x' > 0 \end{array} \right. \tag{8.52}$$

The approximate solution must fulfill the Consistency Condition (Leveque, 2002), forcing the integral of the exact solution (8.49) and the integral of the locally linearized solution, (8.51) to be the same. Thanks to this constraint it is possible to obtain the following expression for the wave speed which updates the bed level,

$$\widetilde{\lambda}_{\mathbf{bn},k} = \frac{\delta(\xi \mathbf{q}_{\mathbf{sn},k})}{\delta z} \tag{8.53}$$

with $\delta z = z_j - z_i$ and $\delta \mathbf{q}_{\mathbf{sn},k} = \mathbf{q}_{\mathbf{sn},j} - \mathbf{q}_{\mathbf{sn},i}$. Regarding equation (4.2) it is necessary to compute the Grass coefficient for defining the bed load discharge in each cell. Following Murillo and García-Navarro (2010a) as the coefficient A_g is not a constant but varies from cell to cell, at every edge k a local $A_{g,k}$ value is defined as an arithmetic mean between neighboring cells. Consequently, the term $\delta \mathbf{q}_{\mathbf{sn},k}$ is written as $\delta \mathbf{q}_{\mathbf{sn},k} = A_{g,k} \delta \mathbf{un}_k$.

Additionally, when applying numerical modeling techniques under a flat bottom situation, the bed level difference is null and consequently the bed wave speed is not defined. In order to overcome this difficulty the computation of the friction slope, $S_{f,k}$ Murillo and García-Navarro (2010b), is proposed. The friction slope is commonly used in a high number of sediment transport empirical laws, Meyer-Peter and Müller (1948); Smart (1984); Ashida and Michiue (1972); Camenen and Larson (2005), as these formulae were derived from 1D steady solid transport experiments. Additionally, its employment is coherent with the fact that transport process implies a loss of energy through the interaction between the sediment and the flow (Smart, 1984; Whittaker and Davies, 1982).

Also it is worth noting that the linearization of $\widetilde{\lambda}_{\mathbf{bn},k}$ in cases of almost flat bottom can lead to unphysical huge values of the bed wave speed. This is avoided by imposing a lower threshold for the bed level difference between cells: up to grain size, d_s, the approximation of the friction slope will be considered. This limitation ensures coherent values in the estimation of the bed wave speed, and wave celerity in (8.53) is approximated by

$$\widetilde{\lambda}_{\mathbf{bn},k} = \frac{\xi \delta \mathbf{q}_{\mathbf{sn},k}}{\delta z'} \tag{8.54}$$

with

$$\delta z' = \begin{cases} \delta z & if \;\; \delta z' > d_s \\ -S_{f,k} d_n & if \;\; \delta z' < d_s \end{cases} \tag{8.55}$$

being d_n the normal distance between cell centers (Murillo and García-Navarro, 2010b).

2D first order finite volume for the Morphodynamic Model

The evaluation of the wave speed, $\widetilde{\lambda}_{\mathbf{bn},k}$ as in (8.54), brings the opportunity of splitting the sediment flux difference $\delta \mathbf{q}_{\mathbf{sn},k}$ in right-going and left-going wave propagations. Consequently the Godunov first order method can be written as

$$\delta \mathbf{q}_{\mathbf{sn},k} = \delta \mathbf{q}_{\mathbf{sn}}{}^{+}_{i,k} + \delta \mathbf{q}_{\mathbf{sn}}{}^{-}_{j,k} \tag{8.56}$$

with

$$\delta \mathbf{q}_{\mathbf{sn}}{}^{+}_{i,k} = \widetilde{\lambda}^{+}_{\mathbf{bn},k}\delta z_k \qquad \delta \mathbf{q}_{\mathbf{sn}}{}^{-}_{j,k} = \widetilde{\lambda}^{-}_{\mathbf{bn},k}\delta z_k \tag{8.57}$$

and $\widetilde{\lambda}^{\pm}_{\mathbf{bn},k} = \frac{1}{2}(\widetilde{\lambda}_{\mathbf{bn},k} \pm |\widetilde{\lambda}_{\mathbf{bn},k}|)$. Therefore,

$$z_i^{n+1} = z_i^n - \sum_{k=1}^{NE} \delta \mathbf{q}_{\mathbf{sn}}{}^{-}_{i,k} \frac{\Delta t\ l_k}{A_i} - \sum_{k=1}^{NE} \delta \mathbf{q}_{\mathbf{sn}\,Ii,k} \frac{\Delta t\ l_k}{A_i} \tag{8.58}$$

where the second term of the right side in (8.58) evaluates the flux in the cell edge and the third term completes the updating formula to consider the spatial variation of A_g, as it was justified in Murillo and García-Navarro (2010a).

Another possibility for defining the Godunov first order method is through a flux scheme, considering outcoming and incoming fluxes through the edges of the cell. Hence the bed level is updated as

$$z_i^{n+1} = z_i^n - \sum_{k=1}^{NE} \xi \mathbf{q}^{*}_{\mathbf{sn},k} \frac{\Delta t\ l_k}{A_i} \tag{8.59}$$

where

$$\mathbf{q}^{*}_{\mathbf{sn},k} = \begin{cases} \mathbf{q}_{\mathbf{sn},i} & \text{if} \quad \widetilde{\lambda}_{\mathbf{bn},k} > 0 \\ \mathbf{q}_{\mathbf{sn},j} & \text{if} \quad \widetilde{\lambda}_{\mathbf{bn},k} < 0 \end{cases} \tag{8.60}$$

being $\mathbf{q}_{\mathbf{sn},i}$ and $\mathbf{q}_{\mathbf{sn},j}$ the bed load discharge computed in the cell i and in the cell j.

Although both numerical schemes (8.58) and (8.59) are completely equivalent, it must be stressed that the flux version is computationally more efficient, as minor algebraic operations are need. Additionally, with the flux form of the numerical scheme in (8.59), ghost cells must be considered in the boundary cells in order to complete the information over the entire cell, Leveque (2002). It is worth noting that the application of ghost cells almost does not penalize the computational effort. In this fashion, since the computational cost when using the flux scheme in (8.59) is less, this alternative has been chosen for obtaining the results displayed in the next sections.

8.5 Stability region

Updated values of $\mathbf{U}_i^{n+1}$ and z_i^{n+1} are defined cell averaging the contributions of the local RPs, and in consequence the time step Δt has to be taken small enough so that there is no interaction of waves from the k neighboring RPs. In the 2D framework, considering unstructured meshes, the relevant distance, that will be referred to as χ_i in each cell i must consider the volume of the cell and the length of the shared k edges (Murillo and García-Navarro, 2010b)

$$\chi_i = \frac{A_i}{\max_{k=1,NE} l_k} \tag{8.61}$$

Considering that each k RP is used to deliver information to a pair of neighboring cells of different size, the distance $\min(A_i, A_j)/l_k$ is relevant, so in case that the water depth is greater than zero in all the regions of the RP solution the time step is limited by

$$\Delta t \leq CFL\, \Delta t^{\widetilde{\lambda}} \qquad \Delta t^{\widetilde{\lambda}} = \frac{\min(\chi_i, \chi_j)}{\max |\widetilde{\lambda}^m|} \tag{8.62}$$

with CFL=1 in case of 1D meshes, CFL=1/2 in case of 2D structured or unstructured meshes (Toro, 1997) and being $\widetilde{\lambda}^m$ the wave speeds.

When the advection structure of the problem is all contained in the system matrices, i.e. coupled-Jacobian approach (Murillo and García-Navarro, 2010a; Castro Diaz et al., 2009; Soares-Frazao and Zech, 2010; Siviglia et al., 2013), the linearised wave speeds provided by the eigenvalues allow to define a suitable CFL condition, retaining the sediment transport part of the system. However, when using uncoupled/asynchronous (De Vriend et al., 1993) or coupled/synchronous models (Holly and Rahuel, 1990; Cao et al., 2002; Wu and Wang, 2004; Xia et al., 2010), it has been considered traditionally that since the wave speeds associated to water surface and bed level present different magnitudes, not straightforward limitation has to be considered in the stability condition. Nevertheless, this is no longer admissible when the celerities are in the same order of magnitude. Therefore, an extra limitation linked to the bed wave speed is required

$$\Delta t \leq CFL\, \Delta t^{\widetilde{\lambda}} \qquad \Delta t^{\widetilde{\lambda}} = \frac{\min(\chi_i, \chi_j)}{|\widetilde{\lambda}^m, \widetilde{\lambda}_b|} \tag{8.63}$$

8.6 Geomorphological collapse

The same strategy proposed in 5.4 for modeling the geotechnical equilibrium bank characteristics is employed here: a simple mass conservative mechanism of slope sliding failure, assuming that the angle of repose of submerged material of the bed can be approximated by the friction angle.

Chapter 9

Weakly-coupled scheme: results

9.1 Introduction

This Chapter gathers the validation tests that allow to show the assessment of the numerical schemes described in Chapter 8. Numerical results have been compared with experimental data and exact solution considering 1D and 2D situations. The bed-load discharge law employed for computing the bed evolution is the Smart CFBS, which was introduced in Chapter 5. Furthermore, in all the simulations a conservative mechanism of slope sliding failure has been considered, 5.4. The experimental tests employed for comparing with the numerical results are the same as the ones proposed in Chapter 6. Therefore the detailed description is omitted and the reference to each particular section from Chapter 6 is given.

9.2 Problems with exact solutions

In this section the numerical solutions for three bidimensional test cases that will be named A, B and C, as summarized in Table 9.1 are presented. The tests are Riemann problems for the movable bed equations, in which the friction shear-stress has been neglected in the momentum equation. The two first test cases, A and B, have been chosen to assess the performance of the numerical scheme assuming that morphological changes can be characterized using constant values of A_g. The third one, Test C, assumes that the value of A_g depends on the water depth. These exact solutions were firstly reported in Murillo and García-Navarro (2010a). The exact solutions were built by nesting several waves, departing from a left state until reaching to define the right state. The CFL condition is equal to 1.0, the mesh size is $x = 0.1m$ and the simulation is computed up to $t = 2s$. The value of the parameter A_g for the Grass law is considered as

$$A_g = \frac{A_{g,o}}{h^r} \tag{9.1}$$

being $A_{g,o} = 0.01$ in all cases, $r = 0$ in test cases A and B, and $r = 1$ in test case C.

Test	h_L	h_R	u_L	u_R	v_L	v_R	z_L	z_R
A	2.0	2.0	0.25	2.3247449	0.05	0.04	3.0	2.846848
B	2.25	1.18868612	0.20	2.4321238	0.045	0.02	5.0	5.124685
C	6.0	5.2	0.3	15.167196	0.015	0.04	3.0	4.631165

Table 9.1: Summary of dam break test cases with exact solution

In order to compare the accuracy of the weakly-coupled technique (WC) proposed in this work, the results obtained with the coupled-Jacobian technique used in Murillo and García-Navarro (2010a) (CJ) are also plotted.

TestA: the solution proposed in this test case is based on two outcoming rarefaction-waves and a central shock together with a contact wave evolving downstream, Figure 9.1. The shock and the contact wave move slowly, compared with the other two waves. The shock absorbs most of the initial step in bed profile. The numerical solution is able to capture the general trend of the flow behavior, without arising numerical problems at the step area. The unit sediment discharge in both directions is also displayed.

TestB: the second solution analyzed is built through two-rarefaction waves, a contact wave and a shock, Figure 9.2. he central wave is a quite slowly-moving rarefaction, bearing most of the initial step of the bed profile, whereas the shock is very weak, almost ineffective for the bed. The computed results are able to depict the moving waves in all the wet domain with an adequate level of accuracy.

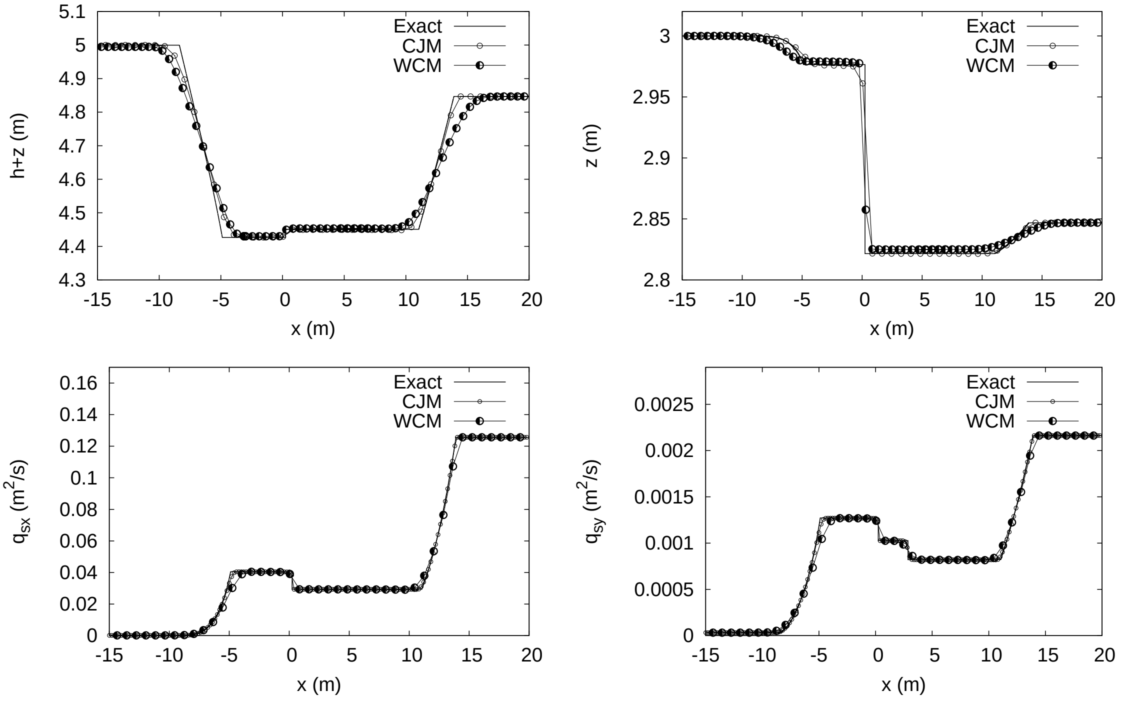

Figure 9.1: Exact and computed solution for Test A

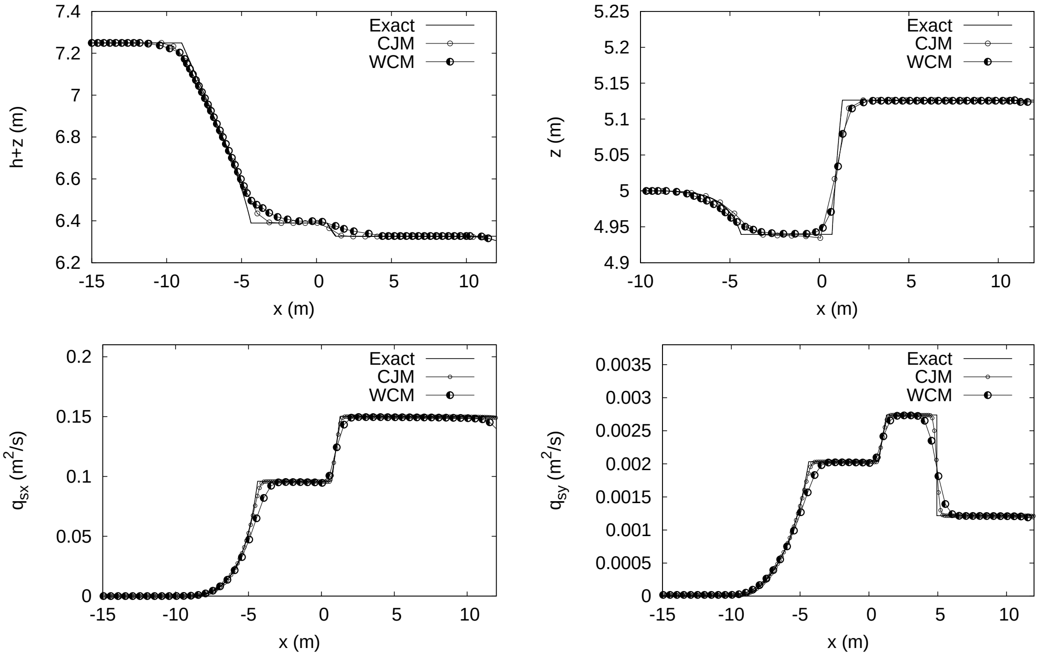

Figure 9.2: Exact and computed solution for Test B

TestC: this solution is constituted by two rarefaction waves, a contact wave and an ending rarefaction, Figure 9.3. Despite of being the A_g variable, the resulting computed results follows closely the exact ones.

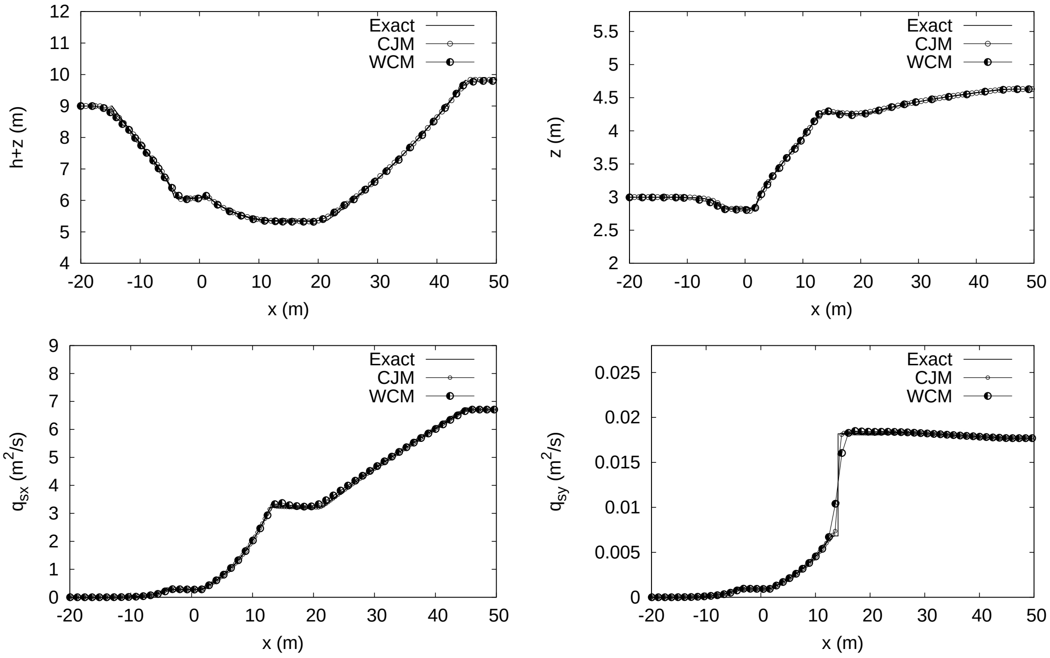

Figure 9.3: Exact and computed solution for Test C

9.3 One dimensional cases

9.3.1 Dam break test cases

These experiments were performed in a flume designed at the UCL Civil Engineering Department (Spinewine and Zech, 2007). Further details are provided in 6.2.1. Table 9.2 summarizes the set of experiments selected in this work. Test A has been chosen to guarantee the correct performance of the numerical schemes in a situation where morphological changes are produced in presence of dry bed and a flat bottom. Test F allows checking the numerical assessment against the different type of waves that may arise in a dam break case over wet bed. Numerical simulations have been performed using $\Delta x = 0.01$ m and CFL $= 1.0$. In all the simulations the bed domain is considered deformable and no boundary condition is imposed at the downstream section.

Test	h_L	h_R	z_L	z_R
A	0.35	0.00	0.00	0.00
F	0.25	0.10	0.10	0.00

Table 9.2: Summary of dam break test cases

Test A

Figure 9.4 displays numerical results and experimental data, for times ranging from 0 to 1.5 seconds. The front wave is numerically well reproduced in space and time, without observing numerical instabilities in the wet/dry boundaries.

As the numerical stability is of paramount importance the time step associated to the hydrodynamic and morphodynamic models is plotted in Figure 9.5. Harder restriction is required by the bed movement, which justifies the inclusion of the bed wave speed in the stability condition as it has been proposed in 8.5.

Whether the CFL limitation related to the bed speed is removed the scheme becomes unstable as it is displayed in Figure 9.6 at times $t = 1.0$ and 1.5 s.

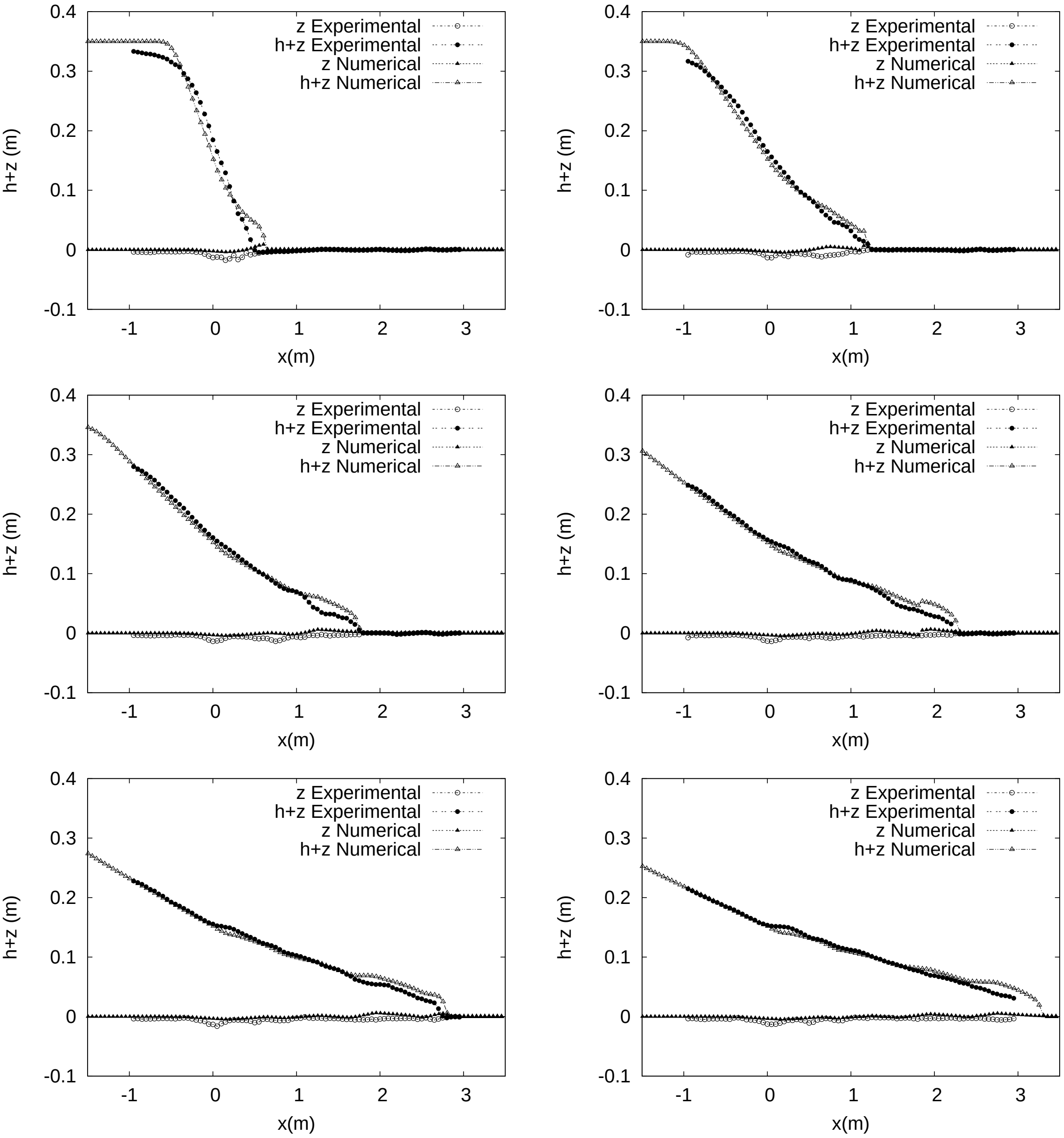

Figure 9.4: Numerical results and experimental data for the dam break test case A at times $t = 0.25$, 0.50, 0.75, 1.0, 1.25 and 1.5 s, using a variable value of A_g computed using Smart CFBS: measured water level surface ($- \bullet -$), measured bed level surface ($- \circ -$), computed water level surface ($-\triangle-$), measured bed level surface ($-\blacktriangle-$)

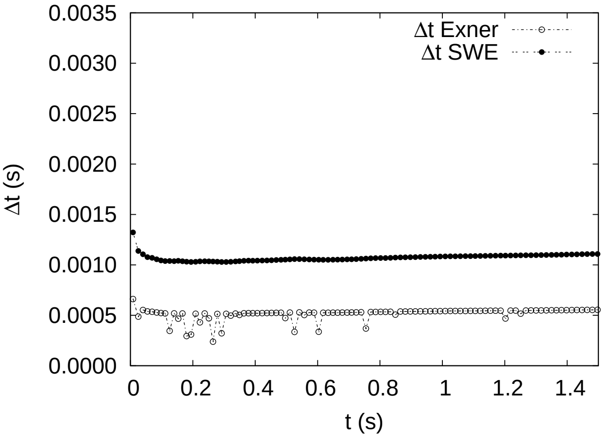

Figure 9.5: Time step evolution in test case A for the water waves speed as in (8.62), $(-\bullet-)$, and for the bed wave speed as in (8.63), $(-\circ-)$ during time simulation

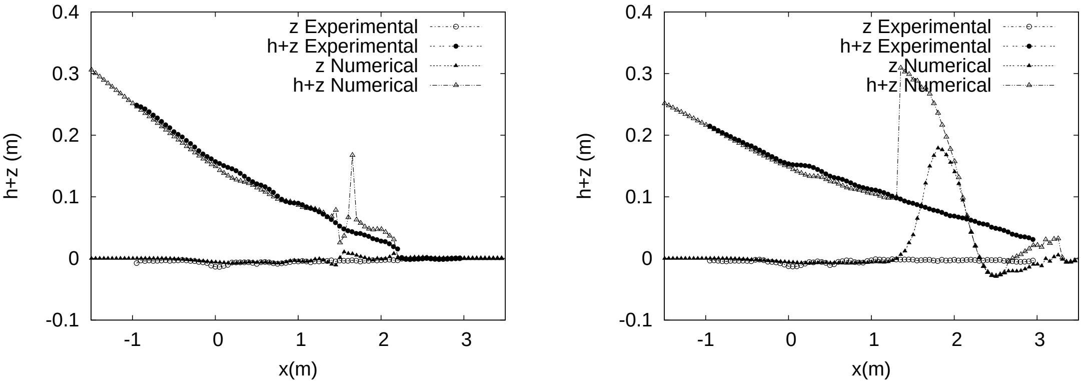

Figure 9.6: Numerical results and experimental data for the dam break test case A at times $t = 1.0$ and 1.5 s, when CFL limitation related to the bed speed is removed

Test F

In this test an initial layer of clear water is present in both sides of the dam break. There is also a downwards step at the bottom. Figure 9.7 gathers numerical results and experimental data for the free surface and bed level at different times, where it can be observed how the shock celerity is well captured by the numerical schemes. Small differences produced in the shock wave are attributable to fast transient energy variations associated to the existence of a hydraulic jump and also to the density variations of the vertical column associated to sediment concentration.

Figure 9.8 shows newly that the time step associated to bed wave celerity is governing the stability condition since the bed changes observed in the bottom configuration are of utmost importance.

Additionally, in Figure 9.9 is plotted the water level surface and the bed evolution at times $t = 1.0$ and 1.5 s when the CFL restriction associated to the bed wave celerity is removed. As it is expected, the scheme becomes unstable since it is not able to handle with the bed changes.

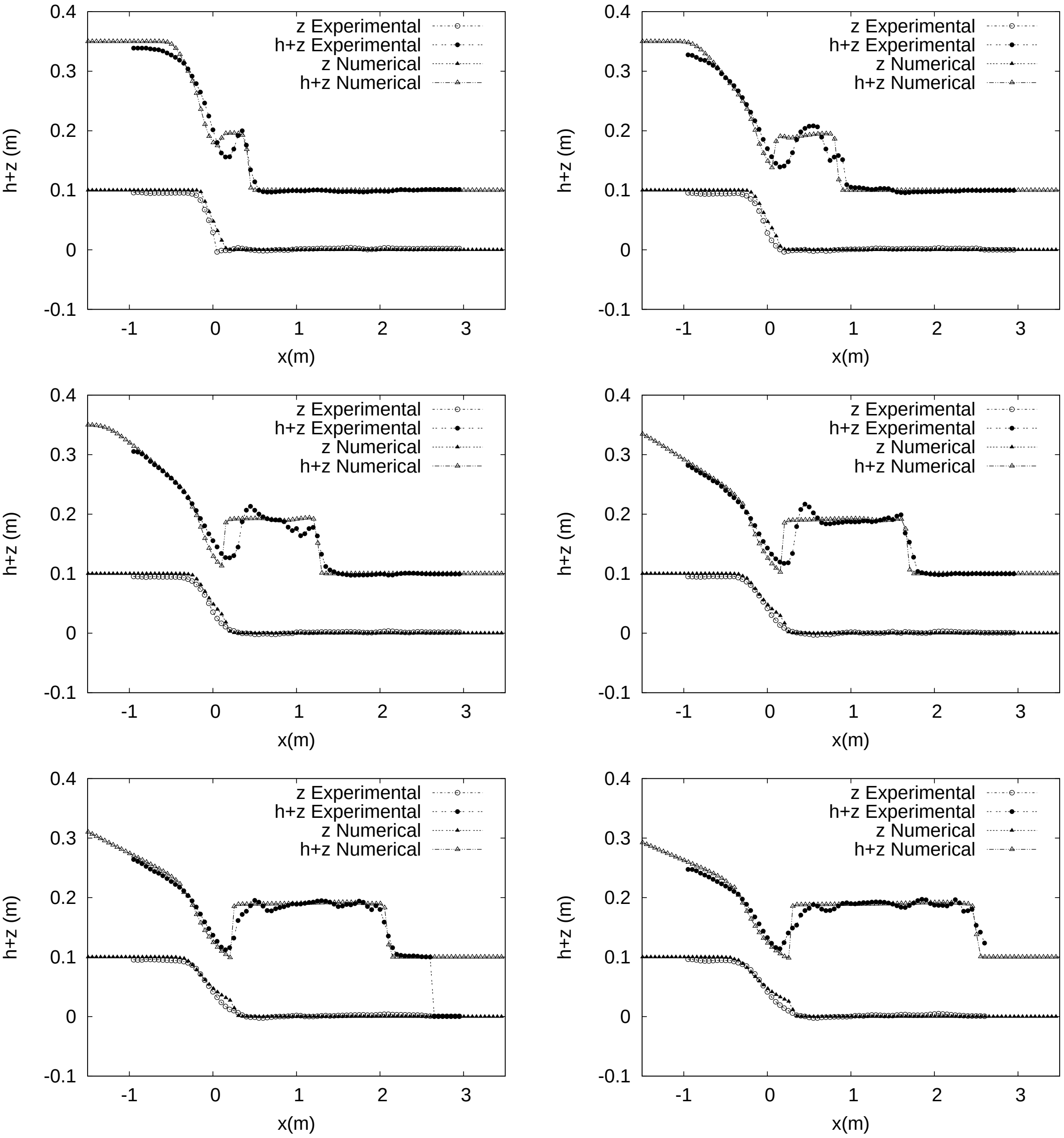

Figure 9.7: Numerical results and experimental data for the dam break test case F at times $t = 0.25$, 0.50, 0.75, 1.0, 1.25 and 1.5 s, using a variable value of A_g computed using Smart CFBS: measured water level surface ($- \bullet -$), measured bed level surface ($- \circ -$), computed water level surface ($-\triangle-$), measured bed level surface ($-\blacktriangle-$)

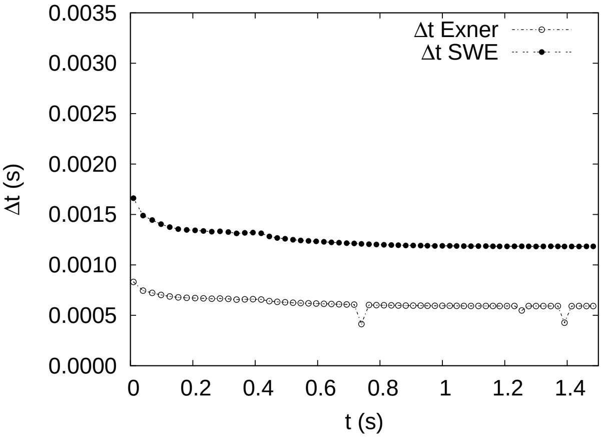

Figure 9.8: Time step evolution in test case F for the water waves speed as in (8.62), ($- \bullet -$), and for the bed wave speed as in (8.63), ($- \circ -$) during time simulation

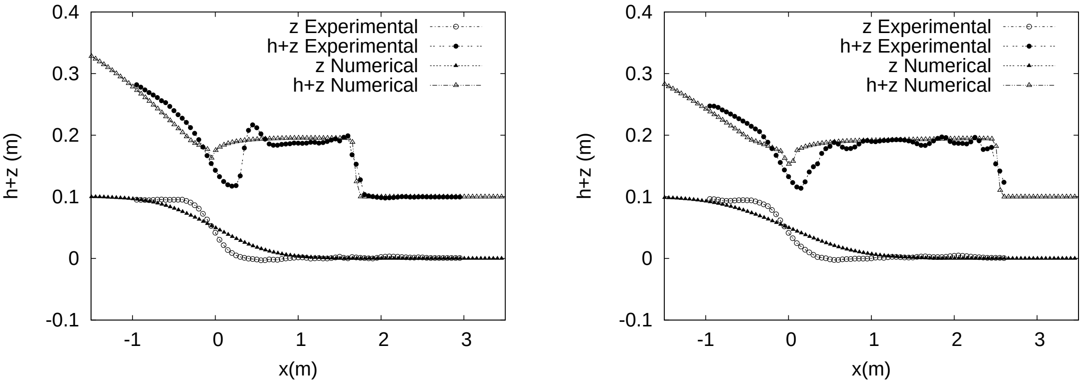

Figure 9.9: Numerical results and experimental data for the dam break test case F at times $t = 1.0$ and 1.5 s, when CFL limitation related to the bed speed is removed

9.3.2 1D Knickpoint test case

Morphological changes due to the transition between two planes with different slope (knickpoint) were measured in (Bellal et al., 2004). This test case is useful to compare the capacity of the numerical schemes to handle with a sudden flow transition from subcritical regime over a mild slope to supercritical regime over a steep slope. A sketch of the experiment, with the initial conditions of bed slope, is shown in Figure 9.10. The knickpoint is defined as the point of abrupt change in the longitudinal bottom profile of the channel.

This experiment was carried out using a coarse and uniform size sand with the following properties $\rho_s = 2680 kgm^{-3}$, $d_{50} = 1.65mm$, $\varphi = 30^o$, negligible cohesion, porosity $p = 0.42$ and was characterized by a Manning roughness factor $n = 0.0165$ sm$^{-1/3}$. Initial conditions employed are: upstream, water level surface (0.028 m) and discharge (9.8 l/s); downstream, a known water surface level at the end of the flume (0.11 m). The domain, 7.4 meters long, is divided using $\Delta x = 0.05$ m. In all simulations CFL = 1.

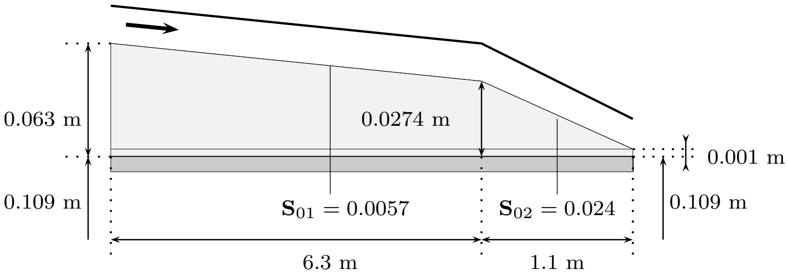

Figure 9.10: Knickpoint sketch

Bed level variation in the longitudinal profile was recorded in time and is compared with the predictions supplied by the numerical schemes in Figure 9.11. The computed solution describes a good trend when comparing with the experimental solution. The erosion located in the knickpoint is predicted at the same rate as the experiment and the final bottom is also well achieved.

Since in this experimental case an important change in the bottom morphology takes place, Figure 9.12 shows the more restrictive time step associated to the wave speeds of water and bed in time simulation. Bed time step imposes a harder restriction than the fluid flow and for this reason has to be considered in (8.62) for preserving the numerical stability of the numerical scheme.

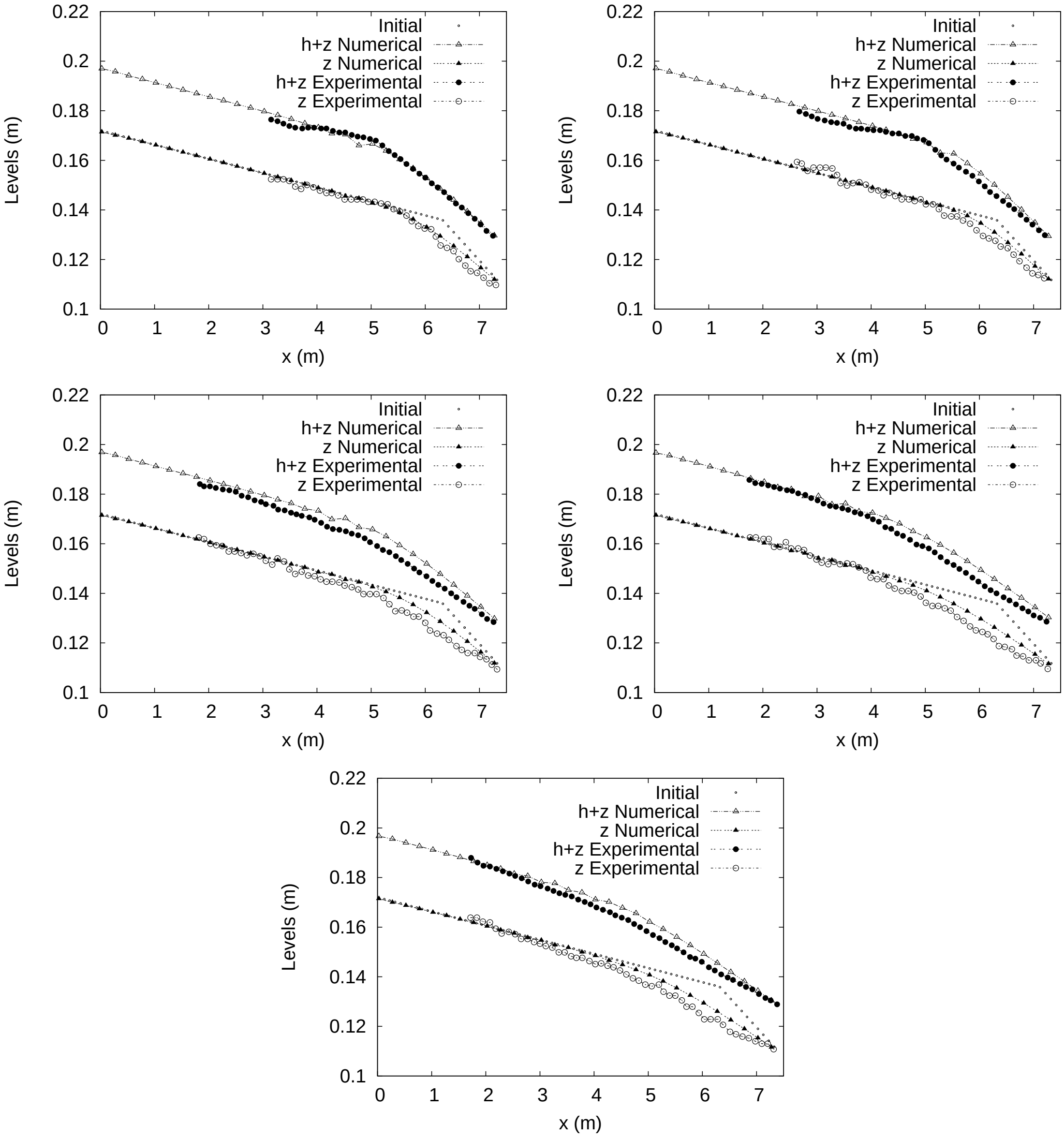

Figure 9.11: Results for the knickpoint test case. Initial bed level $(\cdots)$, measured bed and water level $(-\bullet-)$ and computed $(-\triangle-)$ at times $t = 165$, 223, 345, 589 and 851 s with variable value of A_g computed using Smart CFBS

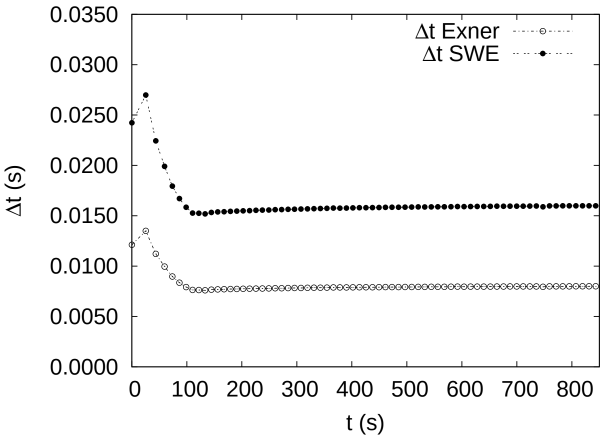

Figure 9.12: Time step evolution for the water waves speed, as in (8.62), (− ● −), and for the bed wave speed as in (8.63), (− ○ −) during time simulation

9.4 Two dimensional cases

9.4.1 2D Numerical modeling of dam failure

This experiment has been previously defined in 6.2.6 and it was studied by Tingsanchali and Chinnarasri (2001). Following prior work developed in Juez et al. (2013b) the 2D numerical simulation has been performed using a coarse unstructured triangular mesh, with a maximum cell size of 0.01m^2. The mesh together with the initial water depth is displayed in Figure 9.13. CFL is imposed equal to 0.5. Free boundary condition is considered at the outflow section. Figure 9.14 displays the bed level evolution when using Smart CFBS formulation. At the crest of the dike strong erosion occurred because of the strong initial discontinuity of water depth and the severe slope downwards the gate. The granular material of the dike is completely mobilized within a short period of time and it is grabbed downstream the dam by the flow.

Figure 9.15(a) shows the water and bed level surface computed after 120 s when using Smart CFBS formulation. As the bed level was recorded in time at three stations SA, SB and SC, located downstream from the edge of the original dam crest, the comparison between experimental data and computed results are displayed in Figure 9.15(b). Numerical results are able to handle the strong morphodynamics changes which take place without displaying numerical oscillations and additionally, well tracking the experimental data. On the other hand, the evolution of the measured and computed water reservoir level is depicted in Figure 9.15(c). Figure 9.15(d) displays the measured and computed overtopping discharge just upstream the breach. Both measurements provide high quality and useful information about this type of phenomena. Numerical schemes allows to obtain a good detail of forecasting capacity for the bed and water level evolution together with an efficient computational cost.

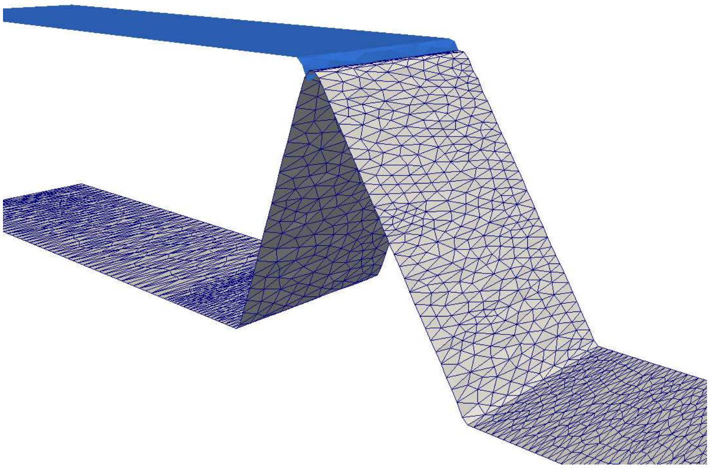

Figure 9.13: Detail of the triangular mesh and initial condition for the water depth

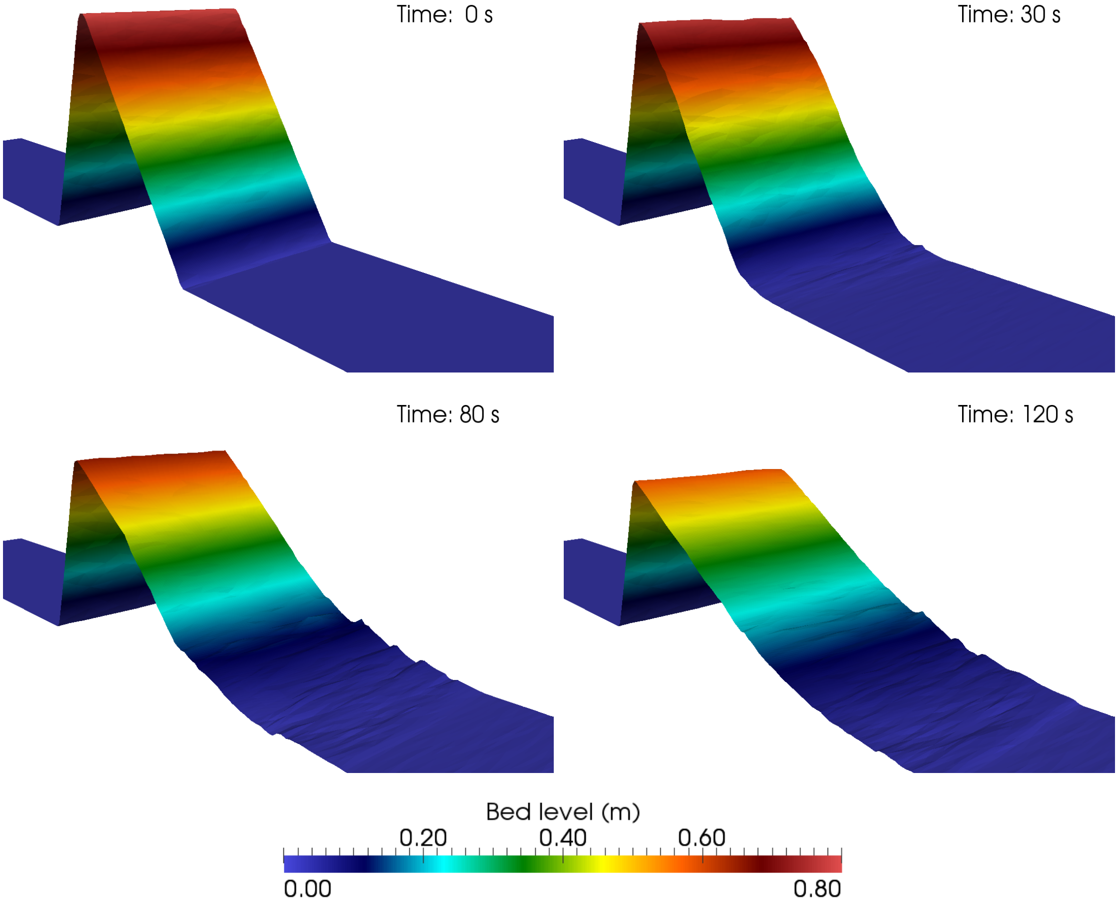

Figure 9.14: Computed results of the bed level evolution when using a variable value of A_g built with Smart CFBS and at times $t = 0$, 30, 80 and 120 s

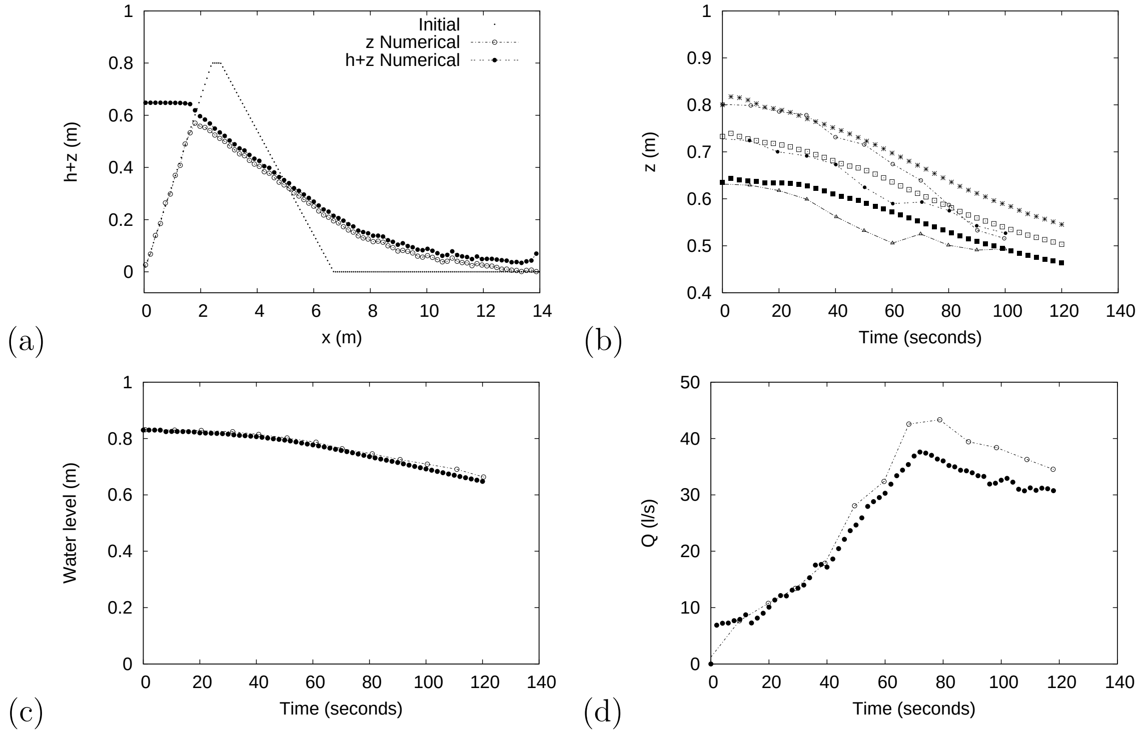

Figure 9.15: (a) Initial bed level (- - -), computed water level surface (—△—) and bed level surface (—▲—) at t = 120 s. (b) Bed level surface evolution in time measured at stations SA (— ○ —) (—□—), SB (— ● —), and SC (—△—) and computed at stations SA (— ⋆ —),SB (—□—), and SC (—■—). (c) Evolution in time of the measured water reservoir level (— ○ —) and computed water reservoir level (— ● —). (d) Evolution in time of the measured (— ○ —) and computed (— ● —) overtopping discharge

For this test case, the time step evolution associated to each wave speed is also studied, Figure 9.16. Initially, heavier restrictions are required by the water flow, as the overtopping event has not provoked yet the dike failure. However, as time advances and the geomorphic changes become more severe, time step restrictions come from the bed celerity. At the end of time simulation, where most of the sediment particle movement has occurred, the time step is newly governed by flow characteristics. In view of these results, it is proved the efficiency of the solver, as only when important bed changes exist the classical time step of water flow is decreased.

Additionally to the study of the time step evolution this test case has been chosen also for comparing the computational time cost with respect to the coupled-Jacobian technique used in Murillo and García-Navarro (2010a) (CJ) and the weakly-coupled scheme (WC) proposed in this work. For this purpose three meshes with increasing number of elements are considered. In Table 9.3 are displayed the ratio between the computational cost when employing Murillo and García-Navarro (2010a) and when considering the procedure explained in this work. Results plotted above belongs to the second mesh. Noticeable computational efficiency is achieved, being more important as the level of mesh refinement is increased. The computational cost time with the

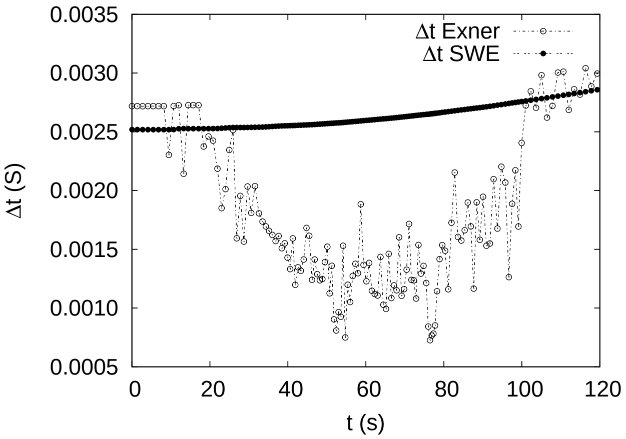

Figure 9.16: Time step evolution for the water waves speed, as in (8.62), (− • −), and for the bed wave speed, as in (8.63), (− ◦ −) during time simulation

CJ is penalized by the high number of algebraic operations need for computing the eigenvalues and eigenvectors. In order to support this fact and employing the second mesh, the time step evolution, associated to the CJ and to WC is displayed in Figure 9.17. Despite of presenting a bigger time step on average when using the CJ, the computational cost is higher.

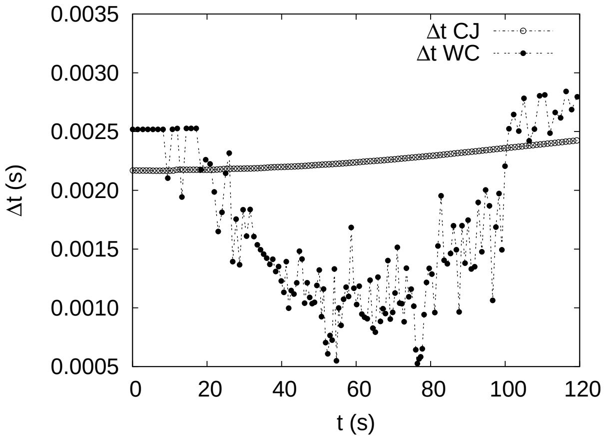

Figure 9.17: Time step evolution following the CJ technique in Murillo and García-Navarro (2010a), (− ◦ −), and the WC technique explained in this work, (− • −) during time simulation

Together with the computational cost time, the RMSE (Root median square error) for the three stations SA, SB and SC obtained when using the CJ and the WC technique, is displayed in Table 9.4. The weakly-coupled technique provides computational results close to the experimental ones whilst the computational time is decreased.

N. of elements	*Ratio of computational cost time* = CJ/WC
2000	8.46
4100	10.15
8300	13.72

Table 9.3: Summary of ratios of computational cost time when using the JCM technique and the WC technique

N. of elements	$RMSE(m)$ SA		$RMSE(m)$ SB		$RMSE(m)$ SC	
	CJ	WC	CJ	WC	CJ	WC
2000	0.065	0.039	0.042	0.034	0.058	0.037
4100	0.043	0.021	0.028	0.019	0.038	0.023
8300	0.028	0.014	0.019	0.012	0.025	0.015

Table 9.4: Summary of the RMSE associated to each station when using the JC technique and the WC technique

9.4.2 2D Dam break with a sudden enlargement

This experiment was performed at the laboratory of the Civil and Environmental Engineering Department of the UCL (Palumbo et al., 2008; Goutière et al., 2011) and has been previously numerically reproduced in 6. During the development of the experiment the water level evolution was recorded at different points as well as the final bed surface at several cross sections, Figure 9.18. An unstructured mesh is considered and CFL condition is imposed equal to 0.5.

Figure 9.18: Plan view of the experimental flume. Locations of the probes (left) and the cross sections (right)

This experimental case represents a complete challenge as it gathers several highlighted situations which can occur in the real engineering life: an area where the flow is genuinely one-dimensional, an abrupt expansion which provokes the change to a two-dimensional flow, important velocity gradients which create a recirculating area, moving shocks close to the wall zone and moreover a severe local erosion together with a noticeable sediment deposition area. It constitutes the perfect benchmark for checking the assessment of the numerical schemes against sudden and strong changes in the flow and the bed. Due to these characteristics other authors have also studied recently this test case (Soares-Frazao and Zech, 2010; Xia et al., 2010; Siviglia et al., 2013).

A series of computed bed surface evolutions are shown in Figure 9.19. The bed deformation is very sensitive since the flow evolves over a initially dry bed: sediment particles start to bounce as soon as the water reaches their position creating a kind of ripples or dunes, at time $t = 2$ s. As the water overtakes the corner of the channel the flow expands, causing the water depth to decrease and the bed level suffers a dramatic local erosion, at time $t = 4$ s. Close to the wall area the flow tends to slow down and the material grabbed upstream is settled. In this zone of the channel the loss of energy is so strong that a bed sharp surface emerges, at times $t = 4$ and 6 s. Downstream, the sediment grains are pushed outward the domain and eventually intersects driving to settling zones, times $t = 6$ and 10 s. At the last time, $t = 20$ s, the drainage of water leads to soften the bed surface although the minimum and maximum sediment peak areas are clearly identified. It is worth noting that the bed ripples plotted have a twofold nature. Firstly they have a numerical origin, since they are generated by the mesh topology as the numerical technique employed in this work make use of the Riemann theory, which is built considering the edges of each cell. Additionally, the bed ripples have also a physical nature, as the flow evolves over a dry bottom.

Once the experiment has been qualitatively described, computed and experimental data are faced. Comparison between the water level measured and the numerical solution is showed in Figure 9.20. The majority of the probes achieve a good trend in relation with the experimental data. Probes U3 and U4 are the ones which provide less accurate results. This is justified by the fact that they are located close to the expansion (probe U3) and close to the wall (probe U4), where three dimensional flow structures are generated due to the sudden expansion and the shock against the lateral side. With the present mathematical model, where the set of equations is depth-averaged, the vertical accelerations are neglected and consequently, this flow behavior cannot be properly treated (Xia et al., 2010).

Figure 9.21 gathers the measured bed level after the dam break event and the numerical predictions at control sections S1, S2, S3, S4 and S5. In all the sections the computed bed surface is able to follow the measured evolution. Section S1 which is the closest to the expansion does not obtain neither the maximum nor the minimum of sediment peaks, although the prediction follows the sediment movement pattern: particles are grabbed from left and settled to the right bank. In control sections, S2, S3 and S4, the computed bed surface follows correctly the tendency of the final bed morphology although the final bed slopes are less sharp than the ones recorded after the experiment. As it has been noted before, since the mathematical model is depth-averaged the vertical accelerations are not considered. Consequently, the erosion/deposition rates are decreased and differences in the granular material lying close to the right wall are expected. Section S5, positioned far away from the area of stronger influence, obtains a good tendency when comparing with the experimental data.

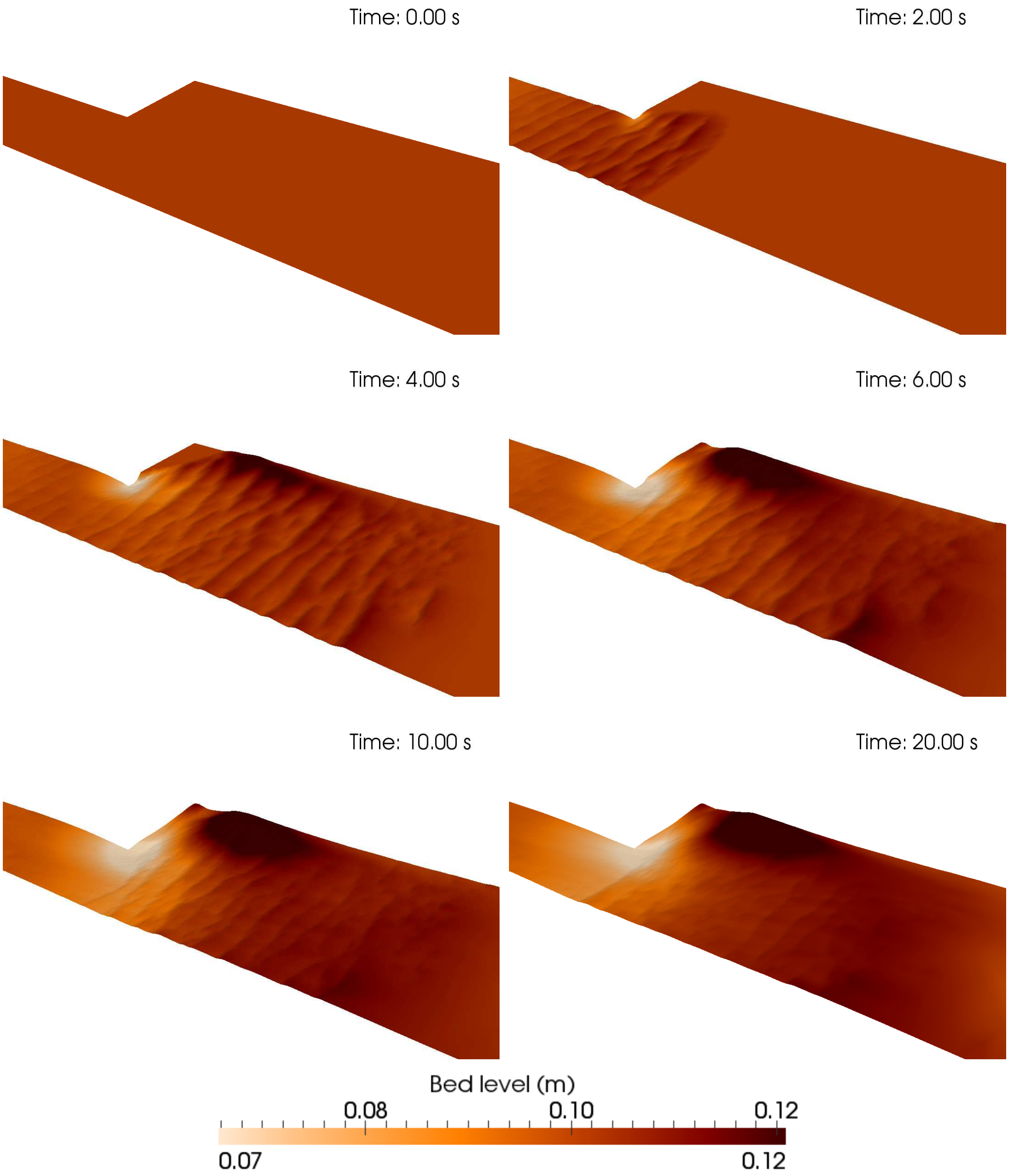

Figure 9.19: Computed bed surface evolution in time

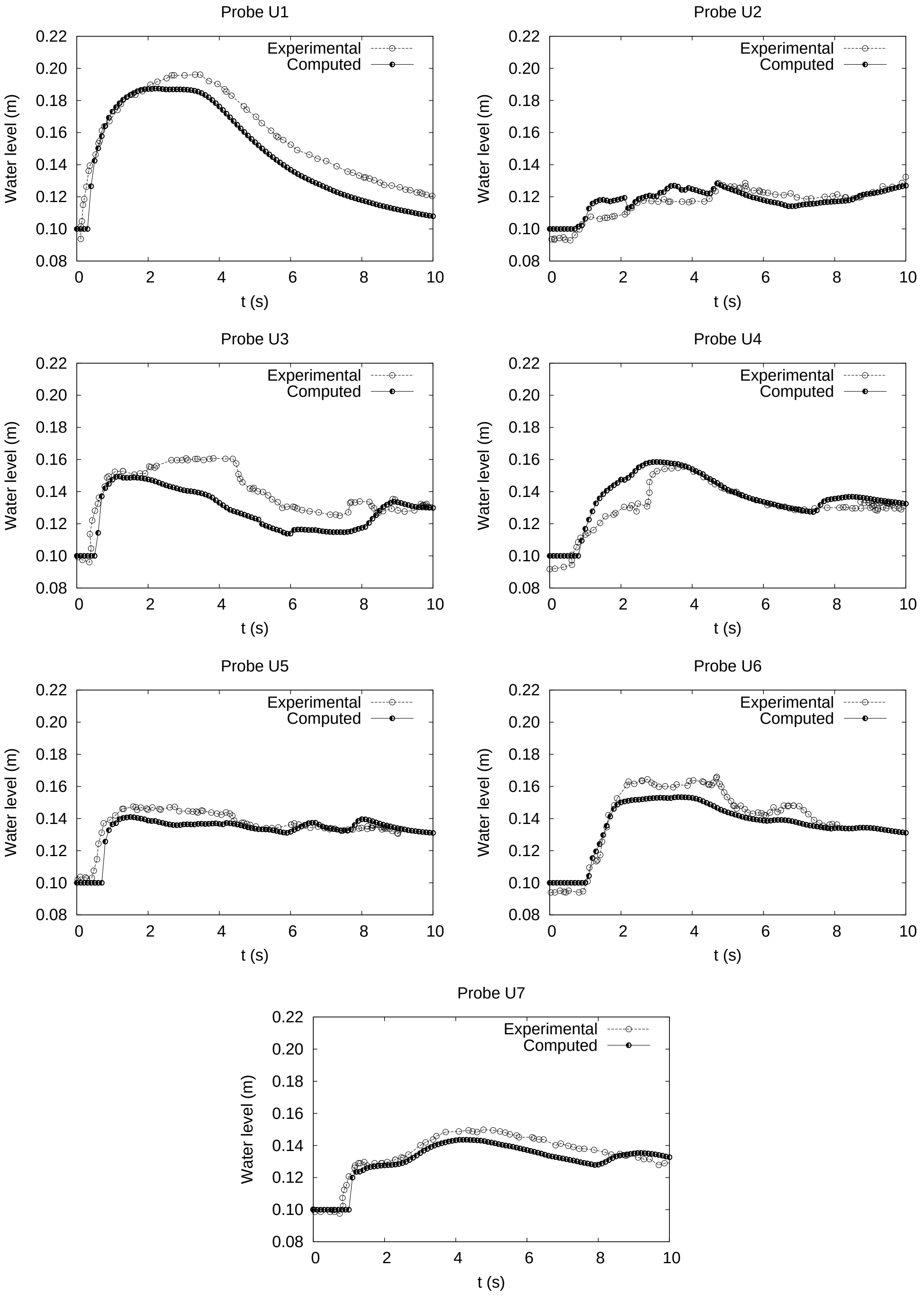

Figure 9.20: Temporal comparison between experimental (−○−) and computed (−●−) results for the water level at probes U1-U7

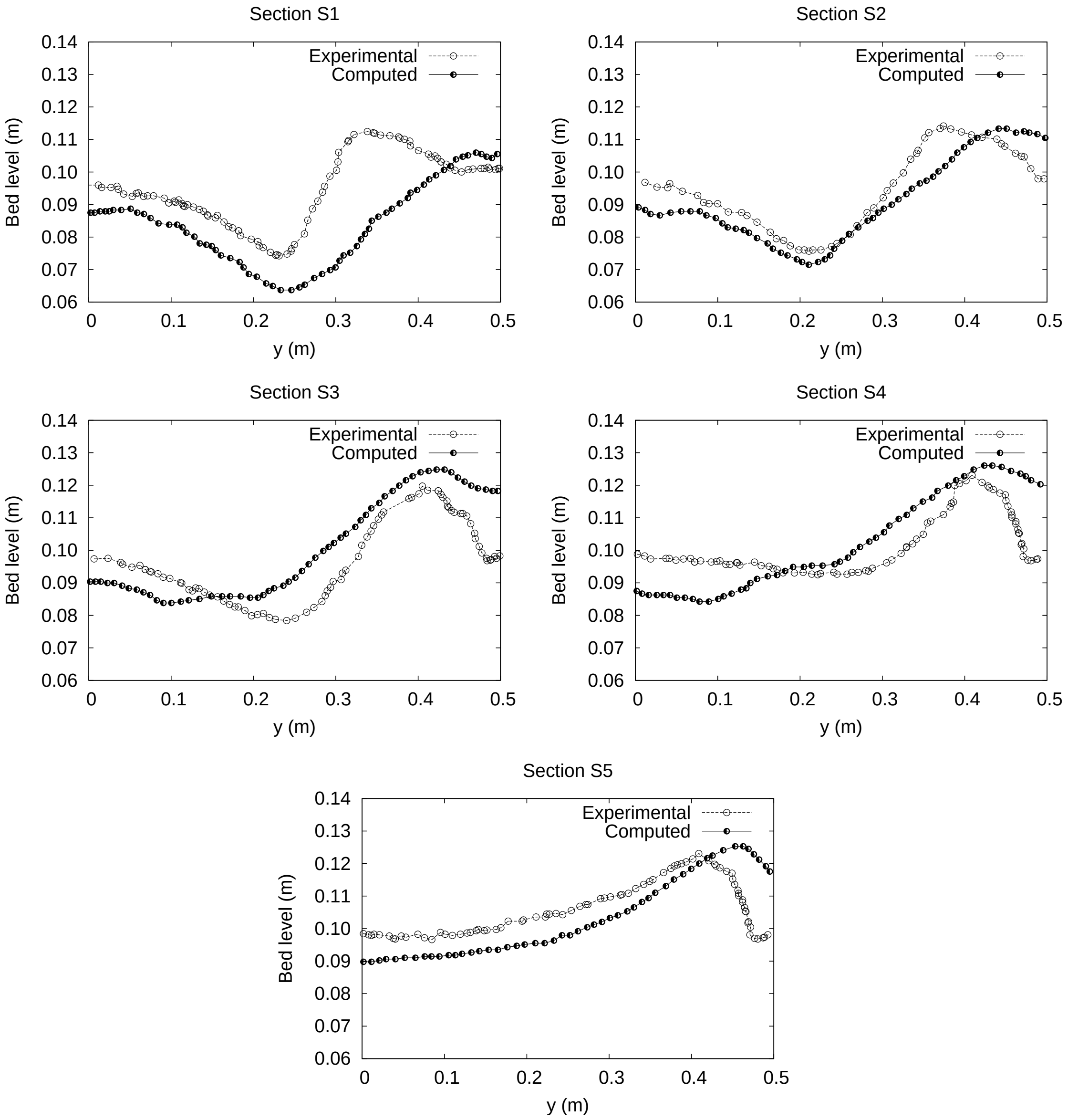

Figure 9.21: Comparison of the experimental (− ○ −) and computed (− ● −) final bed surface at cross sections S1-S5

Comparison of the computational cost time and the accuracy obtained when using the coupled-Jacobian technique (CJ) from Murillo and García-Navarro (2010a) and the weakly-coupled scheme (WC) proposed in this work is displayed in Table 9.5. For the sake of brevity only the RMSE associated to section S2 is showed. The CJ technique provides more accurate results in this case at the cost of increasing the computational time.

$N.\ of\ elements$	$Ratio\ of\ computational\ cost\ time : CJ/WC$	$RMSE(m) : S2$	
		CJ	WC
2000	5.23	0.015	0.024
4300	8.15	0.009	0.015
8100	14.02	0.006	0.012

Table 9.5: Summary of ratios of computational cost time and the RMSE for section S2 when using the CJ technique and the WC technique

Chapter 10

Weakly-coupled scheme: conclusions

A 2D numerical scheme for wave flows over mobile beds has been detailed. The numerical scheme solves a weak coupled model which includes the 2D SWE and the 2D Exner sediment continuity equation. It is written considering a finite volume method based on a Roe type solver and allows to verify that stable results can be obtained without employing a coupled-Jacobian and computationally expensive scheme. Following the first part of this thesis the Smart CFBS sediment empirical law has been considered. The explicit scheme has shown robust stability, always controlled by an augmented CFL condition.

The first two experimental cases considered, developed in 1D, have been performed to solve dam break situations over dry/wet initial conditions and with different morphodynamic configuration. Advance front celerity has been well captured in the dam break as well as the bed changes. Regarding the 1D knickpoint test case, the existence of variable flow regime or morphodynamic discontinuities does not ruin the forecast capacity of the numerical scheme leading to stable results.

Regarding the bidimensional cases, the comparison with the exact solutions showed that the computed results are similar to the ones obtained with a coupled-Jacobian model. In the next experiment, the dike collapse by overtopping, numerical performance of the solution in a 2D mesh is checked under severe changes in the bed surface level. Self-stable results have been obtained for both the water level and the bottom changes. Finally, in the 2D dam break with an abrupt expansion numerically reproduced, the free surface and bed level predictions have been well computed in time and space.

Since in practical applications, both stability and efficiency characteristics are required, the main challenge of this work has been to combine the interactions between flow and bed without using a coupled-Jacobian matrix as the proposed in Murillo and García-Navarro (2010a) with a higher computational effort. Also, when plotting the time step restrictions associated to the water wave celerities and to the bed wave celerity it has been checked how only severe changes in bottom morphology affect the time step restriction of the weakly-coupled model proposed in this work.

10.1 Further research

The proposed explicit finite-volume Godunov-type numerical scheme should be compared in terms of efficiency and accuracy with other implicit numerical techniques suggested in the literature (Garegnani et al., 2013; Bilanceri et al., 2012). When employing an implicit strategy the time step chosen can be bigger in relation with an explicit however, however the main drawback is the convergence speed of he linear solver used to solve the algebraic system as well as the convergence of the linearization process. A throughly study should be addressed.

Part II

Mass motion over steep areas

Chapter 11

Introduction

Several catastrophic events during the past decades have showed that important flood induced by a dam-break is in relation with a strong erosion in the bed and in the banks. These rapid and variably geomorphodynamic processes affect significantly to the flow behavior compounding the harmful effects of the flooding waves. For this reason, the numerical modeling of severe transient geomorphic flows is an active topic in the research field.

In addition, the study of these geomorphic flows/landslides and their movement constitutes an important environmental issue as they play a key role in landscape evolution. Currently, the triggering mechanisms, mechanical properties and assessment of likelihood and consequences as well as the development of measures to limit their impact, is an active topic in the field of the geophysical flows research.

As this phenomena involved a mixture of mud, sand and water sliding down a slope together, the study of granular flows constitutes an starting point for the understanding of the more complex mass movement phenomena mentioned before (Denlinger and Iverson, 2004). Therefore, several experiments on granular dry flows have been carried out in the past (Savage and Hutter, 1989; Iverson and Denlinger, 2001; Pouliquen and Forterre, 2002; Lajeunesse et al., 2004; Mangeney et al., 2010) as the initial target to be overcame by the numerical modeling tools.

Since the computational models open a wide range of possibilities for handling with this type of phenomena a numerical scheme has been developed for the analysis of dry granular flows. Moreover, taking advantage of the numerical experimentation an extra work has been carried out in order to push the knowledge about the dry granular behavior.

11.1 State of the art of the numerical techniques

Granular dry flows show fluid-like behavior where the front of the avalanche moves as a thin layer along high distances. Well known approaches for describing geophysical flows consider the Saint-Venant equations as an starting point. Depth averaged equations were first employed for solving geomorphologic flows by Savage and Hutter (1989), where granular mass sliding was modeled including Coulomb-like basal frictions, and assuming a cohesionless Mohr-Coulomb type material. Since then, new mathematical models have appear in the literature. In Denlinger and Iverson (2004) an extensive and complete review of predictive models for geomorphologic flows was provided and special attention was devoted to the computation of the Coulomb stresses conjugated to the deformation in solid-like behavior avalanches. Contrary to the Saint-Venant equations, defined in a Cartesian coordinate, the Savage-Hutter model uses a curvilinear coordinate along the topography. Denlinger and Iverson (2004) formulated the depth-averaged governing equations referenced to a rectangular Cartesian coordinate system (with Z vertical) and in their new approach the estimated frictional stresses were defined with independence of the orientation of the coordinate system. The model was tested against analytical solutions and experimental data. Bouchut et al. (2003) introduced an extra term in the original Savage-Hutter mathematical model, related to the curvature of the bottom, which is usually neglected when compared in terms of magnitude, in order to ensure the equilibrium at rest of the mass whatever the flow conditions (topography, friction coefficients, etc). Some phenomenas, such as landslides, where the curvature terms play an important role can be found in Favreau et al. (2010); Moretti et al. (2012). In Bouchut and Westdickenberg (2004) this model was extended to consider an arbitrary coordinate system for shallow flow over a 2D topography, retaining the curvature terms. In recent works concerning geomorphologic flows over 2D irregular bed topographies (Pirulli et al., 2007; Pirulli and Mangeney, 2008) this term was omitted and promising computational results were obtained. Following Pirulli et al. (2007); Pirulli and Mangeney (2008) curvature terms related with the geometry are not considered here and the rheology of the material will be described using a Coulomb-type friction law.

Once a mathematical model is selected, another separate issue is the numerical scheme used. Considering the hyperbolic nature of the depth averaged equations, Godunov type schemes are commonly used in literature (Denlinger and Iverson, 2004; Mangeney-Castelnau et al., 2003). Godunov type schemes can be constructed departing from the definition of approximate solvers of the Riemann problem (RP). Approximate solvers provide a comprehensible definition of the conserved variables in the inner states of the same RP. Among the most successful and disseminated approximate solvers, Roe's method (Roe, 1986) and the HLL method (Harten et al., 1983), were defined to approximate solutions for hyperbolic system of equations without source terms. When including the presence of source terms in the system of equations, it is possible to extend the numerical schemes defined for the homogeneous case using point-wise explicit or implicit discretizations of the source terms. In Mangeney-Castelnau et al. (2003), internal stresses represented by the Coulomb friction law were discretized using a point-wise implicit discretization. Numerical experimentation has shown that point-wise discretizations lead to undesirable results, as non uniform discharge values in steady solutions (Burguete et al., 2008b; Murillo et al., 2008). A proper discretization of the frictional source terms must ensure a correct balance among fluxes and source terms (well-balanced property). Following previous work in well balanced numerical schemes for the shallow flow equations in presence of bed variations (Hubbard, M. E. and García-Navarro, P., 2000), in Denlinger and Iverson (2004), the Roe scheme was applied in combination with an upwind technique applied to the internal stresses. The apparent topography method to deal with generic source terms in Bouchut and Westdickenberg (2004), based on the well-balanced property, was applied successfully to the simulation of the spreading of a granular column over a rough horizontal plane in Mangeney-Castelnau et al. (2005) and over a over an inclined plane in Mangeney-Castelnau et al. (2007). Contrary to shallow water flows, where quiescent flow is given in cases of horizontal water level surface, in granular flows, steady state configurations include correct modeling of starting and stopping flow conditions (Bouchut and Westdickenberg, 2004; Mangeney-Castelnau et al., 2007; Pirulli et al., 2007; Pirulli and Mangeney, 2008).

The presence of source terms leads to non-strictly hyperbolic systems of equations and, as a consequence, they have an impact in the solution of the RP. In the shallow water equations with variable topography, different approximations to the Riemann problem have been presented in the literature (Alcrudo and Benkhaldoun, 2001; Chinnayya et al., 2004; LeFloch and Thanh, 2007; Bernetti et al., 2008; Rosatti and Begnudelli, 2010; LeFloch and Thanh, 2011). The properties of these RP solutions not only must guarantee the well-balanced property, but also, the associated numerical scheme must ensure convergence to the solution. Convergence to the solution is not an easy task, as in problems with source terms the total number of waves can be larger than the number of characteristic fields (LeFloch and Thanh, 2011). Two augmented solvers which consider intrinsically the presence of source terms, named ARoe (Augmented Roe) and HLLCS (HLL with Contact wave and Source terms), were presented in Murillo and García-Navarro (2010b) and Murillo and García-Navarro (2012b) respectively. Both schemes include an extra static wave for considering the effect of the source terms in the stability region. The ARoe solver was exploited in Murillo and García-Navarro (2012a) allowing correct approximate solutions of wave Riemann problems involving complex rheology when using depth average equations. An accurate and robust first order finite volume scheme, able to handle correctly transient problems including modeling of starting and stopping flow conditions was presented in Murillo and García-Navarro (2012a). Then, in contrast with prior works, Bouchut and Westdickenberg (2004); Pirulli et al. (2007), where numerical fluxes were constructed to ensure well-balanced arguments, in Murillo and García-Navarro (2012a), the definition of the complete approximate solution ensured correct integral estimations of the source terms under all type unsteady of flow conditions. It is worth mentioning, that, in general, only in cases of quiescent equilibrium, the source terms can be integrated exactly. In any other case, the approximate solver provides the rules to avoid unphysical results, allowing the correction of the estimations made for the source terms if necessary. This result is of utmost importance when modeling of starting and stopping flow conditions and can be applied with independence of the type of rheological model selected.

In presence of steep slopes the usual hypothesis of hydrostatic pressure in the vertical direction Z in the shallow water equations is not longer admissible. This fact has consequences when deriving the mathematical model. In global coordinates (X, Y, Z) (Figure 12.1), the gravity vector has a simple form

$$\mathbf{g} = -(g_X, g_Y, g_Z)^T = (0, 0, -g)^T \tag{11.1}$$

and the bed vector $\mathbf{S}_o$ can be written as

$$\mathbf{S}_o = (\tan\theta, \tan\gamma) = \left(-\frac{\partial Z_b}{\partial X}, -\frac{\partial Z_b}{\partial Y}\right) \tag{11.2}$$

where Z_b is the bed level surface in global coordinates. If a coordinate system linked to the topography (x, y, z) is preferred, the gravity vector must be projected following the new system of coordinates. By means of two rotations around the angles γ and θ, as in Pirulli (2005),

$$\mathbf{g} = -(g_x, g_y, g_z) = \left(\begin{array}{ccc} -g\sin\theta, & -g\sin\gamma\cos\theta, & -g\cos\theta\cos\gamma \end{array}\right)^T \tag{11.3}$$

The correct discretization of numerical fluxes and source terms is an important issue in both coordinate systems, when the bed slopes may change from cell to cell. Therefore, in order to preserve steady state configurations, and with independence of the numerical solver selected, it is necessary to ensure exact balance among fluxes and source terms, including the correct modeling of starting and stopping flow conditions.

11.2 State of the art for the experimental works

Due to the fact that avalanches are initiated on steep slopes, pioneer experimental studies concerning granular flows were focused on the grain movement over constant inclined planes with slopes larger than the material repose angle Wieland et al. (1999); Pouliquen (1999); Pouliquen and Forterre (2002); Mangeney et al. (2010). This type of movement is governed by the gravity component along the slope direction. Experiments developed in Pouliquen (1999); Mangeney et al. (2010) were performed over a genuine 1D configuration whilst Wieland et al. (1999); Pouliquen and Forterre (2002) were devoted to 2D events. All of them brought the opportunity of studying unstable granular masses, focusing on the maximum spreading or the avalanche front and tail speeds.

dditionally to these prior laboratory works, in Lajeunesse et al. (2004); Boutreux and deGennes (1997) other type of configuration was experimentally addressed: the sudden release of a surface over a quasi-horizontal surface. In such case, the weight of the sand grains was the responsible for the onset of the movement, while the frictional forces were in charge of the stopping condition. These experiments, being free from the influence of the topography, were of utmost importance, since they provided results concerning the quantity of mass mobilized by the flow, the final shape and the maximum spreading of the granular mass.

Another important configuration which has been recently mimicked in the laboratory consists of granular flows traveling over erodible topography, Mangeney et al. (2010); Roche et al. (2011). This phenomena is easily found in nature, as under certain circumstances landslides can move over deposits built up by earlier events. The strong effects of erosion processes can significantly increase the mobility of avalanches, changing drastically the final distribution of the granular mass, Mangeney-Castelnau et al. (2005); Bouchut et al. (2008); Mangeney et al. (2010).

The study of granular flows in combination with obstacles has also acquired prominence during the last years. The impact of the obstacle in the flow behavior needs to be understood for a better design of civil engineering elements such as mast of electrical power lines, buildings, ski lifts, dams and other man-made structures. Several works have dug on this active research field, some of them analyzing the flow overtopping on dike elements Hakonardottir et al. (2003); Faug et al. (2008) and other ones focusing on the shock waves generated by the impact between the flow and the single obstacle Gray et al. (2003); Hakonardottir and Hogg (2005); Hauksson et al. (2007).

Following the previous effort made by the authors mentioned above Gray et al. (2003); Hakonardottir et al. (2003); Hakonardottir and Hogg (2005); Hauksson et al. (2007), one of the main concern of this work is in relation with the study of the variable nature of the moving shocks and their complex birth and propagation. Since we want to get closer to the phenomenology which takes place in nature, a series of laboratory experiments have been carried out for studying novel an real-life configuration: 2D spread of the granular mass over variable topography with a changing slope and multiple shock waves derived from the presence of multiple obstacles. The experimental avalanche is triggered by a simple mechanism: a granular mass which is suddenly released from a semi-spherical container. The full description of the experimental facility, methods and cases is found in Caviedes et al. (2014). To provide a physical insight into these phenomena, the spatial and temporal spreading dynamics and the morphology of the resulting shape are investigated and discussed in this work through the wave theory (Roe, 1986). For this purpose, the computational scheme developed for dry granular flow in this work as previous goal is the basis for performing the numerical experimentation. Since the computational scheme has been previously tested and validated the numerical results obtained are free of distorting numerical effects allowing to study the physical features involve in the granular flows.

11.3 Outline

In this work, the results presented in Murillo and García-Navarro (2010b, 2012a) are extended to provide appropriate numerical schemes for mathematical models of 2D granular flow written in global and local system of coordinates. Taking advantage of this fact a numerical experimentation has been performed through the basis of a novel experimental work. In Chapter 11 weak solutions for Riemann problems over steep and variable slopes are presented focusing in the analysis and definition of the correct numerical discretization of both fluxes and source terms in local coordinates. Also, a detailed definition of the numerical fluxes based on the analysis of the approximate solution is provided. The results are extended to global coordinates in Chapter 12. The augmented approximate solver in Murillo and García-Navarro (2010b, 2012a) is modified in both systems of coordinates to consider the effect of bed slope in pressure distribution and frictional effects. In Chapter 13, the numerical solvers are tested against 1D and 2D experimental data in order to check the suitability of the mathematical models described in this work following global and local system of coordinates. Conclusions and further research are written in Chapter 14. Regarding the experimental work, in Chapter 15 it is brought together a summary of the laboratory setup where the experiments have been carried out and in addition, it is also depicted extra consideration about the friction law employed. Chapter 16 is devoted to the comparison between the experimental data and the computed results, focusing on the discussion of the physics involved in the granular flow behavior. Finally, the conclusions of the laboratory work and future research line are written in Chapter 17.

Chapter 12

Mathematical model and numerical scheme following local coordinates

12.1 Introduction

In this Chapter, a mathematical model for describing granular flow in local coordinates, LC from now on, is presented. It assumes that the flow is oriented in a predominantly longitudinal direction and is confined to a layer which is thin compared to the scale of interest. Hydrostatic pressure distribution in the normal direction to the bed is assumed and a Coulomb type bed friction is used to model the basal stress. The set of depth averaged equations developed in Chapter 3 for the one layer model are also valid in this phenomena. Additionally, a numerical scheme is developed regarding the particularities of the problem.

12.2 Mathematical model

Bearing in mind the expression for the gravity vector in (11.3), the depth averaged equations expressing volume and momentum conservation are written as follows

$$\frac{\partial \mathbf{U}}{\partial t}+\frac{\partial \mathbf{F}(\mathbf{U})}{\partial x}+\frac{\partial \mathbf{G}(\mathbf{U})}{\partial y}=\mathbf{S}_{\tau}+\mathbf{S}_{b} \tag{12.1}$$

where

$$\mathbf{U}=\begin{pmatrix} h, & hu, & hv \end{pmatrix}^{T} \tag{12.2}$$

are the conserved variables, with h representing granular material depth in the z coordinate and (u, v) the depth averaged components of the velocity vector along x, y

coordinates. The fluxes are given by

$$
\begin{aligned}
\mathbf{F} &= \left(hu, hu^2 + \frac{1}{2} g_z h^2, huv \right)^T \\
\mathbf{G} &= \left(hv, huv, hv^2 + \frac{1}{2} g_z h^2 \right)^T
\end{aligned}
\tag{12.3}
$$

and the source terms of the system are split in two kind of terms. The term $\mathbf{S}_\tau$ represents the frictional effects in the bed, and is defined as

$$
\mathbf{S}_\tau = \left(0, -\frac{\tau_{b,x}}{\rho}, -\frac{\tau_{b,y}}{\rho} \right)^T \tag{12.4}
$$

with $\tau_{b,x}, \tau_{b,y}$ the bed shear stress in the x and y direction respectively and ρ the density of the fluid. These tangential forces are evaluated in this work through a Coulomb law

$$
\mathbf{S}_\tau = (0, -g_z h \tan\theta_b, -g_z h \tan\theta_b)^T \tag{12.5}
$$

being θ_b the dynamic friction angle between the bed and the flowing mass. The term $\mathbf{S}_b$ is defined as

$$
\mathbf{S}_b = (0, \; -g_x h, -g_y h)^T \tag{12.6}
$$

and expresses the variation of the pressure force in the x and y direction respectively. Note that no bed derivatives are included. Instead the relevant quantity is the gravity acceleration projection. Figure 12.1 shows a 1D sketch of the relative position of local and global coordinates.

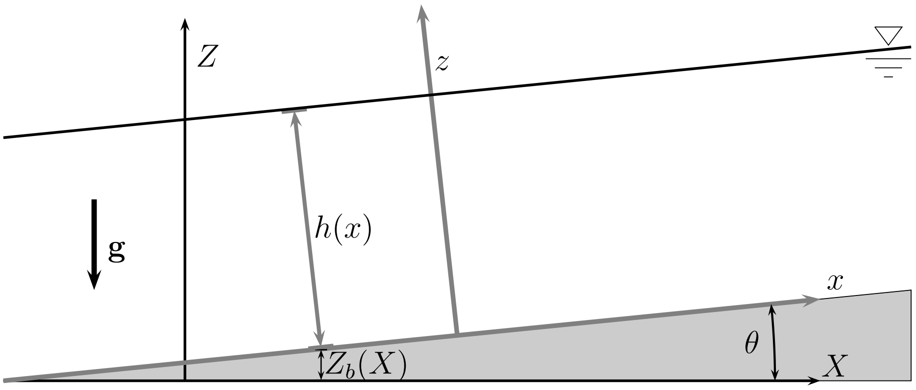

Figure 12.1: 1D sketch of global and local coordinates

System (12.1) is time dependent, non linear, and contains source terms. Under the hypothesis of dominant advection it can be classified and numerically dealt with as belonging to the family of non strictly hyperbolic systems (LeFloch and Thanh, 2011). The mathematical properties of (12.1) include the existence of a Jacobian matrix, $\mathbf{J_n}$, of the flux normal to a direction given by the unit vector $\mathbf{n}$, $\mathbf{E_n} = \mathbf{F}n_x + \mathbf{G}n_y$, defined as

$$\mathbf{J_n} = \frac{\partial \mathbf{E_n}}{\partial \mathbf{U}} = \frac{\partial \mathbf{F}}{\partial \mathbf{U}} n_x + \frac{\partial \mathbf{G}}{\partial \mathbf{U}} n_y \tag{12.7}$$

whose components are

$$\mathbf{J}_n = \begin{pmatrix} 0 & n_x & n_y \\ (g_z h - u^2)n_x - uvn_y & vn_y + 2un_x & un_y \\ (g_z h - v^2)n_y - uvn_x & vn_x & un_x + 2vn_y \end{pmatrix} \tag{12.8}$$

12.3 Finite Volume Model

To introduce the finite volume scheme, (12.1) is integrated in a grid cell Ω_i in the plane defined by the local coordinates (x, y). Using Gauss theorem system in (12.1) is written as

$$\frac{\partial}{\partial t} \int_{\Omega_i} \mathbf{U} d\Omega + \oint_{\partial \Omega_i} \mathbf{E_n} dl = \int_{\Omega_i} (\mathbf{S}_\tau + \mathbf{S}_b) d\Omega \tag{12.9}$$

where vector $\mathbf{n}$ is outward to the cell Ω_i, as displayed in Figure 12.2.

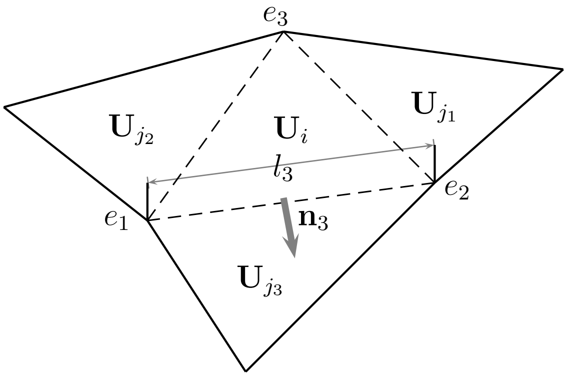

Figure 12.2: Cell parameters

The second integral in (12.9) can be explicitly expressed as a sum over the cell edges,

$$\frac{\partial}{\partial t} \int_{\Omega_i} \mathbf{U} d\Omega + \sum_{k=1}^{NE} \int_{e_k}^{e_{k+1}} \mathbf{E}_{\mathbf{n}k} dl_k = \int_{\Omega} (\mathbf{S}_\tau + \mathbf{S}_b) d\Omega_i \tag{12.10}$$

with $\mathbf{n}_k = (n_x, n_y)$ the outward unit normal vector to the cell edge k, dl_k is aligned in the direction of the edge and NE is the number of edges in cell i, as shown in Figure 12.2.

Assuming a first order in space approach, (12.10) becomes

$$\frac{\partial}{\partial t}\int_{\Omega_i} \mathbf{U} d\Omega + \sum_{k=1}^{NE} \mathbf{E}_{\mathbf{n}k} l_k = \int_{\Omega} (\mathbf{S}_\tau + \mathbf{S}_b) d\Omega_i \tag{12.11}$$

Also, the volume integrals of the source terms are expressed in terms of appropriate contour integrals by projecting the source terms onto the normal direction $\mathbf{n}_k$ to each cell edge as follows

$$\int_{\Omega_i} (\mathbf{S}_\tau + \mathbf{S}_b) d\Omega_i \approx \sum_{k=1}^{NE} \int_{x'} \left[(\mathbf{S}_{\mathbf{n}\tau} + \mathbf{S}_{\mathbf{n}b})_k dx'_k \right] l_k \tag{12.12}$$

being x' the coordinate normal to cell edge k, as shown in Figure B.1.

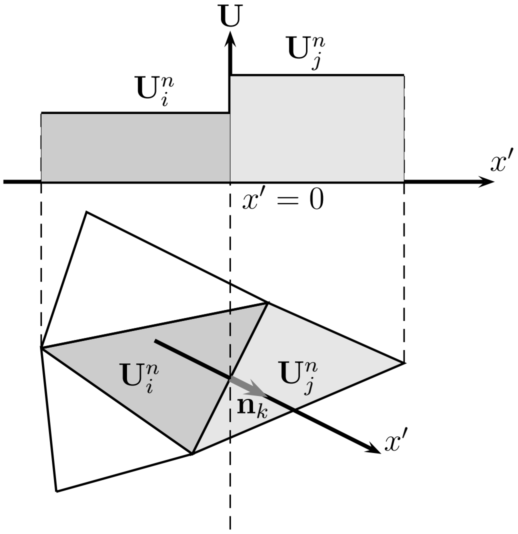

Figure 12.3: Riemann problem in 2D along the normal direction to a cell side

The normal projection of the friction term is written as

$$\mathbf{S}_{\mathbf{n}\tau} = (0, -g_z h \tan(\theta_b) n_x, -g_z h \tan(\theta_b) n_y)^T \tag{12.13}$$

and the normal projection of pressure force over the bed is expressed as

$$\mathbf{S}_{\mathbf{n}b} = (0,\ -g_x h n_x, -g_y h n_y)^T \tag{12.14}$$

It is worth emphasizing that source terms in (12.13) and (12.14) recover exactly the differential formulation in 1D meshes and in 2D cartesian structured meshes at each edge. Then, the initial system of equations in (12.1) is transformed in

$$\frac{\partial}{\partial t}\int_{\Omega_i} \mathbf{U} d\Omega + \sum_{k=1}^{NE} \left(\mathbf{E_n} - \int_{x'} (\mathbf{S}_{\mathbf{n}\tau} + \mathbf{S}_{\mathbf{n}b})_k dx' \right)_k l_k = 0 \tag{12.15}$$

and will be solved using approximate linear solutions of initial value problems according to the Godunov method, where $\mathbf{U}_i^n$ is the cell-average value of the solution $\mathbf{U}(x, y, t)$ for the ith cell at time t^n

$$\mathbf{U}_i^n = \frac{1}{A_i}\int_{\Omega_i} \mathbf{U}(x, y, t^n) d\Omega \tag{12.16}$$

being A_i the cell area.

12.3.1 Definition of the Riemann problem

Although in first order approximation all conserved variables and also the bed elevation at each cell are defined as piecewise uniform functions, it is possible to evaluate the change in bed surface elevation by means of linear functions in order to obtain the vector of gravitational acceleration in (11.3). These means that, when moving from cell to cell the value of g_z in $\mathbf{E_n}$ and in $\mathbf{S}_{\mathbf{n}\tau}$ may change, and also the components g_x and g_y in $\mathbf{S}_{\mathbf{n}b}$. On the other hand, with independence of the numerical solver selected it is necessary to ensure exact balance among fluxes and source terms in order to keep in time steady state configurations. This point is of paramount importance when performing numerical approaches for both fluxes and source terms.

In this work, the piecewise representation of the variables and the definition of gravity forces affected by the presence of uneven bed levels, are brought together in order to ensure the well-balance property. This is done by defining a discrete approximation of the gravity vector in the x' direction at each one dimensional RP,

$$\mathbf{g}_{\mathbf{n},k} = -(g_x, g_z)_k^T = -\left(g \sin\psi, g\cos\psi\right)_k^T \tag{12.17}$$

where ψ represents the angle of the bed normal with respect to the vertical in the one dimensional problem defined along x'. The value of ψ is computed in this work by projecting the bed slope defined in (11.2) in the normal direction of the edge as follows

$$\tan\psi = \mathbf{S}_o\mathbf{n} = \tan\theta\, n_x + \tan\gamma\, n_y \tag{12.18}$$

Now, considering that at each RP the problem is one-dimensional and defined by a single angle ψ, the flux $\mathbf{E_n}$ can be approximated by

$$\mathbf{E_n} \approx \begin{pmatrix} h(u\, n_x + v\, n_y) \\ (h\, u^2 + \frac{1}{2} g_z h^2) n_x + h\, u\, v\, n_y \\ (h\, v^2 + \frac{1}{2} g_z h^2) n_y + h\, u\, v\, n_x \end{pmatrix} \tag{12.19}$$

The source terms are reformulated as

$$\begin{aligned} \mathbf{S_{n}}_{\tau} &\approx (0, -g\ \cos(\psi) h \tan(\theta_b) n_x, -g\ \cos(\psi) h \tan(\theta_b) n_y)^T \\ \mathbf{S_{n}}_{b} &\approx (0,\ -g \sin(\psi) h n_x, -g \sin(\psi) h n_y)^T \end{aligned} \tag{12.20}$$

Then, at each k edge in Figure B.1, the following local RP along the x' direction is defined

$$\frac{\partial \mathbf{U}}{\partial t} + \frac{\partial (\mathbf{E_n})}{\partial x'} - \mathbf{S_n} = 0 \tag{12.21}$$

with $\mathbf{S_n} = \mathbf{S_{n}}_{\tau} + \mathbf{S_{n}}_{b}$, and the following initial conditions

$$\mathbf{U}(x', 0) = \begin{cases} \mathbf{U}_i & if \quad x' < 0 \\ \mathbf{U}_j & if \quad x' > 0 \end{cases} \tag{12.22}$$

Even when ignoring the exact solution of the associate RP $\mathbf{U}(x', t)$, it is possible to provide its variation by integrating (12.21) over a suitable control volume. Figure 12.4 shows a local RP with initial values $\mathbf{U}_i, \mathbf{U}_j$, and a control volume given by the time interval $[0, \Delta t]$ and the space interval $[-\Delta x', \Delta x']$, where

$$-\Delta x' \leq \lambda_{min} \Delta t, \quad \Delta x' \geq \lambda_{max} \Delta t \tag{12.23}$$

being $\lambda_{min}, \lambda_{max}$ the minimum and maximum wave velocities respectively in the domain at $t = \Delta t$, given by the eigenvalues of (12.7). Integrating (12.21) over the control volume $[0, \Delta t] \times [-\Delta x', \Delta x']$

$$\int_{-\Delta x'}^{+\Delta x'} \int_0^{\Delta t} \left(\frac{\partial \mathbf{U}}{\partial t} + \frac{\partial \mathbf{E_n}}{\partial x'} - \mathbf{S_n} \right) dx' dt = 0 \tag{12.24}$$

and reordering the following expression of integral volume for $\mathbf{U}(x', t)$ is obtained

$$\int_{-\Delta x'}^{+\Delta x'} \mathbf{U}(x', t = \Delta t) dx' \ = \ \Delta x' \left(\mathbf{U}_j + \mathbf{U}_i \right) - \delta(\mathbf{E_n})_k \Delta t + \int_{-\Delta x'}^{\Delta x'} \int_0^{\Delta t} \mathbf{S_n} dx' dt \tag{12.25}$$

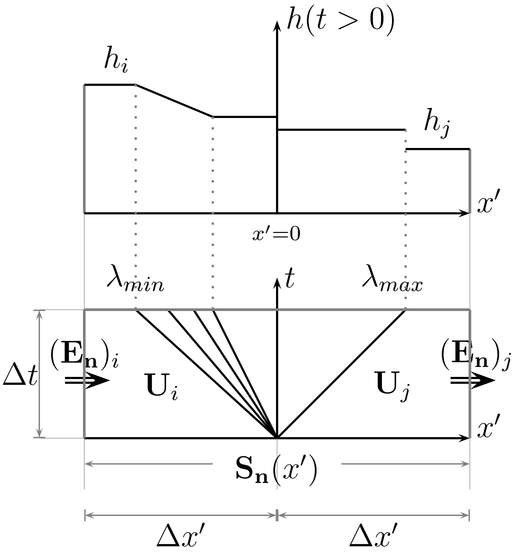

Figure 12.4: Integration control volume defined by a time interval $[0, \Delta t]$ and a space interval $[-\Delta x', \Delta x']$

with $\delta(\mathbf{E_n})_k = (\mathbf{E_n})_j - (\mathbf{E_n})_i$.

In order to ensure self similar solutions of the RP in the (x', t) plane, the source term is involved in the Riemann solver as a singular source at the discontinuity point $x' = 0$. Considering that source terms are not necessarily constant in time, the following time linearization of the nonconservative term is applied (Vázquez-Cendón, 1999; Murillo and García-Navarro, 2010b)

$$\int_{-\Delta x'}^{\Delta x'} \int_{0}^{\Delta t} \mathbf{S_n}\, dx' dt \;\approx\; \Delta t \int_{-\Delta x'}^{+\Delta x'} \mathbf{S_n}(x', 0)\, dx' \;=\; \Delta t\, (\bar{\mathbf{S}}_\mathbf{n})_k^n \tag{12.26}$$

where $\bar{\mathbf{S}}_\mathbf{n} = \bar{\mathbf{S}}_{\mathbf{n}\tau} + \bar{\mathbf{S}}_{\mathbf{n}b}$, and $\bar{\mathbf{S}}_{\mathbf{n}\tau}$ and $\bar{\mathbf{S}}_{\mathbf{n}b}$ are suitable numerical source matrices. Once all the terms of the volume integral in (12.25) are defined, the variation of the conserved variables is assumed to be given by

$$\int_{-\Delta x'}^{+\Delta x'} \mathbf{U}(x', t = \Delta t)\, dx' = \Delta x' \left(\mathbf{U}_i + \mathbf{U}_j\right) - \delta \mathbf{M}_k \Delta t \tag{12.27}$$

with

$$\delta \mathbf{M} = \delta \mathbf{E_n} - \bar{\mathbf{S}}_\mathbf{n} \tag{12.28}$$

12.3.2 Integration of the bed slope source term

As stated previously, it is necessary to ensure exact balance among fluxes and source terms with independence of the numerical solver selected in order to preserve steady state configurations. Frictionless, quiescent equilibrium over a sloping bed is represented in Figure 12.5.

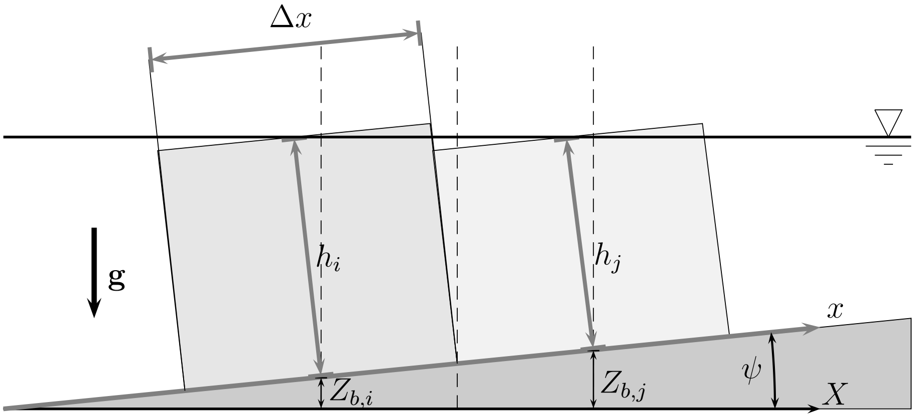

Figure 12.5: Quiescent equilibrium

For the sake of clarity, a one dimensional mesh with uniform cell size Δx is considered. The surface level is uniform per cell along X so that the the geometrical relation between variables h and Z_b in cells i and j is

$$\delta(Z_b + h\cos\psi) = (Z_b + h\cos\psi)_j - \delta(Z_b + h\cos\psi)_i = 0 \tag{12.29}$$

The momentum equation reduces to

$$\delta\left(g\cos\psi\frac{h^2}{2}\right) = \int_{-\Delta x/2}^{\Delta x/2} -g\sin(\psi)h\,dx \tag{12.30}$$

Under the hypothesis of smooth variation of the variables, and considering that $\delta Z_b = \Delta x\sin\psi$ and $\delta\frac{h^2}{2} = \widetilde{h}\delta h$, equation (12.30) becomes

$$g\cos\psi\widetilde{h}\delta h = -g\widetilde{h}\delta Z_b \tag{12.31}$$

with $\widetilde{h} = 1/2(h_i + h_j)$. Therefore the condition in (12.29) is recovered. The 1D idea is easily extended to 2D, and $\bar{\mathbf{S}}_{\mathbf{n}b}$ in (12.26) is defined as

$$\bar{\mathbf{S}}_{\mathbf{n}b} = \begin{pmatrix} 0 \\ -g_z\widetilde{h}\frac{\delta Z_b}{\cos(\psi)}n_x \\ -g_z\widetilde{h}\frac{\delta Z_b}{\cos(\psi)}n_y \end{pmatrix} \tag{12.32}$$

12.3.3 Integration of the friction stress source term

The importance of the discrete equilibrium in cases of still granular mass to provide well-balanced schemes has been widely reported (Mangeney-Castelnau et al., 2003, 2005), but it is important to stress that the well balanced property must include the presence of different types of shear stresses: turbulent stress, dispersive stress, inertial stress, viscous stress, yield stress and Coulomb frictional stress. Not all stresses act along or simultaneously in the same location of the granular mass column. Nevertheless, since the conceptual model is depth-averaged, all terms may be mathematically lumped in the same formula. In the present work, only friction induced by a Coulomb law is considered.

The discrete bed friction, $\tau_{b,k}$, must produce a resistance against the flow direction. In case of $|u_{\mathbf{n}}| > 0$, $\tau_{b,k}$ is computed as

$$\tau_{b,k} = \frac{u_{\mathbf{n}}}{|u_{\mathbf{n}}|} |\tau_{b,k}| \tag{12.33}$$

In case that $|u_{\mathbf{n}}| = 0$, $\tau_{b,k}$ is defined acting against the movement produced by the variation of the surface level

$$\tau_{b,k} = \begin{cases} |\tau_{b,k}| & \text{if} \quad \delta(Z_b + h\cos\psi)_k \leq 0 \\ -|\tau_{b,k}| & \text{if} \quad \delta(Z_b + h\cos\psi)_k > 0 \end{cases} \tag{12.34}$$

In both cases $|\tau_{b,k}|$ is calculated as

$$|\tau_{b,k}| = g_z \rho \widetilde{h} \tan(\theta_b) \tag{12.35}$$

Figure 12.6 considers a 1D test case with quiescent equilibrium over a sloping bed that involves Coulomb-type resistance forces.

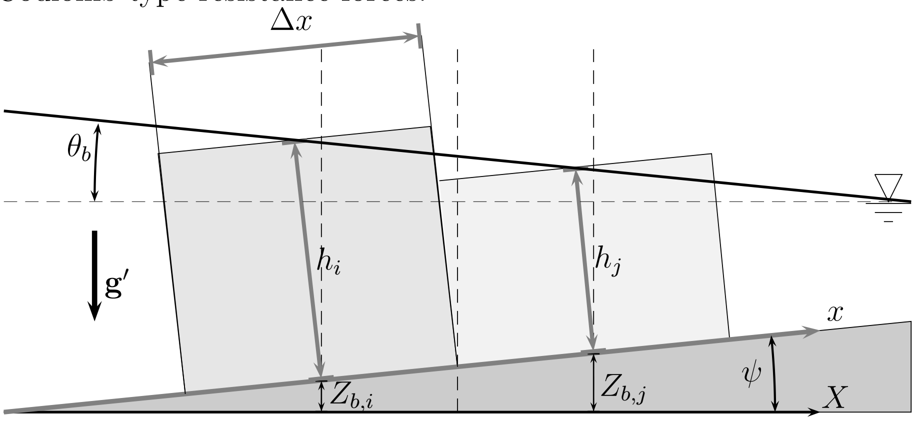

Figure 12.6: Quiescent equilibrium involving Coulomb stress

In this case the surface level has a uniform slope along X characterized by $\tan\psi = \tan\theta_b$. The geometric relation between variables h and Z_b in cells i and j is

$$\frac{\delta(Z_b + h\cos\psi)}{\Delta x\cos\psi} = tan\theta_b \tag{12.36}$$

In this case, the momentum equation reduces to

$$\delta\left(g\cos\psi\frac{h^2}{2}\right) = \int_{-\Delta x/2}^{\Delta x/2}(-g\sin(\psi)h + g\cos\psi h\tan\theta_b)\,dx \tag{12.37}$$

Under the hypothesis of smooth variation of the variables, the integral term in equation (12.37) becomes

$$\delta\left(g\cos\psi\frac{h^2}{2}\right) = g\widetilde{h}(-\delta Z_b + \cos\psi\tan\theta_b\Delta x) \tag{12.38}$$

that can be written as follows

$$g\cos\psi\widetilde{h}\delta h + g\widetilde{h}\delta Z_b = g\widetilde{h}\cos\psi\tan\theta_b\Delta x \tag{12.39}$$

leading to the equilibrium condition in (12.36). Then, $\bar{\mathbf{S}}_{\mathbf{n}\tau}$ in (12.26) is defined in a 2D mesh as follows

$$\bar{\mathbf{S}}_{\mathbf{n}\tau} = \begin{pmatrix} 0 \\ -\frac{\tau_b}{\rho}d_n n_x \\ -\frac{\tau_b}{\rho}d_n n_y \end{pmatrix}_k \tag{12.40}$$

12.3.4 Consistency Condition

The local RP in (12.21) is approximated by using the following constant coefficient linear problem

$$\frac{\partial\hat{\mathbf{U}}}{\partial t} + \mathbf{L}_{\mathbf{n},k}\frac{\partial\hat{\mathbf{U}}}{\partial x'} = 0 \tag{12.41}$$

with the following initial conditions

$$\hat{\mathbf{U}}(x',0) = \begin{cases} \mathbf{U}_i & if \quad x' < 0 \\ \mathbf{U}_j & if \quad x' > 0 \end{cases} \tag{12.42}$$

The term $\hat{\mathbf{U}}(x',t)$ represents the linearized solution given by the Roe approach, augmented to include the presence of source terms.

On the other hand, the Consistency Condition (Toro, 2009) states that the integral of the approximate solution $\hat{\mathbf{U}}(x', t)$ of the linearized RP over control volume $[0, \Delta t] \times [-\Delta x', \Delta x']$ must be equal to the integral of the exact solution $\mathbf{U}(x', t)$ given in (12.25)

$$\int_{-\Delta x'}^{\Delta x'} \hat{\mathbf{U}}(x', t = \Delta t)\, dx' = \int_{-\Delta x'}^{\Delta x'} \mathbf{U}(x', t = \Delta t)\, dx' \tag{12.43}$$

Therefore according to (12.27)

$$\int_{-\Delta x'}^{\Delta x'} \hat{\mathbf{U}}(x', t = \Delta t)\, dx' = \Delta x' \left(\mathbf{U}_i + \mathbf{U}_j\right) - \delta \mathbf{M}_k \Delta t \tag{12.44}$$

Bearing in mind (12.44), (12.41) is integrated over the control volume pictured in Figure 12.7

$$\int_{x'=-\Delta x'}^{x'=\Delta x'} \int_{t=0}^{t=\Delta t} \left(\frac{\partial \hat{\mathbf{U}}}{\partial t} + \mathbf{L}_{\mathbf{n},k} \frac{\partial \hat{\mathbf{U}}}{\partial x'} \right) dx' dt = 0 \tag{12.45}$$

and reordering, the following expression is obtained at each k edge

$$\int_{-\Delta x'}^{\Delta x'} \hat{\mathbf{U}}(x', t = \Delta t)\, dx' = \Delta x' \left(\mathbf{U}_i + \mathbf{U}_j\right) - \mathbf{L}_{\mathbf{n},k} \delta \mathbf{U}_k \Delta t \tag{12.46}$$

and since we want to satisfy (12.44), the constraint that follows is

$$\delta \mathbf{M}_k = \mathbf{L}_{\mathbf{n},k} \delta \mathbf{U}_k \tag{12.47}$$

The construction of the constant linear matrix $\mathbf{L}_{\mathbf{n},k}$ is based on the definition of an approximated Jacobian matrix of the non-linear flux $\mathbf{E}_{\mathbf{n}}$, $\widetilde{\mathbf{J}}_{\mathbf{n},k}$ (Roe, 1986)

$$\delta (\mathbf{E}_{\mathbf{n}})_k = \widetilde{\mathbf{J}}_{\mathbf{n},k} \delta \mathbf{U}_k \tag{12.48}$$

and is exploited here. This approach provides a set of 3 real eigenvalues $\widetilde{\lambda}_k^m$

$$\widetilde{\lambda}_k^1 = (\widetilde{\mathbf{u}}\mathbf{n} - \widetilde{c})_k, \qquad \widetilde{\lambda}_k^2 = (\widetilde{\mathbf{u}}\mathbf{n})_k, \qquad \widetilde{\lambda}_k^3 = (\widetilde{\mathbf{u}}\mathbf{n} + \widetilde{c})_k \tag{12.49}$$

and 3 eigenvectors $\widetilde{\mathbf{e}}_k^m$. With them, it is possible to define matrix $\widetilde{\mathbf{P}} = (\widetilde{\mathbf{e}}^1, \widetilde{\mathbf{e}}^2, \widetilde{\mathbf{e}}^3)$ as

$$\widetilde{\mathbf{P}}_k = \begin{pmatrix} 1 & 0 & 1 \\ \widetilde{u} - \widetilde{c} n_x & -\widetilde{c} n_y & \widetilde{u} + \widetilde{c} n_x \\ \widetilde{v} - \widetilde{c} n_y & \widetilde{c} n_x & \widetilde{v} + \widetilde{c} n_y \end{pmatrix}_k \tag{12.50}$$

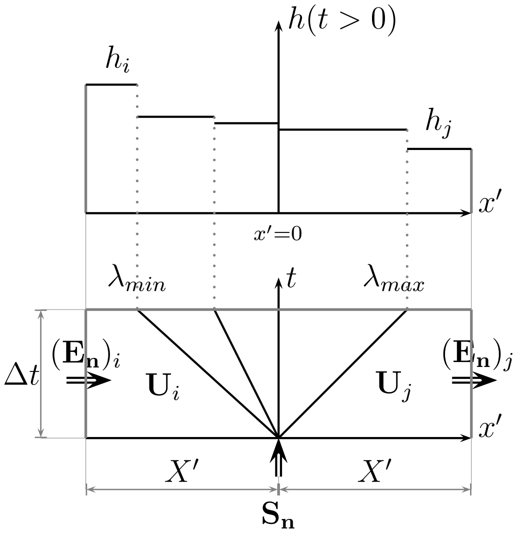

Figure 12.7: Integration control volume in interval $[0, \Delta t] \times [-\Delta x', \Delta x']$ and interpretation of the source term

with the following Roe's averages

$$\widetilde{u}_k = \frac{u_i\sqrt{h_i}+u_j\sqrt{h_j}}{\sqrt{h_i}+\sqrt{h_j}}, \qquad \widetilde{v}_k = \frac{v_i\sqrt{h_i}+v_j\sqrt{h_j}}{\sqrt{h_i}+\sqrt{h_j}}, \qquad \widetilde{c}_k = \sqrt{g\cos(\psi)\frac{h_i+h_j}{2}} \tag{12.51}$$

The approximate matrices $\widetilde{\mathbf{P}}$, and $\widetilde{\mathbf{P}}^{-1}$ diagonalize $\widetilde{\mathbf{J}}_k$

$$\widetilde{\mathbf{P}}_k^{-1}\widetilde{\mathbf{J}}_{\mathbf{n},k}\widetilde{\mathbf{P}}_k = \widetilde{\mathbf{\Lambda}}_k \tag{12.52}$$

with $\widetilde{\mathbf{\Lambda}}_k$ a diagonal matrix with eigenvalues $\widetilde{\lambda}_k^m$ in the main diagonal

$$\widetilde{\mathbf{\Lambda}}_k = \begin{pmatrix} \widetilde{\lambda}^1 & 0 & 0 \\ 0 & \widetilde{\lambda}^2 & 0 \\ 0 & 0 & \widetilde{\lambda}^3 \end{pmatrix}_k \tag{12.53}$$

The difference in vector $\mathbf{U}$ across the grid edge is projected onto the matrix eigenvectors basis

$$\delta\mathbf{U}_k = \widetilde{\mathbf{P}}_k\mathbf{A}_k \tag{12.54}$$

where $\mathbf{A}_k = \begin{pmatrix} \alpha^1 & \alpha^2 & \alpha^3 \end{pmatrix}_k^T$ contains the set of wave strengths

$$\alpha_k^{1,3} = \frac{\delta h_k}{2} \pm \frac{1}{2\widetilde{c}_k}\left(\delta\mathbf{q}_k - \widetilde{\mathbf{u}}_k\delta h_k\right)\mathbf{n}_k \quad \alpha_k^2 = \frac{1}{2\widetilde{c}_k}\left(\delta\mathbf{q}_k - \widetilde{\mathbf{u}}_k\delta h_k\right)\mathbf{n}_{T,k} \tag{12.55}$$

In order to link the source terms to the set of eigenvalues they are also projected onto the matrix eigenvectors basis

$$(\bar{\mathbf{S}}_{\mathbf{n}\tau})_k = (\widetilde{\mathbf{P}}\mathbf{B}_\tau)_k \qquad (\bar{\mathbf{S}}_{\mathbf{n}b})_k = (\widetilde{\mathbf{P}}\mathbf{B}_b)_k \tag{12.56}$$

with $\mathbf{B}_{\tau,k} = (\beta^1_\tau, \beta^2_\tau, \beta^3_\tau)^T_k$ and $\mathbf{B}_{b,k} = (\beta^1_b, \beta^2_b, \beta^3_b)^T_k$ leading to the following source strengths

$$\begin{aligned} \beta^{1,3}_{\tau,k} &= \mp\tfrac{1}{2\widetilde{c}_k}(\widetilde{S_{2\tau}}n_x + \widetilde{S_{3\tau}}n_y), \quad \beta^2_{\tau,k} = 0 \\ \beta^{1,3}_{b,k} &= \mp\tfrac{1}{2\widetilde{c}_k}(\widetilde{S_{2b}}n_x + \widetilde{S_{3b}}n_y), \quad \beta^2_{b,k} = 0 \end{aligned} \tag{12.57}$$

where source terms are expressed in a general form as $\bar{\mathbf{S}}_{\mathbf{n}\tau} = (0, \widetilde{S_{2\tau}}, \widetilde{S_{3\tau}})^T$ and $\bar{\mathbf{S}}_{\mathbf{n}b} = (0, \widetilde{S_{2b}}, \widetilde{S_{3b}})^T$. Using (12.28), (12.48) and (12.56) matrix $\delta\mathbf{M}_k$ can be expressed as

$$\delta\mathbf{M}_k = \widetilde{\mathbf{J}}_{\mathbf{n},k}\delta\mathbf{U}_k - \widetilde{\mathbf{P}}_k(\mathbf{B}_\tau + \mathbf{B}_b)_k = \sum_{m=1}^{3}\left(\widetilde{\lambda}\,\theta\alpha\widetilde{\mathbf{e}}\right)^m_k \tag{12.58}$$

with

$$\theta^m_k = \left(1 - \frac{\beta}{\widetilde{\lambda}\alpha}\right)^m_k \qquad \beta = \beta_\tau + \beta_b \tag{12.59}$$

or in matrix form

$$\delta\mathbf{M}_k = (\widetilde{\mathbf{P}}\widetilde{\mathbf{\Lambda}}\mathbf{\Theta}\widetilde{\mathbf{P}}^{-1})_k\delta\mathbf{U}_k \tag{12.60}$$

Therefore the value for the desired matrix $\mathbf{L}_{\mathbf{n},k}$ in (12.47) is

$$\mathbf{L}_{\mathbf{n},k} = (\widetilde{\mathbf{P}}\widetilde{\mathbf{\Lambda}}\mathbf{\Theta}\widetilde{\mathbf{P}}^{-1})_k \tag{12.61}$$

where $\mathbf{\Theta}$ is a diagonal matrix

$$\mathbf{\Theta}_k = \begin{pmatrix} \theta^1 & 0 & 0 \\ 0 & \theta^2 & 0 \\ 0 & 0 & \theta^3 \end{pmatrix}_k \tag{12.62}$$

that relates fluxes and source terms and that becomes equal to the identity matrix in absence of source terms.

Since the source terms are assumed at a fixed position, the solution will consist of 3 propagating waves of speed equal to the $\widetilde{\lambda}^m_k$ eigenvalues, and an extra wave located at $x' = 0$ and fixed in time.

12.3.5 2D first order finite volume model

The definition of matrix $\mathbf{L}_{\mathbf{n},k}$ is of great importance. It allows to define directly right-going and left-going wave propagations that provide the variation in time of the conserved variables

$$\delta\mathbf{M}_k = \delta\mathbf{M}^-_{i,k} + \delta\mathbf{M}^+_{j,k} = \mathbf{L}^-_{i,k}\delta\mathbf{U}_k + \mathbf{L}^+_{j,k}\delta\mathbf{U}_k \tag{12.63}$$

with

$$\delta\mathbf{M}^-_{i,k} = (\widetilde{\mathbf{P}}\widetilde{\mathbf{\Lambda}}^-\mathbf{\Theta}\widetilde{\mathbf{P}}^{-1})_k\delta\mathbf{U}_k \qquad \delta\mathbf{M}^+_{j,k} = (\widetilde{\mathbf{P}}\widetilde{\mathbf{\Lambda}}^+\mathbf{\Theta}\widetilde{\mathbf{P}}^{-1})_k\delta\mathbf{U}_k \tag{12.64}$$

and $\widetilde{\mathbf{\Lambda}}^\pm = \frac{1}{2}(\widetilde{\mathbf{\Lambda}} \pm |\widetilde{\mathbf{\Lambda}}|)$, that can be expressed as

$$\delta\mathbf{M}^-_{i,k} = \sum_{m=1}^{3}\left(\widetilde{\lambda}^-\theta\alpha\widetilde{\mathbf{e}}\right)^m_k \qquad \delta\mathbf{M}^+_{j,k} = \sum_{m=1}^{3}\left(\widetilde{\lambda}^+\theta\alpha\widetilde{\mathbf{e}}\right)^m_k \tag{12.65}$$

Following Godunov's method, the updated value $\mathbf{U}_i^{n+1}$ is defined cell averaging the contributions of the local RP shaping the contour cell and Godunov first order method is written as Murillo and García-Navarro (2010b)

$$\mathbf{U}_i^{n+1} = \mathbf{U}_i^n - \sum_{k=1}^{NE}\delta\mathbf{M}^-_{i,k}\frac{\Delta t\, l_k}{A_i} \tag{12.66}$$

with the following equivalent 1D formulation

$$\mathbf{U}_i^{n+1} = \mathbf{U}_i^n - \frac{\Delta t}{\Delta x}[\delta\mathbf{M}^-_{i+1/2} + \delta\mathbf{M}^+_{i-1/2}] \tag{12.67}$$

Superindex $^-$ becomes necessary to distinguish from outcoming fluxes to cell i at edge k, that will be referred to as $\delta\mathbf{M}^+_{j,k}$, as they update the adjacent j cell sharing the k edge.

12.3.6 Stability region

The time step limitation well known for the homogeneous case is not able to control the numerical stability in complex cases woth wet/dry fronts over irregular and rough topography. Only when implemented in combination with several numerical fixes can be used to ensure a reliable stability control as in Murillo and García-Navarro (2012a). Furthermore, the proposed numerical fixes enable the stability control avoiding the reduction of the time step below the size given by the classical CFL condition. In approximate solutions of the homogeneous case, unphysical solutions are overcome by means of well known entropy fixes. In Murillo and García-Navarro (2012a) it was argued that in presence of source terms, the augmented approximate solvers require new types of fixes, in particular a friction fix and a depth-positive ensuring fix. Source fixes modify the source strength waves β if necessary and ensure correct estimations of the source terms. The details can be found in Murillo and García-Navarro (2012a) and are not repeated here. They are applied directly in this work when performing numerical experiments, as were defined under a general framework. The careful understanding of the extended Riemann solvers is useful to ensure robust finite volumes schemes controlled by the classical CFL condition.

In the 2D framework, considering unstructured meshes, the relevant distance, that will be referred to as χ_i in each cell i must consider the volume of the cell and the length of the shared k edges.

$$\chi_i = \frac{A_i}{\max_{k=1,NE} l_k} \tag{12.68}$$

Considering that each k RP is used to deliver information to a pair of neighboring cells of different size, the distance $\min(A_i, A_j)/l_k$ is relevant. According to Murillo and García-Navarro (2010b) the time step is limited by

$$\Delta t \leq CFL\ \Delta t^{\tilde{\lambda}} \qquad \Delta t^{\tilde{\lambda}} = \frac{\min(\chi_i, \chi_j)}{\max|\widetilde{\lambda}^m|} \tag{12.69}$$

with CFL=1/2, as the construction of finite volume schemes from direct application of one-dimensional fluxes leads to reduced stability ranges (Toro, 2001).

Chapter 13

Mathematical model and numerical scheme following global coordinates

13.1 Introduction

A mathematical model together with its numerical scheme for dry granular flow over steep areas and using global coordinates, GC from now on, is presented in this Chapter.

13.2 Mathematical model

The 2D shallow equations are written following global coordinates (X, Y, Z) as follows

$$\frac{\partial \mathbf{U}}{\partial t} + \frac{\partial \mathbf{F}(\mathbf{U})}{\partial X} + \frac{\partial \mathbf{G}(\mathbf{U})}{\partial Y} = \mathbf{S}_\tau + \mathbf{S}_b \tag{13.1}$$

where

$$\mathbf{U} = (H, HU, HV)^T \tag{13.2}$$

are the conserved variables with H representing granular material depth in the Z coordinate and (U, V) the depth averaged components of the velocity vector. The fluxes are given by

$$\begin{aligned} \mathbf{F} &= \left(HU, HU^2 + \frac{1}{2} g_\psi H^2, HUV \right)^T \\ \mathbf{G} &= \left(HV, HUV, HV^2 + \frac{1}{2} g_\psi H^2 \right)^T \end{aligned} \tag{13.3}$$

with $g_\psi = g\cos^2\psi$ and ψ the direction cosine of the bed normal with respect to vertical, as depicted in Figure 13.1.

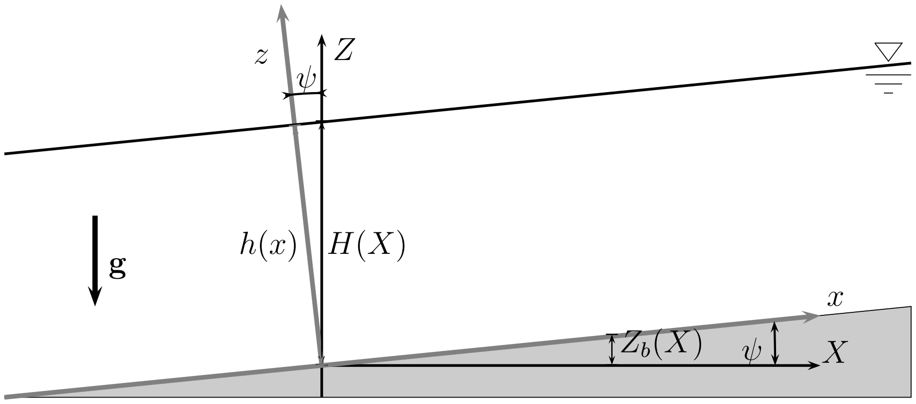

Figure 13.1: Relation among local and global coordinates

The term $\mathbf{S}_\tau$ expresses bed frictional effects

$$\mathbf{S}_\tau = \left(0, -\frac{\tau_{b,X}}{\rho}, -\frac{\tau_{b,Y}}{\rho}\right)^T \tag{13.4}$$

with $\tau_{b,X}, \tau_{b,Y}$ the bed shear stress in the X and Y direction respectively, with ρ the density of the fluid. If a Coulomb friction is considered, $\mathbf{S}_\tau$ assumes the following form

$$\mathbf{S}_\tau = (0, -g_\psi H \tan\theta_b, -g_\psi H \tan\theta_b)^T \tag{13.5}$$

being θ_b the dynamic friction angle between the bed and the flowing mass. The term $\mathbf{S}_b$

$$\mathbf{S}_b = \left(0,\ -g_\psi H\frac{\partial Z_b}{\partial X}, -g_\psi H\frac{\partial Z_b}{\partial Y}\right)^T \tag{13.6}$$

expresses the variation of the pressure force along the bottom in the X and Y direction respectively.

In order to clarify the physical basis of $g_\psi = g\cos^2\psi$ a one-dimensional problem involving a uniform slope is considered in Figure 13.1. Assuming that the surface level is parallel to the bed, the pressure is hydrostatic in the local axis z,

$$p(z) = \rho g\cos\psi(h - z) \tag{13.7}$$

and the relation among local and global variables is given by

$$z = Z\cos\psi \qquad h = H\cos\psi \tag{13.8}$$

Hence the following pressure distribution in Z can be written

$$p(Z) = \rho g \cos^2\psi (H - Z) \tag{13.9}$$

that, if integrated in Z, generates the pressure force $g_\psi H^2/2$ present in the left hand side of (13.1).

On the other hand, gravity and friction Coulomb forces exerted over the bed in the local x direction over a length Δx are given by

$$\rho g h(\sin\psi - \cos\psi \tan\theta_b)\Delta x \tag{13.10}$$

They can be simply projected in X by multiplying terms in (13.10) by $\cos\psi$. Considering that $\Delta X = \Delta x \cos\psi$ and $h = H\cos\psi$ they reduce to

$$\rho g H \cos^2\psi \left(\frac{\partial Z_b}{\partial X} - \tan\theta_b\right)\Delta X \tag{13.11}$$

leading to the source term $\mathbf{S}_b$ in (13.1).

13.3 Finite Volume Model

The same steps used to define the finite volume scheme for system in (12.1) can be applied to (13.1). For the sake of conciseness only the relevant differences will be remarked here. Again, the piecewise representation of the variables and the definition of gravity forces affected by the presence of uneven bed levels, are brought together to ensure the well-balance property at each RP, and the angle ψ is now defined as

$$\tan\psi = \mathbf{S}_o\mathbf{n} = \tan\theta n_X + \tan\gamma n_Y \tag{13.12}$$

where n_X and n_Y are the components of the unit normal vector $\mathbf{n}$ outward to the cell Ω.

Then, at each k edge a local RP along the X' direction is defined, being X' the coordinate normal to the cell edge k. The problem is defined using a single angle ψ, and the flux $\mathbf{E_n}$ can be approximated by

$$\mathbf{E_n} \approx \begin{pmatrix} H(U\,n_X + V\,n_Y) \\ (H\,U^2 + \frac{1}{2}g_\psi H^2)n_X + H\,U\,V\,n_Y \\ (H\,V^2 + \frac{1}{2}g_\psi H^2)n_Y + H\,U\,V\,n_X \end{pmatrix} \tag{13.13}$$

with $g_\psi = g\cos^2\psi$. The source terms are reformulated as

$$\begin{aligned}\mathbf{S}_{\mathbf{n}\tau} &\approx (0, -g\cos^2\psi\tan\theta_b H n_X, -g\cos^2\psi\tan\theta_b H n_Y)^T \\ \mathbf{S}_{\mathbf{n}b} &\approx (0,\ -g\cos\psi\sin\psi H n_X, -g\cos\psi\sin\psi H n_Y)^T\end{aligned} \tag{13.14}$$

Next, appropriate integrals of the source terms, $\bar{\mathbf{S}}_{\mathbf{n}\tau}$ and $\bar{\mathbf{S}}_{\mathbf{n}b}$, are defined.

13.3.1 Integration of the bed slope source term

As in local coordinates, it is necessary to ensure exact balance among fluxes and source terms in steady state configurations. Quiescent frictionless equilibrium over a sloping bed is represented in Figure 13.2.

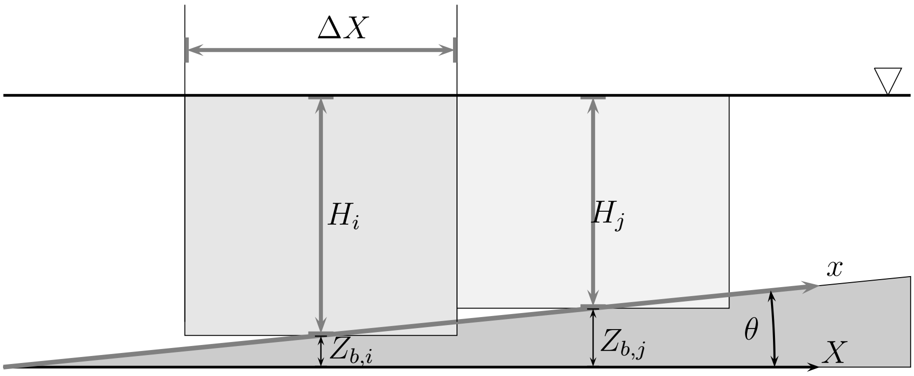

Figure 13.2: Frictionless quiescent equilibrium in global coordinates

For the sake of clarity, a one dimensional mesh with uniform cell size ΔX is considered. Surface level is constant along X and the geometrical relation between variables H and Z_b in cells i and j is

$$\delta(Z_b + H) = 0 \tag{13.15}$$

The momentum equation reduces to

$$\delta\left(g\cos^2\psi\frac{H^2}{2}\right) = \int_{-\Delta X/2}^{\Delta X/2} -g\cos^2\theta H\tan\psi\ dX = -g\cos^2\psi\widetilde{H}\delta Z_b \tag{13.16}$$

having used $\delta Z_b = \Delta X\tan\psi$. Also using $\widetilde{H} = 1/2(H_i + H_j)$,

$$g\cos^2\psi\widetilde{H}\delta H = -g\cos^2\psi\widetilde{H}\delta Z_b \tag{13.17}$$

so condition in (13.15) is recovered. In 2D, $\bar{\mathbf{H}}_\mathbf{n}$ is now defined as

$$(\bar{\mathbf{H}}_{\mathbf{n}})_k = \begin{pmatrix} 0 \\ -g_\psi \widetilde{H} \delta Z_b n_x \\ -g_\psi \widetilde{H} \delta Z_b n_y \end{pmatrix}_k \tag{13.18}$$

13.3.2 Integration of the friction stress source term

Bed friction τ_b must produce a resistance against the flow direction, so in case that $|U_{\mathbf{n}}| > 0$, $\tau_{b,k}$ is computed as

$$\tau_{b,k} = \frac{U_{\mathbf{n}}}{|U_{\mathbf{n}}|} |\tau_{b,k}| \tag{13.19}$$

otherwise, the sign is defined acting against the movement produced by the variation of the surface level

$$\tau_{b,k} = \begin{cases} |\tau_{b,k}| & \text{if} \quad \delta(Z_b + H)_k \leq 0 \\ -|\tau_{b,k}| & \text{if} \quad \delta(Z_b + H)_k > 0 \end{cases} \tag{13.20}$$

In both cases $|\tau_{b,k}|$ is defined by

$$|\tau_{b,k}| = g_\psi \rho \widetilde{H} \tan(\theta_b) \tag{13.21}$$

Figure 13.3 considers a one dimensional test case with friction quiescent equilibrium over a sloping bed that involves Coulomb-type resistance forces.

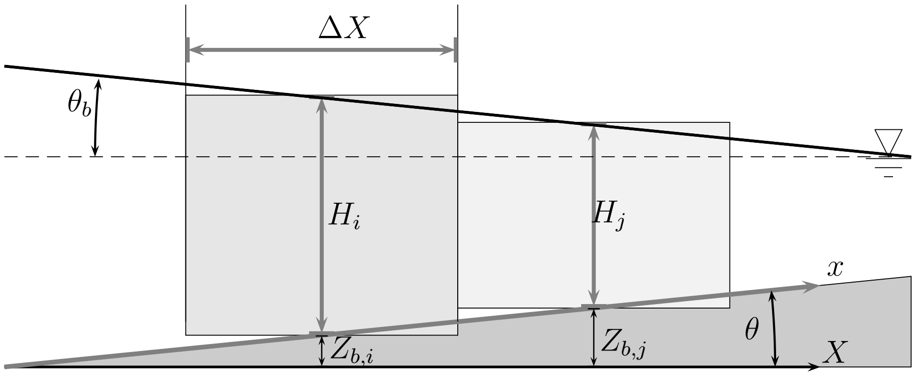

Figure 13.3: Quiescent equilibrium involving Coulomb stress in global coordinates

In this case the level surface has a constant slope given by $\tan\theta_b$ and the geometric relation between variables H and Z_b in cells i and j is

$$\frac{\delta(Z_b + H)}{\Delta X} = tan\theta_b \tag{13.22}$$

Under the hypothesis of smooth variation of the variables, the momentum equation reduces to

$$\delta\left(g\cos^2\psi\frac{H^2}{2}\right) = -g\cos^2\psi\widetilde{H}\delta Z_b + g\cos^2\psi\widetilde{H}\tan\theta_b\Delta X \tag{13.23}$$

that can be written as follows

$$\widetilde{H}\delta H = -\widetilde{H}\delta Z_b + \widetilde{H}\tan\theta_b\Delta X \tag{13.24}$$

leading to condition in (13.22). Then, $\bar{\mathbf{S}}_{\mathbf{n},k}$ is defined in a 2D mesh as follows

$$(\bar{\mathbf{S}}_{\mathbf{n}})_k = \begin{pmatrix} 0 \\ -\frac{\tau_b}{\rho}d_n n_x \\ -\frac{\tau_b}{\rho}d_n n_y \end{pmatrix}_k \tag{13.25}$$

13.3.3 Approximate solution

The approximate solutions given to define numerical fluxes can be straightforward followed by simply modifying Roe's averages, (12.51), as follows

$$\widetilde{u}_k = \frac{U_i\sqrt{H_i}+U_j\sqrt{H_j}}{\sqrt{H_i}+\sqrt{H_j}}, \qquad \widetilde{v}_k = \frac{V_i\sqrt{H_i}+V_j\sqrt{H_j}}{\sqrt{H_i}+\sqrt{H_j}}, \qquad \widetilde{c}_k = \sqrt{g\cos^2\psi\frac{H_i+H_j}{2}} \tag{13.26}$$

modifying accordingly wave strengths and source strengths using definitions of source terms in (13.18) and (13.25).

Chapter 14

Results following local and global coordinates

14.1 Introduction

In this Chapter the numerical solvers developed previously are tested against 1D and 2D experimental data in order to check the suitability of the mathematical models described in this work allowing comparisons between results provided following global and local system of coordinates.

14.2 Quiescent equilibrium and start/stop flow conditions

In this section two different academic numerical test cases are performed in order to prove that quiescent equilibrium and start/stop flow conditions are ensured for both global and local system of coordinates over a irregular two-dimensional bed. In all numerical experiments the bed level z and initial the free surface level $d = h + z$ are given by

$$z = \sqrt{(x/2)^2 + (y/2)^2} \quad d = -\sqrt{(x/2)^2 + (y/2)^2} + 0.2 \tag{14.1}$$

Therefore, the initial granular mass will not cover all the domain, as shown in Figure 14.1.

The initial mass is always in repose. The stress will be considered purely frictional. In each test case a different value of internal friction angle θ_b will be imposed. The computational domain, 0.3m × 0.3m, is defined setting the origin of coordinates in its center. As quiescent equilibrium and adequate start/stop flow conditions are defined

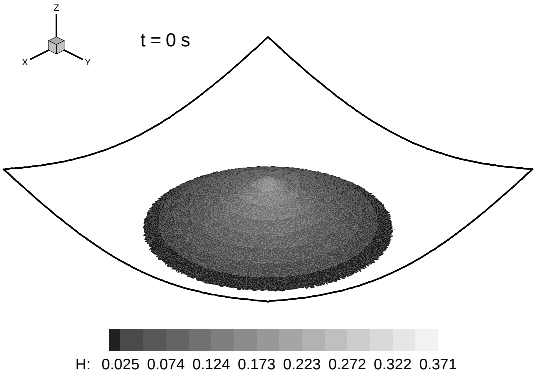

Figure 14.1: 3D contour view of the initial free surface level using GC

in this work with independence of the type of mesh, the computational domain will be discretizated in each case using rectangular, triangular structured and triangular unstructured meshes that will be referred to as M_1 (30.000 cells), M_2 (30.000 cells), M_3 (30.000 cells).

In the first test case the internal friction angle is $\theta_b = 40^o$. As the free surface slope is smaller than the maximum allowable slope that ensures static equilibrium, given by θ_b, the initial configuration is supported by internal stresses. Thus, the initial shape has to be retained in time and equal to the initial state. Figures 14.2 and 14.3 show the 3D contour view and 2D contour view for the free surface level and velocity modulus at times $t = 0$ s and $t = 0.4$ s when using GC and LC respectively in meshes M_1, M_2 and M_3. The temporal evolution of the maximum modulus of the flow velocity when using the three meshes and the LC (left) and GC (right) formulations is shown in Figure 14.4. In all cases a nil value of velocity is ensured in time with independence of the mesh topology employed. The numerical solutions do not change in time. Discrete equilibrium is provided in time with independence of the type of mesh employed for both coordinate systems.

The value of internal friction in the second test case is $\theta_b = 30^o$. The internal stresses cannot support the initial free surface and it evolves in time. Figures 14.5 and 14.6 show the contour views for the computed free surface level and velocity modulus at time $t = 1.0$ s when using GC and LC and meshes M_1, M_2 and M_3. In each case the initial mass has evolved until stop flow conditions are reached. Another static surface level is computed, where the new slope is smaller than the equilibrium one, defined by θ_b. Differences in the transient states appear depending on the type of mesh employed. For the sake of clarity, differences among the computed surface elevations will be discussed in a separate section. Figure 14.7 displays the temporal evolution of the maximum modulus of the flow velocity when using the three meshes and the LC (left) and GC (right) formulations. In all cases a nil value of velocity is ensured once static equilibrium is computed with independence of the mesh topology employed.

It is worth noticing that contrary to Pirulli et al. (2007), the mesh influence in struc-

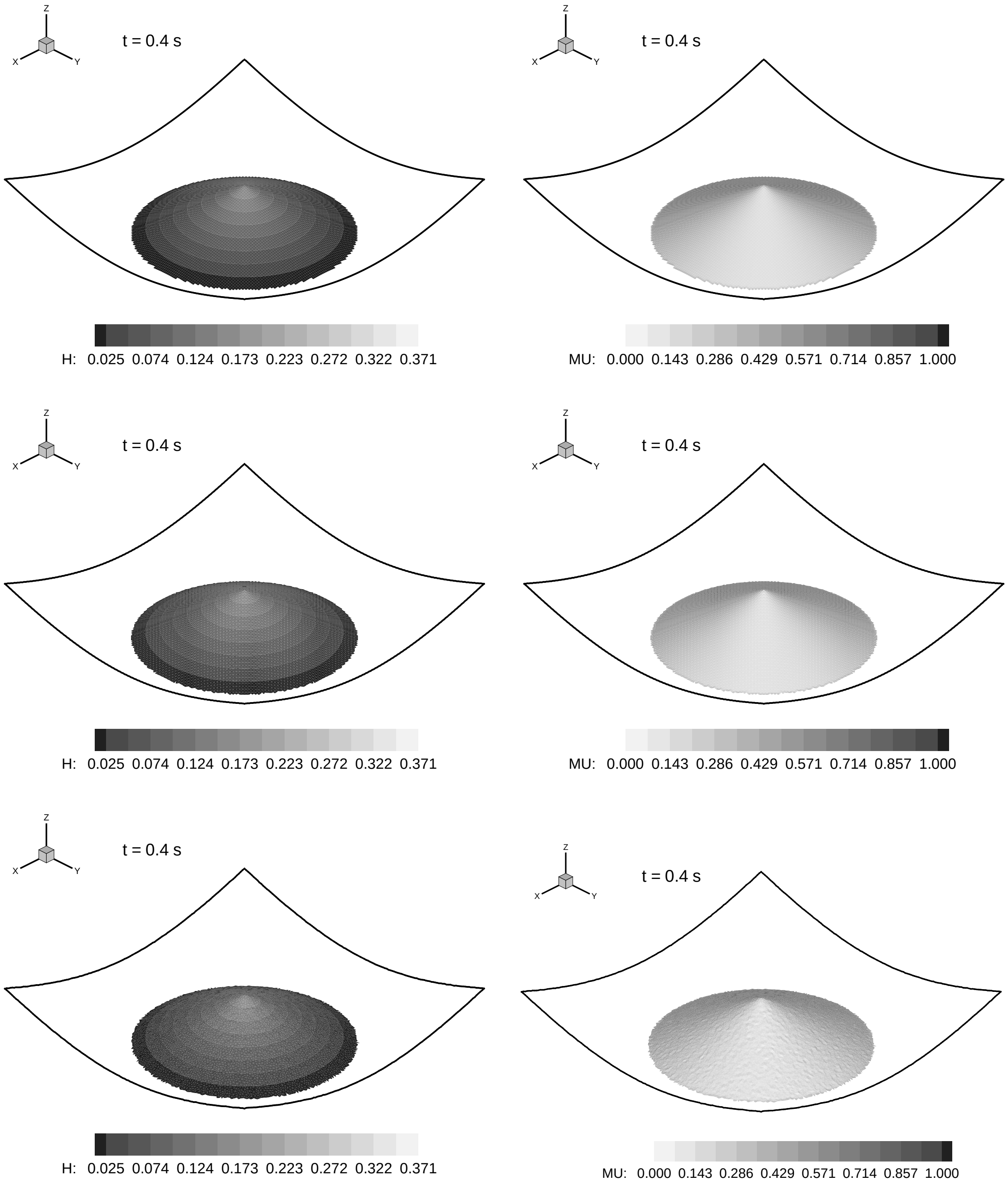

Figure 14.2: Friction angle $\theta_b = 40^o$. 3D contour views for (left) the free surface level and (right) velocity modulus at time $t = 0.4$ s using GC and (upper) mesh M_1, (middle) mesh M_2 and (lower) mesh M_3

tured grids can not be reduced by increasing the number of cells involved in the numerical computation. In Figure 14.8 is showed the numerical free surface level for meshes M_1 and M_2 when using LC (left) and GC (right) formulations, but now involving five times more cells, i.e., 150000 cells which implies a cell area equal to 2.4e-6 m^2. Computed results are also affected by the mesh topology.

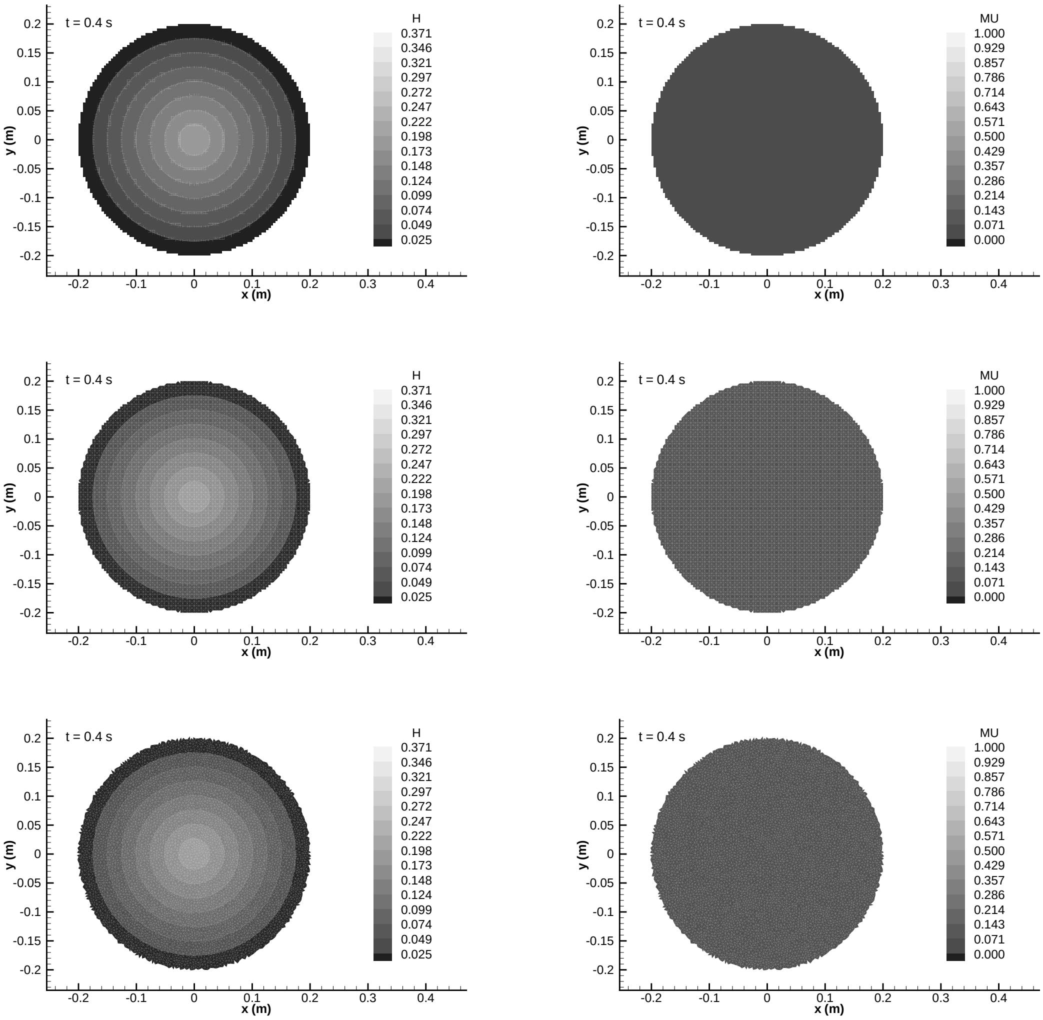

Figure 14.3: Friction angle $\theta_b = 40^o$. 2D contour views for (left) the free surface level and (right) velocity modulus at time $t = 0.4$ s using LC and (upper) mesh M_1, (middle) mesh M_2, (lower) mesh M_3

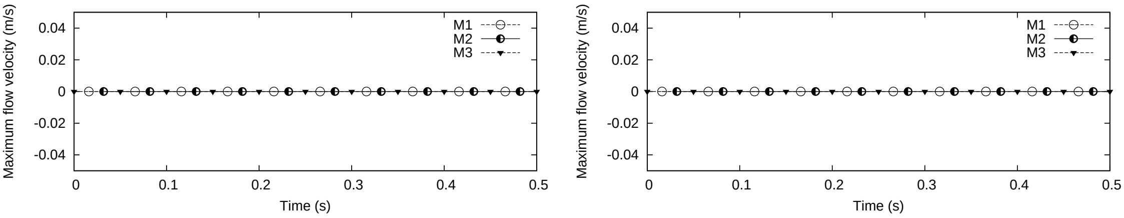

Figure 14.4: Friction angle $\theta_b = 40^o$. Temporal evolution of the maximum value of the module of flow velocity when using rectangular mesh M_1, structured triangular mesh M_2 and unstructured mesh M_3 with LC (left) and GC (right)

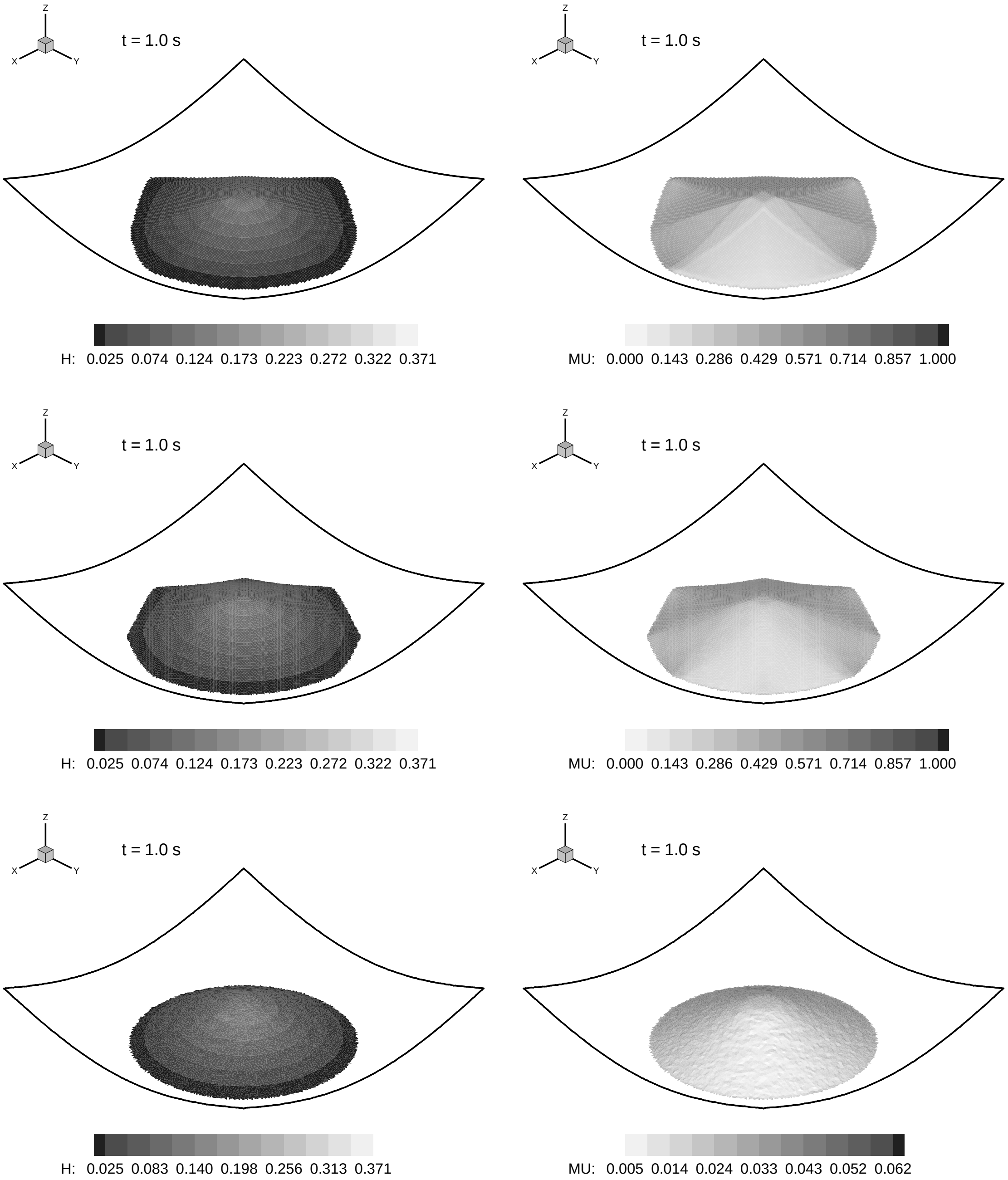

Figure 14.5: Friction angle $\theta_b = 30^o$. 3D contour views for (left) the free surface level and (right) velocity modulus at time $t = 1$ s using GC and (upper) mesh M_1, (middle) mesh M_2 and (lower) mesh M_3

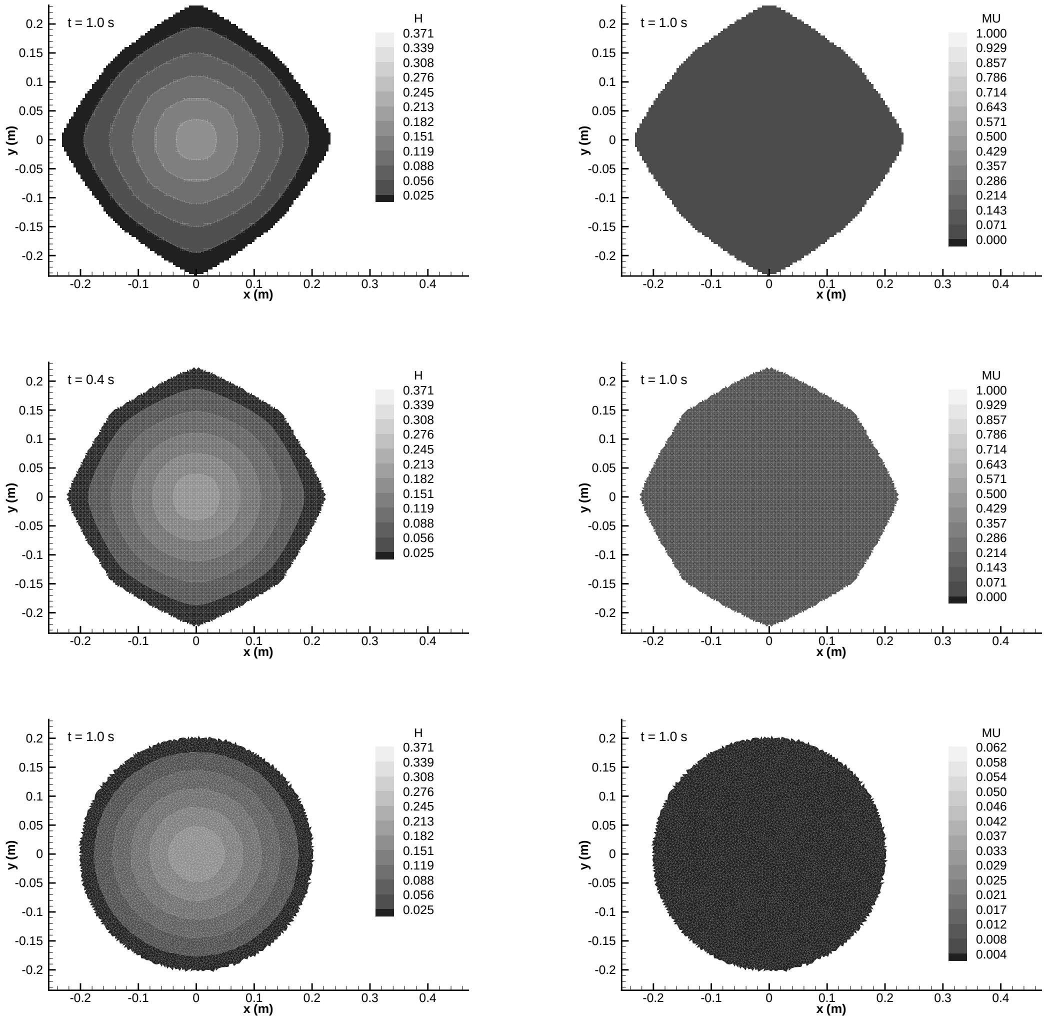

Figure 14.6: Friction angle $\theta_b = 30^o$. 2D contour views for (left) the free surface level and (right) velocity modulus at time $t = 1$ s using LC and (upper) mesh M_1, (middle) mesh M_2 and (lower) mesh M_3

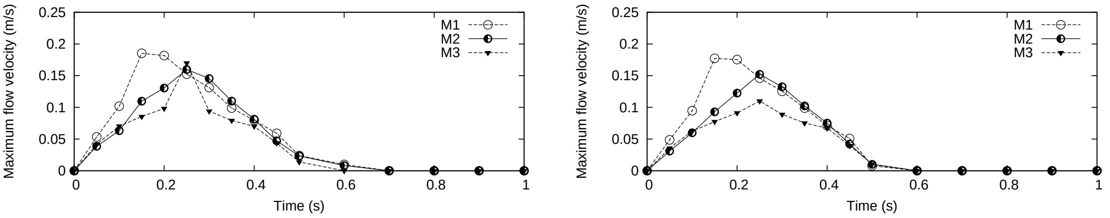

Figure 14.7: Friction angle $\theta_b = 30^o$. Temporal evolution of the maximum value of the module of flow velocity when using rectangular mesh M_1, structured triangular mesh M_2 and unstructured mesh M_3 with LC (left) and GC (right)

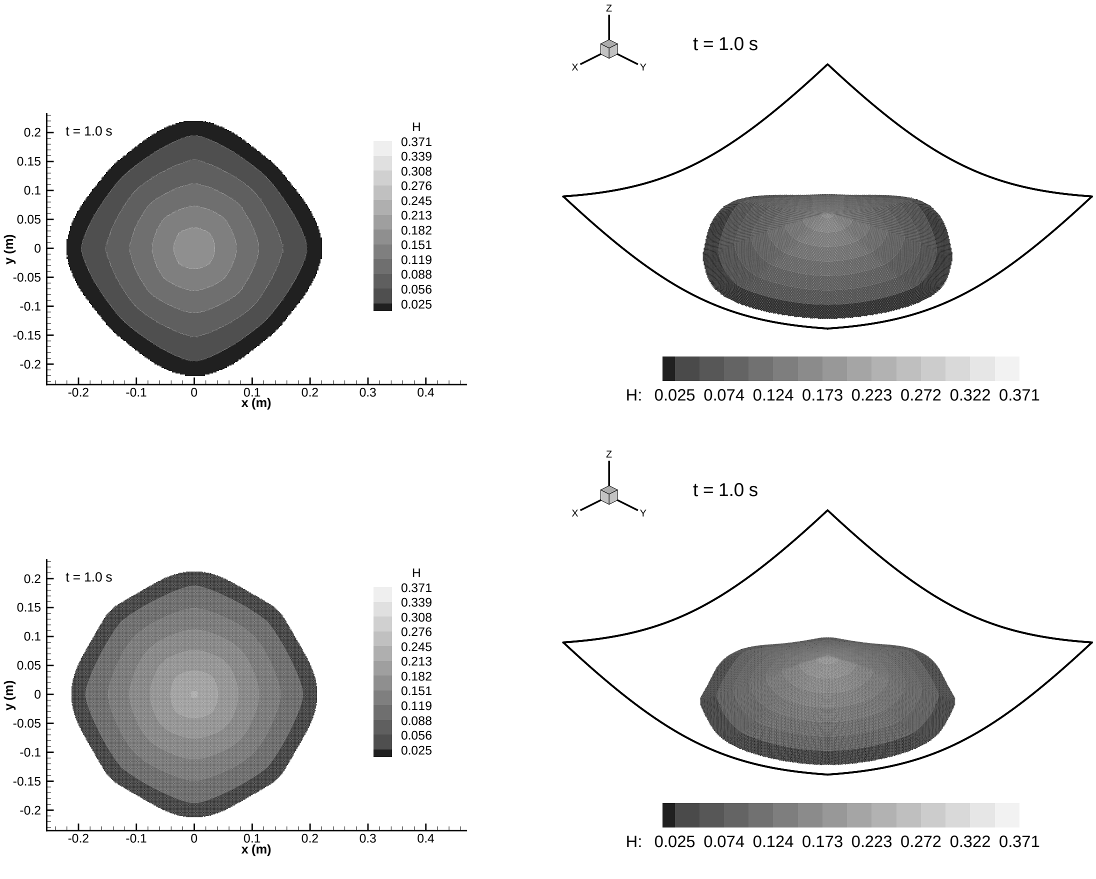

Figure 14.8: Friction angle $\theta_b = 30^o$. 3D and 2D contour views for the free surface level at time $t = 1$ s when using LC (left) and GC (right) and (upper) mesh M_1, and (lower) mesh M_2 with 150000 cells

14.3 Dam break test cases with exact solution

Following earlier works in Faccanoni and Mangeney (2012); Mangeney, A. and Heinrich, Ph. and Roche, R. (2000), the performance of the numerical scheme in (12.66) is analyzed in dam break problems with exact solutions involving a constant bed slope and a Coulomb frictional stress, using both local and global systems of coordinates. In order to derive the exact solution, the system of equations in (12.1) in LC is written in non-conservative form

$$\begin{gathered} h_t + u\, h_x + h\, u_x = 0 \\ u_t + g\ \cos\varphi h_x + u\, u_x = -g\cos\varphi P \end{gathered} \tag{14.2}$$

with $P = (\tan\varphi + \tan\theta_b)$. Following Watson et al. (1992), and setting $g' = g\cos\varphi$ the change of variables

$$\begin{gathered} \mathcal{X} = X - g'\tfrac{1}{2}Pt^2 \quad \mathcal{T} = t \\ \mathcal{U} = U - g'Pt \quad\ \ \mathcal{H} = h \end{gathered} \tag{14.3}$$

leads to the following homogeneous system of equations,

$$\begin{gathered} \mathcal{H}_\mathcal{T} + \mathcal{U}\,\mathcal{H}_\mathcal{X} + \mathcal{H}\,\mathcal{U}_\mathcal{X} = 0 \\ \mathcal{U}_\mathcal{T} + g'\,\mathcal{H}_\mathcal{X} + \mathcal{U}\,\mathcal{U}_\mathcal{X} = 0 \end{gathered} \tag{14.4}$$

. This result allows to obtain the exact solution of a dam break problem over variable bed and friction, using the result of a frictionless dam break in a wide horizontal channel over dry bed, given by the Ritter solution Ritter (1892)

$$\mathcal{H}(\mathcal{X},\mathcal{T}) = \frac{\mathcal{H}_o}{9}\left(2 - \frac{\mathcal{X}}{\mathcal{T}\,\sqrt{g'\mathcal{H}_o}}\right)^2 \tag{14.5}$$

with $\mathcal{H}_o = h_o$ the initial upstream water depth.

Alternatively, the equations formulated in global coordinates (13.1) can be written in non-conservative form as

$$\begin{gathered} H_t + u\, H_X + H\, U_X = 0 \\ U_t + g\ \cos^2\varphi H_X + U\, U_X = -g\ \cos^2\varphi\,(\tan\varphi + \tan\theta_b) \end{gathered} \tag{14.6}$$

Calling $g' = g\cos^2\varphi$, the change of variables in (14.3) provides the analytical solution in (14.5).

The definition of the direction cosine of the bed normal with respect to vertical is estimated using the projection of the bed slope defined in the normal direction of the edge. In these 1D test case the computational values of the direction cosine given by

(12.18) and (13.12) are exact. Figure 14.9 shows the exact and numerical solutions of a dam break problem over dry bed after 0.5 s in (left) LC and in GC (right) using a 1D mesh, $\Delta x = 0.1$m, setting $h_o = 10$m, φ=40^o and θ_b=24.5^o. The plots are shown using (left) h and x variables and (right) H and X variables. Note that the rarefaction tail and the advancing front positions are accurately captured by both numerical schemes.

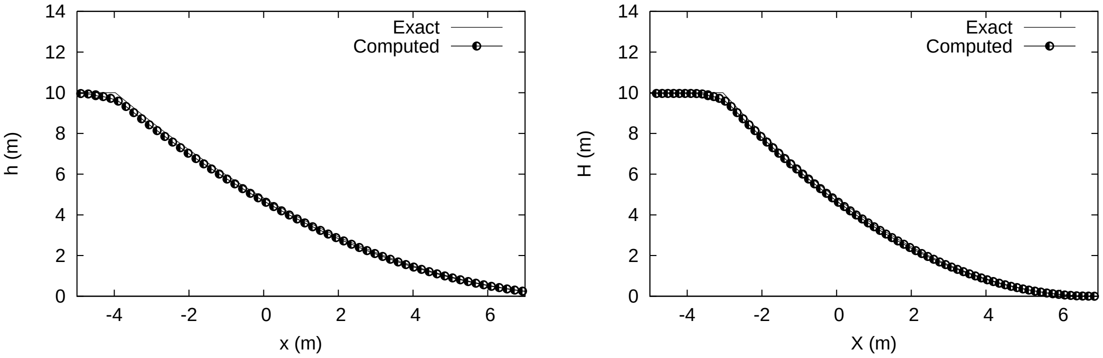

Figure 14.9: Exact and numerical solutions of a dam break problem over dry bed after 0.5 s in (left) LC system and in GC (right) using a 1D mesh

This 1D exact solution is also useful to check the performance of the numerical schemes presented in this work in 2D unstructured meshes. 2D rectangular structured meshes are not tested, as 1D and 2D formulations are completely equivalent in this test. On the other hand, even though the flow is 1D, unstructured meshes force the computation of numerical fluxes in arbitrary directions. Then, 2D numerical discretization must ensure correct 1D advance of the exact solution.

In order to allow correct comparisons among numerical results, the same mesh has been used in both local and global formulations. The definition of the bed level surface is not straightforward and requires adequate projections depending on the coordinate system selected. Figure 14.10 shows the longitudinal profile of the solution in a centered section in an unstructured 2D mesh with a cell area of approximately 3 cm^2 using approaches in (left) (12.18) and (right) (13.12). No noticeable differences appear with respect the exact solution for both coordinate systems. The position of the advancing front wave and the tail of the dam break are well captured by the numerical scheme.

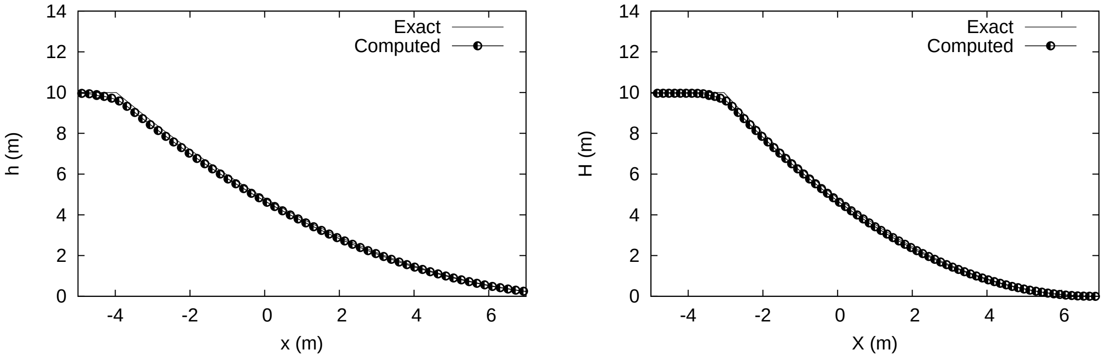

Figure 14.10: Exact and numerical solution in a longitudinal profile of the dam break problem over dry bed after 0.5 s (left) in LC system and (right) in GC using a 2D triangular unstructured mesh

14.4 Experimental 1D dam break

Experimental data are used to validate the models under realistic conditions. The morphodynamic changes that take place during the dam break in a genuinely 1D flow, the run out distance and the final height of the surface are numerically reproduced. The experiment presented in this section was carried out by Mangeney et al. (2010) in a straight narrow channel of 10 cm width with a rough rigid bed and an inclination angle equal to 30^o. The granular material was composed by glass beads, with a diameter ranging from 600 μm to 800 μm and an internal friction angle $\theta_b = 25^o$. The granular material was released after the opening of a gate. A sketch of the experiment is presented in Figure 14.11. The domain is discretized using a triangular unstructured mesh, with a cell area of 1 mm^2 and it was computed using CFL = 0.5. The same mesh discretization has been used in both LC and GC computations.

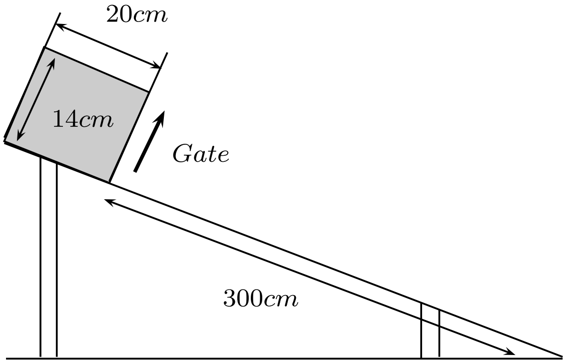

Figure 14.11: Sketch of the 1D dam break experiment

Figure 14.12, shows a sequence of 3D views of the computed free surface level evolution in time using the global system of coordinates. Glass beads move quickly, leading to a symmetric flooding wave that saturates all the wide flume. At time $t = 2.3$ s most of the morphodynamic changes have been produced.

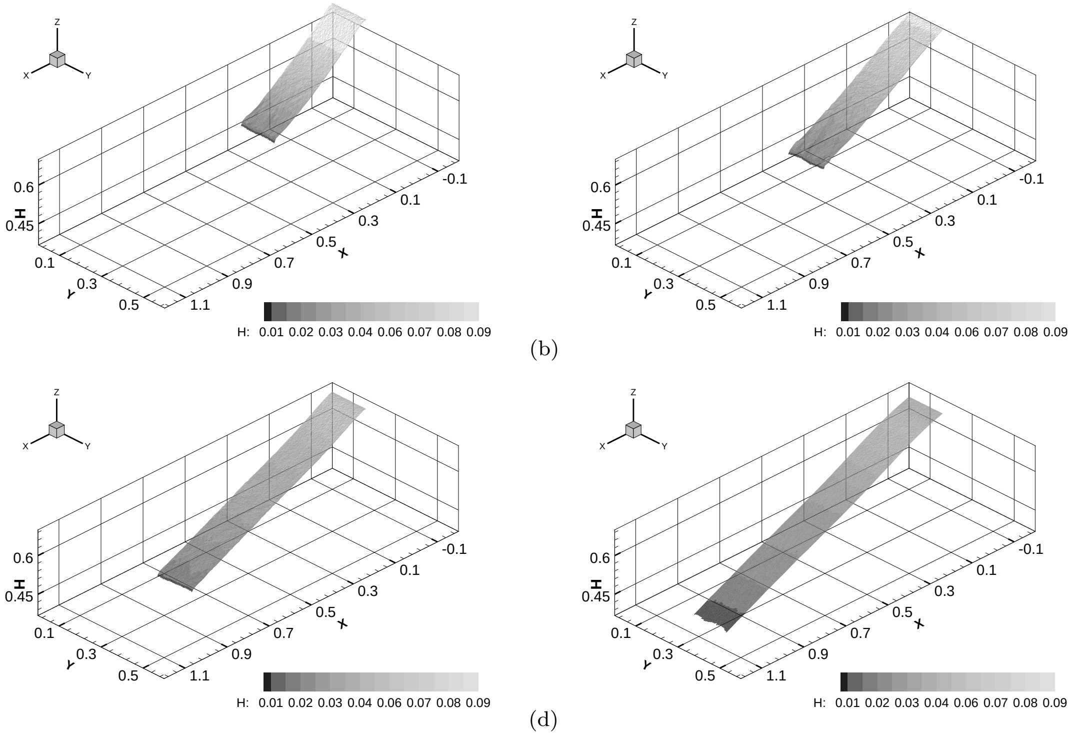

(a) (b) (c) (d)

Figure 14.12: 3D contour plot of the free surface level using GC at times (a) t=0.3s, (b) t=0.6s, (c) t=0.9s and (d) t=2.3s

Figure 14.13 compares the simulated and measured depth in a longitudinal profile at times $t = 0.32$ s, $t = 0.80$ s and $t = 2.30$ s, using (left) LC and (right) GC. Both reference systems, employing their corresponding source terms discretization, provide similar numerical results.

The most important difference is found at $t = 0.32$ s. It is caused by the perturbation generated during the experiment when part of the glass beads are dragged by the vertical movement when opening the gate. As it is well known, the shallow water equations neglect the vertical accelerations and are therefore unable to model this type of situations. In the other two instants of time the numerical scheme is able to predict accurately the temporal evolution of the surface level as well as the maximum spreading of the experiment, at $t = 2.3$ s.

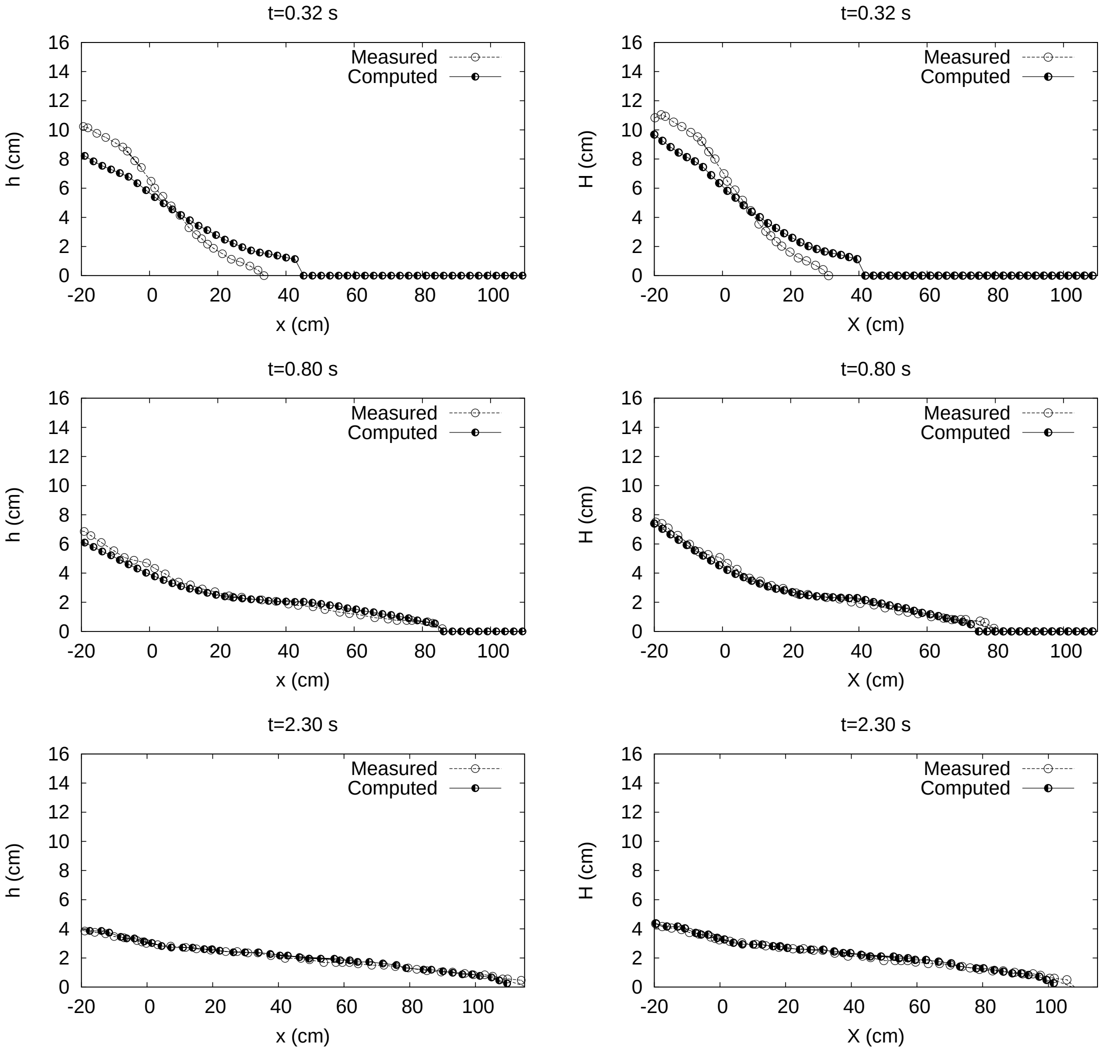

Figure 14.13: Comparison of measured and computed longitudinal profiles at times t = 0.32 s, t = 0.80 s and t = 2.30 s, using (left) LC and (right) GC

14.5 Experimental spreading of cylindrical granular mass

In this section the numerical simulation of the spreading of a cylindrical granular mass over a flat plane is considered, so both local and global formulations are equivalent. Numerical results are compared with experimental data presented in Lajeunesse et al. (2004) where glass beads were initially enclosed within a cylinder. The density of the glass beads was ρ=2500 kgm^{-3}, with a diameter d=350±50 μm. The material was characterized by an internal friction angle $\tan\theta_b$=32^o. Once the cylinder was removed, the granular material collapsed and flowed over the horizontal plane which was made of sandpaper substrate. The movement of this granular flow was recorded with high-speed cameras.

$Test$	H_i	R_i	$a = H_i/R_i$
A	0.03948	0.0705	0.56
B	0.05640	0.0705	0.80
C	0.15120	0.0280	5.40

Table 14.1: Summary of experimental cylindrical test cases

Table 14.1 summarizes the initial conditions of the glass beads within the cylinder in terms of the different aspect ratios $a = H_i/R_i$ used in the experiments, with R_i and H_i, the radius and the height of the cylinder respectively. The variation in a allows to check the limits of the mathematical model under the different regimes observed in the experiments.

Before numerical schemes are applied, a suitable mesh must be defined. The symmetry in the initial conditions makes this test case a good candidate for the analysis of the influence of the mesh discretization in the numerical solution. To analyze this possible dependence four different grids are defined: rectangular (M_1), triangular bidiagonal structured (M_{2A}), triangular diagonal structured (M_{2B}) and triangular unstructured (M_3). Triangular diagonal mesh M_{2B} is presented here following Pirulli et al. (2007). In all the cases, the squared domain 1m × 1m, was divided in 190000 cells. Figure 14.14 shows a detail of each mesh.

Test case A involves a small aspect ratio and, as a consequence most of the morphodynamic changes take place in the flanks of the cylinder. Figure 14.15 compares the measured data and numerical results in a centered cross-sectional area, at times $t=0$s, $t=0.080$s, $t=0.160$s and $t=0.240$s using $M3$. Computed results obtained in Mangeney-Castelnau et al. (2005) have also been included for comparison. Most of the significant changes take place in the first 0.080 seconds. The morphodynamic evolution is captured accurately by the numerical scheme at all times. Even the numerical results provided here are similar to those obtained in Mangeney-Castelnau et al. (2005), it is remarkable that, contrary to Mangeney-Castelnau et al. (2005), the present model

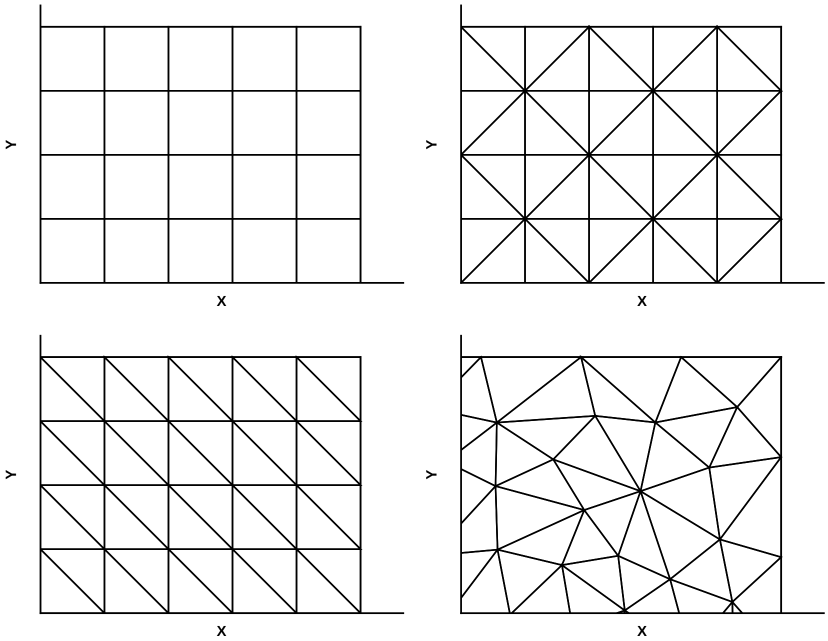

Figure 14.14: Test case A. Detail of each mesh employed: (upper-left) M_1, (upper-right) M_{2A}, (lower-left) M_{2B}, (lower-right) M_3

do not requires the definition of lower cutoff tolerances when computing the surface elevation. 3D contour plots of the free surface level (left) and of the modulus of the flow velocity (right) are depicted using meshes (upper) M_1 and (lower) M_{2A} in Figure 14.16, and using meshes (upper) M_{2B} and (lower) M_3 in Figure 14.17, at a time t=0.24s after the cylinder removal. When comparing numerical results, it becomes clear that, as it was remarked in Pirulli et al. (2007) with a mesh type equal to M_{2B}, when using structured meshes, the physical flows of the problem are masked by the propagation of an external effect introduced artificially by the mesh. Only the triangular unstructured mesh M_3 avoids the misleading preference directions of flood propagation that appear if using structured meshes. This behavior can be explained if considering that the numerical scheme involves the normal direction at each cell edge of the computational domain. In a structured mesh normal directions are orientated following the x or the y axis, therefore flow can only develop from cell to cell following two directions. In case of using an unstructured mesh an arbitrary distribution of the projections is provided, and flow can evolve using multiple directions. In any case, the stopping conditions are always ensured, resulting in a map of nil velocity with a non-uniform surface level. Figure 14.18 provides the temporal evolution of the maximum modulus of the flow velocity considering the four types of mesh studied, showing how at the final stage a quiescent equilibrium condition is achieved with independence of the mesh topology employed. It is worth noticing that as the numerical methods considered here, employ a piecewise representation of the variables within each cell, when migrating to a 3D view the information of the cells is extrapolated to the nodes and this is the reason of the appearance of a slightly roughly surface level. When observing the cross sections in

Figure 25, where the information has been taken from the center of each cell, a smooth surface level is displayed.

In this work it is clearly shown how regular meshes provide privileged flow propagation directions, that can not be corrected by using refinements of the computational mesh. In Pirulli et al. (2007), numerical experiments regarding the propagation of an semi-spherical mass were done using a triangular diagonal mesh, as mesh M_{2B}. The distortion made in the evolved solution drove to misleading results, and authors in Pirulli et al. (2007) concluded unfortunately that mesh dependency could be reduced by further mesh refinement.

Test B, presenting a higher aspect relation, mobilizes a bigger quantity of material, leading to a strong deformation both in the flanks and in the central part of the cylinder. Figure 14.19 compares the computed and experimental surface level in a centered cross-sectional area using M_3. Computed results obtained in Mangeney-Castelnau et al. (2005) have also been included for comparison. At times t=0.100s and t=0.180s, most of the granular mass is put in motion. The numerical simulation is able to capture accurately both maximum spread out and thickness of the layer. Differences are observed at the stopping stage at t=0.240s, where the numerical results tend to overestimate the sand peak with respect to the experimental one. Figure 14.20 shows 3D contour plots of the free surface level (left) and of the modulus of the flow velocity (right) at time t=0.24s, when the material reaches an static equilibrium. Figure 14.21 displays the maximum modulus of the flow velocity against time when using M_3. Bearing in mind both Figures, it can be observed how the symmetry in the solution is preserved and the velocity becomes nil in all the domain when obtaining the equilibrium stage at time t=0.24s.

In test C, the aspect ratio a is not small enough to consider vertical accelerations negligible. Even though this case cannot be well modeled using shallow water hypothesis, it is important to check whether the numerical scheme is robust enough in cases with large variations in terms of surface elevation and spreading out. Numerical results obtained for test case C are shown in Figure 14.22 at times t=0 s, $t = 0.080$ s, $t = 0.200$ s and $t = 0.240$ s using M_3. As remarked in Mangeney-Castelnau et al. (2005), even though large differences appear at the initial times, specially at time $t = 0.080$ s where the vertical acceleration strongly affects the dynamic of the granular mass, the solver is able to capture correctly the final stage. 3D contour plots of the free surface level (left) and of the modulus of the flow velocity (right) at time t=0.24s, are displayed in Figure 14.23. Again, the stopping conditions are achieved, keeping symmetry in the solution and retaining a nil velocity in all the domain.

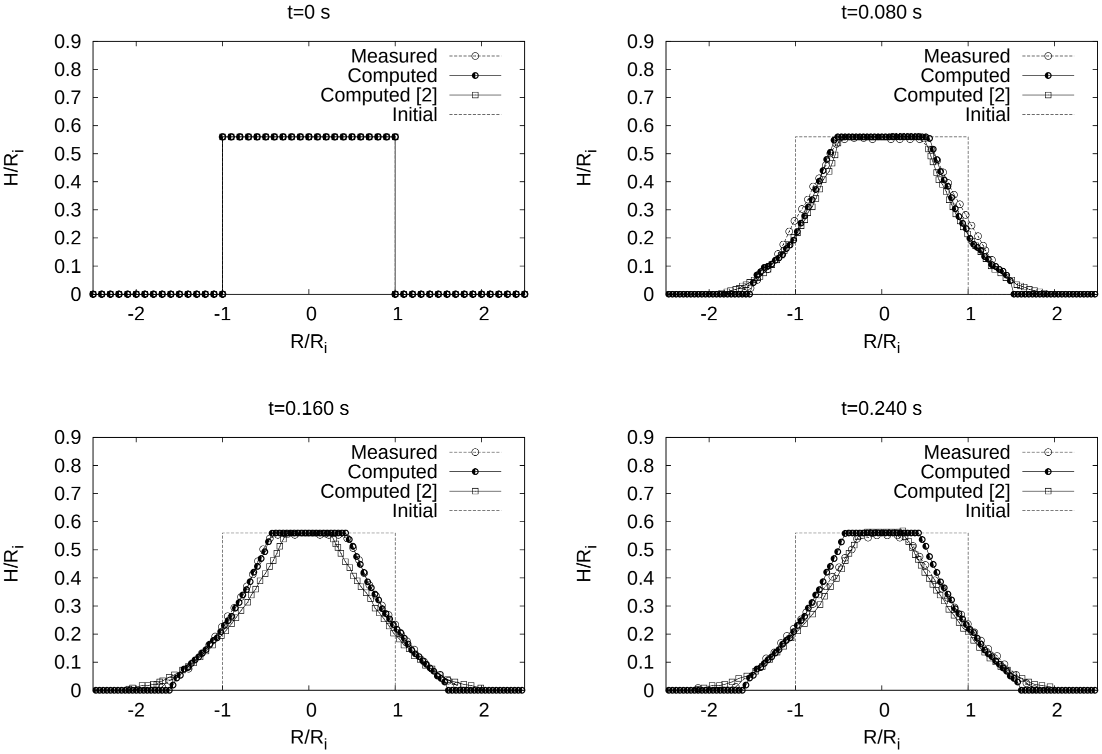

Figure 14.15: Test case A. Comparison between experimental and computed results at $t = 0$ s, $t = 0.080$ s, $t = 0.160$ s and $t = 0.240$ s using M_3

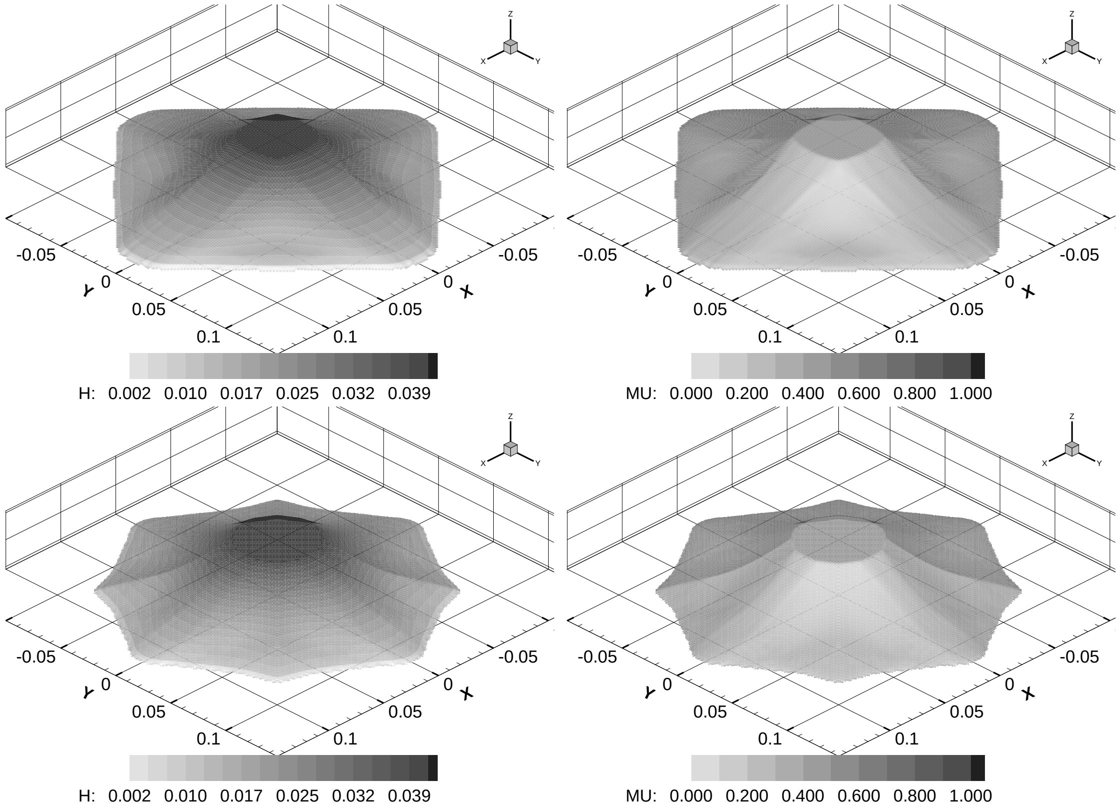

Figure 14.16: Test case A. 3D contour plot of the free surface level (left) and modulus of the flow velocity (right) using rectangular mesh M_1 (upper) and structured triangular mesh M_{2A} (lower) at time t=0.24s

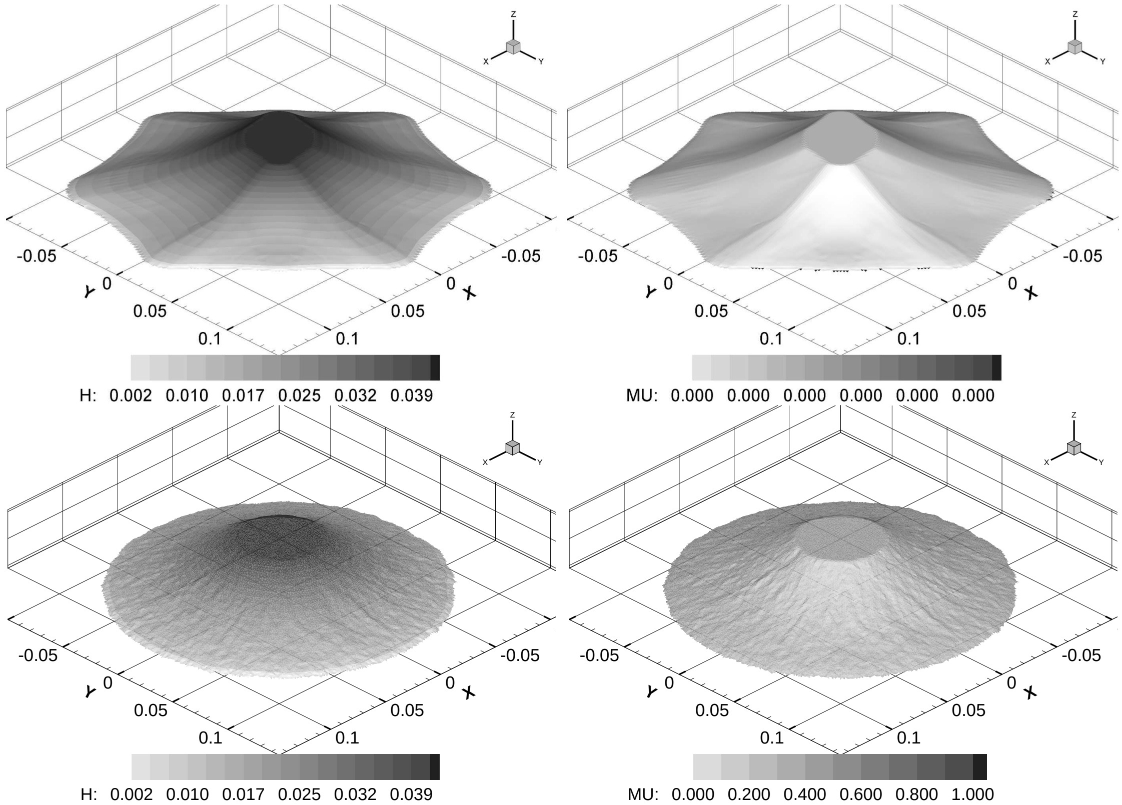

Figure 14.17: Test case A. 3D contour plot of the free surface level (left) and modulus of the flow velocity (right) using structured triangular mesh M_{2B} (upper) and unstructured triangular mesh M_3 (lower) at time t=0.24s

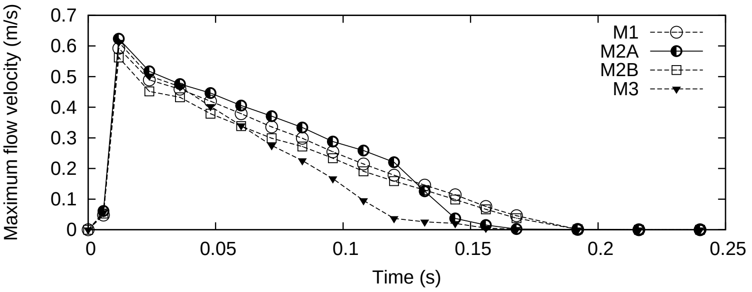

Figure 14.18: Test case A. Temporal evolution of the maximum modulus of flow velocity using rectangular mesh M_1, structured triangular mesh M_2 and unstructured triangular mesh M_3

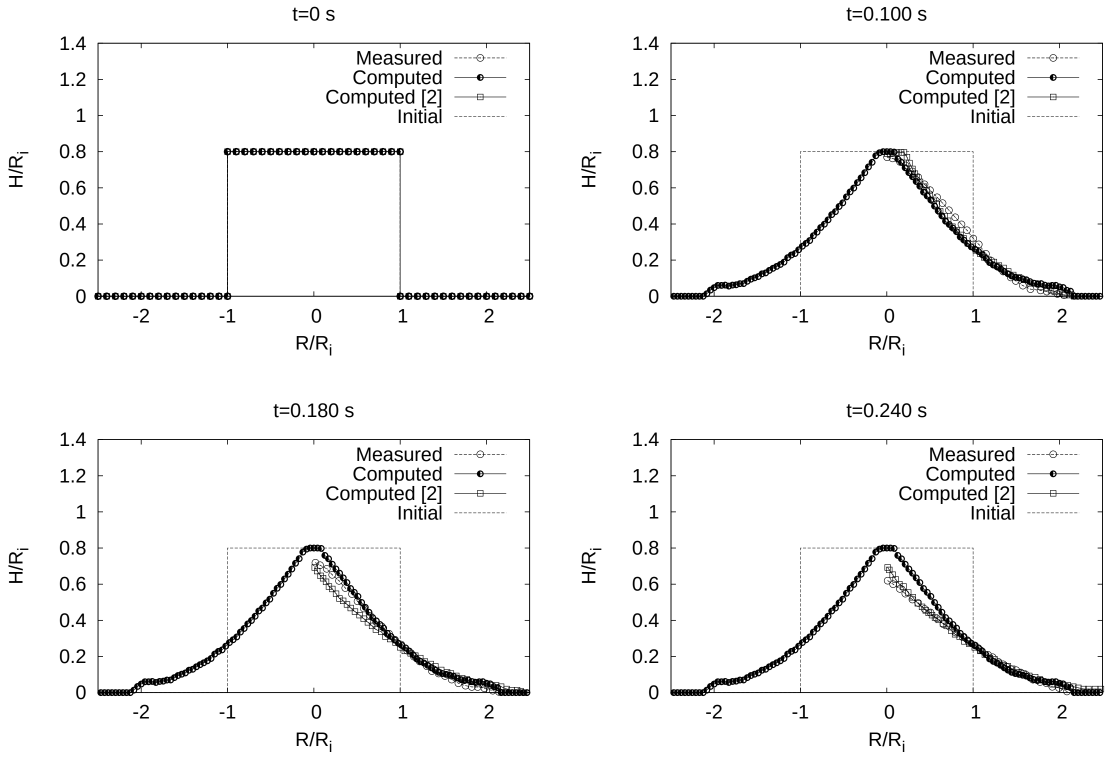

Figure 14.19: Test case B. Comparison between experimental and computed results at $t = 0$ s, $t = 0.100$ s, $t = 0.180$ s and $t = 0.240$ s using M_3

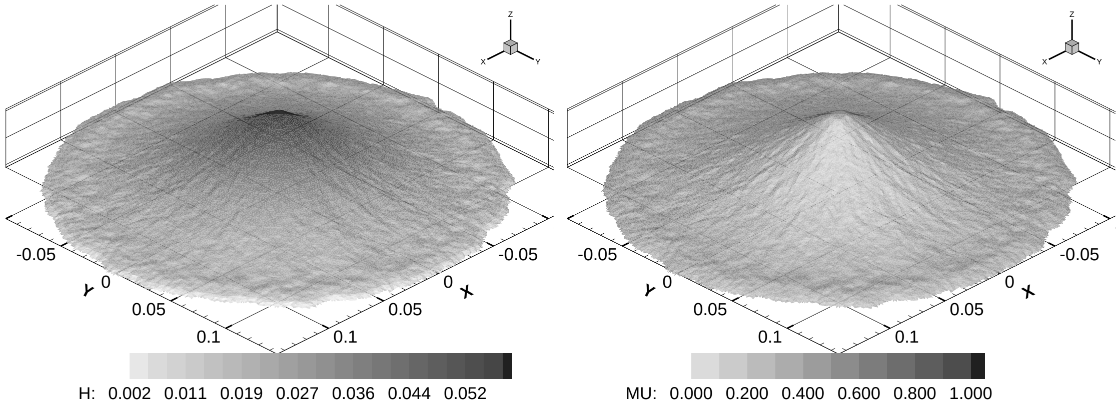

Figure 14.20: Test case B. 3D contour plot of the free surface level (left) and modulus of the flow velocity (right) at time t=0.24s using M_3

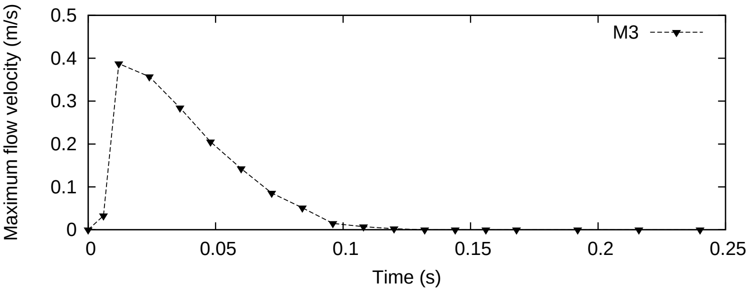

Figure 14.21: Test case B. Temporal evolution of the maximum modulus of the flow velocity using unstructured triangular mesh M_3

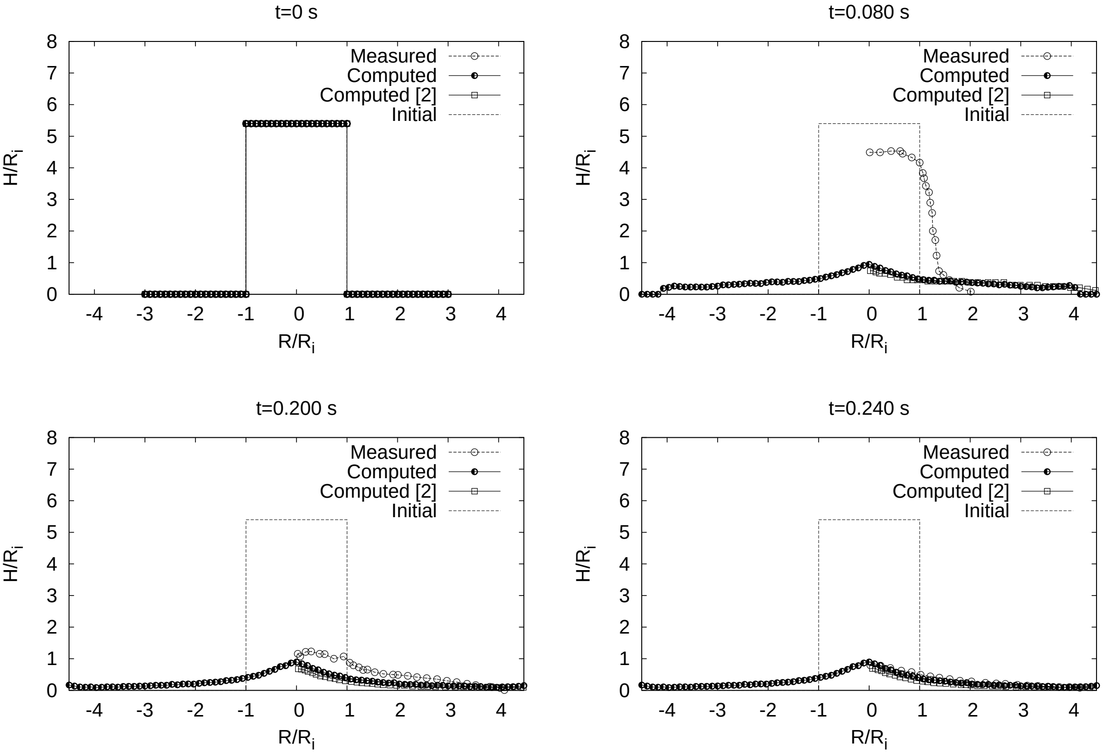

Figure 14.22: Test case C. Comparison between experimental and computed results at t=0 s, t = 0.080 s, t = 0.200 s and t = 0.240 s using M_3

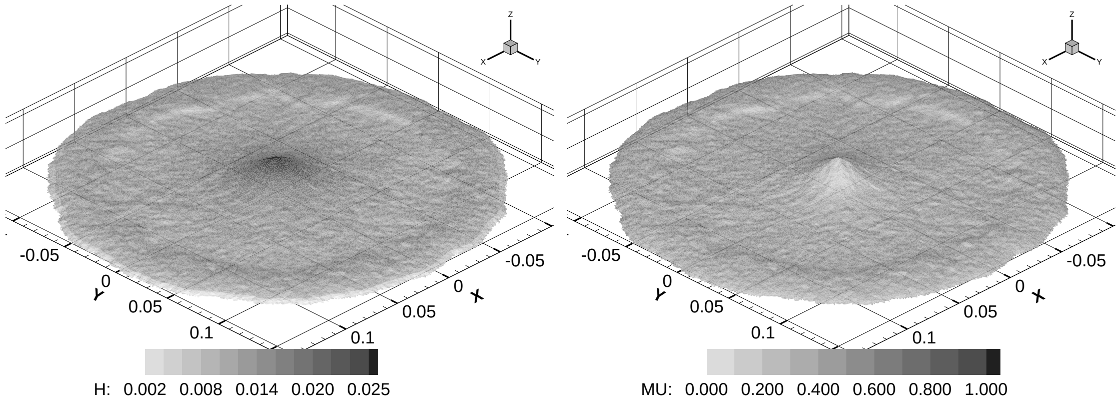

Figure 14.23: Test case C. 3D contour plot of the free surface level (left) and modulus of the flow velocity (right) at time t=0.24s using M_3

14.6 Experimental spreading of granular mass over a fixed rough inclined plane

The set of experiments presented in this section were carried out over a rough inclined plane, 2 m long and 70 cm wide, with different slopes as reported in Pouliquen and Forterre (2002). Glass beads, with 0.5 mm ± 0.04 in diameter, were confined within a spherical cap, Figure 14.24, with a maximum depth of 3.1 cm. The internal friction angle was estimated equal to 18^o. The temporal evolution of the free surface level in a period of 6 s was obtained by analysis of the images taken with a CCD camera during the flow. The numerical schemes will be used to predict the spreading of the granular flow influenced by a uniform longitudinal slope. It is worth noticing that in the same work, [4], numerical simulations were also performed but considering a friction law more sophisticated than the simple Coulomb law.

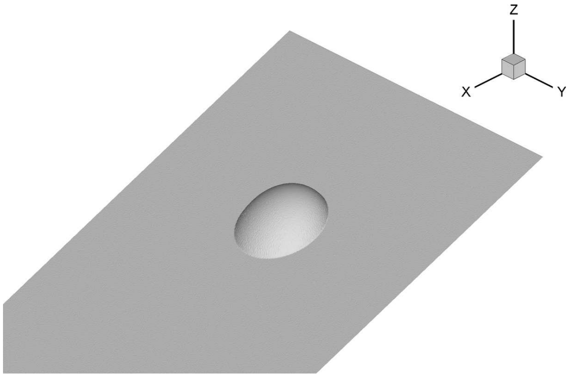

Figure 14.24: 3D contour plot of the initial condition

Again, three different types of grids are defined: rectangular (M_1), triangular structured (M_2) and triangular unstructured (M_3). In all cases the cell area is 2 mm^2, and each mesh contains the same number of cells. The CFL is set equal to 0.4 in all cases. It is worth emphasizing that, the definitions of the bed level and initial layer depth at the different cells depend on the coordinate system selected. Figure 14.25 shows the longitudinal profile of the initial condition for the layer thickness using local coordinates and global coordinates. While symmetric initial conditions appear in the local reference, initial conditions in the global reference present a deformation associated to the projection of the layer thickness in the vertical direction, leading to larger values of depth.

Figure 14.26 shows 3D contour plots of the numerical results for the free surface level using (upper-left) M_1, (upper-right) M_2 and (lower) M_3 at time t=0.96 s using GC. The final shape of the spreading mass is strongly mesh dependent when using structured meshes. Only unstructured mesh M_3, characterized by an arbitrary definition of the cell topology avoids undesirable effects in the solution. Therefore, only the numerical solutions obtained using an unstructured are shown from now on.

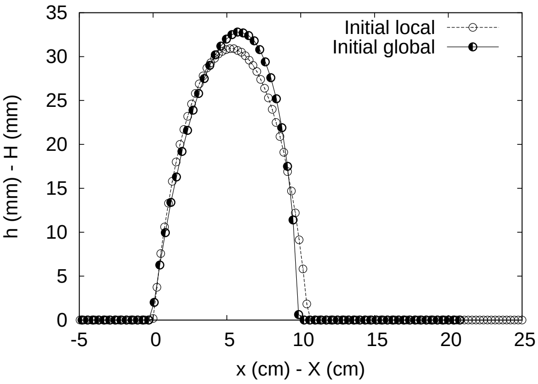

Figure 14.25: Longitudinal profile of the initial condition for the layer thickness using LC and GC

Figure 14.27 shows the calculated free surface level at different times, with a bed slope angle equal to 23^o using (left) LC and (right) GC. Both coordinate systems provide accurate results. In general, the temporal spreading of the granular flow is accurately captured by both numerical schemes, allowing to predict reasonably well the thickness layer evolution and the run out of the flow. Figure 14.28 shows the numerical results at time t=6 s when stooping conditions have been reached.

A temporal sequence of plant views is plotted in Figure 14.29, numerically obtained using the global coordinate system. In the first instants of time, the mass put in motion spreads over the longitudinal and transversal direction before it is oriented to the steeper direction which provokes the stretching of the flow. The tail of the flow remains at rest whereas the front propagates down the initial stage.

Figure 14.30 shows the computational and experimental results obtained at rest conditions, t=6s, using LC (left) and GC (right). Both measured and computed length and thickness of the granular material change according to the inclination, ranging from 19^o to 24^o. Both local and global formulations provide similar accuracy and perform adequately in all cases, predicting faithfully the thickness of the movable layer and the spreading over the rough plane as the inclination angle is augmented.

14.7 Experimental spreading of granular mass over a initially static layer

Another experiment was also performed in Pouliquen and Forterre (2002), over the same inclined plane but including a initially static layer, with a thickness of 2.7 mm. If assuming that the initially static layer behaves as an erodible bed, extra equations describing the interaction between layers are required and the definition of the approximate solver changes (Rosatti et al., 2008b). Following Pouliquen and Forterre (2002) in this work the evolution of the spreading mass is considered here assuming that local thickness involves the initial static layer. The spherical cap was removed in this case over this layer. Figure 14.31 presents the longitudinal profile for the free surface level compared with the experimental data obtained in this test using local and global coordinates. Both systems of coordinates provide to similar results. The largest differences are noticed at time t=0.24 s. At times t=0.72 s an t=1.68 s numerical results provide a good tendency with the experimental data driving to the final stage, at t=3.6 s. Although the maximum run out tends to be slightly overestimated with respect the measurement observed in the laboratory, the temporal evolution of the flow has been tracked generally well by the numerical scheme.

Figure 14.32 shows a 3D view of the predicted thickness evolution considering the presence of an initial deformable layer (right) and over rigid bed (left) at times t = 0.24, 0.72, 1.68 and 3.6 s using global coordinates. In both cases the slope angle is 23^o. The evolution of the granular mass in both cases is completely different. In presence of an initial layer, the advancing front tends to decelerate and in this fashion the front is widened until reaching certain shape and then it propagates down the slope. In case of not having an initial layer the shape of the avalanche is better conserved during the longitudinal run out.

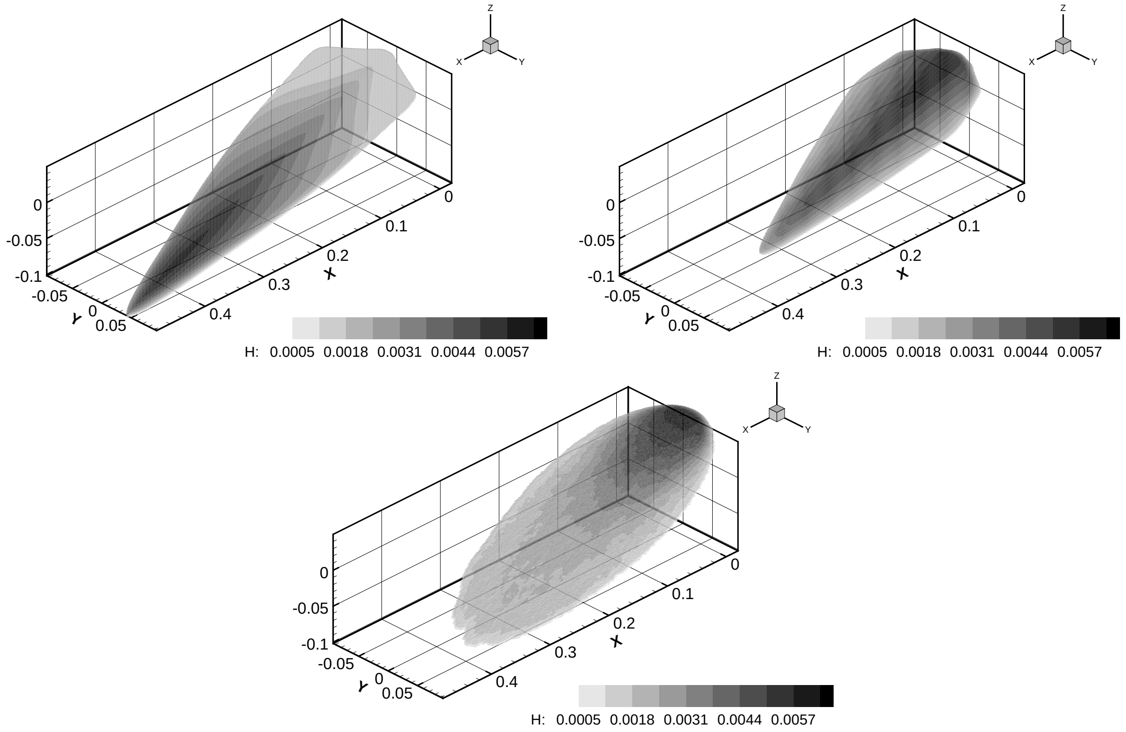

Figure 14.26: 3D contour plots of the free surface level using (upper-left) M_1, (upper-right) M_2 and (lower) M_3 at time t=0.96 s using GC

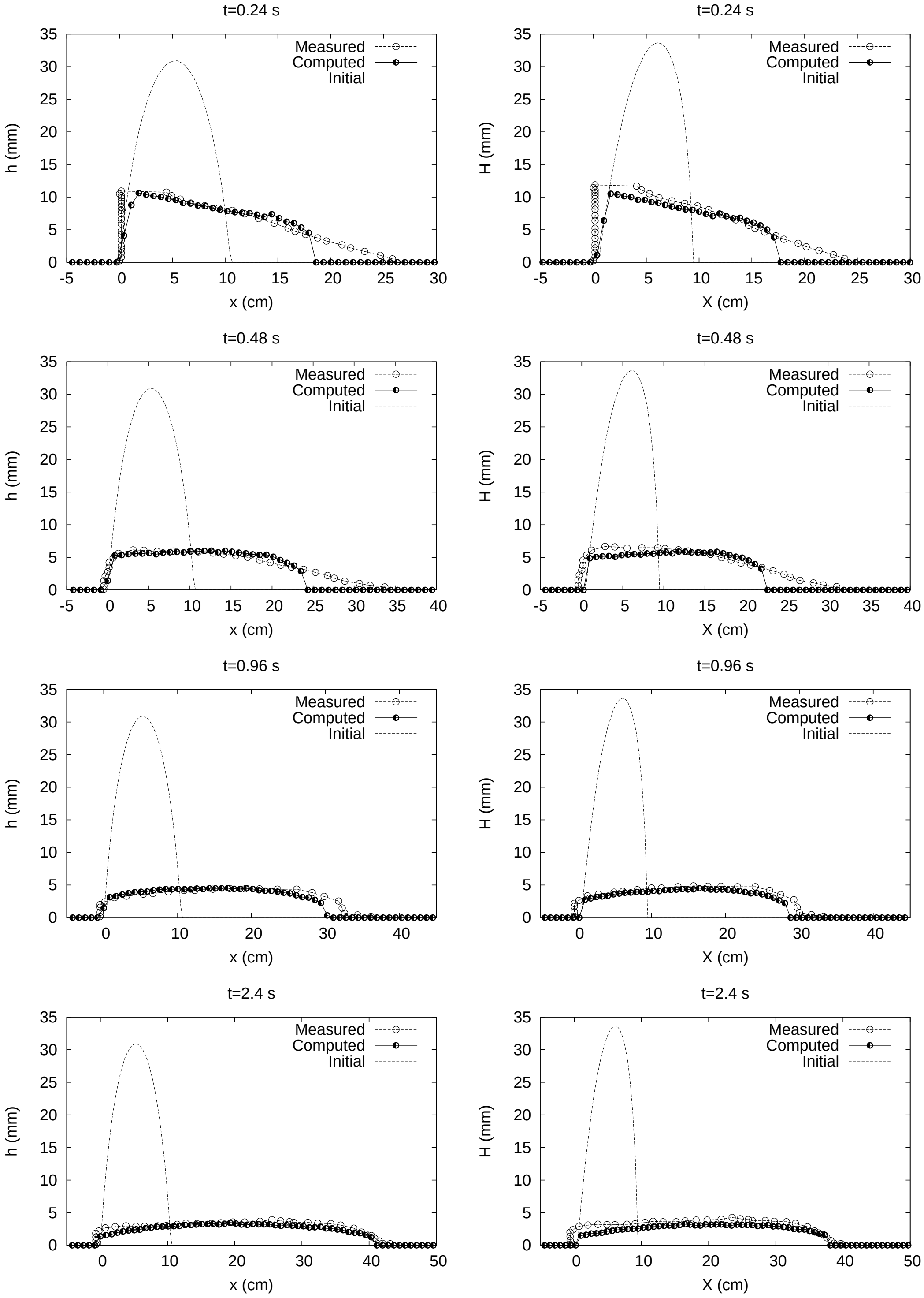

Figure 14.27: Bed slope angle of 23^o. Measured and computed thickness profiles along $y = 0$ at times $t = 0.24$, 0.48, 0.96 and 2.40 s, using (left) LC and (right) GC

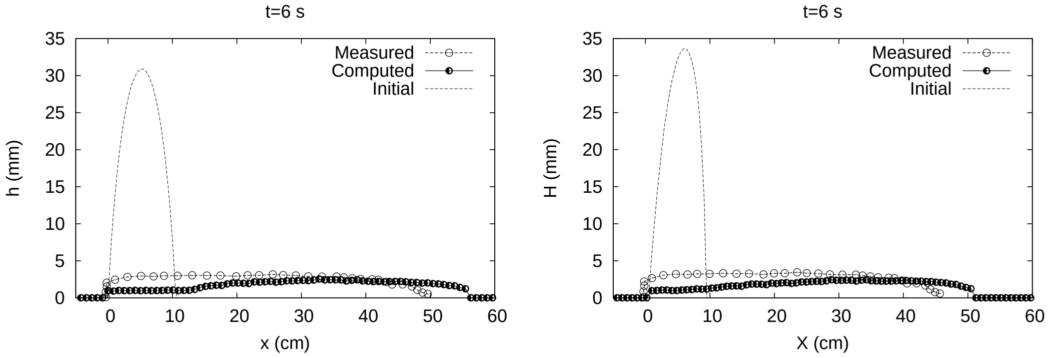

Figure 14.28: Bed slope angle of 23^o. Measured and computed thickness profiles along $y = 0$ at time $t = 6$ s, using (left) LC and (right) GC

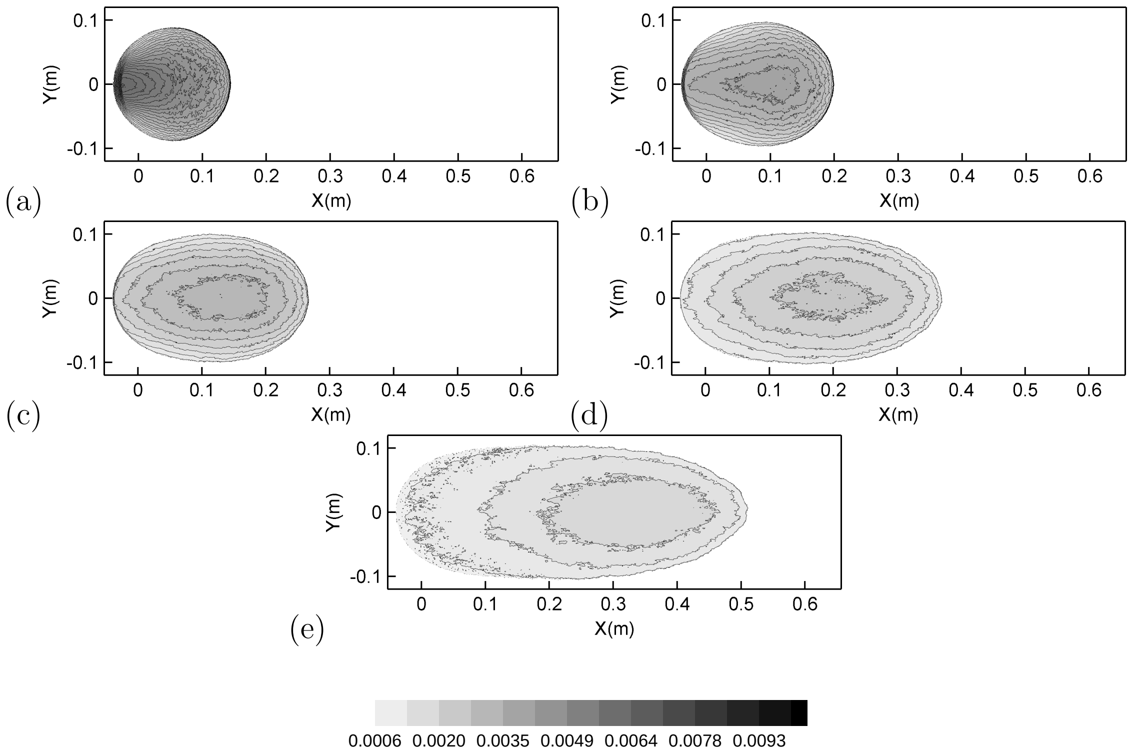

Figure 14.29: Temporal evolution: contours of constant thickness every 0.5 mm at times $t = 0.24$ s (a), $t = 0.48$ s (b), $t = 0.96$ s (c), $t = 2.40$ s (d) and $t = 6$ s (e) with a slope angle of 23^o using GC

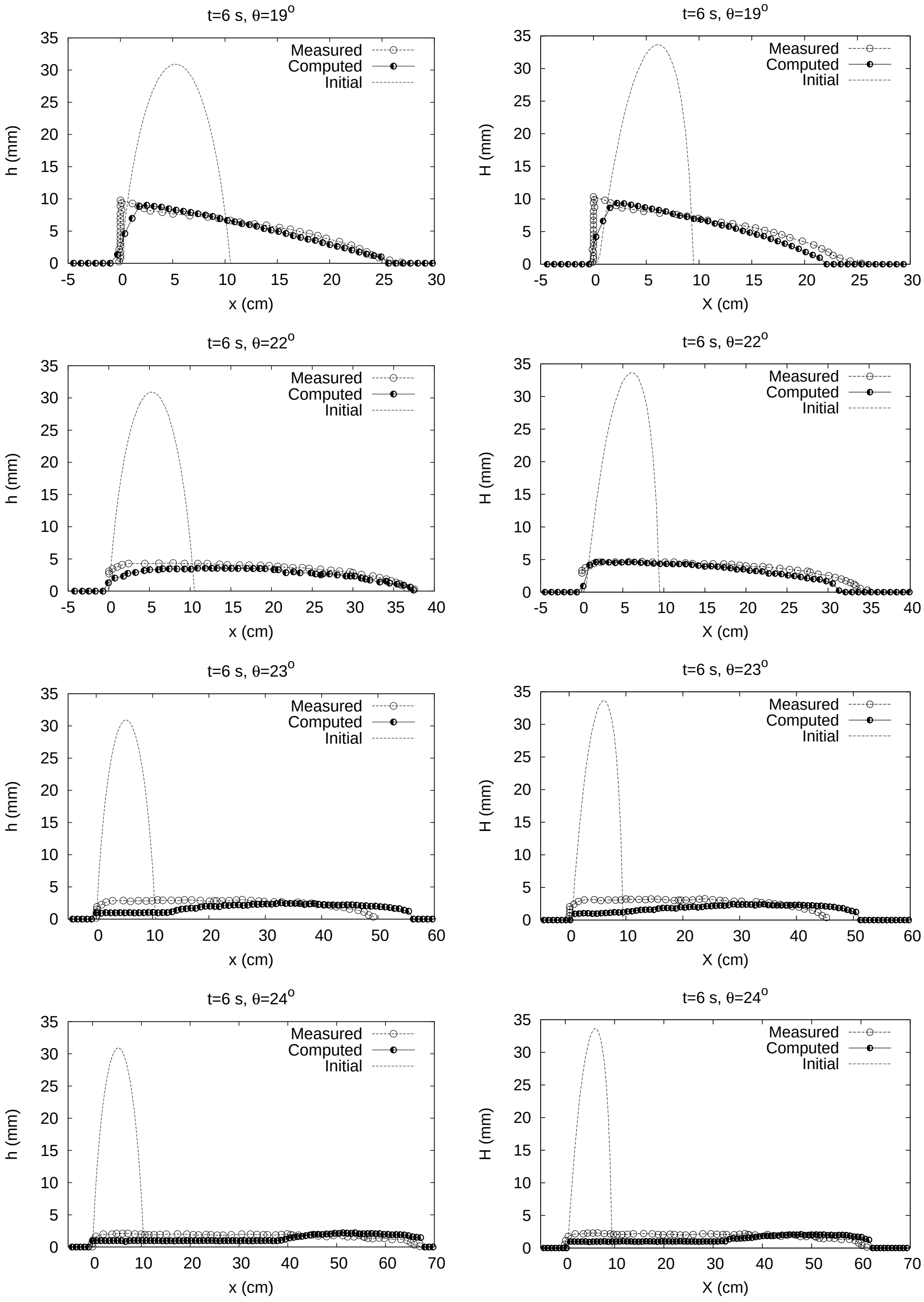

Figure 14.30: Measured and computed thickness profiles along y = 0 for the free level surface obtained at t=6s with slope angles equal to 19^o, 22^o, 23^o and 24^o, using (left) LC and (right) GC

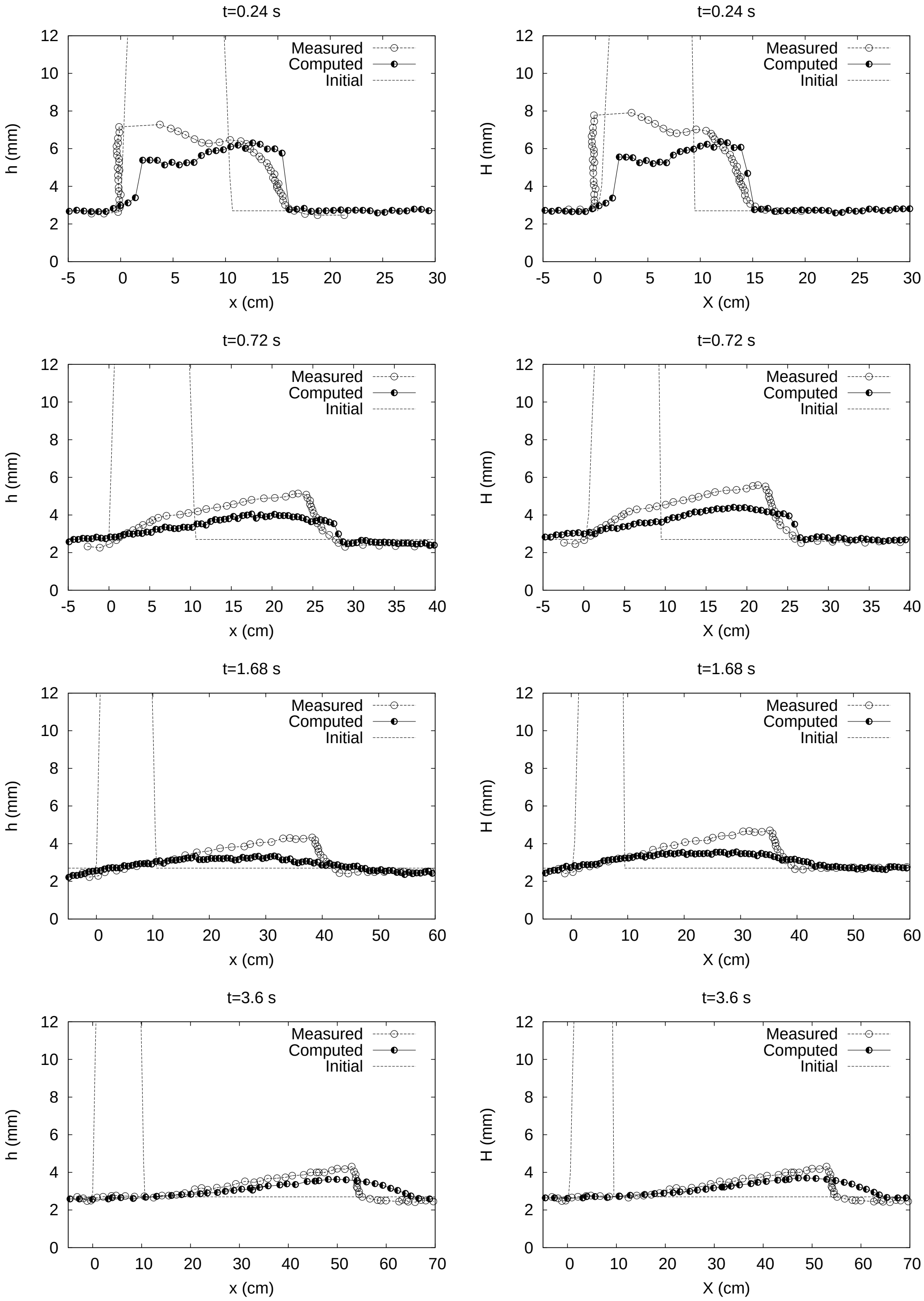

Figure 14.31: Bed slope angle 23^o. Measured and computed thickness profiles along y = 0 at times $t = 0.24$ s, $t = 0.72$ s, $t = 1.68$ s and $t = 3.6$ s with an initial static layer using (left) LC and (right) GC

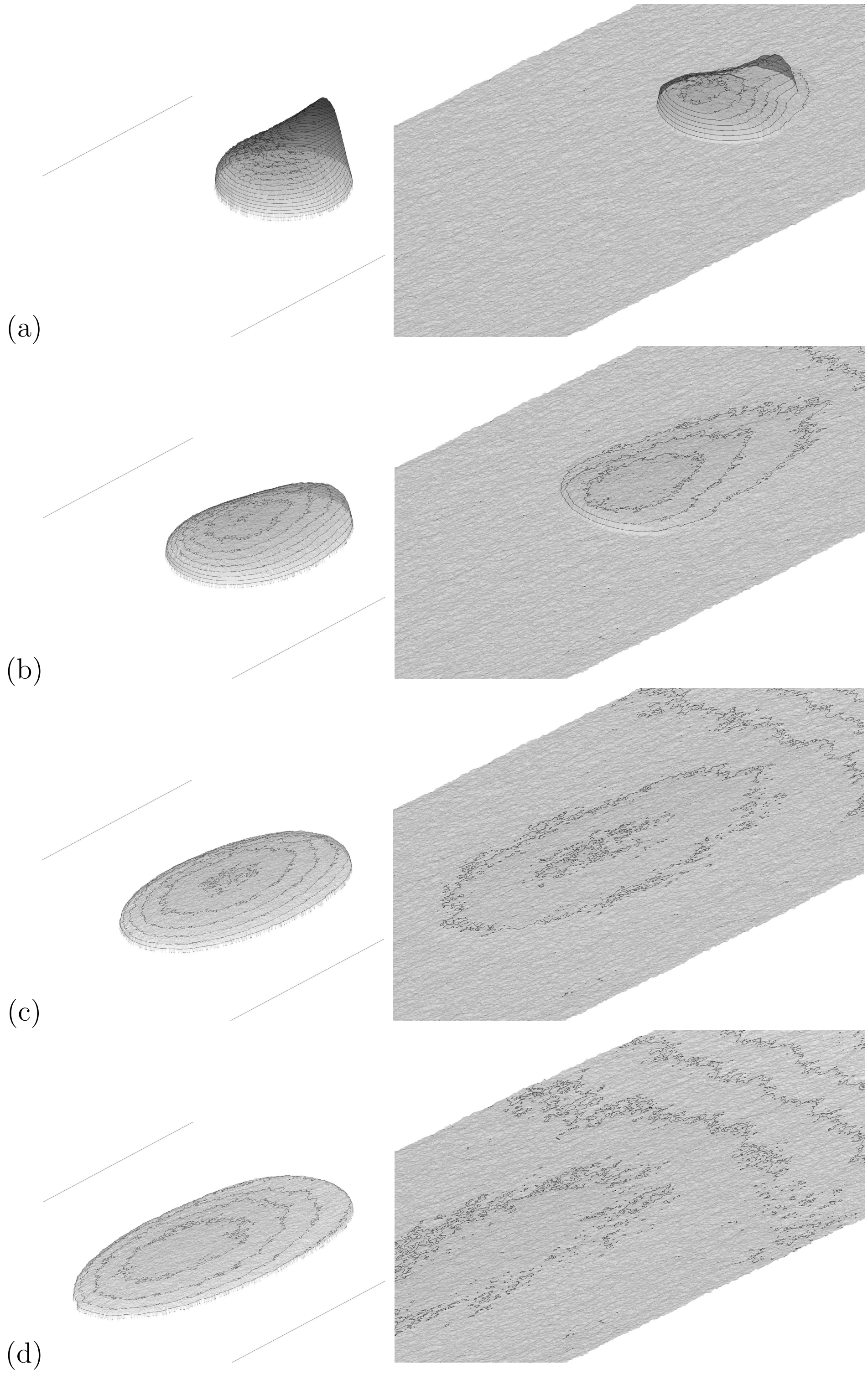

Figure 14.32: Bed slope angle 23^o. 3D view of the surface level evolution at times $t = 0.24$ s (a), $t = 0.72$ s (b), $t = 1.68$ s (c), $t = 2.40$ s (d) and $t = 3.6$ s (right) over a rough plane and (left) over an initial static layer using GC

14.8 Spreading of granular mass over a rough parabolic inclined plane

The developed numerical scheme has been further tested by comparison with a laboratory experiment on a chute with a complex basal topography performed by Gray et al. (1999). This experiment is of utmost importance for the validation of the proposed model because the chute includes a longitudinal constant bed slope but also a variable bed slope in the transversal direction. The geometry is defined departing from a symmetric reference surface, 175 cm long, with an inclination angle of 40^o. Over this surface a parabolic function, $Y^2/2R$, with R=110 cm, is used to define the shape of the chute. Next, a transition region, 215 cm long, smoothly links the chute with a horizontal plane. A spherical cap, full of quartz chips of mean diameter 2-4 mm, is located over the chute. The internal friction angle of the material is estimated equal to 40^o and the basal angle of friction equal to $\delta = 30^o$ (Gray et al., 1999). The projection of this spherical surface over the slope plane drives to an elliptical shape. The major axis has a length of 32 cm and the maximum height is 22 cm. This laboratory test case was numerically reproduced in Pirulli et al. (2007) focusing on the differences when dealing with an isotropic or anisotropic stress tensor. Following Pirulli et al. (2007) internal and basal friction are numerically modeled by considering isotropy and defining an internal friction angle equal to 30^o.

Figure 14.33 shows a 3D plot of the initial configuration. During the experiment, photogrammetric techniques were used to obtained the position of the avalanche boundary at different times. The mass moves rapidly downstream and reaches the horizontal zone of run out. At that point the velocity of the front is reduced by the change in the slope direction and consequently, the granular mass spreads transversally.

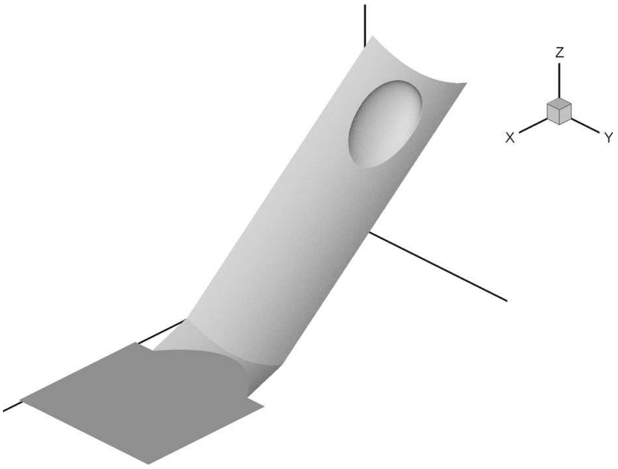

Figure 14.33: Initial configuration of the spherical cap over the parabolic chute

Numerical simulations are shown only on a triangular unstructured mesh, with a cell area equal to 6 mm^2, for both local and global formulations. Again, the definitions of the bed level and initial layer depth at the different cells depend on the coordinate system selected. The generation of the initial conditions is not a trivial task, as transversal sections in the chute do not present a uniform slope. In all simulations CFL is 0.5.

The computed evolution of the granular flow over the parabolic chute, using global coordinates, is presented in Figure 14.34. The spreading of the granular mass is in accordance with the description of the observed phenomena during experiments.

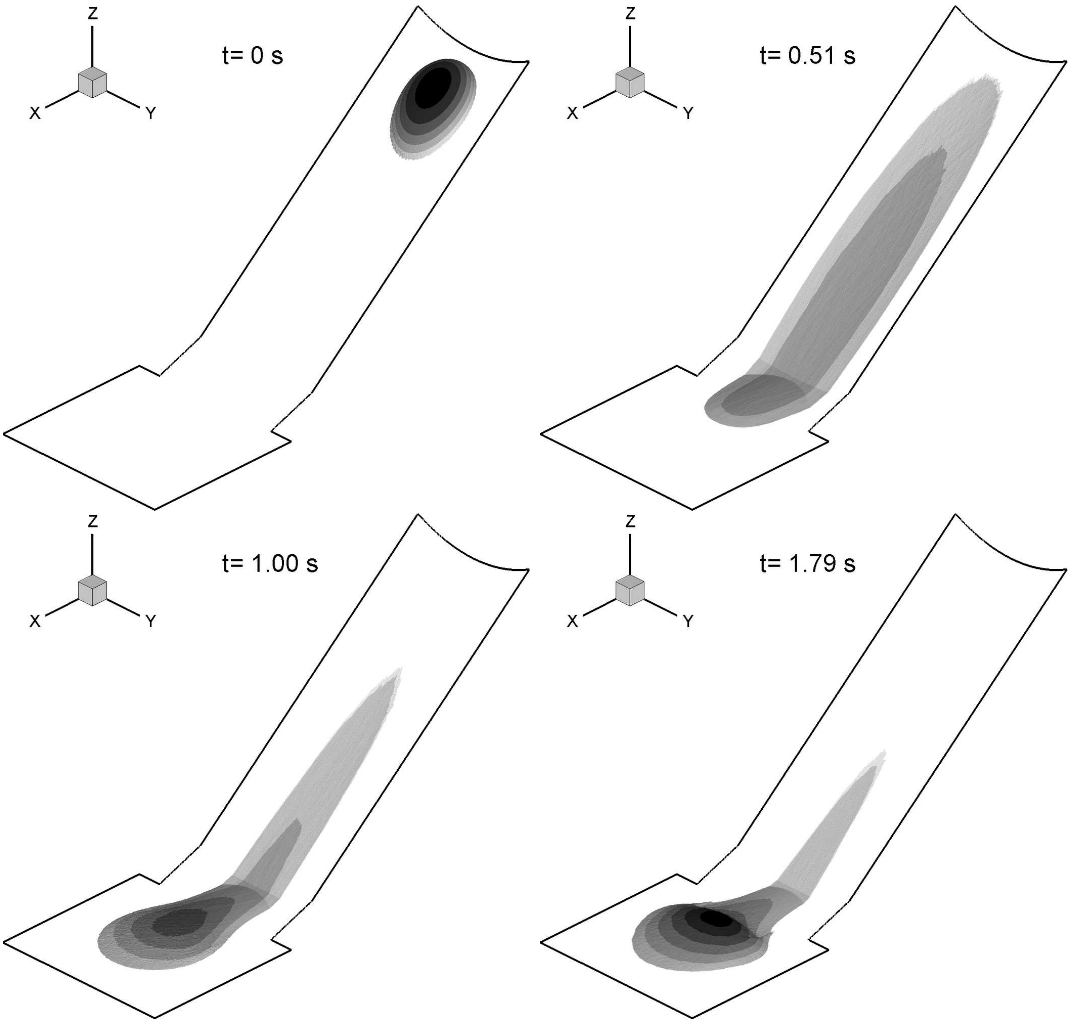

Figure 14.34: 3D contour views for the free surface level at times t = 0 s, t = 0.51 s, t = 1 s, t = 1.79 s using GC

The predicted spreading evolution computed using GC is tested against experimental data in Figure 14.35, where a sequence of plant views is plotted. At the initial times, t=0.51 s and t=1.00 s, inertial effects are more relevant than frictional ones and the material mass rapidly accelerates. At time t=1.51 s, the spreading of the mass has reached the horizontal zone and the material tends to deposit, evolving in the transversal direction, up to a rest stage at time t=1.79s. Numerical results follow closely the same experimental trend observed.

The results obtained using a local system of coordinates are presented in Figure 14.36.

Despite the change in the value of the initial conditions and of the equivalent distances, the numerical solution predicts accurately the time evolution of the spreading.

In order to check the performance of the numerical scheme presented in this work in presence of stopping conditions over uneven 2D slopes, Figure 14.37 shows the comparison between the computed results obtained in this work and the ones obtained in Pirulli et al. (2007) when assuming isotropy or anisotropy of normal stresses and using LC at time t=1.79 s. As it is displayed, the adequate discretization of the source terms provides accurate results in the front and in the lateral sides. However, the computed results located in the tail of the moving mass do not agree with the experimental results.

In order to measure the influence of gravity projections, another numerical simulation is performed not including the gravity projections in the global formulation. Numerical results are plotted in Figure 14.38. Large difference appear if comparing with experimental observations. This reduced model is not able to reproduce correctly the stopping conditions observed in the experiment.

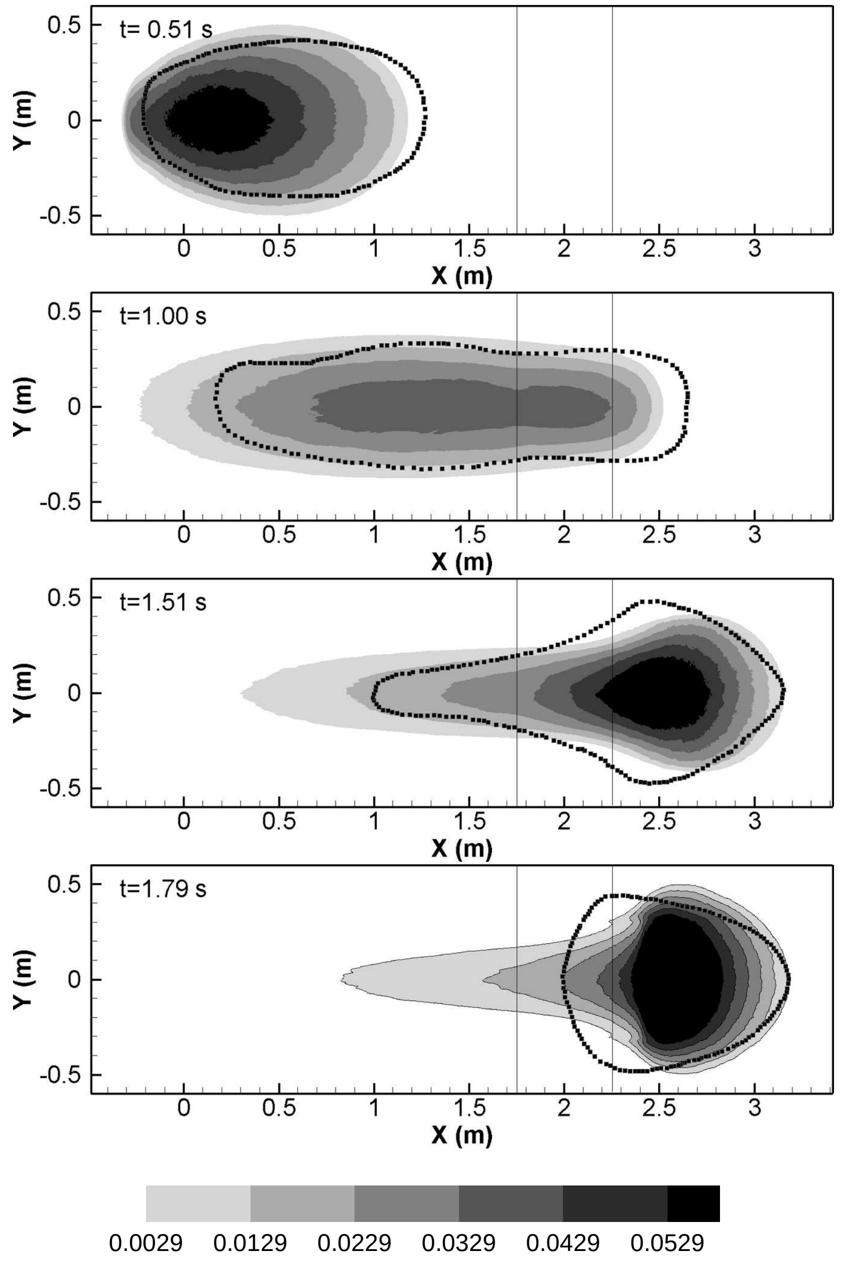

Figure 14.35: Computed contours of surface level at times $t = 0$ s, $t = 0.51$ s, $t = 1$ s, $t = 1.51$ s, $t = 1.79$ s using GC. Dashed line indicates the position of the granular mass during the experiment. Solid lines at $X = 1.75$ m and at $X = 2.15$ m indicate the position of the transition zone

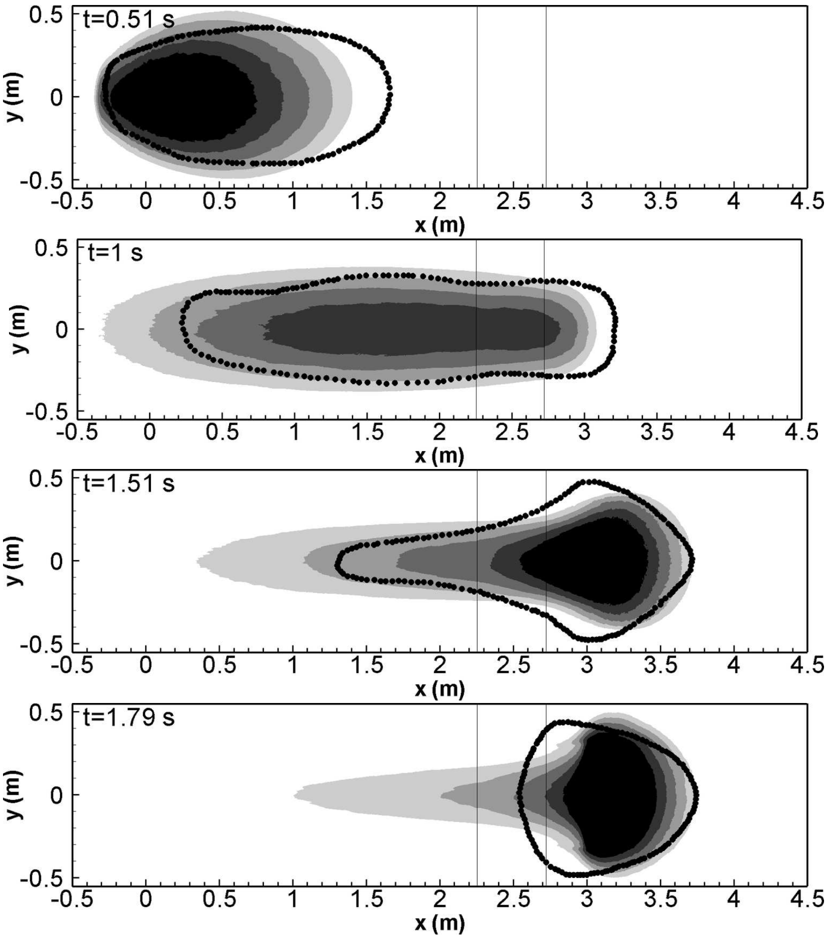

Figure 14.36: Computed contours of surface level at times t = 0 s, t = 0.51 s and t = 1.79 s using LC. Dashed line indicates the position of the granular mass during the experiment. Solid lines at x = 2.28 m and at x = 2.71 m indicate the position of the transition zone

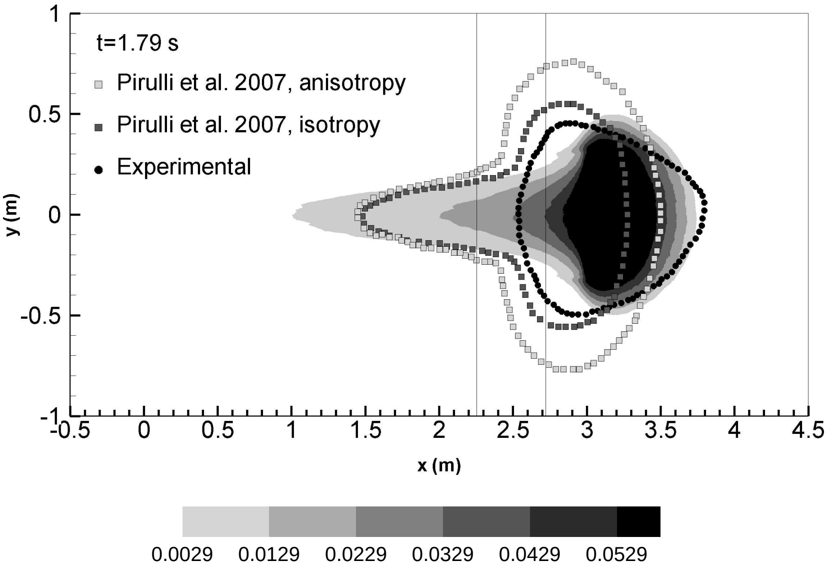

Figure 14.37: Computed contours of surface level at time $t = 1.79$ s using LC. Dashed line indicates the position of the granular mass during the experiment. Solid lines indicate the position of the transition zone

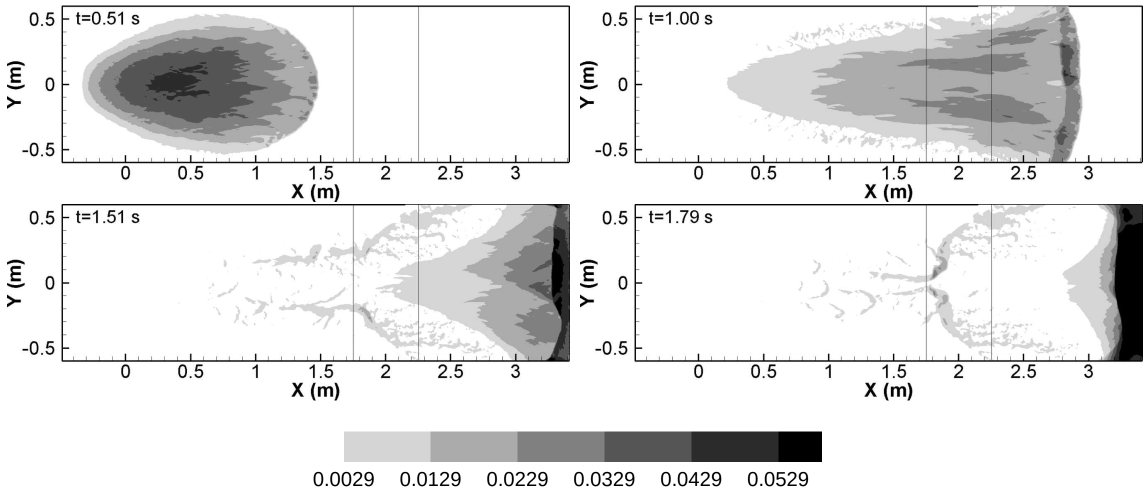

Figure 14.38: Computed contours of surface level at times $t = 0$ s, $t = 0.51$ s, $t = 1$ s, $t = 1.51$ s, $t = 1.79$ s using GC. Solid lines at $X = 1.75$ m and at $X = 2.15$ m indicate the position of the transition zone

Chapter 15

Conclusions for the local and global coordinates

In this work granular flow has been simulated using 2D finite volume schemes. Numerical schemes have been constructed for both global and local coordinate system involving complex topography. Each formulation has been developed focusing on the projections of the gravity vector required in each case. Source term discretization is based on the analysis of quiescent equilibrium, prior to be included in the approximate RP.

Numerical assessment of the schemes proposed in this work is done using exact solutions and both one and two-dimensional experimental test cases. Comparisons with exact solutions and laboratory experimental data confirm that the numerical approaches for vertical cosine in (12.18) and (13.12) are valid when dealing with unstructured mesh in one and two-dimensional flows.

It has been checked how, in two-dimensional flows, structured meshes introduce artificial effects. In rectangular/triangular structured meshes, privileged spreading directions appear, distorting the numerical results.

Numerical experiments confirm the suitability of the numerical schemes when dealing with a range of inclination angles. The thickness of the movable layer and the spreading over the rough plane is well captured. The prediction of the final height of the deposit is also accurately reproduced when incorporating an initially static layer. It has been proved that the presented numerical schemes are able to reproduce experimental data even in cases involving changes in both transversal and longitudinal bed slopes.

It is remarkable that when using a local systems of coordinates the definition of both the topography and initial conditions is not a simple task. These additional efforts can be avoided if using a global system of coordinates without compromising the quality of the results. Moreover the majority of the topographic data for natural spaces are based on digital elevation models (DEMs), which are referenced to a global framework.

The complete understanding of the augmented Riemann solvers defined together with the numerical fixes (entropy fix, friction fix and time step fix) allows to obtain accurate numerical predictions even in cases of complex topography and with independence of the reference coordinate system employed. The results and conclusions of this part of the document have been published in Juez et al. (2013a).

15.1 Further research

Although in all the numerical experiments presented in this work simple friction laws have been employed, the results presented can be used as the basis for the analysis of more complex rheological models able to handle with more sophisticated fluids, such as the ones made of a mixture of sand and water.

The presence of water within the land should be also carefully studied. The pore pressure is the responsible of the mobilization of large amounts of material after intense rainstorms. Moreover, the movement of the landslide provoke an important erosion of the granular material already present on the bed. This fact can significantly modify the behavior of the flow, leading to unexpected situations. Both processes, the infiltration and the erosion, should be included in the mathematical model.

Chapter 16

Small-scale environmental problems

16.1 Introduction

Since a numerical scheme for dry granular flow has been developed and tested in previous Chapters, and following previous work, a series of laboratory studies which constitute a further step in mimicking natural phenomena have been described and simulated. Three situations have been considered with some common properties: a two-dimensional configuration, variable slope of the topography and the presence of obstacles. The setup and measurement technique employed during the development of these experiments are deeply explained in Caviedes et al. (2014), where the author of this thesis has also been involved. In this Chapter two issues are addressed: the experimental setup employed during the development of the experimental work and in addition, extra considerations about the friction law involved in the mathematical model considered.

16.2 Experimental setup

The experimental setup is briefly addressed in this section as a detailed explanation is provided in Caviedes et al. (2014). The laboratory experiment was carried out on an inclined rough plane with a changing slope and without lateral walls. Three experiments were carried out with this experimental facility. Each of them was defined by a particular obstacle configuration. Experiment 1 consisted of a single semisphere obstacle located on longitudinal axis of the slope. Experiment 2 had the same semisphere obstacle as in the prior experiment but included also two smaller semisphere obstacles positioned upstream. Experiment 3 had a square bar as obstacle across the transversal direction of the slope. The initial condition was the same for the three experiments and consisted of a semispheric cap full of sand at the upstream end of the facility. Sand grain diameters ranged from 1 mm to 2 mm. The granular avalanche was triggered by the sudden release of the semispheric deposit. A schematic representation of the experimental setup is displayed in Figure 16.1.

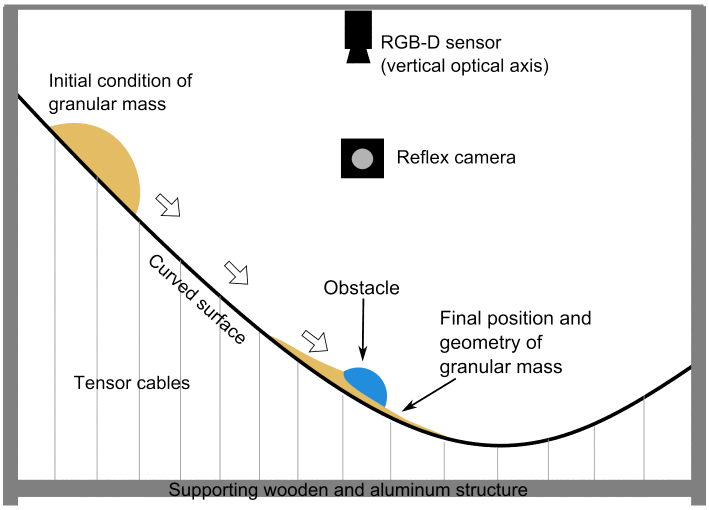

Figure 16.1: Schematic representation of the experimental setup

Three-dimensional temporal and spatial data of the moving mass was throughly collected. The measurement technique employed included an RGB-D sensor on the top of the experimental facility and a reflex camera which was set up from different views to complete the data.

16.3 Extra considerations about the friction law

The description of the rheological laws which govern geophysical granular flows is not a trivial task, as it is necessary to delve into their physical origins at the grain scale. The main advantage of the depth averaged equations is precisely, that the dynamics of the flowing layer can be predicted without knowing in detail the internal structure of the flow (Pouliquen and Forterre, 2008). The complex three dimensional rheology of the granular mass is mainly considered through the basal friction term. Assuming a simple constant Coulomb-like basal friction is generally sufficient to capture the main flow structures and has been widely used to describe granular motion (Pouliquen and Forterre, 2002; Bouchut et al., 2003; Kerswell, 2005; Pirulli et al., 2007; Juez et al., 2013b). This basal friction term is governed by a dynamic angle of friction which is usually several degrees less than the traditional static friction angle (Cui and Gray, 2013).

However, when considering complex transient situations which involve realistic topography and propagating shocks, more sophisticated basal friction laws may need to be considered. The assumed dense quasi-static regime may fail and an intermediate liquid regime can develop in which the collision forces take center stage. In the search of accurate quantitative predictions several authors (Pouliquen and Forterre, 2002; Forterre and Pouliquen, 2003; Pirulli et al., 2007) have studied in detail the onset and overall behavior of the gravity-driven flows. As it was stated in Pouliquen (1999); Pouliquen and Forterre (2002), experimental works have proved the existence of two critical angles: an initial static angle which governs the onset of the movement, θ_{start}, and another lower angle, which is in charge of the stopping phenomena, θ_{stop}. A relationship between both angles can be found in Pouliquen and Forterre (2002), providing a way of explaining the hysteresis behavior of granular slope stability (Douady et al., 1999). Additionally, Da Cruz et al. (2005) discussed another way of computing the friction coefficient in terms of the relevant timescales controlling grain motion (mean deformation and confining pressure). Both approaches, Pouliquen and Forterre (2002); Da Cruz et al. (2005), despite of providing a full description of the granular behavior at different regimes present the main drawback of requiring ad hoc parameters. In this way, the accuracy of the predictions are tied to the accuracy of the calibration which is usually supplied by small-scales laboratory test.

In order to avoid these calibration parameters, but pursuing a more sophisticated friction term we propose to consider new features. Regarding the fact that the conservation equations in (8.1) are depth averaged, the tangential forces generated by the stresses may have different and wide nature: turbulent stress τ_t, dispersive stress τ_d, Coulomb-type frictional stress τ_f, yield stress τ_y and even viscous stress τ_μ. Not all stresses act along or simultaneously at the same location of the material column. However, since the conceptual model is depth-averaged, all terms may actually coexist and may be mathematically lumped in the same formula. For this reason, and because the mathematical structure of the equations is the same as the one of the shallow-water equations, Manning's law (Manning, 1895) is considered in the present work, additionally to the dry frictional Coulomb's law.

This empirical model is based on a power-law velocity model where the friction exerted over the bed is written as the product of a friction coefficient and the square velocity profile. Depth averaging this expression and considering turbulent flow on the basis of the flow, Burguete et al. (2008a), drives to define the new tangential forces as

$$\begin{array}{l} \tau_{t,x} = \rho g_\psi \frac{n^2 u\sqrt{u^2+v^2}}{h^{1/3}} \\ \tau_{t,y} = \rho g_\psi \frac{n^2 v\sqrt{u^2+v^2}}{h^{1/3}} \end{array} \tag{16.1}$$

where n is the Manning-Strickler's coefficient which is related to the bed topography roughness. With the inclusion of this friction term in the momentum equations, the effect of very thin layers where only a small number of grains are present in the vertical column is taken into account. Since under these conditions only few layers of granular material exist, and all of them are mobilized, the local dissipation of the potential energy needs to be increased in such area. In this fashion, the stopping conditions of the moving mass is not only reached when the slope of the surface level equals the slope of the friction angle. Thanks to the mathematical structure of Manning's law, the smaller the granular depth is, more friction dissipation is generated at the base of the flow. Hence, the sum of tangential forces of (12.4) applied over the moving mass are evaluated as

$$\begin{aligned} \tau_{b,x} &= \tau_{f,x} + \tau_{t,x} \quad \textit{i.e.} \quad \tau_{b,x} = \rho g_{\psi} h \tan\theta_b + \rho g_{\psi} \tfrac{n^2 u\sqrt{u^2+v^2}}{h^{1/3}} \\ \tau_{b,y} &= \tau_{f,y} + \tau_{t,y} \quad \textit{i.e.} \quad \tau_{b,y} = \rho g_{\psi} h \tan\theta_b + \rho g_{\psi} \tfrac{n^2 v\sqrt{u^2+v^2}}{h^{1/3}} \end{aligned} \tag{16.2}$$

Chapter 17

Results for the small-scale environmental problems

17.1 Introduction

The purpose of this section is twofold: first, we aim to validate the computed results obtained by comparison against the experimental data. Therefore, the forecasting capabilities of the shock-capturing scheme are explored when considering a fast 2D transient condition with a variable topography which includes obstacles. Additionally, a discussion on the physics involved in the granular flow behavior is developed. Some fluid-mechanical characteristics are identified, providing useful information for future design guidelines of dikes or other man-made civil elements.

All the simulations have been performed using an unstructured Delaunay triangular mesh, since only this type of mesh avoids the presence of misleading preferential flow directions as shown in the previous part of this thesis (Juez et al., 2013b). A maximum cell area of 6 mm^2 is considered with a stability condition of CFL = 0.5. The bed domain is considered non-deformable and no boundary conditions are imposed.

Comparisons between experimental and computational results are based on quantitative temporal 3D information detailed in Caviedes et al. (2014). 2D plan views and a number of probes located at points of interest, shown in Table 17.1, are analyzed in depth. A summary of all the probes is presented in Figure 17.1.

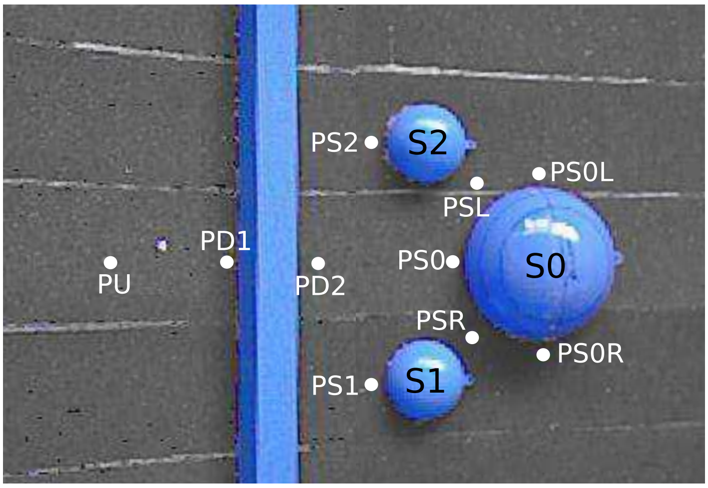

Figure 17.1: Probes location

Probe	*X (mm)*	*Y (mm)*
PU	500	500
PD1	600	500
PD2	680	500
PS0	760	500
PS1	705	410
PS2	705	590
PSL	770	550
PSR	770	450
PS0L	814	570
PS0R	814	430

Table 17.1: Probe locations

17.1.1 Gravity driven flow facing up a single obstacle

The understanding of the flow behavior against obstacles gathers a great interest as it is crucial in the design of elements which protect civil buildings and structures from several types of material slides (snow avalanches, debris flows, rockfalls or pyroclastic flows). Prior works have also pointed out the importance of this kind of configuration, carrying out 1D laboratory experiments with cylindrical obstacles Gray et al. (2003); Cui and Gray (2013) and with square blocks Hauksson et al. (2007). Being conscious that a landslide is a genuinely 2D flow, although under particular circumstances it can be constrained by bed topography driving to a 1D flow, we have developed a 2D experimental case. For this purpose, in the experiment considered in this subsection a single obstacle with semispherical shape is located within the flow region. This semisphere can be seen as an obstacle and also as a characteristic of the bed topography. Figure 17.2 shows a three-dimensional plot of the initial configuration and Figure 17.3 shows different views of the shock around the semisphere captured during the laboratory work.

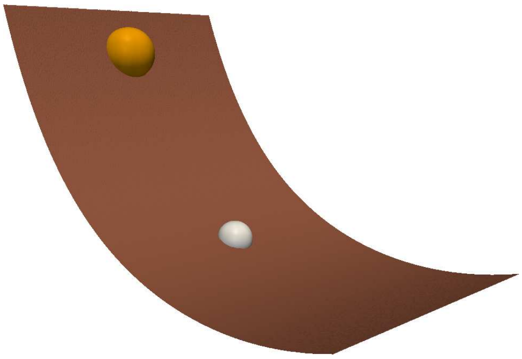

Figure 17.2: Initial configuration with the sand deposit at the beginning of the slope and the obstacle downwards

Before comparing computed results with the experimental data, the influence of the dynamical friction angle and the effect of the Manning's term is studied. For this purpose numerical results obtained by using two different dynamical angles, $\theta_b = 22^o$ and $\theta_b = 30^o$ are shown in Figure 17.4 at the final stage of the experiment. As it is observed, when using $\theta_b = 22^o$ the friction term is diminished in comparison to the inertia terms and the granular mass exceeds the obstacle, which results in two symmetric sand deposits downwards. On the other hand, when applying $\theta_b = 30^o$, the flow is stopped before overrunning the obstacle.

Additionally, the effect of the gravity projections considered in the numerical scheme is also analyzed. For this purpose, Figure 17.5 displays the final stage with two different dynamical angles, $\theta_b = 22^o$ and $\theta_b = 30^o$ and without considering the projections. As it observed, the overall surface level is completely different from Figure 17.4 and an important mismatch of a physically-based behavior is observed. Therefore, the effect of the gravity projections is need it is retained from now on in all the computed results.

Bearing in mind the granular movement observed in the experiments, more accurate results are obtained when using an intermediate dynamical angle equal to $\theta_b = 26^o$, Figure 17.6 (a). Once the effect of the dynamical angle is clearly identified, the effect of Manning's law is taken into account in the friction term. In this fashion, the final stage of the granular avalanche, shown in Figure 17.6 (b), displays some differences with respect to 17.6(a): the front of the avalanche keeps the same maximum spreading and the lateral movement is almost identical. However, noticeable discrepancies appear in the tail of the avalanche: whereas with the unique existence of the friction angle the effects of the thin layer are not taken into consideration and the tail is shortened, when considering the Manning's law the tail is enlarged, providing a better physical description of the phenomena.

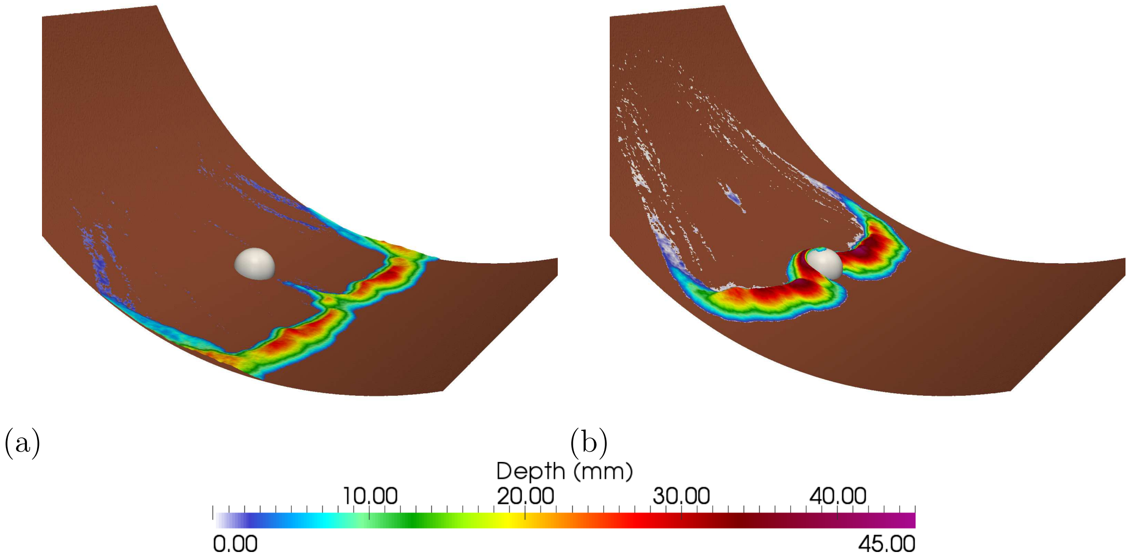

Figure 17.5: Final stage of the granular avalanche with two different dynamical friction angles $\theta_b = 22^o$ (a) and $\theta_b = 30^o$ (b) and without considering the gravity projections at the final stage of the movement

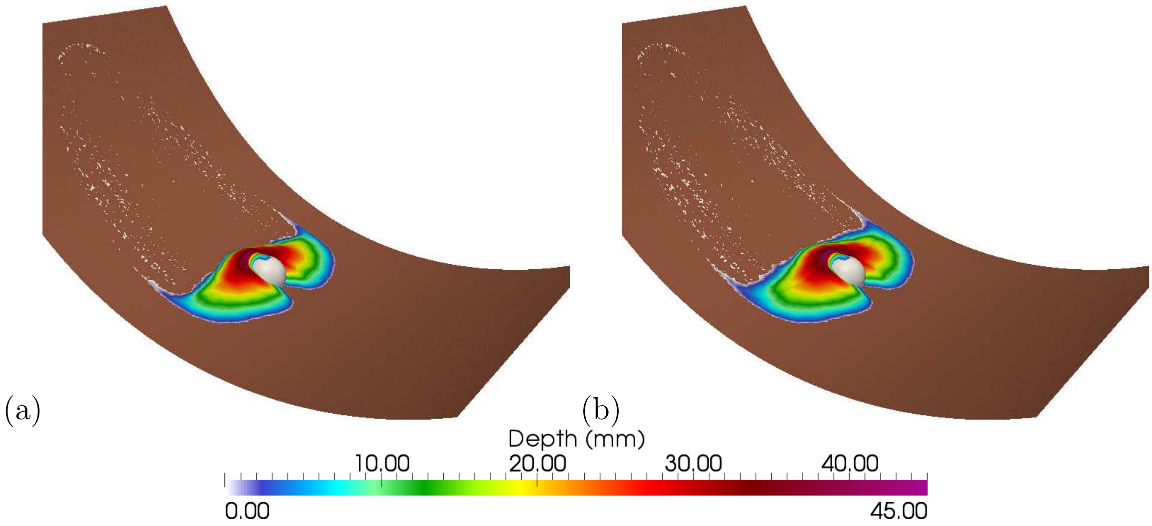

Figure 17.6: Final stage of the granular avalanche when using only the dynamical friction angle with $\theta_b = 26^o$ (a) and when summing the Manning's law (b) at the final stage of the movement

A temporal sequence of 3D views, numerically obtained, is plotted in Figure 17.7. Additionally, in Figures 17.9 and 17.10 a temporal series of 2D plan views with experimental data and computational results are presented. Since the sand cap is suddenly removed, the overall granular mass is put in motion and the initial shape is lost quickly. The flow spreads over the longitudinal and transversal direction until it reaches the obstacle, at $t = 540\,ms$. At this point, two interesting flow structures are formed: a wake region downslope from the semisphere, and a shock region upstream and to the sides of the semisphere. The shock evolves symmetrically around the sphere until the avalanche front remains at rest at $t = 1000\,ms$. From this temporal point, only the granular tail is still in motion up to an equilibrium stage at $t = 2000\,ms$. An important phenomena reported in Caviedes et al. (2014) is the existence of a stagnation area, i.e. an area where the granular mass has a local zero velocity. This structure is also observed in the computational results in Figure 17.8, and is temporally well described as it occurs at the same time, $t = 850\,ms$, as it was observed in the laboratory. From a numerical point of view, it is remarkable the robustness of the computed solution in the wet/dry fronts: the computed solution is able to handle with these situations without ruining the stability of the numerical solution. This characteristic is of utmost importance since it is present during the movement of the granular mass and when impacting against the obstacle: a part of the sand arrives to the top of the semispheric cap.

When analyzing the numerical results against the experimental data, the overall behavior of the granular mass is well described. Temporal evolution of the sand run out is accurately tracked in time. Furthermore, although the shock is a genuinely 3D structure, it is well reproduced by the depth averaged model considered in this work. However, some differences appear around the shocks area and at the final stage, where the computed results tend to overestimate the sand depth in the vicinity of the semisphere. Both situations are explained by the fact that the mass located in the avalanche tail is not stopped at the adequate position by the numerical scheme. Hence, an extra quantity of mass evolves downslope increasing the sand depth up to reach a rest condition. This fact is clearly understood when computing the absolute error between numerical and experimental results, Figure 17.11. Red areas, located at the sides of the obstacle showed a higher prediction for the sand depth, whereas the blue areas positioned at the avalanche tail show an underestimation of the mass. Nevertheless, the error at the avalanche front is close to zero, which implies an accurate tracking of the transient moving mass.

All the probes measured in the laboratory work (except PU, which in this experiment was not recorded) are compared with the computed results, Figure 17.12. PD1 shows a time lag with respect to the experimental measurement. This is due to the fact that, during the experiment, the opening of the sand container was not instantaneous, in contrast to the computational assumption under which a sudden dam break of the initial sand cap is considered. Additionally, differences between experimental and numerical results are observed from time $t = 1100\,ms$ and are associated to the different behavior of the avalanche tail observed with the experimental and computed results: in the laboratory work the tail area is spatially stopped before and consequently, the sand depth is stretched. In PD2, which is located downstream from PD1, the time lag perturbation of the gate is less evident. Numerical results are in good agreement with experimental data. An interesting phenomena is observed in the computational solution: the sand depth grows quickly up to time $t = 750\,ms$, then drops up to time $t = 1100\,ms$ and then the sand layer is increased again. Since the avalanche front moves quickly, the granular mass is split into two regions: the front and the tail. Once the front remains at rest, the tail is still in motion and goes on traveling downslope.

Therefore, the final height of the sand layer at point PD2 is the sum of two moving masses: first the front and then the tail. PS1 and PS2 provide an accurate prediction of the sand flow and the same explanations given for the jump in the sand depth at PD2 is applicable here. PSL, PSR, PS0L, PS0R, PS0 are placed in the vicinity of the obstacle, providing information of the shocks upstream and to the sides of the semisphere. All of them tracked accurately the temporal evolution. Nevertheless, the final sand depth is overestimated as a consequence of the extra granular mass which comes from the tail area.

In addition to the probes, in Figure 17.13 a longitudinal profile at $y = 500\,mm$ is shown. The tendency of the experimental measurement is well reproduced by the computed solution, although the predicted surface level is overestimated over the obstacle. This larger amount of material located in the front of the avalanche comes from the tail area.

(a) Downstream view (b) Upstream view (c) Side view

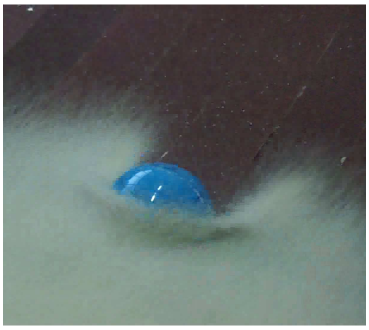

(d) Upstream high view

Figure 17.3: Flow features and structures in Experiment 1

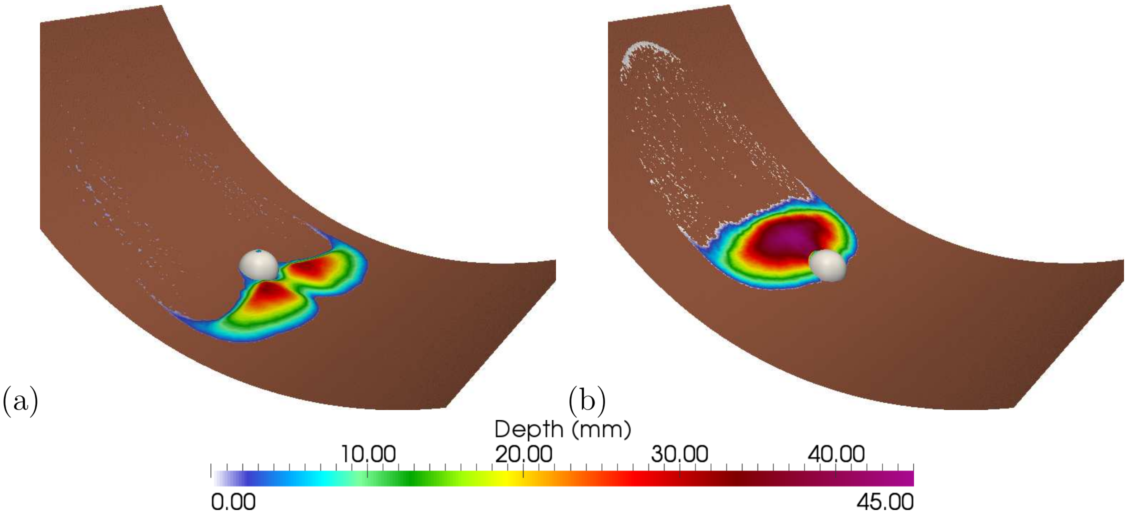

Figure 17.4: Final stage of the granular avalanche with two different dynamical friction angles $\theta_b = 22^o$ (a) and $\theta_b = 30^o$ (b) at the final stage of the movement

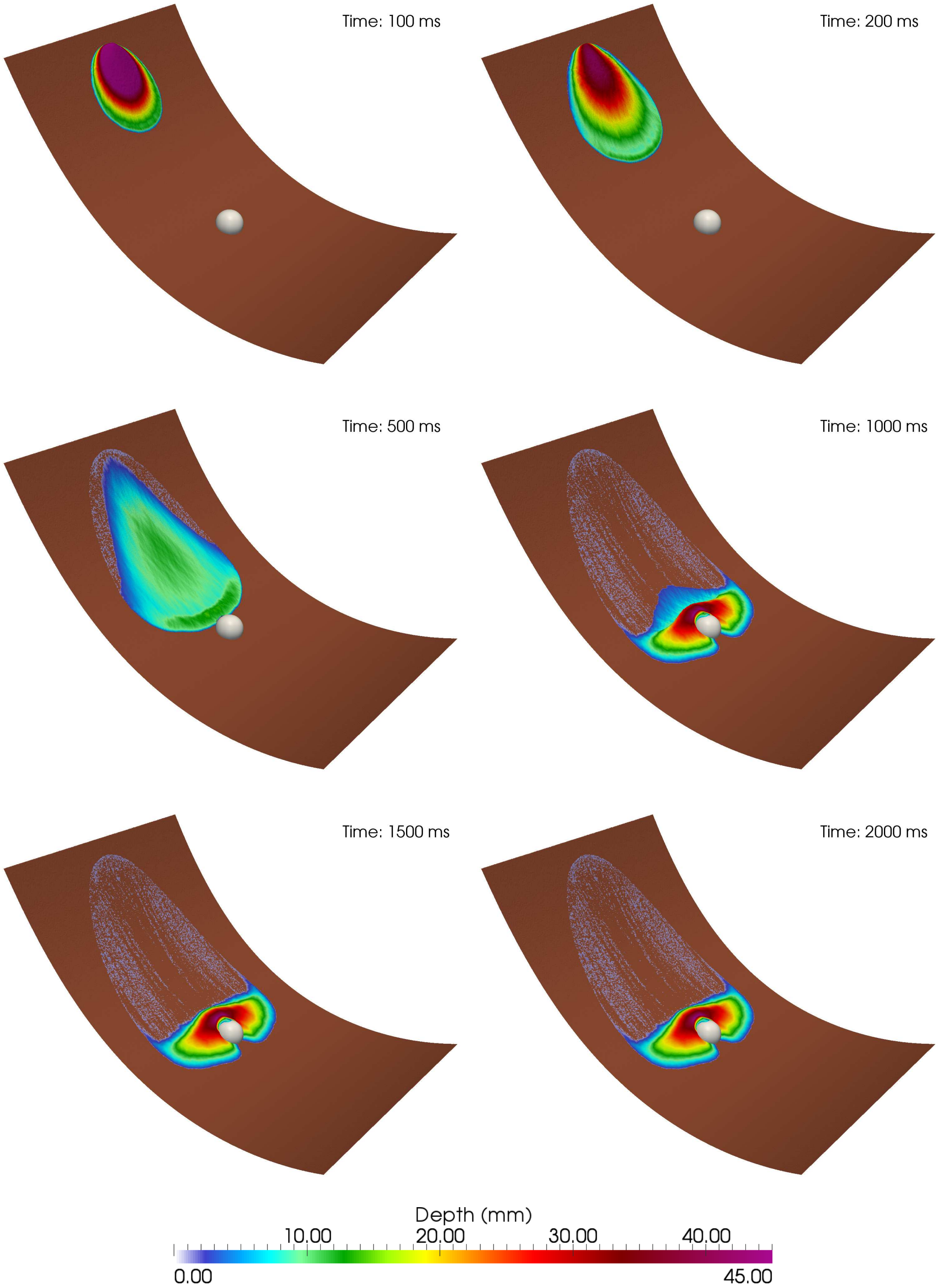

Figure 17.7: 3D contour views for the free surface level at times $t = 100$ ms, $t = 200$ ms, $t = 500$ ms, $t = 1000$ ms, $t = 1500$ ms and $t = 2000$ ms

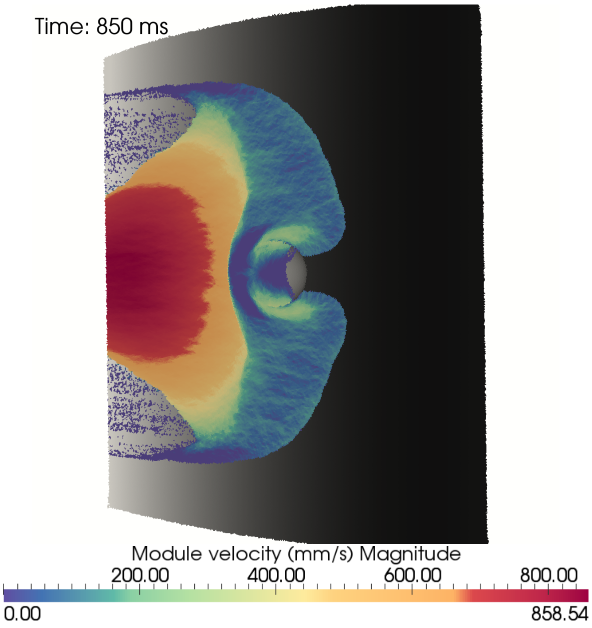

Figure 17.8: 2D plant view of the computed velocity field at time $t = 850$ ms

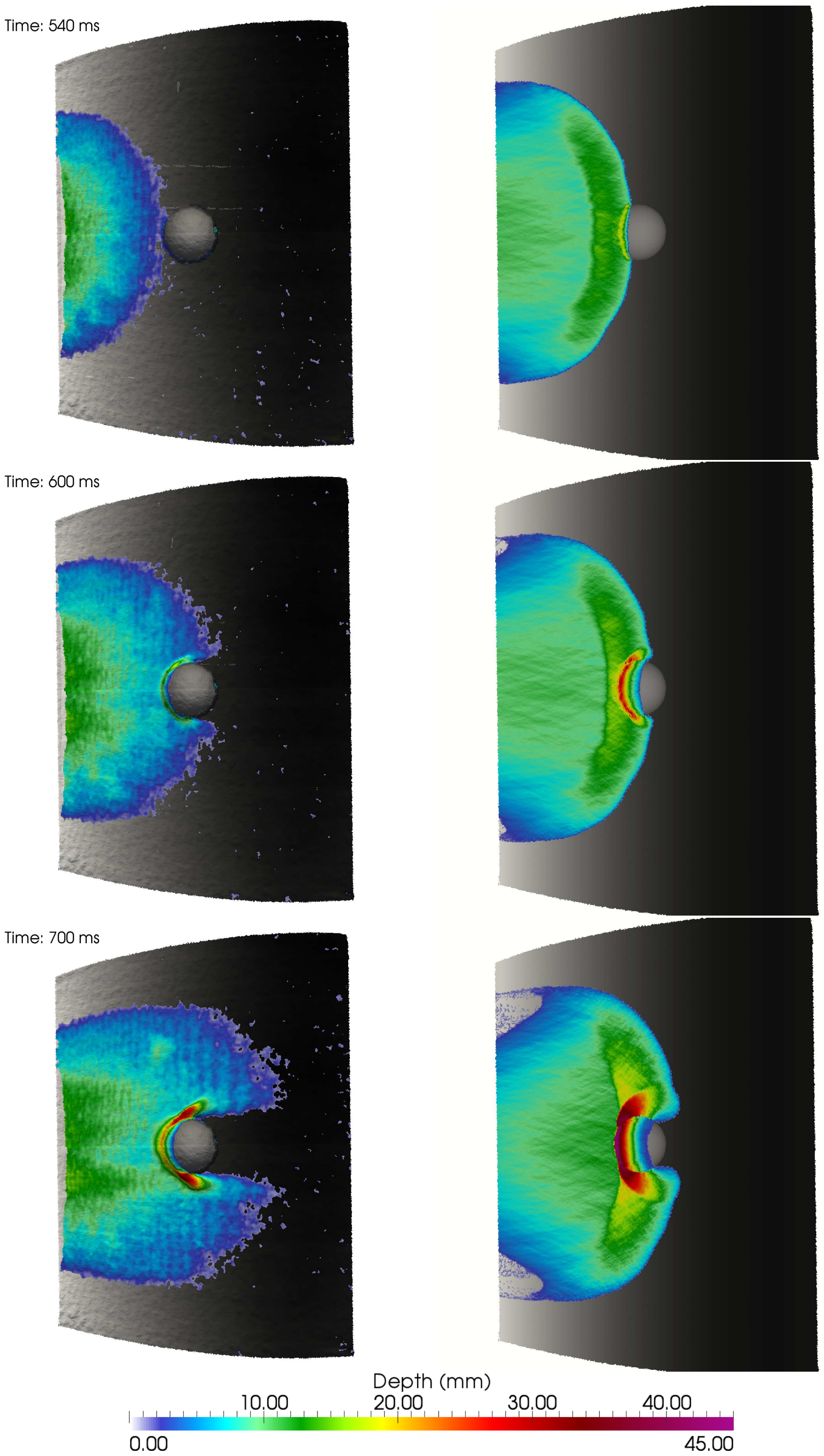

Figure 17.9: 2D plant views for the sand depth obtained experimentally (left side) and computationally (right side) at times $t = 540$ ms, $t = 600$ ms, $t = 700$ ms

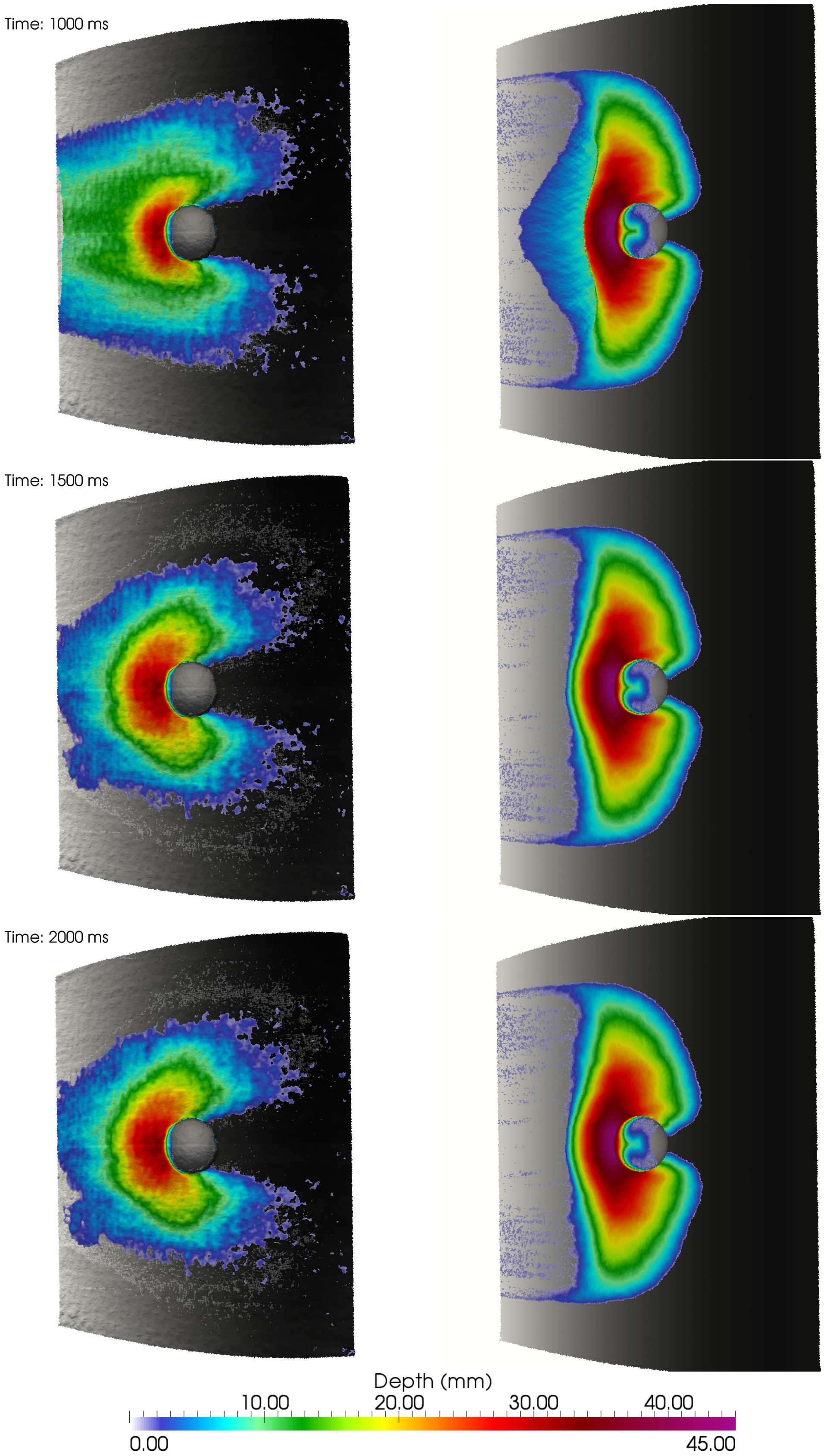

Figure 17.10: 2D plant views for the sand depth obtained experimentally (left side) and computationally (right side) at times $t = 1000$ ms, $t = 1500$ ms, $t = 2000$ ms

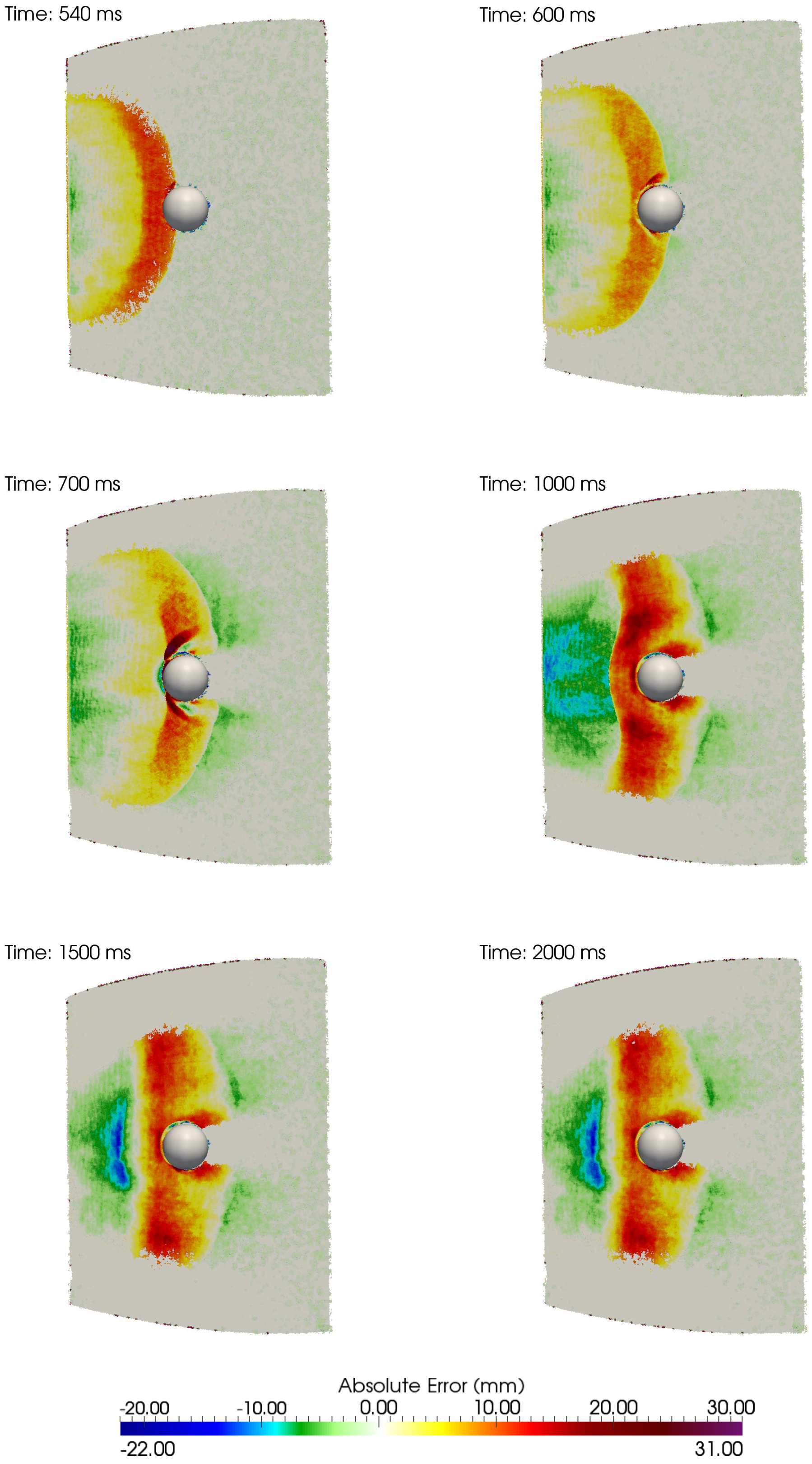

Figure 17.11: 2D plant views displaying the absolute error at times $t = 540$ ms, $t = 600$ ms, $t = 700$ ms, $t = 1000$ ms, $t = 1500$ ms, $t = 2000$ ms

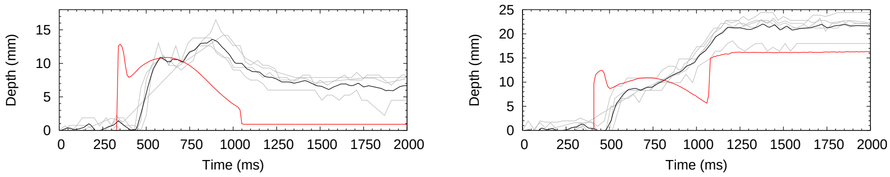

(a) PD1 (b) PD2

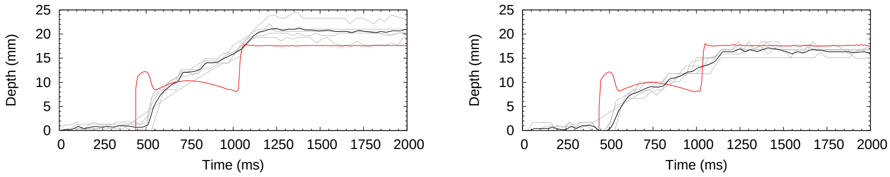

(c) PS1 (d) PS2

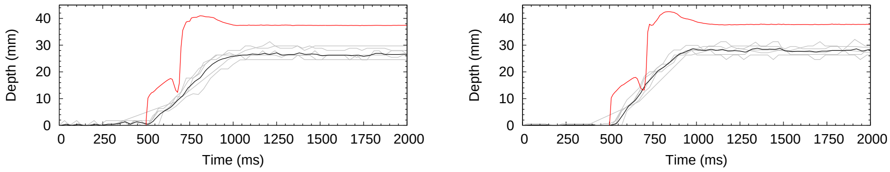

(e) PSL (f) PSR

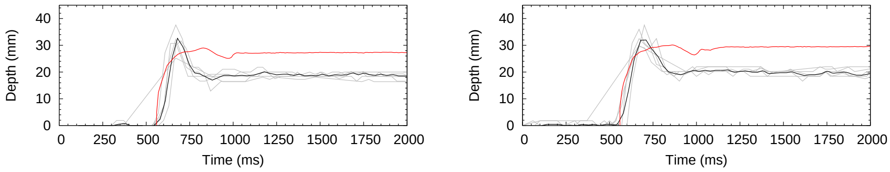

(g) PS0L (h) PS0R

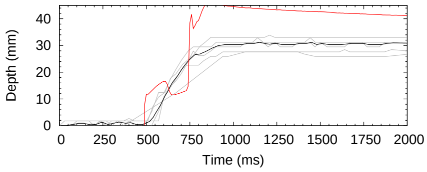

(i) PS0

Figure 17.12: Computational and experimental probe results

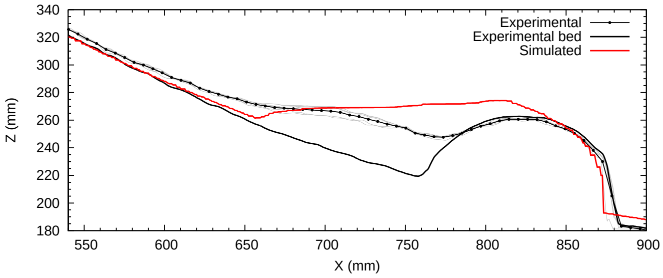

Figure 17.13: Longitudinal section ($y = 500\,mm$) for Experiment 1 at the final stage

17.2 Gravity driven flow facing up three obstacles

The next step in this work is considering a configuration which involves several obstacles. In this situation the shock propagation is expected to be influenced by the presence of other moving waves in their vicinity. To our knowledge, this particular configuration has not been addressed in other works. Figure 17.14 displays a sketch of the initial configuration of the experiment. In Figure 17.15 the images captured in the laboratory work display the flow structures around the obstacles.

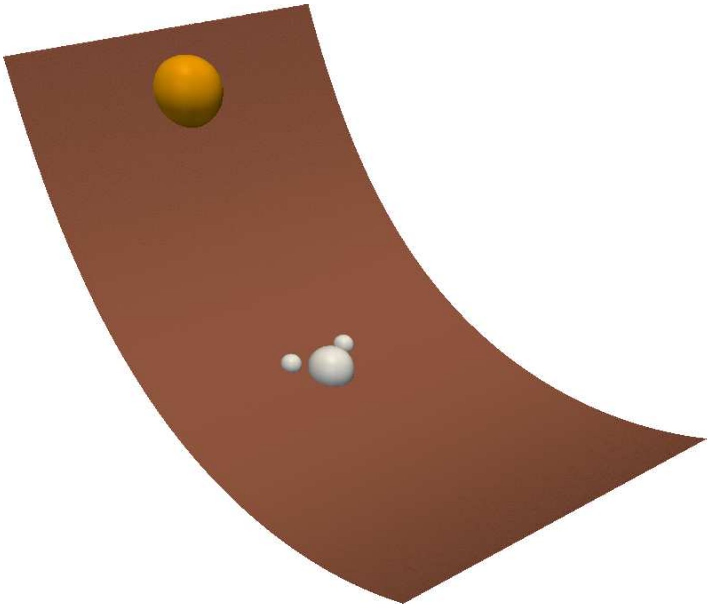

Figure 17.14: Initial configuration with the sand deposit at the beginning of the slope and the three obstacle downwards

The temporal computed evolution of the mass spreading is plotted in 3D and 2D plan views in Figures 17.16, 17.18, 17.19. The first instants of time, prior to the sand reaching the obstacles, are similar to the ones obtained in the experiment with one obstacle. The abrupt opening of the sand container triggers the sand avalanche. The mass is accelerated rapidly downslope towards the obstacles. Both lateral and longitudinal spreadings are observed. The impact of the sand flow against the small semispheres is accurately tracked by the numerical model at time $t = 460\,ms$. At this point the flow undergoes an abrupt transition in flow regimes, since a shock is derived in front of each obstacle at time $t = 640\,ms$ and $t = 740\,ms$. In the vicinity of the shocks the horizontal scales of the phenomena no longer exceed the vertical scales, which constitute a challenge for the shallow approach. Despite the complexity, the computed results describe correctly this complex wave structure, which is generated by the interactions of each obstacle. It is worth noting how the waves numerically reproduced in this experiment, are significantly influenced among themselves. On the other hand, once the flow overtakes the three obstacles, the maximum runout is quickly reached and at time $t = 1500\,ms$ the quiescent equilibrium stage is already achieved. The final shape of the computational results is similar to the obtained in the previous experiment. However, when analyzing the experimental results, it is observed how the surface angle described by the particles in the avalanche front is larger in the three obstacles configuration. With this latter configuration the shocks developed have significantly more influence in the flow behavior and make the sand grains move not only by rolling, but also by salting. This grain mechanism of movement is not affordable with the model proposed in this work and such behavior can not be mimicked.

On the other hand, it is interesting to observe how the numerical results are able to reproduce the initial immersion of the small caps by the sand mass, time $t = 640\,ms$, and the later reappearance of the obstacles, time $t = 1500\,ms$. Furthermore, the stagnation area pointed out in the laboratory work at time $t = 900\,ms$ is also well reproduced with the simulated results, Figure 17.17.

The main differences between computational and experimental data are due to the overestimated lateral spreading and by the fact that the mass located in the avalanche tail is not adequately stopped. Figure 17.20 displays the absolute error and the major differences are found in the lateral sides, the vicinity of the obstacles and the avalanche tail. This behavior is fairly similar to the observed in the previous experiment.

The temporal accuracy of the computed results at particular locations during the development of the sand avalanche is validated against the measurements developed during the laboratory work at particular locations as it is described in Caviedes et al. (2014). Figure 17.21 displays all probes plotted in Figure 17.1 except PU which is out of the field of view in this experiment. The overall behavior of all the probes is similar to the one observed during the experiment with one obstacle. The probes located closer to the sand container, PD1 and PD2, are influenced by the sand release procedure, since, from the computational point of view it is instantaneous, but experimentally it takes a short period of time. This fact provokes a time lag between laboratory data and numerical results. The differences at probes PS1 and PS2 are generated by the numerical behavior of the avalanche: the moving mass is split into two groups: the front and the tail. The tail spreads faster during the first instants of time and consequently, it achieves the equilibrium stage earlier. Then, the mass coming from the tail arrives and the final depth elevation is increased. This phenomena is also responsible for the higher computational sand elevation at probes PSL, PSR, PS0L and PS0R. Nevertheless, the numerical results are able to well reproduce the temporal evolution of this particular avalanche which includes complex transient and local 3D shocks.

Figure 17.22 displays a longitudinal profile located at $y = 500\,mm$. The overestimated computational sand depth is due to the differences in the tail of the avalanche, where a larger downwards mobilization of the material has occurred. Notwithstanding, the numerical prediction is able to reproduce the fact the the main obstacle is not overtopped.

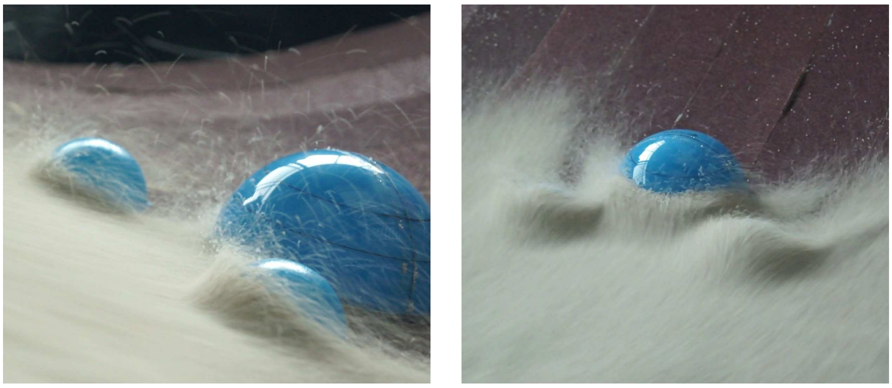

(a) Shocks at S1 and S2

(b) Shock at S0

(c) Shocks

(d) S0 stagnation, S1 and S2 overflow

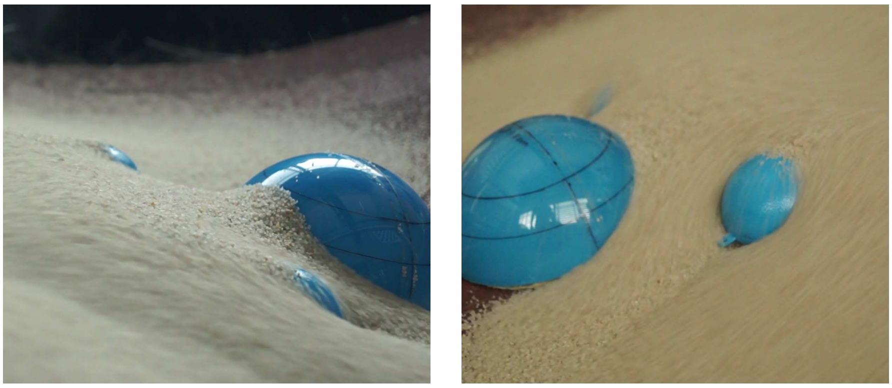

(e) Stagnation in S1 and S2

(f) Flow around S2

Figure 17.15: Flow features and structures in Experiment 2

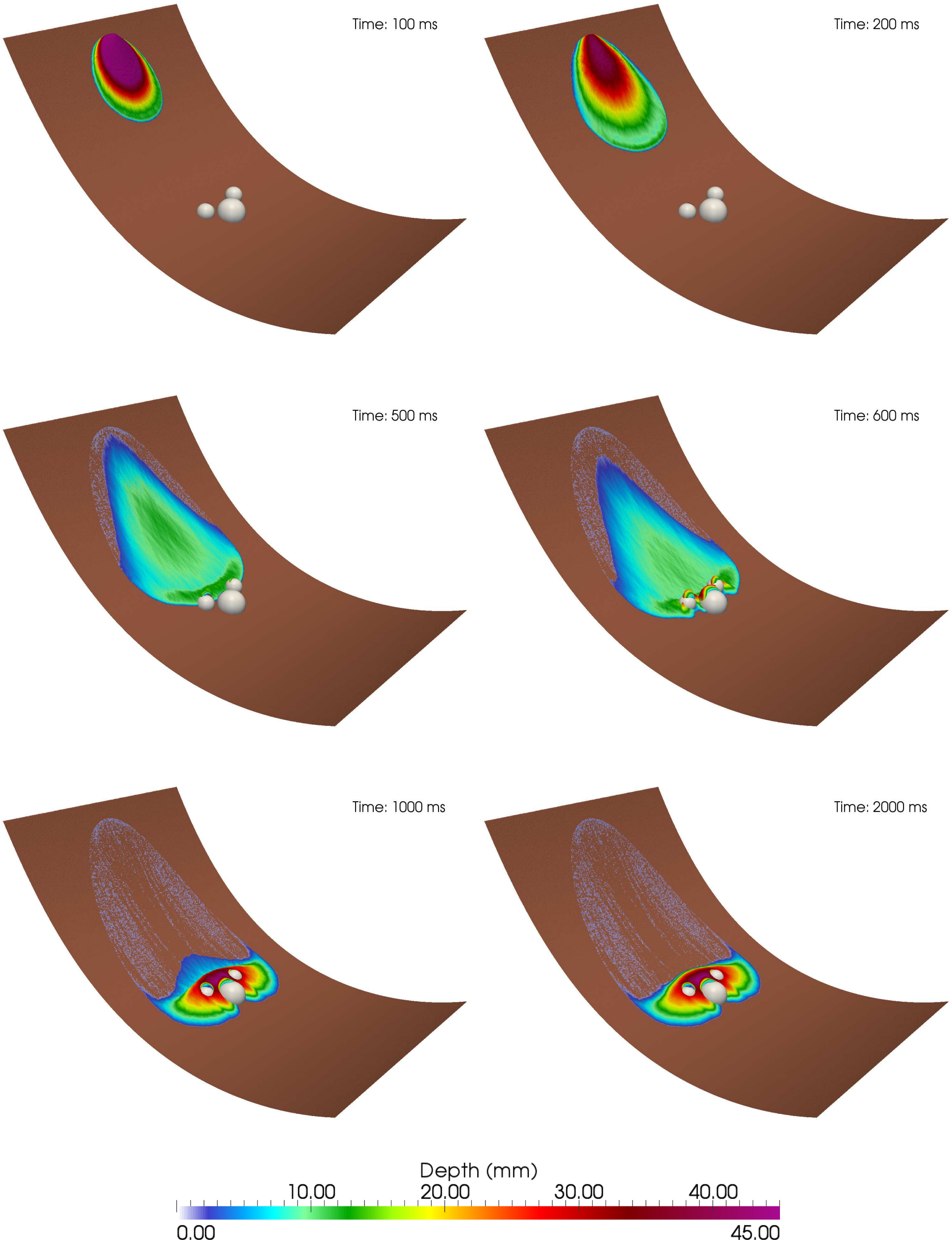

Figure 17.16: 3D contour views for the free surface level at times $t = 100$ ms, $t = 200$ ms, $t = 500$ ms, $t = 600$ ms, $t = 1000$ ms and $t = 1500$ ms

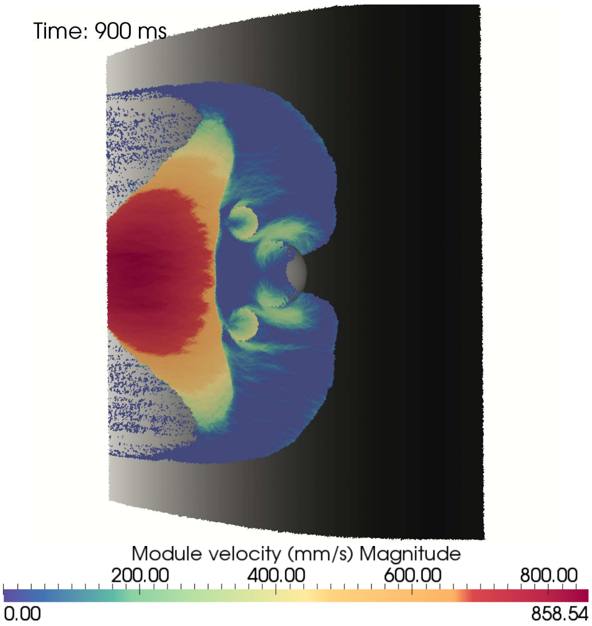

Figure 17.17: 2D plant view of the computed velocity field at time $t = 900$ ms

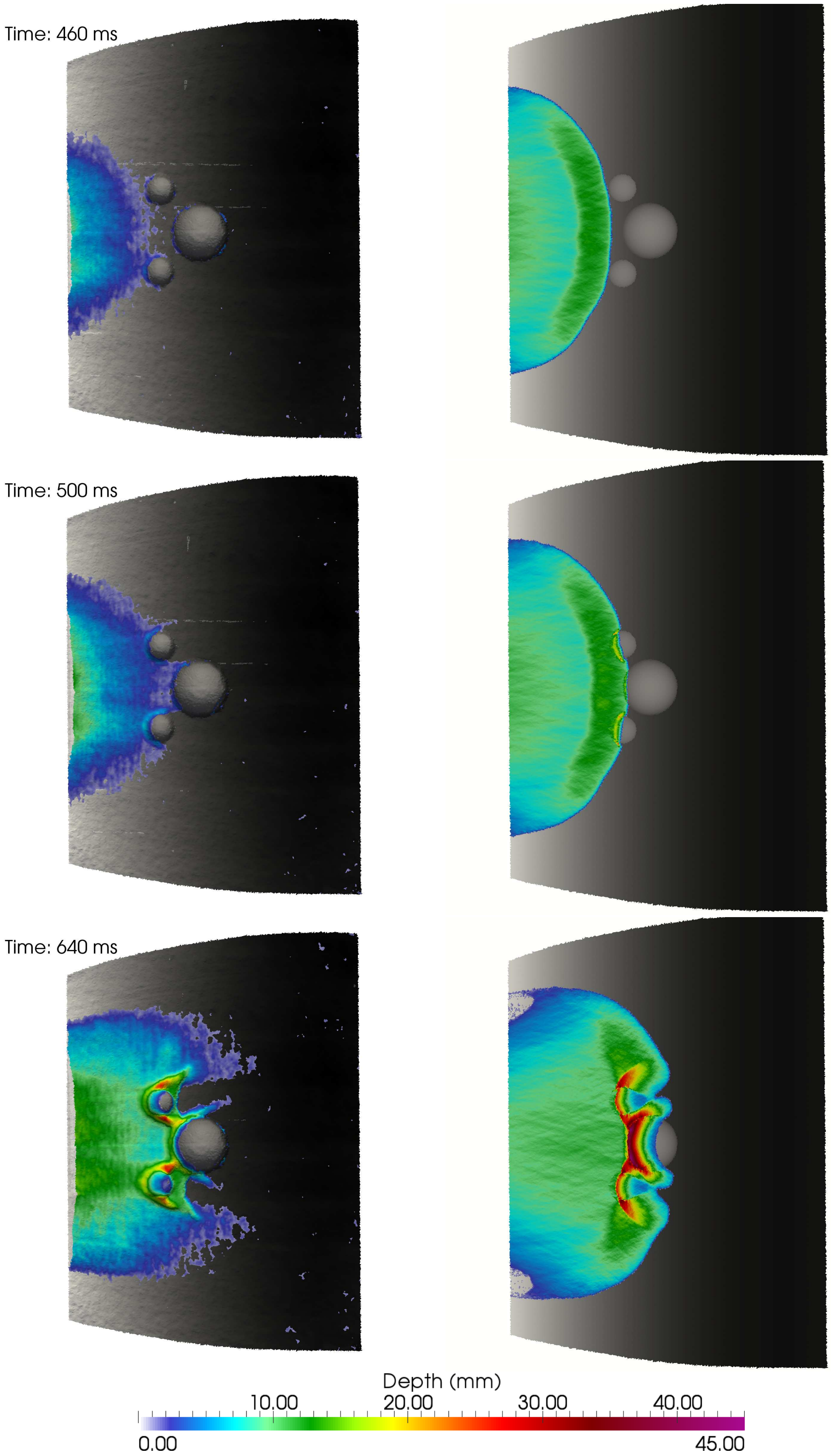

Figure 17.18: 2D plant views for the sand depth obtained experimentally (left side) and computationally (right side) at times $t = 460$ ms, $t = 500$ ms, $t = 640$ ms

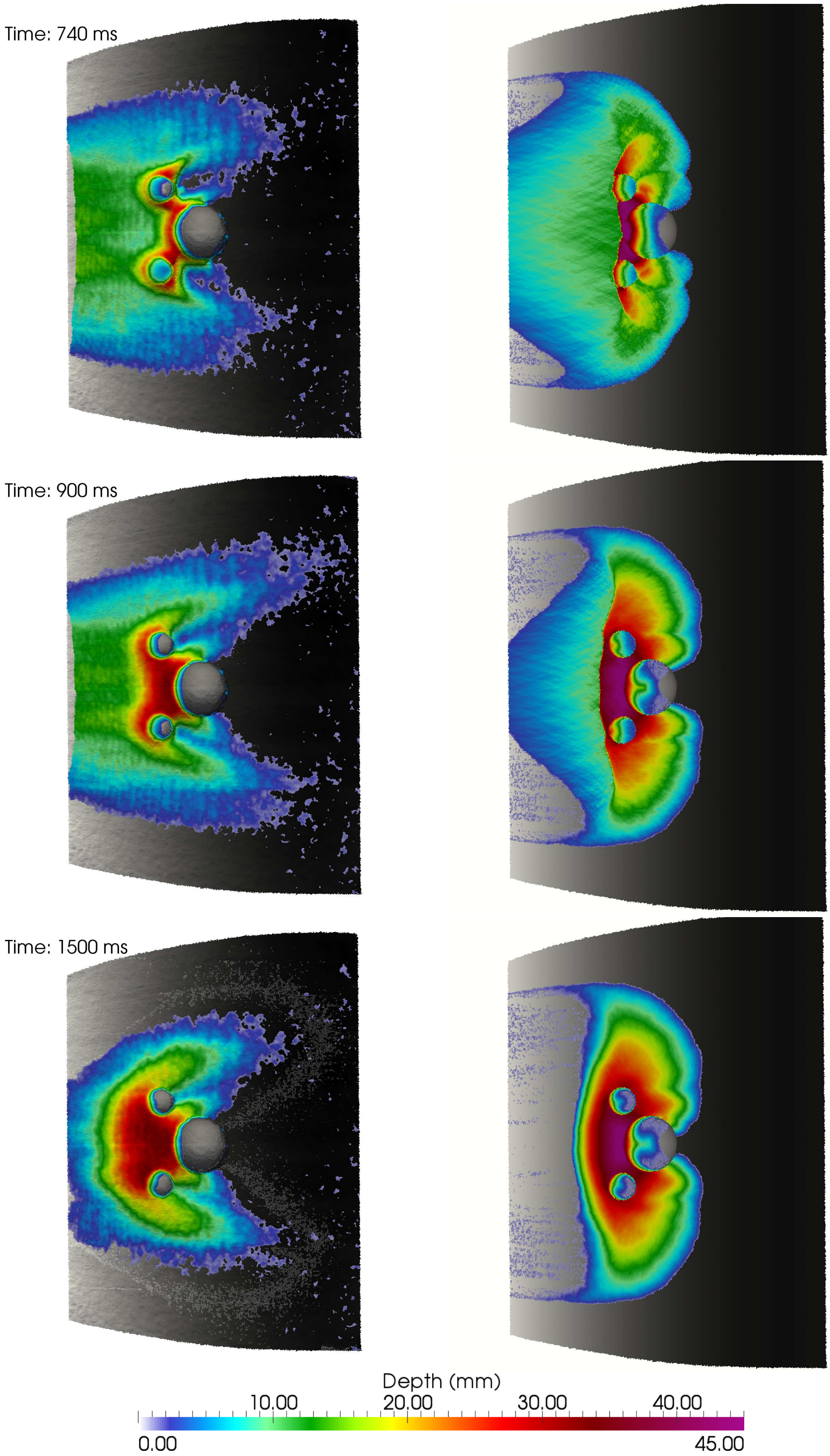

Figure 17.19: 2D plant views for the sand depth obtained experimentally (left side) and computationally (right side) at times t = 740 ms, t = 900 ms, t = 1500 ms

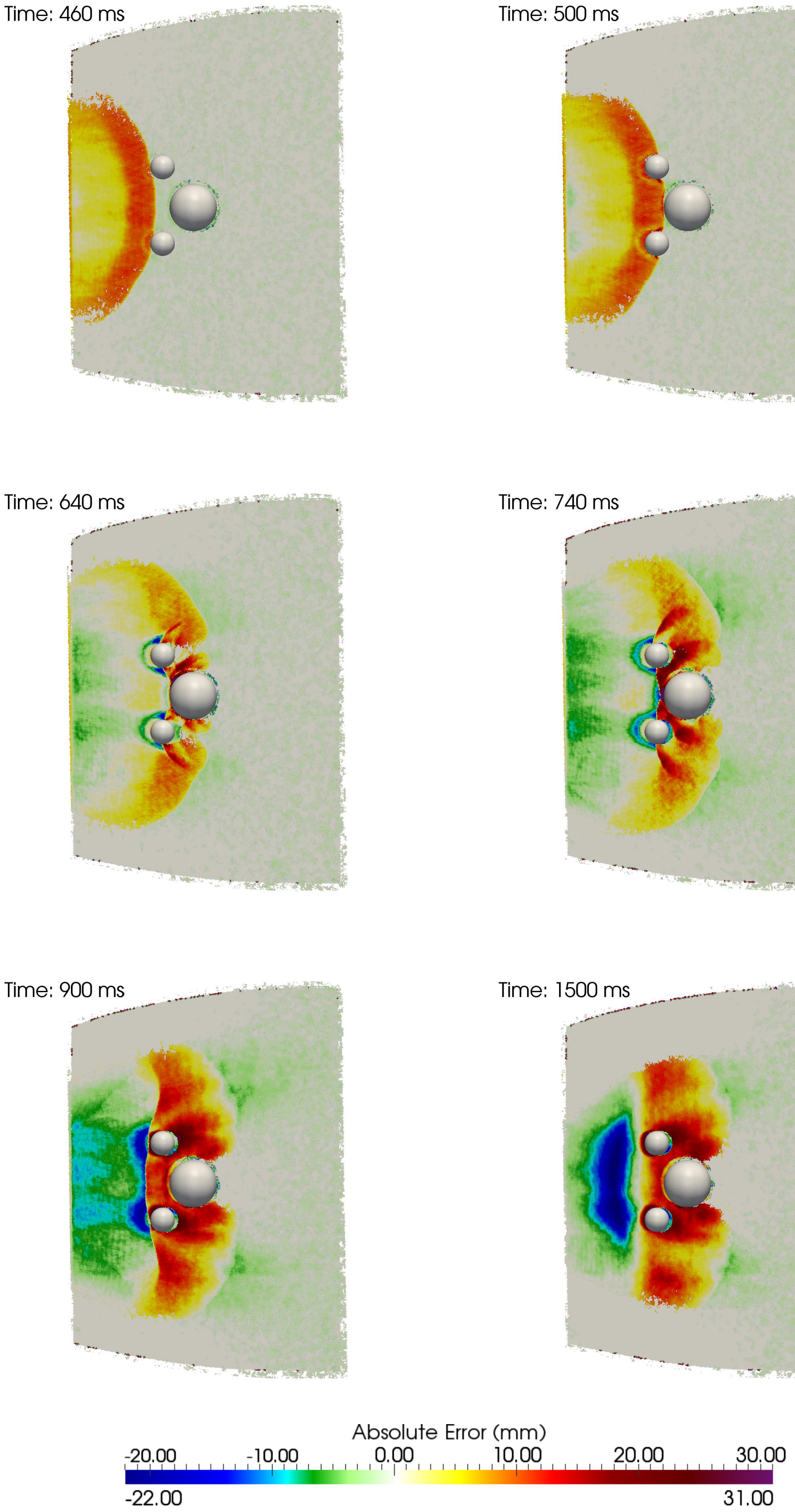

Figure 17.20: 2D plant views displaying the absolute error at times $t = 460$ ms, $t = 540$ ms, $t = 640$ ms, $t = 740$ ms, $t = 900$ ms, $t = 1500$ ms

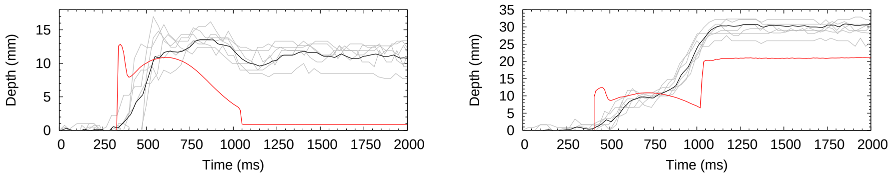

(a) PD1 (b) PD2

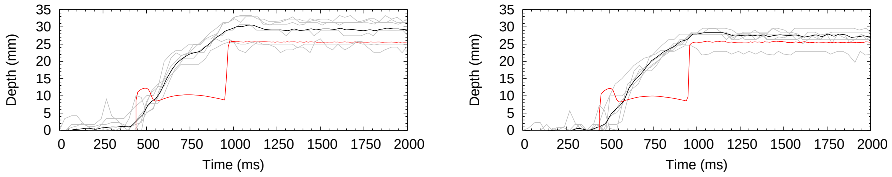

(c) PS1 (d) PS2

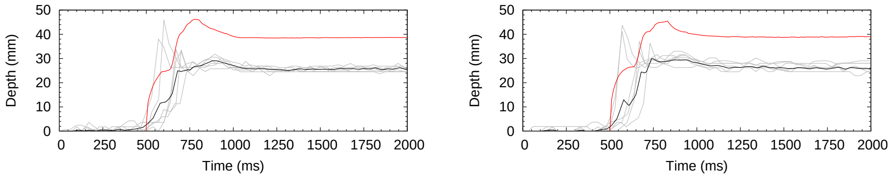

(e) PSL (f) PSR

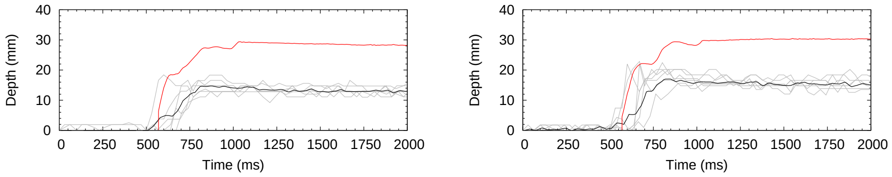

(g) PS0L (h) PS0R

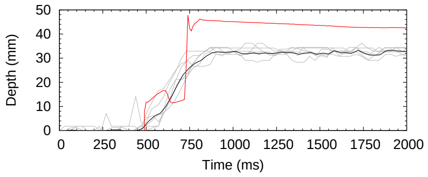

(i) PS0

Figure 17.21: Computational and experimental probe results

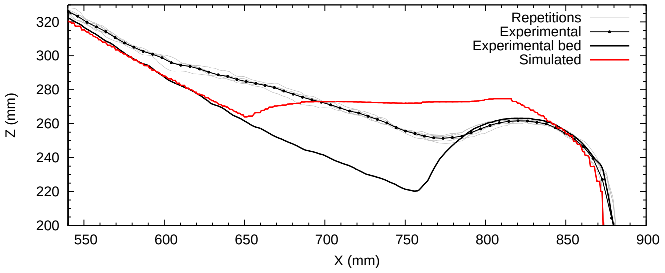

Figure 17.22: Longitudinal section ($y = 500\,mm$) for Experiment 2 at the final stage

17.2.1 Gravity driven flow facing up a dike

Another important configuration in real applications is an oncoming flow against barriers. The design and location of this type of structures highly governs the dynamical description of the granular flow and its final shape. The two principal phenomena observed in this configuration are the presence of deflection waves upstream of the dike and the overtopping generated when the flow depth exceeds the height of the dike crest. Previous works focused on small-scale laboratory experiments with dike structures and granular flows such as the ones by Hakonardottir et al. (2003); Faug et al. (2008). In both works, the granular material was confined in a 1D configuration and the start/go mechanism was not studied in detail, as no data about the plan view spreading of the material was provided.

Figure 17.23 shows a 3D view of the initial configuration of the experiment. The images captured during the laboratory work around the dike are displayed in Figure 17.24

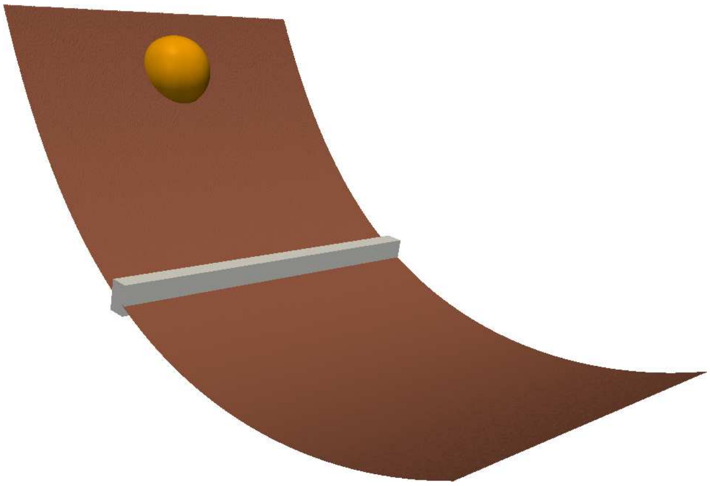

Figure 17.23: Initial configuration with the sand deposit at the beginning of the slope and the dike downwards

Figure 17.25 displays a temporal sequence of 3D views. Once the sand is released on the top of the slope the flow is accelerated downwards. The inertia of the moving mass is high enough for it to fly over the dike, for example at times $t = 490\,ms$, $t = 610\,ms$. Nevertheless, the most of the mass is retained by the dike structure, and the maximum run out of the avalanche is highly shortened by the dike effect, see times $t = 710\,ms$ and $t = 910\,ms$. At time $t = 1040\,ms$ most of the morphodynamic changes have taken place and at time $t = 2000\,ms$ the mass has reached an equilibrium stage.

Comparison with the experimental data is shown in Figures 17.26 and 17.27. At times $t = 490\,ms$ and $t = 610\,ms$ the computational results are affected by the time lag of the sand release procedure. Afterwards, differences among the instants of time are located in the tail of the avalanche. In the computational results the tail moves faster than in the experimental data and consequently, the depth elevation upstream from the dike is higher and in the tail region it is smaller. These differences during the transient stage


(a) Impact (b) Wave break

(c) Overtopping (d) Overflow

Figure 17.24: Flow features and structures for Experiment 3

of the avalanche are reduced once the equilibrium stage is reached, at time $t = 2000\,ms$. The front and the tail of the avalanche are well reproduced by the numerical model. The maximum run out obtained with the computational model tends to be slightly underestimated. This can be justified by the high level of energy that the grains have during the avalanche and that allow them to fly further downstream from the dike. With the depth averaged assumption considered in this work, the vertical acceleration is neglected and consequently, the vertical motion is underestimated.

The transient absolute errors are displayed in Figure 17.28. As it has been explained above, the larger differences at times $t = 490\,ms$, $t = 610\,ms$ and $t = 710\,ms$ are found at the front and at the tail, since in the computed results, the head of the avalanche moves faster and the sand accumulates upstream from the dike and at the tail. Nevertheless, the final stage provides a limited error all over the domain. At that time, the main error area is located in the middle of the slope material accumulated upstream from the dike. This is consistent with the phenomena observed at the plan views, Figure 17.27 at time $t = 2000\,ms$, since in the numerical solution the area with constant slope is wider than in the experimental data. Moreover, the quasi zero error area located on the top of the dike, i.e. the overtopping area, at the final stage is remarkable. Computational and experimental data match accurately.

The computational results are also validated against the probe results obtained in Caviedes et al. (2014), but excluding PS0R, PS0L and PS0 because they showed no information in this experimental case, Figure 17.29. As it has been noted in the previous experiments, the probes located upslope are more influenced by the sand release procedure. Consequently, a temporal lag in the peak flow is observed at probes PU and PD1. Probe PD2 display an accurate tracking of the temporal evolution of the sand depth evolution. PS1 and PS2 present a good trend of the experimental dynamics although the surface level is underestimated downwards the dike. This is coherent with the 2D views shown in Figure 17.27 at time $t = 2000\,ms$: the maximum run out is slightly shorten in the computational solution.

Figure 17.30 shows the longitudinal section at $y = 500\,mm$. Regarding the observed computed and experimental bed topography differences, i must be noted that the conceptual model is depth averaged and the region downstream from the dike can not be correctly described. Therefore, it has been decided to design a *vertical* dike for the simulation. Nevertheless, both computational and experimental data display the same tendency, describing a uniform slope upstream from the dike. The main differences are focused on the tail, where numerical solution presents a more severe slope. Additionally, the maximum run out is overestimated with the computed prediction, which is justified by the highly fluidized mass observed in the laboratory work, which allows the material granular to fly further during the overtopping event.

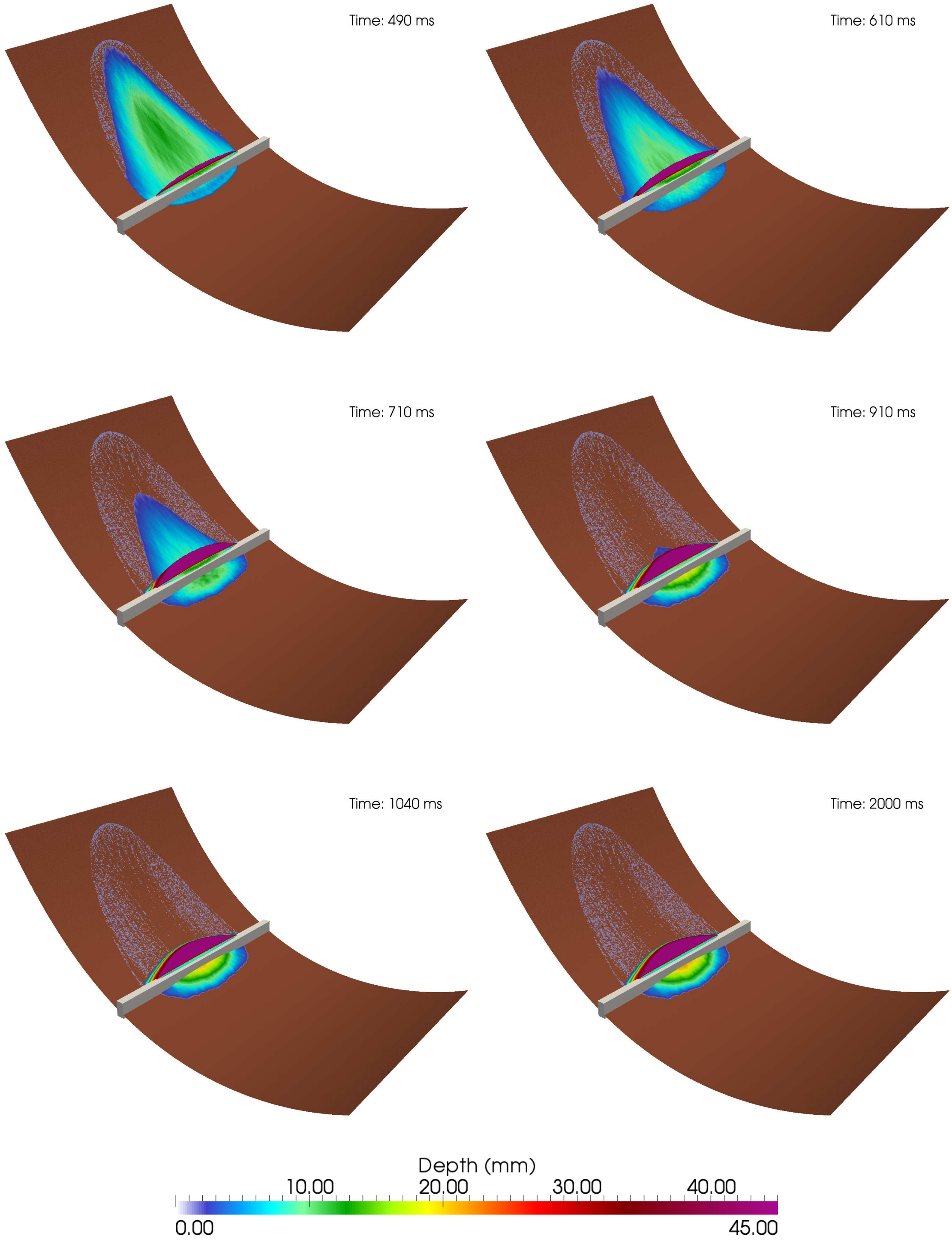

Figure 17.25: 3D contour views for the free surface level at times t = 490 ms, t = 610 ms, t = 710 ms, t = 910 ms, t = 1140 ms and t = 2000 ms

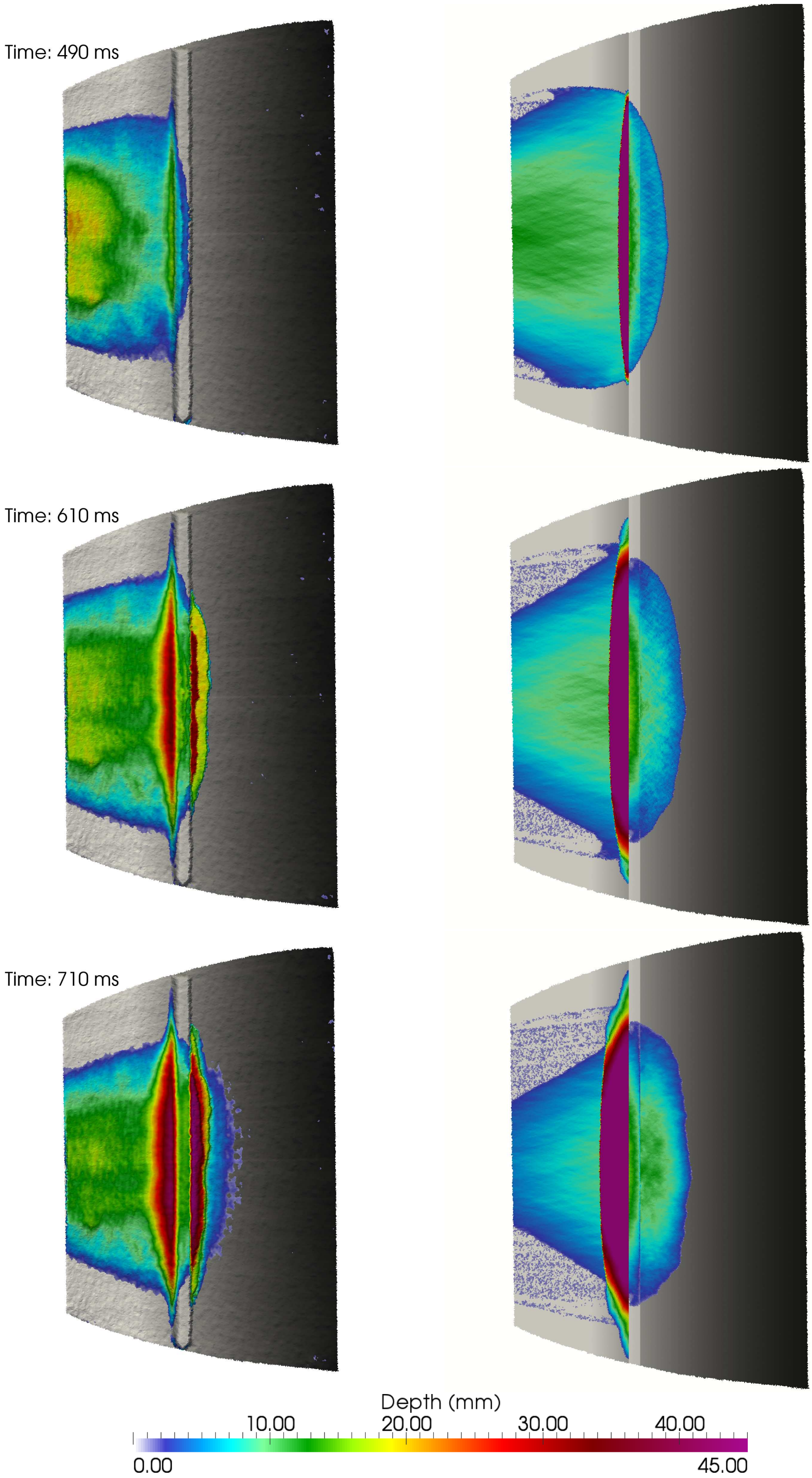

Figure 17.26: 2D plant views for the sand depth obtained experimentally (left side) and computationally (right side) at times $t = 490$ ms, $t = 610$ ms, $t = 710$ ms

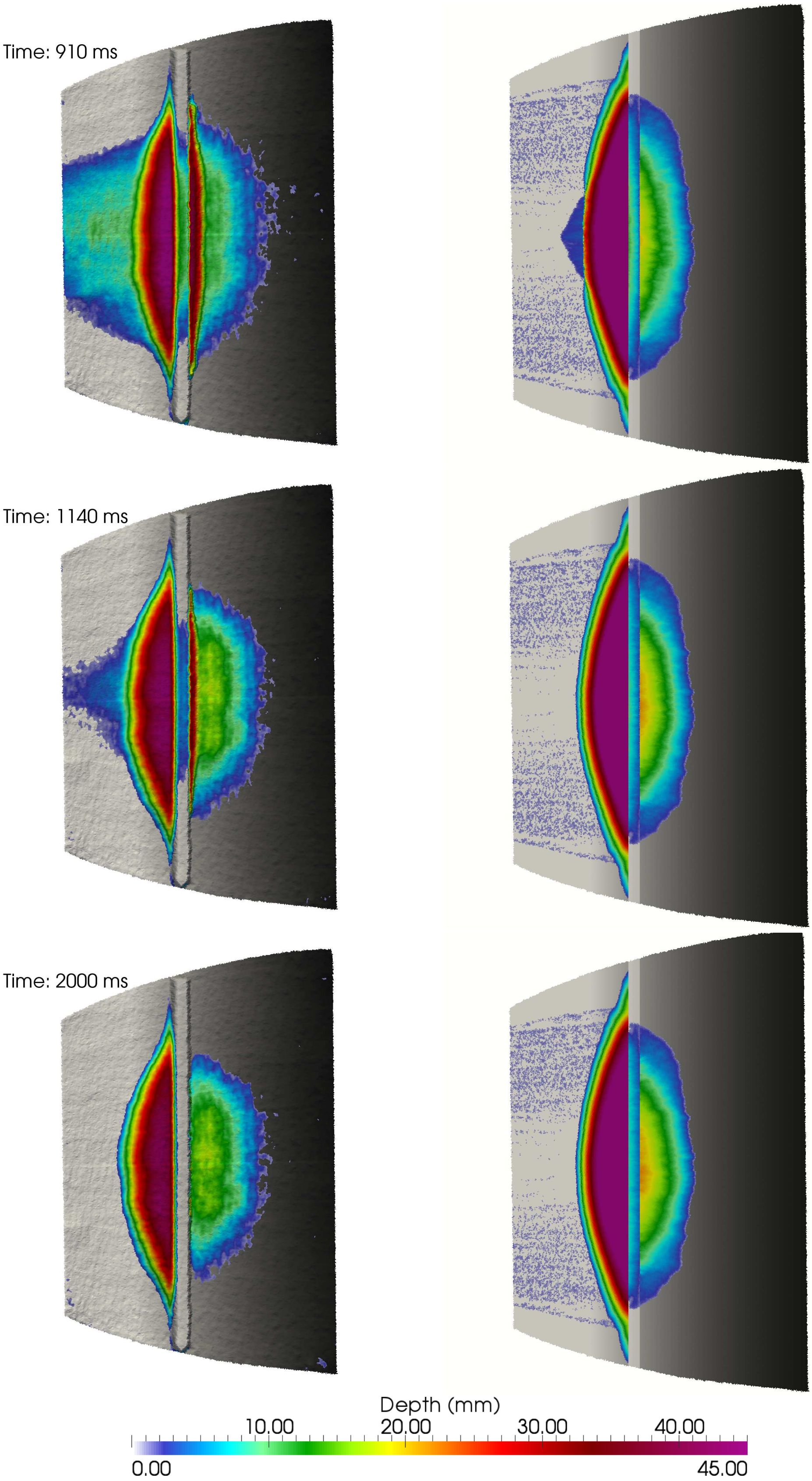

Figure 17.27: 2D plant views for the sand depth obtained experimentally (left side) and computationally (right side) at times $t = 910$ ms, $t = 1140$ ms, $t = 2000$ ms

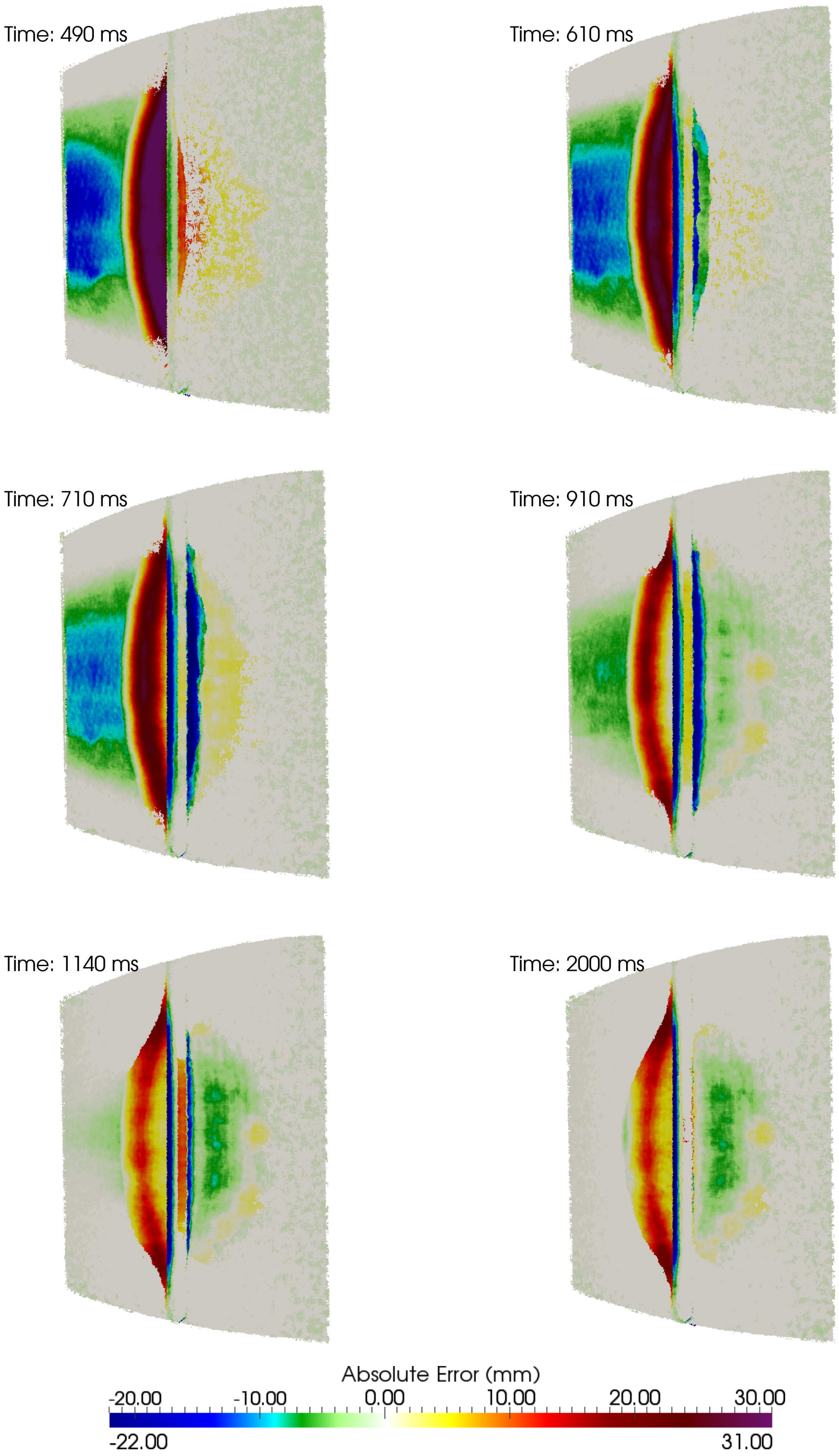

Figure 17.28: 2D plant views displaying the absolute error at times t = 490 ms, t = 610 ms, t = 710 ms, t = 910 ms, t = 1140 ms, t = 2000 ms

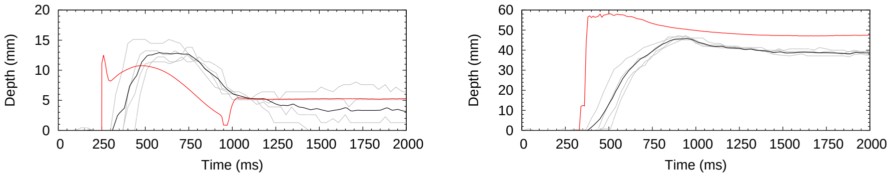

(a) PU (b) PD1

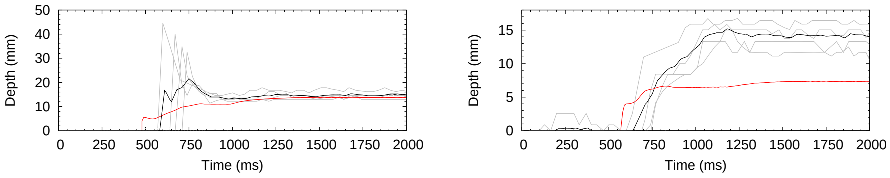

(c) PD2 (d) PS1

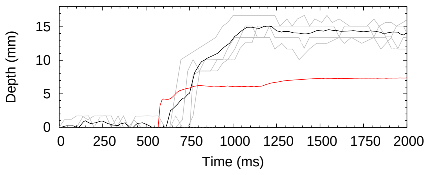

(e) PS2

Exp. repetitions —— Exp. Average —— Simulated ——

Figure 17.29: Computational and experimental probe results

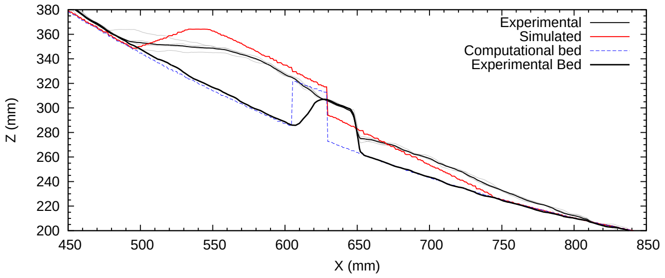

Figure 17.30: Longitudinal section ($y = 500\,mm$) for Experiment 3 at the final stage

Chapter 18

Conclusions for the small-scale environmental problems

The dry granular flow has been simulated using a 2D Finite Volume scheme considering the features of gravity projections derived for unstructured meshes previously developed and validated in this work. Thanks to the reliability on the numerical scheme a series of experimental cases which represent small-scale up-to-date environmental problems have been studied.

The main singularity of the experiments is focused on the presence of obstacles, over a rough and complex topography, which in turn implies shock formation. These moving shocks are the key for the understanding of the flow behavior and are well reproduced by the numerical scheme considered. Three experiments have been modeled and analyzed.

The first experiment is based on granular flow around a semispherical obstacle. The computed results are able to accurately track in time the movement and spreading of the mass. Additionally, the two phenomena observed during the development of the experiment, namely the stagnation area upstream from the obstacle and the shock around it, are also numerically reproduced.

The second experiment consists of granular flow around two small semispherical obstacles and one semispherical obstacle located downstream. The complexity of this case is larger, since the shock structure involves the presence of additional moving waves which interact with each other. Nevertheless, the temporal prediction of the computed results displays a good agreement in comparison with experimental data.

The third experiment is of granular flow over a square dike where a overflow takes place. The temporal prediction and the maximum run out are well reproduced by the numerical model.

The main flow structures are well captured in time and space by the numerical scheme in the three experiments: the impact, the shock formation, the overflow and the maximum run out. The small differences in the shocks are justified by the depth averaged assumption considered, as the vertical accelerations around the obstacles are neglected. Moreover, thanks to the robustness of the numerical scheme, able to handle with complex stop/go conditions and wet/dry situations, distorting numerical effects are avoided. Hence, the forecasting capabilities of the computed results can be used for the future design of civil infrastructures or for the understanding of more complex and ambitious rheological models.

18.1 Further research

Erosion processes seem to play a key role in the granular flow dynamics and consequently, they have to be taken into account in natural flow modeling. However the description of the erosion processes related to the flowing/static transition in granular material is still a challenge. Furthermore, the inclusion of the water is required, since the infiltration processes constitute a trigger mechanism for the landslides movements. Experimental/numerical investigation is required for facing up both features.

Moreover the nature soil heterogeneity should be also addressed, since no experimental studies have been carried out in this direction. The bed shear stress can be modified by the interlocking among particles, leading to obtain different flow structures.

Desarrollo de esquemas numéricos robustos y basados en modelos físicos para procesos de transporte y cambios geomorfodinámicos

Conclusiones generales

En la primera parte de esta tesis se han estudiado los cambios morfodinámicos que se producen en los cauces de los ríos. El análisis cuantitativo acerca del comportamiento de las distintas formulaciones de fondo ante situaciones 1D y 2D transitorias ha permitido comprobar que la nueva interpretación de la fórmula de Smart obtiene los resultados más precisos en todos los casos propuestos. Además, las diferencias con respecto al resto de relaciones empíricas es mayor ante situaciones 1D. Por otra parte, se ha comprobado que a través de la estrategia numérica propuesta para acoplar el modelo hidrodinámico y el morfodinámico, el coste computacional se reduce significativamente, pero sin perder una buena precisión en los resultados obtenidos. Se ha verificado cómo la solución computacional se inestabiliza si la nueva celeridad asociada al fondo no se tiene en cuenta en el criterio de estabilidad. Como trabajo futuro se incluiría el estudio del transporte de sedimento en suspensión, el efecto provocado por una granulometría no uniforme y la variación temporal y espacial de la densidad de la mezcla fluida.

Con respecto a la parte de deslizamientos de terreno, se ha comprobado como la inclusión de las proyecciones de la gravedad en los términos de presión y fricción son necesarias para obtener soluciones precisas. La utilización de coordenadas locales o globales proporciona resultados idénticos y permiten predecir de forma precisa deslizamientos granulares secos ante geometrías irregulares e importantes cambios de régimen hidrodinámico. Además, ningún parámetro adicional es necesario para satisfacer las condiciones de comienzo y parada del movimiento. El mismo esquema numérico es empleado para reproducir computacionalmente los experimentos propuestos en la última parte de la tesis. Los resultados obtenidos son satisfactorios y las estructuras complejas de choques que se generan alrededor de los obstáculos son correctamente reproducidas. Como trabajo futuro se propone la inclusión de granulometría variable, la incorporación de agua en el flujo de material granular y el estudio de la erosión en la base del deslizamiento.

Bibliography

Abderrezzak, K. K. and Paquier, A. 2011. Applicability of Sediment Transport Capacity Formulas to Dam-Break Flows over Movable Beds. *Journal of Hydraulic Engineering 137*, 209–221.

Alcrudo, F. and Benkhaldoun, F. 2001. Exact solutions to the Riemann problem of the shallow water equations with a bottom step. *Computers and Fluids 30*, 643–671.

Aricò, C. and Tucciarelli, T. 2008. Diffusive Modeling of Aggradation and Degradation in Artificial Channels. *Journal of Hydraulic Engineering 134(8)*, 1079–1088.

Ashida, K. and Michiue, M. 1972. Study on hydraulic resistance and bedload transport rate in alluvial streams. *Transactions, Japan Soc. Civil Eng. 206*, 569–589.

Bellal, M., Iervolino, M., and Zech, Y. 2004. Knickpoint migration process: experimental and numerical approaches. *Proc., 12th Conf. on "Sediment and Sedimentation Particles". Prague, Czech Republic* , –.

Bermúdez, A. and Vázquez-Cendón, M. E. 1994. Upwind methods for hyperbolic conservation laws with source terms. *Computers and Fluids 23*, 1049–1071.

Bernetti, R., Titarev, V., and Toro, E. 2008. Exact solution of the Riemann problem for the shallow water equations with discontinuous bottom geometry. *Journal of Computational Physics 227*, 3212–3243.

Bilanceri, M., Beux, F., Elmahi, L., Guillard, H., and Salvetti, M. 2012. Linearized implicit time advancing and defect correction applied to sediment transport simulations. *Computers and Fluids 63*, 82–104.

Bouchut, F., Fernández-Nieto, E. D., Mangeney, A., and Lagrée, P. Y. 2008. On new erosion models of Savage-Hutter type for avalanches. *Acta Mechanica 199,* 1-4, 181–208.

Bouchut, F., Mangeney-Castelnau, A., Perthame, B., and Vilotte, J. 2003. A new model of Saint-Venant and Savage-Hutter type for gravity driven shallow water flows. *C. R. Acad. Sci. Paris Ser. I,* 336, 531–536.

Bouchut, F. and Westdickenberg, M. 2004. Gravity driven shallow water models for arbitrary topography. *Community of Math Sciences 2,* 3, 359–389.

Boutreux, T. and deGennes, P. 1997. Evolution of a step in a granular material: the Sinai problem. *Comptes rendus de l academie des sciences. Serie II Fascicule B-Mechanique Physique Chimie Astronomie 325,* 2, 85–89.

Burguete, J., García-Navarro, P., and Murillo, J. 2008a. Friction term discretization and limitation to preserve stability and conservation in the 1D shallow-water model: Application to unsteady irrigation and river flow. *International Journal of Numerical Methods in Fluids 54*, 403–425.

Burguete, J., García-Navarro, P., and Murillo, J. 2008b. Preserving bounded and conservative solutions of transport in one-dimensional shallow-water flow with upwind numerical schemes: Application to fertigation and solute transport in rivers. *International Journal of Numerical Methods in Fluids 56*, 1731–1764.

Camenen, B. and Larson, M. 2005. A general formula for non-cohesive bed load sediment transport. *Estuarine, Coastal and Shelf Science 63*, 249–260.

Canestrelli, A., Dumbser, M., Siviglia, A., and Toro, E. 2010. Well-balanced high-order centred schemes on unstructured meshes for shallow water equations with fixed and mobile bed. *Advances in Water Resources 33*, 291–303.

Cao, Z., Day, R., and Egashira, S. 2002. Coupled and decoupled numerical modeling of flow and morphological evolution in alluvial rivers. *Journal of Hydraulic Engineering 128*, 306–321.

Cao, Z., Pender, G., and Carling, P. 2006. Shallow water hydrodynamic models for hyperconcentrated sediment-laden flows over erodible bed. *Advances in Water Resources 29(4)*, 546–557.

Castro Diaz, M., Fernandez Nieto, E., Ferreiro, A., and Pares, C. 2009. Two-dimensional sediment transport models in shallow water equations. A second order finite volume approach on unstructured meshes. *Computer Methods in Applied Mechanics and Engineering 198*, 2520–2538.

Caviedes, D., Juez, C., Murillo, J., and García-Navarro, P. 2014. Experimental study of 2D granular flow over a complex topography with obstacles using a consumer-grade RGB-D sensor. *Under review in Journal of Fluid Mechanics –*, –.

Chinnayya, A., LeRoux, A., and Seguin, N. 2004. A well-balanced numerical scheme for the approximation of the shallow water equations with topography: the resonance phenomenon. *International Journal On Finite Volumes 1*, 1–33.

Cordier, S., Le, M., and Morales de Luna, T. 2011. Bedload transport in shallow water models: Why splitting (may) fail, how hyperbolicity (can) help. *Advances in Water Resources 34*, 980–989.

Cui, X. and Gray, J. 2013. Gravity-driven granular free-surface flow around a circular cylinder. *Journal of Fluid Mechanics 720*, 314–337.

Da Cruz, F., Emam, S., Prochnow, M., Roux, J., and Chevoir, F. 2005. Rheophysics of dense granular materials: Discrete simulation of plane shear flows. *Physical Review 72*, 021309.

Dal Maso, G., LeFloch, P., and Murat, F. 1995. Definition and weak stability of nonconservative products. . *Math. Pures Appl. 74*, 483–548.

De Vriend, H., Zyserman, J., Nicholson, J., Roelvink, J., Pechon, P., and Southgate, H. 1993. Medium-term 2DH coastal area modelling. *Journal of Coastal Engineering 21*, 193–224.

Denlinger, R. and Iverson, R. 2004. Granular avalanches across irregular three dimensional terrain: 1. Theory and computation. *Journal of Geophysical Research 109,* F1, F01014.

Douady, S., Andreotti, B., and Daerr, A. 1999. On granular surface flow equations. *The European Physical Journal B 11*, 131–142.

Dressler, R. F. 1954. Comparison of theories and experiments for the hydraulic dam-break wave. *Int. Assoc. Sci. Hydrology 3*, 319–328.

Einstein, H. 1950. *The bed-load function for sediment transportation in open channel flows.* Tech. Rep.

Engelund, F. and Fredsoe, J. 1976. Sediment transport model for straight alluvial channels. *Nordic Hydrology 7:5*, 293–306.

Faccanoni, G. and Mangeney, A. 2012. Exact solution for granular flows. *International Journal for Numerical and Analytical Methods in Geomechanics 26*, –.

Faug, T., Gauer, K., Lied, K., and Naaim, M. 2008. Overrun length of avalanches overtopping catching dams: cross-comparison of small-scale laboratory experiments and observations from full-scale avalanches. *Journal of Geophysical Research 113*, F03009.

Favreau, P., Mangeney, A., Lucas, A., Crosta, G., and Bouchut, F. 2010. Numerical modeling of landquakes. *Geophysical Research Letters 37*, L1530.

Forterre, Y. and Pouliquen, O. 2003. Long-surface-wave instability in dense granular flows. *Journal of Fluid Mechanics 486*, 21–50.

Fraccarollo, L. and Capart, H. 2002. Riemann Wave description of erosional dam-break flows. *Journal of Fluid Mechanics 461*, 115–133.

Garegnani, G., Rosatti, G., and Bonaventura, L. 2013. On the range of validity of the Exner-based models for mobile-bed river flow simulations. *Journal of Hydraulic Research 51(4)*, 380–391.

GOUTIÈRE, L., SOARES-FRAZAO, S., SAVARY, C., LARAICHI, T., AND ZECH, Y. 2008. One-dimensional model for transient flows involving bed-load sediment transport and changes in flow regimes. *Journal of Hydraulic Engineering 134(6)*, 726–735.

GOUTIÈRE, L., SOARES-FRAZAO, S., AND ZECH, Y. 2011. Dam-break flow on mobile bed in abruptly widening channel: experimental data. *Journal of Hydraulic Research 49(3)*, 367–371.

GRASS, A. 1981. *Sediments transport by waves and currents.* SERC London Cent. Mar. Technol, Report No. FL.

GRAY, J., TAI, Y., AND NOELLE, S. 2003. Shock waves, dead zones and particle-free regions in rapid granular free-surface flows. *Journal of Fluid Mechanics 491*, 161–81.

GRAY, J., WIELAND, K., AND HUTTER, K. 1999. Gravity-driven free surface flow of granular avalanches over complex basal topography. *Proc. Royal Soc. London Ser. A, 455*, 1841.

HAKONARDOTTIR, K. AND HOGG, A. 2005. Oblique shocks in rapid granular flows. *Physics of Fluids 17*, 077101.

HAKONARDOTTIR, K., HOGG, A., BATEY, J., AND WOODS, A. 2003. Flying avalanches. *Geophysical Research Letters 30*, 2191.

HARTEN, A., LAX, P., AND LEER, B. V. 1983. On upstream differencing and Godunov-type schemes for hyperbolic conservation laws. *SIAM Review 25:1*, 35–61.

HAUKSSON, S., PAGLIARDI, M., BARBOLINI, M., AND JOHANNESSON, T. 2007. Laboratory measurements of impact forces of supercritical granular flow against mast-like obstacles. *Cold Regions, Science and Technology 49*, 54–63.

HOLLY, F. M. AND RAHUEL, J. L. 1990. New numerical/physical framework for mobile-bed modelling. I: Numerical and physical principles. *Journal of Hydraulic Research 28(4)*, 401–416.

HUBBARD, M. E. AND GARCÍA-NAVARRO, P. 2000. Flux difference splitting and the balancing of source terms and flux gradients. *Journal of Computational Physics 165*, 89–125.

HUDSON, J. 2001. *Numerical techniques for morphodynamic modelling.* Ph.D. thesis, Department of Mathematics, The University of Reading, Whiteknigths, Reading.

HUDSON, J. AND SWEBY, P. K. 2002. Formulations for Numerically Approximating Hyperbolic Systems Governing Sediment Transport. *Journal of Scientific Computing 19*, 225–251.

HUDSON, J. AND SWEBY, P. K. 2005. A high-resolution scheme for the equations governing 2D bed-load sediment transport. *International Journal of Numerical Methods in Fluids 47*, 1085–1091.

Iverson, R. and Denlinger, R. 2001. Flow of variably fluidized granular masses across three-dimensional terrain. A Coulomb mixture theory. *Journal of Geophysical Research 106,* B1, 537–552.

Juez, C., Murillo, J., and García-Navarro, P. 2013a. 2D simulation of granular flow over irregular steep slopes using global and local coordinates. *Journal of Computational Physics 255*, 166–204.

Juez, C., Murillo, J., and García-Navarro, P. 2013b. Numerical assesment of bed load discharge formulations for transient flow in 1D and 2D situations. *Journal of Hydroinformatics* -, In press.

Julien, P. 1998. *Erosion and Sedimentation.* Cambridge University Press.

Kalinske, A. 1947. Movement of sediment as bed load in rivers. *Trans. AGU 28*, 615–620.

Kassem, A. A. and Chaudry, M. H. 1998. Comparison of coupled and semicoupled numerical models for alluvial channels. *Journal of Hydraulic Engineering 124(8)*, 794–802.

Kerswell, R. 2005. Dam break with Coulomb friction: A model for granular slumping? *Physics of Fluids 17.*

Lajeunesse, E., Mangeney-Castelnau, A., and Villote, J. P. 2004. Spreading of a granular mass on a horizontal plane. *Physics of Fluids 16*, 2371–2381.

LeFloch, P. and Thanh, M. 2007. The Riemann problem for shallow water equations with discontinuous topography. *Community of Math Sciences 5*, 865–885.

LeFloch, P. and Thanh, M. 2011. A Godunov-type method for the shallow water equations with discontinuous topography in the resonant regime. *Journal of Computational Physics 230*, 7631–7660.

Leveque, R. 2002. *Finite Volume Methods for Hyperbolic Problems.* Cambridge University Press, New York.

Luque, R. F. and van Beek, R. 1976. Erosion and transport of bedload sediment. *Journal of Hydraulic Research 14*, 127–144.

Lyn, D. and Altinakar, M. 2002. St. Venant-Exner equations for near-critical and transcritical flows. *Journal of Hydraulic Engineering 128(6)*, 579–587.

Mangeney, A., Roche, O., Hungr, O., Mangold, N., Faccanoni, G., and Lucas, A. 2010. Erosion and mobility in granular collapse over sloping beds. *Journal of Geophysical Research 115*, F03040.

Mangeney, A. and Heinrich, Ph. and Roche, R. 2000. Analytical and numerical solution of the dam-break problem for application to water floods, debris and dense snow avalanches. *Pure and Applied Geophysics 157*, 1081–1096.

Mangeney-Castelnau, A., Bouchut, F., Thomas, N., Vilotte, J. P., and Bristeau, M. 2007. Numerical modeling of self-channeling granular flows and of their levee-channel deposits . *Journal of Geophysical Research 112*, F02017.

Mangeney-Castelnau, A., Bouchut, F., Vilotte, J. P., Lajeunesse, E., Aubertin, A., and Pirulli, M. 2005. On the use of Saint-Venant equations for simulating the spreading of a granular mass . *Journal of Geophysical Research 110*, B09103.

Mangeney-Castelnau, A., Vilotte, J. P., Bristeau, M. O., Perthame, B., Bouchut, F., Simeoni, C., and Yernini, S. 2003. Numerical modeling of avalanches based on Saint-Venant equations using a kinetic scheme. *J. Geophys. Res. 108*, 2527.

Manning, R. 1895. On the flow of water in open channels and pipes. *Transactions of the Institution of Civil Engineers of Ireland 20*, 161–207.

Meyer-Peter, E. and Müller, R. 1948. *In: Report on the 2nd Meeting International Association Hydraulic Structure Research.* Stockholm, Sweden.

Moretti, L., Mangeney, A., Capdeville, Y., Stutzmann, E., Huggel, C., Schneider, D., and Bouchut, F. 2012. Numerical modeling of the Mount Steller landslide flow history and of the generated long period seismic waves. *Geophysical Research Letters 39*, L16402.

Murillo, J. and García-Navarro, P. 2010a. An Exner-based coupled model for two-dimensional transient flow over erodible bed. *Journal of Computational Physics 229*, 8704–8732.

Murillo, J. and García-Navarro, P. 2010b. Weak solutions for partial differential equations with source terms: Application to the shallow water equations. *Journal of Computational Physics 229*, 4327–4368.

Murillo, J. and García-Navarro, P. 2011. Improved Riemann solvers for complex transport in two-dimensional unsteady shallow flow. *Journal of Computational Physics 230*, 7202–7239.

Murillo, J. and García-Navarro, P. 2012a. A Riemann solver for unsteady computation of 2D shallow flows with variable density. *Journal of Computational Physics 231:4*, 1963–2001.

Murillo, J. and García-Navarro, P. 2012b. Augmented versions of the HLL and HLLC Riemann solvers including source terms in one and two dimensions for shallow flow applications. *Journal of Computational Physics 231*, 6861–6906.

Murillo, J., García-Navarro, P., and Burguete, J. 2008. Time Step Restrictions For Well Balanced Shallow Water Solutions In Non-Zero Velocity Steady States. *International Journal of Numerical Methods in Fluids 56*, 661–686.

Murillo, J., García-Navarro, P., and Burguete, J. 2009. Conservative Numerical Simulation of Multicomponent Transport in Two-Dimensional Unsteady Shallow Water Flow. *Journal of Computational Physics 228*, 5539–5573.

Nielsen, P. 1992. *Coastal Bottom Boundary Layers and Sediment Transport. Advanced Series on Ocean Engineering.* World Scientific Publishing.

Palumbo, A., Soares-Frazao, S., Goutiere, L., Pianese, D., and Zech, Y. 2008. *Proc., River Flow 2008 International Conference on Fluvial hydraulics, Cesme.*

Parker, G. 1979. Hydraulic geometry of active gravel rivers. *Journal of Hydraulic Engineering 105:9*, –.

Peña, E., Fe, J., Sánchez-Tembleque, F., Puertas, J., and Cea, L. 2008. Experimental validation of a sediment transport two-dimensional depth-averaged numerical model using PIV and 3D Scanning technologies. *Journal of Hydraulic Research Vol. 46*, 489–503.

Pirulli, M. 2005. Numerical modelling of landslide runout. *Ph.D. Degree in Geotechnical Engineering* , .

Pirulli, M., Bristeau, M., Mangeney-Castelnau, A., and Scavia, C. 2007. The effect of the earth pressure coefficients on the runout of granular material. *Environmental Modelling and Software 22*, 1437–1454.

Pirulli, M. and Mangeney, A. 2008. Results of Back-Analysis of the Propagation of Rock Avalanches as a Function of the Assumed Rheology. *Rock Mechanics and Rock Engineering 41*, 59–84.

Pouliquen, O. 1999. Scaling laws in granular flows down rough inclined planes. *Physics of Fluids 11*, 542–548.

Pouliquen, O. and Forterre, Y. 2002. Friction law for dense granular flows: application to the motion of a mass down a rough inclined plane. *Journal of Fluid Mechanics 453*, 133–151.

Pouliquen, O. and Forterre, Y. 2008. Flows of Dense Granular Media. *Annual Review of Fluid Mechanics 40*, 1–24.

Ritter, A. 1892. Die Fortpflanzung der Wasserwelle. *Vereine Deutscher Ingenieure Zeitswchrift 36*, 947–954.

Roche, O., Attali, M., Mangeney, A., and Lucas, A. 2011. On the run-out distance of geophysical gravitational flows: Insight from fluidized granular collapse experiments. *Earth and Planetary Science Letters 311,* 3, 375–385.

Roe, P. 1986. *Numerical Methods in Fluid Dynamics.* Vol II. Oxford University Press, Oxford.

Rosatti, G. and Begnudelli, L. 2010. The Riemann Problem for the one-dimensional, free-surface Shallow Water Equations with a bed step: theoretical analysis and numerical simulations. *Journal of Computational Physics 229*, 760–787.

Rosatti, G., Murillo, J., and Fraccarollo, L. 2007. Generalized Roe schemes for 1D two-phase, free-surface flows over a mobile bed. *Journal of Computational Physics 54*, 543–590.

Rosatti, G., Murillo, J., and Fraccarollo, L. 2008a. Generalized Roe schemes for 1D, two-phase, free-surface flows over a mobile bed. *Journal of Computational Physics 227(4)*, 10058–10077.

Rosatti, G., Murillo, J., and Fraccarollo, L. 2008b. Generalized Roe schemes for 1D two-phase, free-surface flows over a mobile bed. *Journal of Computational Physics 227*, 10058–10077.

Savage, S. and Hutter, K. 1989. The motion of a finite mass of granular material down a rough incline. *Journal of Fluid Mechanics 199*, 177–215.

Serrano, A., Murillo, J., and García-Navarro, P. 2012. Finite volumes for 2D shallow-water flow with bed-load transport on unstructured grids. *Journal of Hydraulic Research 50(2)*, 154–163.

Siviglia, A., Stecca, G., Vanzo, D., Zolezzi, G., Toro, E., and Tubino, M. 2013. Numerical modelling of two-dimensional morphodynamics with applications to river bars and bifurcations. *Advances in Water Resources 52*, 243–260.

Smart, G. 1984. Sediment transport formula for steep channels. *Journal of Hydraulic Engineering 3*, 267–276.

Soares-Frazao, S., Canelas, R., Cao, Z., Cea, L., Chaudhry, H., Moran, A., Kadi, K., Ferreira, R., Fraga-Cadorniga, I., Gonzalez-Ramirez, N., Greco, M., Huang, W., Imran, J., Coz, J. L., Marssoli, R., Paquier, A., Pender, G., Pontillo, M., Puertas, J., Spinewine, B., Swartenbroekx, C., Tsubaki, R., Villaret, C., Wu, W., Yue, Z., and Zech, Y. 2012. Dam-break flows over mobile beds: experiments and benchmark tests for numerical models. *Journal of Hydraulic Research 50:4*, 364–375.

Soares-Frazao, S. and Zech, Y. 2010. HLLC scheme with novel wave-speed estimators appropiate for two-dimensional shallow-water flow on erodible bed. *International Journal of Numerical Methods in Fluids 66(8)*, 1019–1036.

Spinewine, B. and Zech, Y. 2004. *Proc., 4th Workshop of IMPACT Project.* Alkema, Rotterdam, The Netherlands.

Spinewine, B. and Zech, Y. 2007. Small-scale laboratory dam-break waves on movable beds. *Journal of Hydraulic Research 45*, 73–86.

Tassi, P., Rheberg, S., Vionnet, C., and Bokhove, O. 2008. Discontinous Galerkin finite element for river bed evolution under shallow flows. *Computer Methods in Applied Mechanics and Engineering 197*, 2930–2947.

Tingsanchali, T. and Chinnarasri, C. 2001. Numerical modelling of dam failure due to flow overtopping. *Hydrological Sciences Journal-Journal des Sciences Hydrologiques 46*, 113–130.

Toro, E. 1994. *Restoration of the contact surface in the HLL Riemann solver.* Show Waves.

Toro, E. 1997. *Riemann solvers and numerical methods for fluid dynamics.* Springer, Berlin.

Toro, E. 2001. *Shock-Capturing Methods for Free-Surface Shallow Flows.* Wiley, New York.

Toro, E. 2009. *Riemann Solvers and Numerical Methods for Fluid Dynamics.* Springer, New York.

Vázquez-Cendón, M. 1999. Improved treatment of source terms in upwind schemes for the shallow water equations in channels with irregular geometry. *Journal of Computational Physics 148*, 497–498.

Watson, G., Peregrine, D., and Toro, E. 1992. Numerical solution of the Shallow Water Equations on a beach using the weighted average flux method. *Comput. Fluid Dynamics* , 495–502.

Whittaker, J. and Davies, T. 1982. Erosion and sediment transport processes in step-pool torrents. *Hydrological Sciences Journal-Journal des Sciences Hydrologiques 27(2)*, 234–244.

Wieland, M., Gray, J., and Hutter, K. 1999. Channelized free-surface flow of cohesionless granular avalanches in a chute with shallow lateral curvature. *Journal of Fluid Mechanics 392*, 73.

Wong, M. 2003. Does the bedload transport relation of Meyer-Peter and Müller fits its own data? *Proc., 30th IAHR-Congress, Thessaloniki, Greece* , 8 pp.

Wu, W., Marsooli, R., and He, Z. 2012. Depth-Averaged Two-Dimensional Model of Unsteady Flow and Sediment Transport due to Noncohesive Embankment Break/Breaching. *Journal of Hydraulic Engineering 138(6)*, 503–516.

Wu, W. and Wang, S. 2004. Depth averaged two dimensional numerical modelling of unsteady flow and non uniform sediment transport in open channels. *Journal of Hydraulic Engineering 130*, 1013–1024.

Wu, W. and Wang, S. 2007. One-Dimensional Modeling of Dam-Break Flow over Movable Beds. *Journal of Hydraulic Engineering 133*, 48–58.

Wu, W. and Wang, S. 2008. One-dimensional explicit finite-volume model for sediment transport with transient flows over movable beds. *Journal of Hydraulic Research 46*, 87–98.

Xia, J., Lin, B., Falconer, R., and Wang, G. 2010. Modelling Dam-break Flows over Mobile Beds using a 2D Coupled Approach. *Advances in Water Resources 33*, 171–183.

Appendix A

Calculus of eigenvalues and eigenvectors for the coupled-Jacobian numerical scheme

The eigenvalues of matrix $\widetilde{\mathbf{J}}_{\mathbf{n}}$ are the roots of the following polynomial:

$$(\widetilde{\lambda}^3 + a_1\,\widetilde{\lambda}^2 + a_2\,\widetilde{\lambda} + a_3) = 0 \tag{A.1}$$

whose coefficients a_1, a_2 and a_3 are given by:

$$a_1 = -2\widetilde{u} \quad a_2 = -p_{bz}\widetilde{B} - \widetilde{c}^2 + \widetilde{u}^2 \quad a_3 = -p_{bz}\widetilde{A} \tag{A.2}$$

Calling $Q = (3a_2 - a_1^2)/9$ and $R = (9a_1a_2 - 27a_3 - 2a_1^3)/54$, the eigenvalues are real if $Q^3 + R^2 < 0$, and are given by

$$\begin{array}{c} \widetilde{\lambda}^2 = 2\sqrt{-Q}\cos(\theta_p/3) - a_1/3 \\ \widetilde{\lambda}^3 = 2\sqrt{-Q}\cos((\theta_p + 2\pi)/3) - a_1/3 \\ \widetilde{\lambda}^4 = 2\sqrt{-Q}\cos((\theta_p - 2\pi)/3) - a_1/3 \end{array} \tag{A.3}$$

with $\theta_p = \arccos(R/\sqrt{-Q^3})$. The eigenvectors $\widetilde{\mathbf{e}}^m$, $m = 1, 2, 3$ associated to $\widetilde{\lambda}^m$, $m = 1, 2, 3$ are given by

$$\widetilde{\mathbf{e}}^m = \begin{pmatrix} 1 \\ \widetilde{\lambda}^m \\ \frac{-\widetilde{c}^2 + \widetilde{u}^2 + \widetilde{\lambda}^m(\widetilde{\lambda}^m - 2\widetilde{u})}{p_{bz}} \end{pmatrix} \tag{A.4}$$

Appendix B

Conservation of the coupled-Jacobian numerical scheme

For the sake of clarity the necessity of the last term in the numerical scheme, B.1, is going to be explained. The lack of this term in the computed method may lead to a non conservative solution, which has been misunderstood by some authors as a diffusivity problem,

$$\mathbf{U}_i^{n+1} = \mathbf{U}_i^n - \sum_{k=1}^{NE} \sum_{m=1}^{4} (\widetilde{\lambda}^- \alpha - \beta^-)_k^m \widetilde{\mathbf{e}}_{JI,k}^m l_k \frac{\Delta t}{A_i} - \sum_{k=1}^{NE} \delta \mathbf{E}_{Ii,k} \mathbf{n}_k l_k \frac{\Delta t}{A_i} \tag{B.1}$$

In case of having a set of equations

$$\frac{\partial \mathbf{U}}{\partial t} + \frac{\partial \mathbf{F}(\mathbf{U})}{\partial x} + \frac{\partial \mathbf{G}(\mathbf{U})}{\partial y} = \mathbf{S}(\mathbf{U}, \mathbf{x}, \mathbf{y}) \tag{B.2}$$

which can be manipulated as follows

$$\frac{\partial \mathbf{U}}{\partial t} + \mathbf{M_n} \left(\frac{\partial \mathbf{U}}{\partial x} + \frac{\partial \mathbf{U}}{\partial y} \right) - \mathbf{H_n} \left(\frac{\partial \mathbf{U}}{\partial x} + \frac{\partial \mathbf{U}}{\partial y} \right) = \mathbf{S_s}(\mathbf{U}, \mathbf{x}, \mathbf{y}) \tag{B.3}$$

where $\mathbf{M_n}$ is the flux normal to a direction given by the unit vector $\mathbf{n}$, $\mathbf{En} = \mathbf{F}n_x + \mathbf{G}n_y$, defined as

$$\mathbf{M_n} = \frac{\partial (\mathbf{En})}{\partial \mathbf{U}} \tag{B.4}$$

and $\mathbf{H_n}$ is the flux associated to the bed slope, projected onto the unit vector $\mathbf{n}$, $\mathbf{T_b n} = \mathbf{S_b} n_x + \mathbf{S_b} n_y$

$$\mathbf{H_n} = \frac{\partial(\mathbf{T_b n})}{\partial \mathbf{U}} \tag{B.5}$$

It is possible to define the following Jacobian matrix, $\mathbf{J_n}$, through the definitions in (B.4) and (B.5)

$$\mathbf{J_n} = \mathbf{M_n} - \mathbf{H_n} \tag{B.6}$$

which will allow us to define system (B.2) as belonging to the family of hyperbolic systems.

$$\frac{\partial \mathbf{U}}{\partial t} + \mathbf{J_n}\left(\frac{\partial \mathbf{U}}{\partial x} + \frac{\partial \mathbf{U}}{\partial y}\right) = \mathbf{S_s}(\mathbf{U}, \mathbf{x}, \mathbf{y}) \tag{B.7}$$

Due to the non linearity of the flow **En**, the Jacobian matrix has to be approximated in order to generate a local linearization. Roe (1986), proposed an approximated Jacobian matrix, $\widetilde{\mathbf{J}}_{\mathbf{n},k}$, for clean water, imposing that

$$\widetilde{\mathbf{J}}_{\mathbf{n}}(\mathbf{U}_i, \mathbf{U}_i) = \mathbf{J_n}(\mathbf{U}_i) \tag{B.8}$$

In Murillo and García-Navarro (2010a) an augmented Roe solver is proposed to allow the inclusion of the sediment transport terms. Hence, it was developed the building of an approximate Jacobian matrix $\widetilde{\mathbf{J}}_{\mathbf{n},k}$ at each k edge of each cell combining the normal flux $\mathbf{E_n} = \mathbf{F}n_x + \mathbf{G}n_y$ with the bed slope source term $\mathbf{T}_{\mathbf{n},b}$ at each cell edge,

$$(\delta\mathbf{E} - \mathbf{T}_b)_k \mathbf{n}_k = (\widetilde{\mathbf{M}}_{\mathbf{n}} - \widetilde{\mathbf{H}}_{\mathbf{n}})_k\ (\mathbf{U}_j - \mathbf{U}_i) \tag{B.9}$$

$$(\delta\mathbf{E} - \mathbf{T_b})_k \mathbf{n}_k = \widetilde{\mathbf{J}}_{\mathbf{n},k} \delta\mathbf{U}_k \tag{B.10}$$

with $\delta(\mathbf{E_n})_k = (\mathbf{E}_j - \mathbf{E}_i)_{\mathbf{n}_k}$, $\delta\mathbf{U}_k = \mathbf{U}_j^n - \mathbf{U}_i^n$, and $\mathbf{U}_i^n$ and $\mathbf{U}_j^n$ the initial values at cells i and j sharing edge k. Figure B.1 collects the previous information in order to solve the Riemann problem in a 2D situation.

On the other hand, the main difficulties in the definition of the approximate Jacobian matrix (B.9) for sediment transport that allows the construction of approximate solutions arises from the presence of a local A_g value, which is variable within each cell, see Figure B.2.

For this reason the net exchange of flow between internal walls must include the difference between the value of the cell in its centroid, $A_{g,i}$, and the value close to the wall within the cell $A_{g,I}$. This fact leads to new definitions of $\mathbf{E}$ at each pair of cells i and j, connected through edge k, that will be referred to as

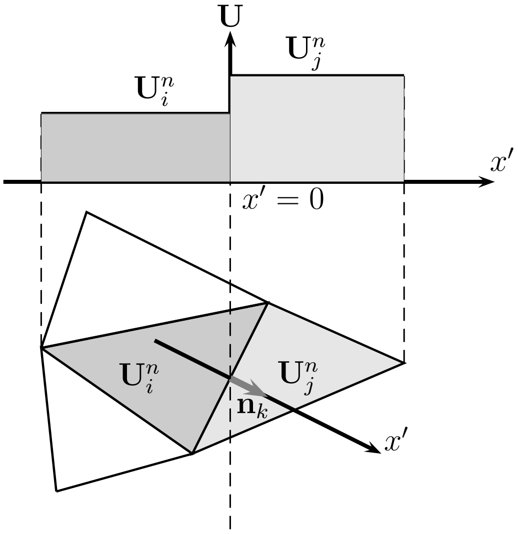

Figure B.1: Riemann problem in 2D along the normal direction to a cell side

$$\mathbf{E}_I = \mathbf{E}(\mathbf{U}_i, A_{g,k}) \qquad \mathbf{E}_J = \mathbf{E}(\mathbf{U}_j, A_{g,k}) \tag{B.11}$$

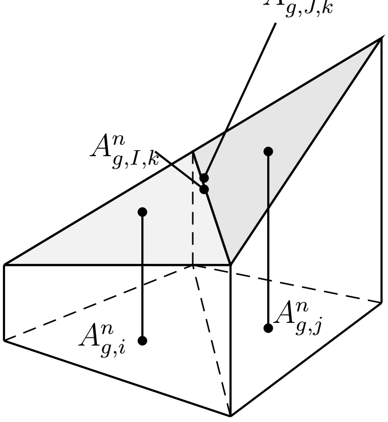

Figure B.2: Linear representation by cells.

Analyzing the flux term $\delta\mathbf{En}$ drives to

$$\begin{aligned} \delta\mathbf{En} &= E_j - E_i = E_J - E_I + (E_j - E_J) - (E_i - E_I) = \\ &= \delta E_{JI} + \delta E_{jJ} - \delta E_{iI} = \\ &= (\delta E_{JI} + \delta E_{Ii}) - \delta E_{Jj} = \\ &= (\delta E^-_{JI} + \delta E_{Ii}) + \delta E^+_{JI} - \delta E_{Jj} = \\ &= (\delta E^-_{JI} + \delta E_{Ii}) - (\delta E^-_{IJ} + \delta E_{Jj}) \end{aligned} \tag{B.12}$$

As it can be appreciated not only a flux crossing the wall, δE^{-}_{JI}, is necessary to ensure a conservative numerical scheme. A flux with information of the variation of $Ag_{I,i}$ is also necessary and this is the additional term which appears in the numerical scheme.